

# Theoretical and computational studies of magnetized dusty plasmas

Joseph Gibson

September 2017

Submitted in partial fulfilment of the requirements for the degree of  
Doctor of Philosophy of Imperial College London

Department of Physics  
Imperial College London  
Prince Consort Road  
London SW7 2BZ



# Declaration

All work presented in this thesis, which I submit for the award of Doctor of Philosophy, is my own unless stated otherwise in the text with a reference to the original work.

**Joseph Gibson**

September 2017

# Copyright

The copyright of this thesis rests with the author and is made available under a Creative Commons Attribution Non-Commercial No Derivatives licence. Researchers are free to copy, distribute or transmit the thesis on the condition that they attribute it, that they do not use it for commercial purposes and that they do not alter, transform or build upon it. For any reuse or redistribution, researchers must make clear to others the licence terms of this work



# Abstract

This dissertation documents my mathematical and computational research on plasmas which contain small, charged particulate matter (dust) in the presence of magnetic fields. Phenomena from two limiting cases of dust dominance are considered, these being where the grains are plentiful enough to introduce new collective plasma behaviours and sparse enough such that the grains are effectively passengers in the plasma.

The study into the former limit looks at the effect which immobile dust grains have on transversely and obliquely propagating Alfvénic solitary waves, with application to cometary and planetary magnetospheres. The spatial structure and permissible range of speeds is derived for the transverse wave. For oblique waves the problem is partially solved, with necessary, but not sufficient, restrictions on the wave speed and direction being found.

Next is a study where dust is not dominant, looking at the plasma structure near to a conducting wall which has an embedded magnetic dipole oriented perpendicular to the surface, with application to dusty crystal experiments and lunar swirls. A study of electron kinetic behaviour is carried out and a novel way to calculate their density is formulated. Once implemented into a sheath model this reveals that a ring of positive space charge appears in the sheath which is capable of influencing dust grain dynamics and repelling incoming ions.



Love and thanks to my parents.

The woods are lovely, dark and deep,  
But I have promises to keep,  
And miles to go before I sleep,  
And miles to go before I sleep.

---

Robert Frost





# Contents

<b>1</b>	<b>Introduction</b>	<b>19</b>
1.1	Plasma . . . . .	19
1.2	Dust and plasma . . . . .	20
1.3	Examples of dust and plasma . . . . .	22
1.3.1	Dusty plasma . . . . .	22
1.3.2	Dust in plasma . . . . .	23
1.4	Focus of this work . . . . .	29
<b>2</b>	<b>Background Theory</b>	<b>30</b>
2.1	Maxwell-Boltzmann distribution . . . . .	30
2.2	Single particle motion in magnetic fields . . . . .	32
2.2.1	Uniform $\mathbf{B}$ . . . . .	32
2.2.2	$\mathbf{E} \times \mathbf{B}$ drifts . . . . .	33
2.2.3	Magnetic mirror . . . . .	34
2.3	The magnetic dipole . . . . .	37
2.4	Plasma-boundary interaction . . . . .	38
2.4.1	Space-charge sheath . . . . .	39
2.4.2	Presheath . . . . .	41
2.5	Dust charging . . . . .	42
2.6	Dusty plasma waves . . . . .	45
2.6.1	Dust-ion acoustic (DIA) waves . . . . .	46
2.6.2	Dust acoustic (DA) waves . . . . .	46
<b>3</b>	<b>Dusty Alfvénic solitary waves</b>	<b>48</b>
3.1	Background . . . . .	48
3.2	Transverse Alfvénic solitary waves . . . . .	50
3.2.1	Dust-free . . . . .	50
3.2.2	With dust . . . . .	56
3.3	Oblique Alfvénic solitary waves . . . . .	62
3.3.1	Dust-free . . . . .	62
3.3.2	With dust . . . . .	67
3.4	Summary . . . . .	72
<b>4</b>	<b>Electron distribution around a magnetic dipole</b>	<b>73</b>
4.1	Experimental observations and simulations . . . . .	73

---

4.2	Theory of radial electric field generation . . . . .	75
4.2.1	Current state . . . . .	75
4.2.2	What can be done . . . . .	77
4.3	Magnetization condition for particles in a dipole field . . . . .	78
4.4	Electron distribution . . . . .	85
4.4.1	1D . . . . .	87
4.4.2	2D . . . . .	93
4.5	Comparison of electron model to observations . . . . .	98
4.6	Summary . . . . .	98
<b>5</b>	<b>Sheath model and its implementation</b>	<b>102</b>
5.1	Sheath model outline . . . . .	102
5.2	Discretisation and finite differences . . . . .	105
5.3	Poisson solver . . . . .	107
5.3.1	Relaxation methods . . . . .	108
5.3.2	Multigrid methods . . . . .	110
5.4	Self consistent Poisson-Density Solution . . . . .	113
5.4.1	Convergence . . . . .	115
5.4.2	Demonstration . . . . .	117
5.5	Fluid ions . . . . .	119
5.6	Benchmarking of solver . . . . .	120
5.6.1	Multigrid tests . . . . .	121
5.6.2	Ion fluid tests . . . . .	122
5.6.3	Newton-Poisson tests . . . . .	122
5.7	Code Implementation . . . . .	126
5.8	Summary . . . . .	126
<b>6</b>	<b>Sheath model results</b>	<b>129</b>
6.1	Results . . . . .	129
6.1.1	Wang's parameters . . . . .	129
6.1.2	Dropmann's parameters . . . . .	134
6.2	Analysis . . . . .	135
6.2.1	Ion reflection . . . . .	135
6.2.2	Radial forces . . . . .	135
6.2.3	Azimuthal ion motion . . . . .	137
<b>7</b>	<b>Conclusions</b>	<b>141</b>
7.1	Summary . . . . .	141
7.2	Future Work . . . . .	142
	<b>Appendices</b>	<b>144</b>
<b>A</b>	<b>Momentum and energy conservation in a dusty plasma</b>	<b>145</b>

---

<b>B Zimmerman field configuration</b>	<b>149</b>
<b>C Cylindrical form of operators and boundary considerations</b>	<b>152</b>
<b>D Ion fluid discretization</b>	<b>156</b>
<b>E Permissions</b>	<b>160</b>

# List of Tables

4.1	Experimental parameters for dust crystal and lunar swirl studies. . . . .	73
4.2	Van Allen radiation belt parameters evaluated at $z = 0$ and $r$ at the typical altitude . . . . .	84

# List of Figures

1.1	Dust grain crystal levitated above the lower electrode as viewed from the side (main) and above (inset). Image credit: Max Planck Institute for Extraterrestrial Physics . . . . .	25
1.2	The archetypal lunar swirl, Reiner Gamma, as photographed by the Lunar Reconnaissance Orbiter. For scale, the large crater is 117km to the east and has diameter of 30km. Image Credit: NASA LRO WAC science team . . . . .	28
2.1	Trajectories of electrons near to an absorbing (but also repelling) wall (a) and the resulting velocity PDF at a height $z$ (b). . . . .	31
2.2	Magnetic field lines in cylindrical coordinates for a dipole centred at the origin with its moment aligned with the $z$ axis. . . . .	38
3.1	Electron (small blue particle) and ion (large red particle) trajectories and electromagnetic fields in the lab (a) and wave (b) reference frames. In (a), the times $t_1 \rightarrow -\infty$ , $t_2 = 0$ , $t_3 \rightarrow \infty$ and so the approaching and leaving wave snapshots should be imagined to be at $x_L \rightarrow \pm\infty$ respectively. . . . .	51
3.2	Sagdeev potential dependence on Alfvén Mach number. $\alpha = 0.5$ is too slow to begin solitary wave formation whereas $\alpha = 2.5$ is too fast to complete the return back to the original state. $\alpha = 1.5$ allows $\beta_z$ to grow from 1 to 2 and back again. All trajectories which leave $\beta_z = 1$ going left will not return. . . . .	54
3.3	Profiles of normalized magnetic field, electric field, transverse electron velocity and plasma density for different wave speeds ( $\alpha = 1.2, 1.4, 1.6, 1.8, 2.0$ ). . . . .	54
3.4	Characteristic width of a solitary wave for a speed $\alpha = 1.5$ with varying Havnes parameter. The minimum value of $H$ is set by equation (3.35) and the maximum follows from (3.38) - to be derived shortly. . . . .	58
3.5	Permitted velocity range of compressive dusty solitary waves as a function of Havnes parameter. . . . .	59
3.6	Sagdeev potentials (a) and wave profiles (b) for different Havnes parameters and a Mach number of $\alpha = 1.5$ . . . . .	60

3.7	Sagdeev potentials and associated magnetic field profiles for parameters which admit both rarefactive and compressive solitary waves (a) and only rarefactive waves (b). In conjunction with Fig. 3.8, one can verify why this choice of parameters produced this result. In (a), $\beta_y$ is relatively weak meaning $\beta_z \approx \beta_\perp$ and so only one of these is plotted. . . . .	65
3.8	Allowed regions of parameter space, $\alpha$ and $\theta$ , for compressive (a) and rarefactive (b) solitary waves. . . . .	66
3.9	Graphical representation of the mutual solution of (3.84) and (3.85). By taking the square of $f(\alpha)$ (dashed line), the position of the roots $\alpha_1$ and $\alpha_2$ stay the same. Then, by subtracting an always positive term $c\alpha^4$ (where $c > 0$ ), the roots of the green curve lie in pairs either side of $\alpha_1$ and $\alpha_2$ , providing the central maxima does not lie under the x axis (which will not be the case). . . . .	69
3.10	Range of allowed parameters for the oblique solitary wave with negatively charged dust. The black outline corresponds to the boundary of the region in Fig. 3.8 (b) and the other lines enclose regions of parameter space in the same way. . . . .	70
3.11	Range of allowed parameters for positively charged dust. . . . .	71
4.1	Electric potential in the sheath above an insulating electrode. Dipole magnetic field lines are also included. . . . .	74
4.2	Void formation as viewed from above. An ordinary dust crystal (A) takes on a ring formation (E) after the magnet is switched on (B) and then returns to its former (I) state after the field is removed at (G). Image credit: D. A. Law . . . . .	76
4.3	Diagram of quantities relevant to deriving the condition of particle-wall collisions. In this case the particle is comfortably able to perform an orbit without striking the wall. . . . .	79
4.4	Plot of $\epsilon$ , for the parameters of Wang. The contour $\epsilon = 1$ is highlighted in red, below this line particles are not magnetized. . . . .	80
4.5	First ( $L_1$ ) and second ( $L_2$ ) order lengthscales for different functions, $f(x)$ . . . . .	82
4.6	Particle performing an orbit around a field line. . . . .	82
4.7	Plot of $\gamma$ on a log scale. The contour $\gamma = 1$ (and so $\log_{10}(\gamma) = 0$ ) is highlighted in red. . . . .	85
4.8	Initial condition for an incoming particle with speed $V$ and impact parameter $b$ , where $R \rightarrow \infty$ . . . . .	87
4.9	Radius of closest approach as a function of impact parameter . . . . .	88
4.10	Particle trajectories for different impact parameters incident on a magnetic dipole at the origin. Highlighted are two trajectories in green and red, just either side of $b = -2\Lambda$ . The red is just below and reaches $r = r_0$ , the green is just above and turns back at $r = \Lambda$ . . . . .	89
4.11	Analytic and computational comparison of electron density . . . . .	90

---

4.12	The exact electron density calculated for a Maxwellian velocity distribution, equation (4.50), in blue. Included are the particle densities trying to replicate this profile by introducing an effective electric potential. In yellow is the Boltzmann distribution for an electric potential given by equation (4.52) and in green is a Boltzmann distribution for the same potential scaled by a factor of three to better fit the exact solution. . . .	91
4.13	For a given electron velocity, particle densities are plotted for the magnetic dipole field (Exact), for an initial guess at the effective potential (Approximate) and an optimized version of this (Approximate with fitting). . . . .	93
4.14	Regions (where the $x$ axis label, $\frac{r}{\Lambda}$ , and the $y$ axis label, $\frac{z}{\Lambda}$ , have been omitted in the figure to maximise area occupied by the plots) accessible to electrons shaded blue as a function of $p_0$ . The region in yellow is not accessible for any value of $p_0$ . . . . .	95
4.15	Particles enter the magnetized region (red), performing orbits the instant they make the transition. The yellow region, traced out by the particle trajectory T, may never be visited. . . . .	96
4.16	Comparison of two forbidden regions of Figs. 4.14 and 4.15 . . . . .	96
4.17	Density scaling factor introduced by magnetic screening. This plot would correspond to normalized particle density in the absence of electric fields.	97
4.18	Overlays of exclusion zones calculated for electrons travelling at the thermal speed and experimental results of: (a) Wang - electric potential, (b) Dropmann - radial acceleration of dust grains in units of $g$ and (c) Saitou - position of dust grain cloud. The colours of the exclusion boundaries are not significant and are only chosen such that they stand out from the colour schemes used by the original authors. . . . .	100
4.19	Electric potential from simulations performed by Zimmerman. The yellow curve gives the exclusion zone for thermal electrons approaching from infinity and the blue gives the exclusion zone for particles which start at the computational boundary. . . . .	101
5.1	Computational domain for sheath model and expected qualitative features. The typical area of influence of the magnet (which has its midpoint at $z_0$ below the electrode surface) is highlighted in blue and is contained within the sheath extending to a height $Z$ and width $R$ . Boundary conditions corresponding to those listed are given and a rough estimate of what to expect for the potentials is given in red. Trajectories of deflected ions are shown at the top. . . . .	104

---

5.2	Restriction from the fine grid (circles) to the coarse grid (crosses). The coarse grid indices are written in bold on the left and top, the fine grid on the bottom and right and because the coarse grid spacing is twice as large, $u_{i,j}^{2h}$ and $u_{2i,2j}^h$ correspond to the value of $u$ at the same point in space. A weighted sum of the neighbouring points highlighted in red is used to determine $u_{i,j}^{2h}$ according to equation (5.16). . . . .	106
5.3	Bilinear interpretation for the general case of continuous $x$ and $y$ (for the prolongation operator, $(x, y)$ will occur on fine grid sites). Intermediate values (blue) $\phi_{x,1}$ and $\phi_{x,2}$ are each found from a weighted sums of $\phi_{1,1}$ , $\phi_{2,1}$ and $\phi_{1,2}$ , $\phi_{2,2}$ respectively. Then, $\phi_{x,y}$ is the result of another weighted sum of these two values. . . . .	108
5.4	Demonstration of Jacobi relaxation for 20 grid points ( $h=0.05$ ). A poor initial guess was intentionally chosen to demonstrate that high frequency features are quickly smoothed out - then begins a long relaxation phase until the solution ( $-\sin(\pi x)$ , shown in black) is reached. . . . .	109
5.5	A 1D example of the two grid method, enumerated previously as 1, 2, 3 i-v, 4 (each box of this figure numbered correspondingly). For this example the source term $\rho = -\pi^2 \sin(\pi x)$ is used, which has the solution $\phi = \sin(\pi x)$ for boundary conditions $\phi(0) = \phi(1) = 0$ . . . . .	112
5.6	Stages of 2-grid (a), 3-grid (b) and 4-grid (c) algorithms for $\gamma = 1, 2$ . The 3-grid example with $\gamma = 1$ has the processes explicitly stated for clarity, the others just use 'S' to indicate Smoothing and 'E' to indicate the calculation of an Exact solution. . . . .	114
5.7	A FMG cycle for 4 grids and $\gamma = 1$ . . . . .	114
5.8	Convergence tests on large ( $L = 10$ ) to small ( $L = 1$ ) domains for different values of $f$ . $f = 1$ is included in all plots to demonstrate how the unweighted approach is hopeless in the cases of (a) and (b). A few selected values in the vicinity of $f_{\text{crit}}$ are included to verify that this value marks the transition to a convergent scheme. Also, the optimum $f$ resulting in the most rapid convergence is plotted, these values being 0.4, 0.55 and 0.9 in (a), (b) and (c) respectively. . . . .	118
5.9	Sites where $v_r, v_z$ and $n$ are known are given in blue, sites where they are not are in red. The green point is another unknown, however, it is about to be evaluated by using values at the sites $(i, j)$ , $(i, j+1)$ , $(i-1, j)$ and $(i+1, j)$ . . . . .	121
5.10	On the left are the multigrid solver's efforts at solving Laplace's equation (when $k = 1$ in the third boundary condition) for increasing values of $J$ and opposite are the normalized errors on a logarithmic scale. The increased error on axis probably results because a definite value of the potential is not known here, just the gradient. . . . .	123
5.11	See caption for Fig. 5.10, in this case $k = 3$ . . . . .	124

---



5.12	Analysis of ion density code error for the planar sheath. In this case $J = 129$ . . . . .	125
5.13	The Newton-Poisson solver is initiated on the analytic solution, but with $f = 0.5$ which is too large. The divergence progressing through each iteration of the Newton-Poisson method, $i$ , is shown. The fact that this is basically independent of $J$ shows that it is futile to attempt to fix this numerical instability with finer grids (as might be an instinctive course of action). . . . .	127
5.14	The solver is initialized with a potential 20% away from the solution. If $f$ is low enough the solver converges and the error of the final value is improved with increasing $J$ . . . . .	128
6.1	Space charge density normalised to that of the ions in the bulk plasma, $en_0$ . From the top down, the magnetic moment is 4, 6 and 8 ( $\times 10^{-8} \text{T m}^3$ ). . . . .	130
6.2	Radial electric field, from the top down, the magnetic moment is 4, 6 and 8 ( $\times 10^{-8} \text{T m}^3$ ). . . . .	131
6.3	Electric potential, from the top down, the magnetic moment is 4, 6 and 8 ( $\times 10^{-8} \text{T m}^3$ ). The vertical extent is extended to 10cm to capture the potential growth emerging at the sheath edge. . . . .	132
6.4	Sheath profiles for the plasma parameters of Wang and the strongest magnet that could be simulated, $\mathcal{M} = \mathcal{M}_{\text{crit}}^W$ . . . . .	133
6.5	Sheath profiles for the plasma parameters of Dropmann and the strongest magnet that could be simulated, $\mathcal{M} = \mathcal{M}_{\text{crit}}^D$ . . . . .	134
6.6	Radial acceleration (normalised to gravitational acceleration, $g$ ) in a Dropmann sheath for $r_d = 5.95 \mu\text{m}$ . The radial acceleration through-out (a) and at the estimated levitation height of $2.7 \text{mm}$ (b) is given. . . . .	137
6.7	Continued overleaf. . . . .	138
6.7	Radial ion drag force, $F_{\text{ions}}$ , electrostatic force, $F_E$ , and their total, $F_{\text{tot}}$ , for increasing values of dust grain radius. For $r_d = 100 \mu\text{m}$ , (a), the electric field dominates and for $r_d = 300 \mu\text{m}$ , (c), the ions do. . . . .	139
6.8	$\mathbf{E} \times \mathbf{B}$ drift velocity (a) and ratio of contributions to $\mathbf{E} \times \mathbf{B}$ (b) . . . . .	140
B.1	Coordinate system to derive the magnetic field due to antiparallel currents. . . . .	150
C.1	Contribution of coarse grid points (crosses) $F_1$ and $F_2$ to the fine grid point (circle) $f$ is weighted by the areas $A_1$ and $A_2$ . . . . .	154
C.2	Contribution of two fine grid points $f_0$ and $f_1$ to the coarse grid value on axis, $F_0$ . . . . .	155
E.1	Permission for Figs. 4.1 and 4.18 (a) originally in [1]. . . . .	160
E.2	Permission for Fig. 4.18 (b) originally in [2]. . . . .	161
E.3	Permission for Fig. 4.18 (c) originally in [3]. . . . .	162
E.4	Permission for Fig. 4.19 originally in [4]. . . . .	163

---



# 1 Introduction

## 1.1 Plasma

“In the beginning was the plasma” [5]. Hannes Alfvén ended his Nobel lecture of 1970 in this way to remind us from what we and our surroundings were born. In fact, one may argue that the world we occupy now is not so different from its genesis, the three states of matter familiar to us: solids, liquids and gases are incredibly rare in the universe, the fourth state, plasma, being at least thousands of times more abundant [6].

**The fourth state of matter** The notion of four states of matter can be credited to Empedocles in the 5th century, who’s account of the four elements of water, earth, air and fire, and their intermingling, can be considered a rudimentary scientific exercise (though clothed in mythology and symbolism). Before him, the Ionian philosophers had singled out one substance or another as being the most fundamental and of these Heraclitus deserves mention for his choice of fire. Though taken out of context, some of his quotes do not inaccurately describe which medium dominates the Universe: “The world, an entity out of everything, was created by neither gods nor men, but was, is and will be eternally living fire” and “The thunderbolt steers the Universe”.

A more credible conjecture of a fourth state came early in the 19th century, when Michael Faraday was considering the diminishing physical properties (shape, softness, colour, opacity etc.) which accompanied phase transitions from solids up to gases. He did not believe that this resignation of properties in the matter ceased at the gaseous stage and conceived a further change “as far beyond vaporization as that is above fluidity” to a new state he called “radiant matter” [7]. However, his logical progression led him to erroneously believe that radiant matter would be qualitatively less rich than gases, a deduction which could not be further from the truth.

Sixty three years later, William Crookes identified Faraday’s radiant matter with what he observed in his low temperature electrical discharge [8] and his experimental work was to be the foundation of a discovery which had profound implications for chemistry and physics. This came two decades later when J.J Thompson explained Crookes’ findings by inferring the existence of electrons [9], the first discovery of a subatomic particle. Consequently, it could finally be understood that the fourth state of matter was a soup of oppositely charged particles and in the early part of the 20th century the field of ‘plasma’ physics was born and nurtured by Irving Langmuir.

**Qualitative properties** A plasma is defined as: *A quasi-neutral gas, sufficiently ionised to exhibit collective behaviours.* “Quasi-neutral” refers to the property that on a macroscopic scale, the charge density is effectively zero and “collective behaviours” refer to any macroscopic phenomena which do not exist in gases. Charged particles are influenced by, and provide sources of, electromagnetic fields and so collective behaviours may be realised in many extra ways than in gases. One fact which illustrates this is that whereas a gas can only support the propagation of sound waves (and allows the passage of light), at least 12 species of wave can exist in a plasma [10]. Another consequence of the involvement of electromagnetism is that the strong forces which are introduced set the ionisation threshold as low as one ion-electron pair per million neutral particles [11].

As well as the name ‘plasma’ [12], Langmuir introduced another term to refer to an important region which accompanies most terrestrial plasmas. In his study of the mercury arc discharge, he observed that in the vicinity of the walls and electrodes, the density of positive ions far exceeded that of the electrons [13]. This positive space charge region, which screens the wall from the plasma, he decided to call the ‘sheath’ and the characteristic width was later found as the Debye length,  $\lambda_{De}$ .

In 1924 it was Langmuir who presented “...phenomena of remarkable beauty which may prove to be of theoretical interest” [14] in an address marking the Centenary of the Franklin Institute in Philadelphia. What he described were streams of minute globules of tungsten sputtered from the cathode of his plasma discharge, possibly the first laboratory observation of dust in a plasma.

## 1.2 Dust and plasma

Plasmas are very rarely pure and often contain an additional component of liquid or solid charged macro-particles referred to as ‘dust’. There is no strict definition for what constitutes a dust grain, but this property of being electrically charged (or, at least, exchanging charge with the plasma) is the key and perhaps only criterion since it is what influences the grain dynamics and modifies the surrounding plasma. Properties such as shape or material composition do not seem to feature, so long as they do not prevent the all important charging process, however, the size of the grains is restricted. Since the dominant charging mechanism is the accumulation of plasma ions and electrons, this sets the lower limit on the size of a dust grain at the nanometer scale, below which the cross section for particle collection becomes negligible. To ensure that the dust can be considered a component of the plasma, the upper limit for grain size is set rather simply as much less than the characteristic size of the plasma. Under this description, examples of dust could range from a micron sized droplet of tungsten in a tokamak to a communications satellite bathed in the solar wind.

After a cursory review of the dusty plasma literature it becomes apparent that the

---

word ‘ubiquitous’ is an autological one<sup>1</sup>. The context in which it appears so often is to emphasise how common dust grains are in “cosmic plasmas, planetary plasmas, plasmas near the earth and plasmas in the laboratory” [15]. It seems to be the case that there is nearly always a supply of dust and so if a plasma is cool enough for grains to exist, it will probably have some present.

Studies of dust in plasma can be divided into a few sub-disciplines loosely distinguished by the degree to which dust modifies, or introduces, collective behaviours. To differentiate between these categories, the relevant quantities are firstly the ratio of the Debye length (since dust grains are themselves surrounded by a sheath) and the inter particle separation  $\Delta$  (set by the density of dust grains,  $\Delta = n_d^{-\frac{1}{3}}$ ). The relative size of these lengths determines to what extent dust grains interact with each other. The other relevant quantity is the Havnes parameter [16],  $H \equiv \frac{Z_d n_d}{n_i}$ , which is a measure of how much charge the dust grains hold as compared to the plasma. It is quite common to see all cases of dust and plasma referred to as ‘dusty plasma’ and the definitions I am about to introduce have been used, but certainly not consistently.

**Dust in plasma** In this case it is the dynamics and properties of individual grains which are of interest. This can range from cases where dust is sufficiently sparse ( $\Delta > \lambda_{De}$ ) such that they can be assumed not to mutually interact and hold much less charge than the background plasma ( $|H| \approx 0$ ), so that the plasma as a whole is unperturbed. In these instances, the interesting questions revolve around topics such as where they go (for example the droplet in the tokamak) or how much charge they hold (perhaps the communications satellite). This second question on the charging of individual grains also overlaps with diagnostics which operate by collection of plasma particles such as Langmuir probes [17].

There is also the case where dust grains are close enough to interact ( $\Delta < \lambda_{De}$ ), but still not plentiful enough to have an appreciable effect on the plasma charge ( $|H| \approx 0$ ). Collective behaviours of the dust appear, such as self arrangement into a crystal formation, but collective behaviours of the plasma are unchanged. It is not uncommon to see these referred to as instances of ‘complex plasma’.

**Dusty plasma** If the amount of charge invested in the dust grains is comparable to that in the plasma ( $H \gtrsim 0$ ), then the ions and electrons no longer preserve quasi-neutrality on their own and plasma behaviour is modified [18] or dominated [19] by this departure. The lengthscales of interest are generally large, meaning that dust particles are considered a continuous plasma component on an equal footing with the ions and electrons, albeit far heavier and with a much larger, variable charge.

This thesis deals with problems belonging to both of the above fields and now it’s time for some more in-depth background for each. The examples provided serve to put

---

<sup>1</sup>An autological word is one which describes itself. For example: short, pentasyllabic and Afrikaans.

into context dust and plasma in the real world, but they are also carefully chosen to outline the topics this thesis will be most relevant to.

## 1.3 Examples of dust and plasma

### 1.3.1 Dusty plasma

The addition of a charged dust component expands the zoo of plasma waves and instabilities further still. Up to two new features need to be accounted for: quasineutrality is no longer preserved exclusively between electrons and ions and sometimes the dynamics of dust grains become important. Whether or not the latter alteration is relevant divides between two families of dusty plasma waves. The first is waves with characteristic timescales too fast for the dust grains to respond and the second is a new ultra low frequency regime where the inertia is provided by the heavy dust grains. An example of each is provided in the next chapter, section 2.6, but for now I shall just describe the qualitative features assuming, as is usually the case, that the dust grains are negatively charged.

In the fast regime, where the dust is stationary, the plasma is robbed of a fraction of its mobile negative charge. An important effect in plasma physics is that electrons will tend to distribute themselves such that they screen out any regions of non-neutral charge. Oftentimes the restoring force of a plasma wave is provided by electric fields and so if the electron population is diminished, the screening of charge is less efficient meaning that the electric fields are able to extend further to couple charged regions of plasma more strongly. There are also consequences for magnetic waves: a drop in electron density will lead to a suppression of the current they can provide and so any magnetic fields are likely to be weakened. To understand the nature of the slow regime, one may picture this as having analogous behaviour to quasineutral plasma. For ordinary plasma waves where the ion inertia dominates, one may roughly picture this as heavy positively charged particles surrounded by an inertia-less negatively charged fluid. Likewise, in a dust inertia dominated wave one now has heavy negative particles immersed in a positively charged inertialess fluid, since the ion inertia can be ignored here too and they outnumber the electrons. Thus, slow waves tend to resemble their plasma counterparts, with modified mass and charge densities.

It is fair to say that the theory of dusty plasma waves far exceeds the work done in the laboratory. Both slow and fast modes of dusty plasma waves have been produced in the laboratory in the form of dust-acoustic [20] and dust-ion acoustic [21] waves respectively. Much theoretical work has been done on the implications of dust for electromagnetic waves for both stationary and dynamic dust [22] [23] [24]. Such publications point out that there are plenty of candidate dusty plasmas in space to support the waves of their study (cometary atmospheres, interstellar molecular clouds, the lower and upper mesosphere and planetary rings to name a few) [25] [26] [27], but, this appears to be, as Verheest described, "...a situation where the theoretical studies concerning waves and

---

instabilities in dusty (space) plasmas are far ahead of what observations can corroborate at present. Due to the paucity of coming solar system missions specifically concerned with planetary or cometary phenomena, the situation is unlikely to change much in the near future.” [28]

There are many effects which complicate the analysis of these waves. First of these is that a dust fluid is likely to consist of a variety grain sizes. In these cases the grain mass and charge are replaced by their average values and so one needs to know the probability distribution of sizes and a model which accurately calculates grain charge as a function of radius. The effect of taking a power law and normal distribution for the grain sizes has been investigated for dust acoustic waves [29]. Secondly, a dust grain’s charge depends on its surroundings, both through the plasma parameters and the density of neighboring grains [30]. Given that at least the former of these will be oscillating in space, dust grains will be charged differently at different points in the wave. A dust grain also takes a finite amount of time to adjust its charge to fit with its new surroundings and so it is possible that for frequencies too fast for the dust to equilibrate one must employ a fully transient model for the grain charge which is a dynamical variable. This effect is responsible for the damping of Langmuir oscillations in a dusty plasma [31]. Strong coupling of the grains may also become an important feature [32] if the dust grain density is sufficiently high.

### 1.3.2 Dust in plasma

Now to give three areas of dust in plasma to which this work will be most pertinent. The common features of these are, loosely speaking, dust grains in the sheath region with an externally applied dipole magnetic field.

#### **Semiconductor processing**

A chemically reactive plasma discharge offers great scope to modify the surface properties of materials, or indeed, to create new ones [33]. Because of this, “plasma processing technology is vitally important to several of the largest manufacturing industries in the world” [34]. I shall now focus on the semiconductor industry, for which the processes of deposition and etching are critical in the fabrication of microchips. The former process allows thin films of metal to be layered onto a wafer and the latter carves out from these the sub-micron features of the circuit. Owing to the delicate nature of microelectronics, contamination by dust grains can degrade reliability by weakening adhesion between layers or cause device failure by shorting the circuit [35]. Given that manufacturers are not inclined to share their findings on tackling this problem, it is difficult to ascertain its exact magnitude. It has been estimated that particulate contamination was responsible for over 50% of device yield losses in 1990 [36], over 80% in 1996 [37] and as of 2006 semiconductor companies were spending billions of dollars annually to tackle the problem [35]. More recent publications still stress that particulate contamination remains a key challenge [38] [39].

---

During a routine inspection in 1989, Gary Selwyn of IBM made an accidental discovery which revealed that particulate contamination was occurring during the plasma processing phase [40], in fact, contamination inside the vessel was to the extent that “often, the level of dust in a plasma process tool exceeds the cleanroom by several orders of magnitude” [41]. Selwyn was intending to determine the chemical concentrations in the plasma by measuring the weak fluorescence induced by laser illumination. Instead of this, he observed the light to be strongly scattered by clouds of micron sized particles hovering over the lower electrode. The explanation for this starts with dust being produced in situ either by nucleation [42] or by flaking off from the walls [43] and then falling down through the vessel under gravity. The walls each have an associated sheath region, the electric field acting to repel the dust grains (which are negatively charged) back into the plasma. Grains will remain in the plasma and continue to fall until the electrostatic repulsion of the lower electrode equals their weight and they levitate ominously above the microchip being fabricated. When the plasma processing is complete, the plasma is switched off and the grains fall onto the chip.

Several methods have been proposed for the removal of dust, each candidate differing in the mechanism by which the particles are pushed: radiation pressure from a high power laser beam [44], modulation of the electrode voltage [45], electrostatic wells [46], thermophoretic force [47] and drag from a jet of plasma [48]. Most relevant to my work here, a collaborator performed experiments with a bar magnet placed under the lower electrode and was able to influence the levitating grains, intimating that this may provide a mechanism for their removal (A. Dyson, private correspondence).

### Laboratory dust in plasma

Though a curse for the semiconductor industry, the discovery that dust particles can be suspended in a laboratory plasma discharge was a blessing for dusty plasma physicists as it provided an ideal environment for their experimental study (see Fig. 1.1) which had been lagging behind the theory at that time. The same basic apparatus is used, with the addition of a mechanism to introduce dust to the discharge and usually an enhanced radial electric field to ensure that the particles remain central and do not disperse under their mutual repulsion. The length and time scales involved are also particularly convenient. Relatively large interparticle spacings and relatively slow speeds allow individual particle dynamics to be fully resolved. The experimentalist also has the opportunity to manipulate the grains either collectively or individually with, for example, electromagnetic fields or light pressure (or any other force which has been suggested for their removal in the previous section). Notable early experiments led to the discovery of Coulomb crystals [49] [50] [51] and provided verification of dust acoustic waves [20] five years after their theoretical inception [18].

The spontaneous self organisation of dust into crystalline states has become an area of great interest [52] as the archetypal complex plasma. Dust grains meet all the criteria to be considered a new state of soft matter, defined by its founder Pierre-Gilles de Gennes

---



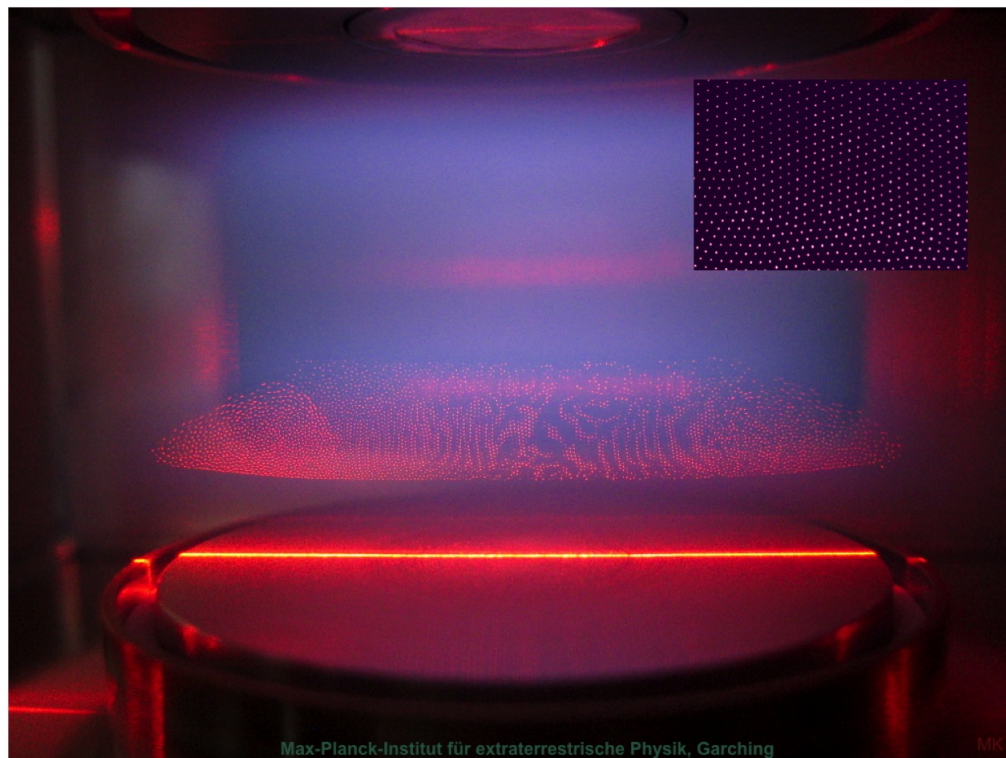


Figure 1.1: Dust grain crystal levitated above the lower electrode as viewed from the side (main) and above (inset). Image credit: Max Planck Institute for Extraterrestrial Physics

to be “supramolecular substances which exhibit special properties such as macroscopic softness or elasticity ... and where the relevant physics is far above the quantum level”. As well being interesting in their own right as a new type of soft matter, complex plasmas are used to act as a macroscopic model system for phenomena in liquids and crystals. To name just a few, the atomistic dynamics in fluids [53], kinetics of heat transport [54] and properties of crystals [55] have been explored. Complex fluids, the counterpart to complex plasmas have played this role in the past [56] (for this de Gennes received the Nobel prize in 1991), but the more versatile nature of plasmas means there is scope to study a greater variety of structures.

The effects of introducing a magnetic field to the arrangement has proved to be an area of great interest. Magnetic fields indirectly influence dust dynamics by inducing motions in the plasma which then impart momentum to the grains. If one is able to accurately characterise the plasma behaviour, this serves as a tool to investigate the forces on the grain. Also, differential motions of the grains can be induced [57], providing the opportunity to examine, for example, the viscous properties of the dusty crystal. With a constant axial magnetic field (this being the axis of symmetry, perpendicular to the lower electrode), one of the phenomena which has interested the community most is the rotation of the dust cloud [57] [58] [59], [60] [61]. It was not until the last of these publications when the effect was truly understood: the magnetic fields deflect the ions, inducing an azimuthal velocity component and then collisions of these with neutral particles ‘stir’ the background gas which, in turn, imparts azimuthal momentum to the dust grains.

Of interest to this thesis are those experiments which have studied the effects of a non-uniform field geometry [62] [63] [3] (A. Dyson, private correspondence). In particular, I will concentrate on the latter three of these where the magnetic field is sourced by a small permanent magnet under the lower electrode providing, to lowest order, a dipole type field. In addition to these, there are nearly identical experiments which have been performed, but they are not strictly speaking complex plasma experiments and will be introduced in the next section. As well as rotational motion of dust, a new feature is observed which has so far not been explained: a radial redistribution of the dust particles. In most cases, a void forms directly above the magnet leaving a ring shaped cloud of dust, although, in one case the opposite was observed: the magnet lead to particles becoming more tightly bound to the axis (A. Dyson). Radial redistribution has been observed in all of the experiments using dipole field geometries and in only one of the five aforementioned experiments using an axial field [57], thus one concludes that the geometry of the field is central to understanding void formation, though, perhaps not providing the only mechanism.

## **Lunar dust**

**Lunar dust plasma environment** The moon is surrounded by a permanent, anisotropic cloud of dust, characterised recently [64] with data from the Lunar Atmosphere and Dust

---

Environment Explorer (LADEE) mission to weigh over 100kg, extending to a typical altitude of 100km and consisting of grains of radius  $0.3 - 1\mu\text{m}$ . This gravitationally confined cloud is sustained by the plumes kicked up by the bombardment of interplanetary dust particles. The anisotropic flux of these particles is the reason why the dust distribution is not spherically symmetric, but strongly enhanced around the morning terminator (the line separating lunar day from night).

The interaction between the moon and solar wind leads to a complex and varied environment containing “a veritable host of fascinating plasma physics” [65]. Supersonic plasma flow and UV and soft X-rays from the Sun impinge upon the exposed dayside. This solar radiation begets a population of photoelectrons dominating the sheath near to the surface ( $< 10\text{m}$ ), the photoelectron current exceeds that incoming from the solar wind resulting in a net positive surface charge [66]. Due to the losses of ions and electrons to the dayside and the high speed of the solar wind, a wake is formed downstream of the moon extending for tens of lunar radii [67]. The nature of the downstream plasma is beyond the scope of this work, but the end result just above the nightside is a tenuous Debye sheath above a negative surface charge [68].

It is worth mentioning the controversial topic of electrostatic lofting of dust grains. In the terminator region, dark and illuminated patches are juxtaposed resulting in large potential differences over small distances. It has been suggested that the resulting electric fields may be strong enough to unstick dust grains from the surface and to launch them to altitudes up to 100km [69]. This population of dust has been conjectured to explain observations made during the Apollo era of light scattering at high altitude [70], however, LADEE did not discover this putative component leaving these effects unexplained.

At any rate, the coexistence of the dust cloud and plasma indicates that the lunar exosphere constitutes an example of dust in plasma. One may, in fact, argue this to be true on a larger scale also: the moon itself is a solitary insulating dust grain suspended in a supersonic plasma flow. Now I turn attention to one specific phenomenon occurring on the lunar surface which has sparked much interest recently and has overlap with this work.

**Lunar swirls** Visually striking, sinuous patterns on the lunar surface (see Fig. 1.2) were first observed by astronomers during the Renaissance and have been the enigmatic subject of intense study over the past few decades. These high albedo features have an optical maturity far lower than their dark surroundings which appear so due to the effects of space weathering. Although the moon does not possess a global magnetic field, data from Apollo 15 and 16 subsatellites revealed that there exist isolated magnetised crustal patches [71] and the size and location of lunar swirls is found to always overlap with one of these ‘magnetic anomalies’ [72].

The leading hypotheses for swirl formation postulate that the magnetic field modifies the plasma environment above the lunar surface. This can be further divided into two categories, the first being the mini-magnetosphere theory, applying to stronger magnetic

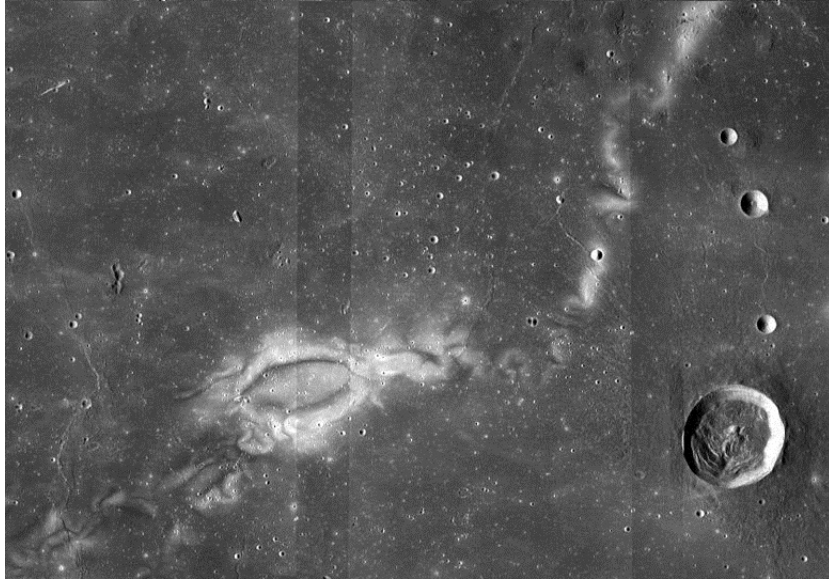


Figure 1.2: The archetypal lunar swirl, Reiner Gamma, as photographed by the Lunar Reconnaissance Orbiter. For scale, the large crater is 117km to the east and has diameter of 30km. Image Credit: NASA LRO WAC science team

anomalies such as Reiner Gamma [73]. A stand off of the solar wind is achieved approximately at the altitude,  $L$ , where lunar magnetic pressure overcomes the ram pressure of the incoming plasma at which point an abrupt boundary layer (magnetopause) of characteristic thickness the electron skin depth,  $d_e$ , forms. Such features are sometimes referred to as ‘magnetic bubbles’, in this analogy having a radius  $L$ , film thickness  $d_e$  and an interior void of plasma. Thus, the patch of surface enclosed by the points to which this bubble adheres is shielded from solar wind ion bombardment. On a far grander scale, it is the same mechanism which protects the Earth’s inhabitants from the solar wind.

For smaller anomalies, where the magnetic field is too weak for a stand off to form, another mechanism has been suggested to prevent ions from reaching the surface [74]. In this case, only the electrons are directly influenced by the magnetic field and strong electric fields arise near the surface due to their redistribution. This process is kinetic in nature, resulting in a new physical regime an order of magnitude smaller than mini-magnetospheres. It has been suggested that these fields mobilise dust particles, with the preferential transport of the finest grains (which are also the brightest) being responsible for the observed patterns [75]. However, it may instead be the case that ions are deflected by the electric fields, again resulting in protection from space weathering. The experiments and simulations related to this phenomenon are the ones I alluded to in the previous section as having coincidental similarity to dusty crystal experiments. These studies, as well as simulations, will be described in more depth in Chapter 4.

The work done in this field not only serves to demystify lunar patterns. The large length scale and possibility of in situ diagnostics provides a natural laboratory with the rare opportunity to study a wealth of plasma phenomena at the finest level [76]. It

---

has also been suggested that a mini-magnetosphere effect could be employed to protect spacecraft, and the crew members inside, from the hazard of interplanetary radiation [77].

## 1.4 Focus of this work

This thesis covers topics from the two branches outlined in sections 1.3.1 and 1.3.2, both involving plasmas where magnetic fields are present. The first, contained in Chapter 3, is a study in the field of dusty plasma physics and extends the theory of dusty plasma waves by considering two nonlinear magnetic plasma waves, as yet unstudied to include immobile dust. The remaining chapters are then dedicated to a second task, a study of plasma boundary interaction with an externally applied magnetic dipole, having application to all three examples outlined in section 1.3.2 on ‘dust in plasmas’. The current state of affairs is outlined at the start of Chapter 4 and then some improvements which can be made will be developed there. The numerical methods required to realise the new model which results are outlined in Chapter 5 and then findings of this are given in Chapter 6. Before all of this can begin, it is necessary to introduce some basic underlying theories.

---

## 2 Background Theory

This chapter is reserved for results which are used throughout this work and are too important or non-trivial to be taken for granted.

### 2.1 Maxwell-Boltzmann distribution

A gas of charged particles moving under the influence of an electric potential,  $\phi(\mathbf{x})$ , presents an unimaginably complicated dynamical problem. Despite this, Boltzmann succeeded in determining how the particles will distribute themselves, both in position and velocity space. Under the assumption that the particles have had enough time to settle to thermal equilibrium, he reasoned that the probability distribution function (PDF) for finding a particle at a position  $\mathbf{x}$  with a velocity  $\mathbf{v}$  is

$$f_{\mathbf{x},\mathbf{v}}(\mathbf{x}, \mathbf{v}) = \mathcal{N} \exp\left(\frac{\frac{1}{2}m\mathbf{v} \cdot \mathbf{v} + q\phi(\mathbf{x})}{k_B T}\right), \quad (2.1)$$

where  $T$  is the temperature,  $\mathcal{N}$  is some normalizing factor to ensure that  $\int d^3\mathbf{x} \int d^3\mathbf{v} f_{\mathbf{x},\mathbf{v}} = 1$  and equation (2.1) is referred to as the ‘Maxwell-Boltzmann distribution’ (MBD). The integral of this over velocity space is commonly referred to as the Boltzmann Relation (BR), giving how the spatial distribution of particles depends on the potential

$$n(\mathbf{x}) = n_0 \exp\left(\frac{e\phi(\mathbf{x})}{k_B T_e}\right), \quad (2.2)$$

with  $n_0$  being the particle density where the potential is zero. The part of the MBD involving velocity is referred to as the Maxwellian Velocity Distribution (MVD)

$$\begin{aligned} f_{\mathbf{v}}(v_x, v_y, v_z) &= \left(\frac{m}{2\pi k_B T}\right)^{\frac{3}{2}} \exp\left(-\frac{m(v_x^2 + v_y^2 + v_z^2)}{2k_B T}\right) \\ &\equiv f_{v_x}(v_x) f_{v_y}(v_y) f_{v_z}(v_z), \end{aligned} \quad (2.3)$$

where

$$f_{v_j}(v_j) = \left(\frac{m}{2\pi k_B T}\right)^{\frac{1}{2}} \exp\left(-\frac{mv_j^2}{2k_B T}\right) \quad (2.4)$$

is the PDF for the  $j^{\text{th}}$  velocity component. The MBD has the astonishing feature that despite the presence of a force field accelerating and decelerating particles, at any point

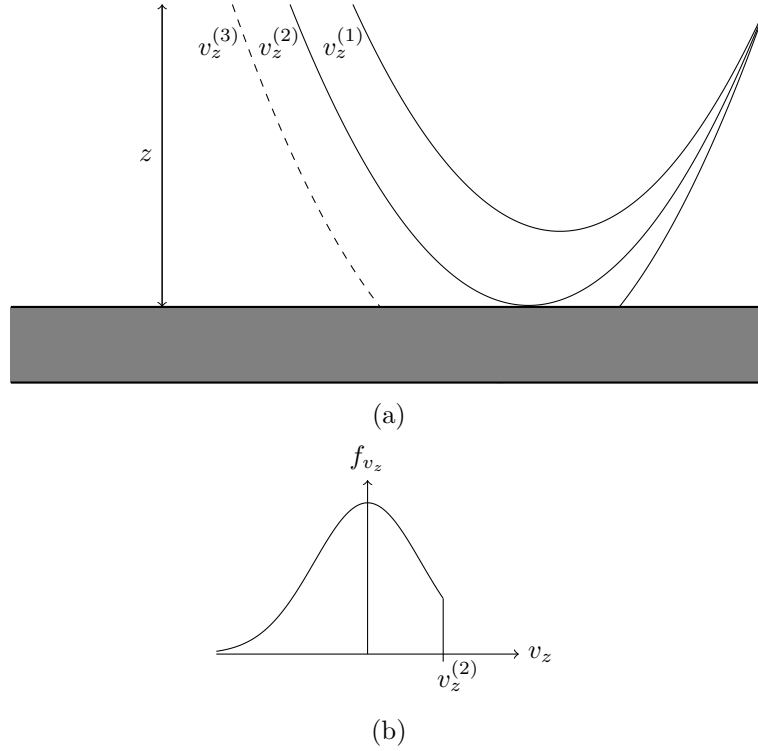


Figure 2.1: Trajectories of electrons near to an absorbing (but also repelling) wall (a) and the resulting velocity PDF at a height  $z$  (b).

in space the velocity distribution is the same. ET Jaynes, a heavyweight of statistical mechanics, pointed out that “a Maxwellian velocity distribution, once established, is maintained automatically, without any help from collisions, as the molecules [particles] move about in any conservative force field” [78, p. 16].

One feature the MBD does not account for is sources and sinks of particles and the following example will provide a useful illustration of how an absorbing surface modifies the picture for a collisionless plasma. In one dimension (1D), imagine electrons with a MVD at infinity and a repelling plane (which is a sink of particles) located at  $z = 0$  with a potential  $\phi_W < \phi(\infty) = 0$ . A particle at some height  $z$  will have got there from infinity - if its  $z$  velocity,  $v_z$ , is negative it is still on its inbound journey and if it’s positive it has at some stage had its motion reflected. Consider the trajectories of Fig. 2.1, showing how three particles contribute to the velocity PDF at a height  $z$  during their inward and outward passages. From energy conservation, the inbound and outbound speeds at  $z$  are the same for each particle and the  $v_z^{(2)}$  trajectory is significant as it is one which just escapes a scrape with the surface. A patch of plasma at  $z$  will feature  $-v_z^{(1)}$ ,  $-v_z^{(2)}$  and  $-v_z^{(3)}$ , as well as  $v_z^{(1)}$  and  $v_z^{(2)}$  but will be missing  $v_z^{(3)}$  which is lost to the wall. To generalize this, the distribution function at a height  $z$  will be zero for velocities  $v_z > v_z^{(W)}(z) \equiv \sqrt{\frac{2e(\phi(z) - \phi_W)}{m}}$ . The self-preserving property of a MVD still applies, however, and the shape is maintained, just with a discontinuous chopped-off region to account for particles lost to the wall (see Fig. 2.1 (b)). What this implies for the density is a reduction in proportion to the fraction of particles which are missing.

Performing this calculation

$$\begin{aligned}
 n &= n_0 \exp\left(\frac{e\phi(\mathbf{x})}{k_B T_e}\right) \frac{\int_{-\infty}^{v_z^{(W)}(z)} f_{v_z}(v_z) dv_z}{\int_{-\infty}^{v_z^{(W)}(\infty)} f_{v_z}(v_z) dv_z} \\
 &= n_0 \exp\left(\frac{e\phi(\mathbf{x})}{k_B T_e}\right) \frac{\left(1 + \operatorname{erf}\left(\sqrt{\frac{m}{2k_B T}} v_z^{(W)}(z)\right)\right)}{\left(1 + \operatorname{erf}\left(\sqrt{\frac{m}{2k_B T}} v_z^{(W)}(\infty)\right)\right)}. \quad (2.5)
 \end{aligned}$$

This form of the electron density has been used to provide a more accurate description of the sheath profile [79].

## 2.2 Single particle motion in magnetic fields

### 2.2.1 Uniform B

In component form, the equations of motion for a particle in a uniform magnetic field,  $\mathbf{B} = B\hat{z}$ , are

$$\frac{dv_x}{dt} = \frac{qB}{m} v_y, \quad (2.6)$$

$$\frac{dv_y}{dt} = -\frac{qB}{m} v_x, \quad (2.7)$$

$$\frac{dv_z}{dt} = 0. \quad (2.8)$$

Equations (2.6) and (2.7) can be decoupled by differentiating the first and substituting it into the second to obtain:

$$\frac{d^2 v_y}{dt^2} = -\omega_c^2 v_y \quad (2.9)$$

where  $\omega_c = \frac{|q|B}{m}$  is the ‘cyclotron frequency’. This equation has a solution

$$v_y = v_{\perp} \sin(\omega_c t), \quad (2.10)$$

for a particle which has a speed  $v_{\perp}$  in the  $x$ - $y$  plane, taken to have  $v_y(t=0) = 0$ . It then follows that  $v_x$  is given by

$$v_x = \pm v_{\perp} \cos(\omega_c t). \quad (2.11)$$

where the  $\pm$  is opposite of the sign of  $q$ . Integrating (2.11) and (2.10) one obtains

$$x = x_0 \pm r_L \sin(\omega_c t), \quad (2.12)$$

$$y = y_0 - r_L \cos(\omega_c t), \quad (2.13)$$

where  $r_L = \frac{mv_{\perp}}{|q|B}$  is the ‘Larmor radius’. Together equations (2.12) and (2.13) describe a circular orbit of radius  $r_L$  and frequency  $\omega_c$  about a ‘guiding centre’ at  $(x_0, y_0, z(t))$ .



Given that the  $z$  motion is unaffected by the magnetic field, orbits describe helices and thus appear to be tied to field lines. If an electric field parallel to  $B$  is present the picture remains the same, except with the guiding centre accelerated by the field in the same way a particle would be.

### 2.2.2 $\mathbf{E} \times \mathbf{B}$ drifts

Now to examine the case when a uniform electric field is also present. Consider some reference frame  $S$ , where there are uniform electric and magnetic fields,  $\mathbf{E}$  and  $\mathbf{B}$ , and a charged particle initially at rest. To solve for the subsequent motion of the particle, it is simpler to first transform to a frame,  $S'$ , where the electric and magnetic fields are parallel - a problem which has just been solved. The electric and magnetic fields in this new frame,  $\mathbf{E}'$  and  $\mathbf{B}'$ , are given by the Lorentz transformations:

$$\mathbf{E}'_{\parallel} = \mathbf{E}_{\parallel} , \quad (2.14)$$

$$\mathbf{B}'_{\parallel} = \mathbf{B}_{\parallel} , \quad (2.15)$$

$$\mathbf{E}'_{\perp} = \gamma (\mathbf{E}_{\perp} + \mathbf{v}_F \times \mathbf{B}) , \quad (2.16)$$

$$\mathbf{B}'_{\perp} = \gamma \left( \mathbf{B}_{\perp} - \frac{\mathbf{v}_F \times \mathbf{E}}{c^2} \right) , \quad (2.17)$$

where  $\mathbf{v}_F$  is the velocity of frame  $S'$  as observed in  $S$  and the  $\parallel$  and  $\perp$  subscripts indicate components parallel and perpendicular to  $\mathbf{v}_F$  respectively. If one takes  $\mathbf{v}_F = -\frac{\mathbf{E} \times \mathbf{B}}{B^2}$ , equations (2.14) and (2.15) become redundant since,  $\mathbf{v}_F$  being perpendicular to  $\mathbf{E}$  and  $\mathbf{B}$ , both of the parallel components are zero. Given this choice of  $\mathbf{v}_F$ , there is no need for the subscripts in  $\mathbf{E}_{\perp}$  and  $\mathbf{B}_{\perp}$  since  $\mathbf{E}$  and  $\mathbf{B}$  are purely perpendicular to  $\mathbf{v}_F$  (the same applying to their primed counterparts). Substituting this velocity into the remaining two equations and further assuming that  $|\mathbf{v}_F| \ll c$  yields

$$\mathbf{E}' = \frac{(\mathbf{E} \cdot \mathbf{B})}{B^2} \mathbf{B} \equiv \mathbf{E}_{\parallel B} , \quad (2.18)$$

and

$$\mathbf{B}' = \mathbf{B} , \quad (2.19)$$

where  $\mathbf{E}_{\parallel B}$  is the component of  $\mathbf{E}$  parallel to  $\mathbf{B}$ . In  $S'$  the electric and magnetic fields are in the same direction and thus the particle motion is described by gyration of radius  $r_L = \frac{m|\mathbf{v}_F|}{qB}$  around a guiding centre which has velocity  $\mathbf{v}_g = \frac{q}{m} \mathbf{E}_{\parallel B} t$ . The only thing left is to transform back to  $S$ , the motion in this frame is described by gyration, again of radius  $r_L$ , around a guiding centre moving at a velocity

$$\mathbf{u} = -\mathbf{v}_F + \mathbf{v}_g = \frac{\mathbf{E} \times \mathbf{B}}{B^2} + \frac{q}{m} \mathbf{E}_{\parallel B} t \quad (2.20)$$

i.e. the guiding centre is accelerated by the projection of the electric field in the  $\mathbf{B}$  direction and has a superimposed drift motion referred to as the ' $\mathbf{E} \times \mathbf{B}$  drift'. If  $\mathbf{E}$  and  $\mathbf{B}$  are purely perpendicular it is just this drift which is observed. It is interesting to note that whilst the gyroradius changes between particle species, the  $\mathbf{E} \times \mathbf{B}$  drift velocity is independent of mass and charge.

### 2.2.3 Magnetic mirror

Following the derivation of Chen [10, p. 27], consider an azimuthally symmetric magnetic field, primarily pointing in the positive  $z$  direction with its magnitude varying with  $z$ . The field lines of this configuration will be directed mostly in the  $z$  direction but will necessarily have a radial component to ensure that the field line density can change in accordance with the magnitude, this radial field,  $B_r$ , following from  $\nabla \cdot \mathbf{B} = 0$ . In cylindrical coordinates this requires

$$\frac{\partial(rB_r)}{\partial r} = -r \frac{\partial B_z}{\partial z} . \quad (2.21)$$

Assuming that  $\frac{\partial B_z}{\partial r}$  varies slowly in the  $r$  direction, one can take it to be constant and thus the integral is easily evaluated

$$B_r = -\frac{1}{2}r \frac{\partial B_z}{\partial z} + f(z) \quad (2.22)$$

and by symmetry  $B_r(r = 0, z) = 0$  requires that  $f(z) = 0$  and so

$$B_r = -\frac{1}{2}r \frac{\partial B_z}{\partial z} . \quad (2.23)$$

This subsection is concerned with how a charged particle will respond to such a field, with a uniform electric field,  $E_z$ , included for generality. Assuming that the particle is tied to the field line described by  $r = 0$  and has a gyroradius small enough not to experience any significant changes in  $B_z$  from the value on axis, the radial velocity is zero and the azimuthal velocity is constant at  $v_\theta = \mp v_\perp$  (where the  $\perp$  indicates directions perpendicular to  $B_z$  and the  $\mp$  corresponds to the particle charge to account for the direction of gyration). Interesting information about the trajectory is thus contained in the  $z$  equation of motion,

$$m \frac{dv_z}{dt} = \pm qv_\perp B_r + qE_z . \quad (2.24)$$

Substituting the form of  $B_r$  from (2.23) into this and using the fact that  $r = r_L$  the dependence on the sign of  $q$  disappears,

$$m \frac{dv_z}{dt} = -\mu \frac{\partial B_z}{\partial z} + qE_z , \quad (2.25)$$

where  $\mu = \frac{1}{2} \frac{mv_{\perp}^2}{B}$  is the ‘magnetic moment’ of the particle with  $B$  the total field strength. The previous analysis for the special case of a particle travelling along the axis generalises to particles off axis too

$$\mathbf{F}_{\parallel} = -\mu \frac{\partial B}{\partial \mathbf{s}} + q\mathbf{E}_{\parallel} \quad (2.26)$$

where  $\mathbf{s}$  is a line element along  $\mathbf{B}$ . Taking the scalar product of both sides with  $\mathbf{v}_{\parallel} = \frac{d\mathbf{s}}{dt}$  gives

$$\frac{d}{dt} \left( \frac{1}{2} mv_{\parallel}^2 \right) = -\mu \frac{dB}{dt} - q \frac{d\phi}{dt} \quad (2.27)$$

and when this is compared to conservation of energy,

$$\frac{d}{dt} \left( \frac{1}{2} mv_{\parallel}^2 + \frac{1}{2} mv_{\perp}^2 + q\phi \right) = 0, \quad (2.28)$$

it is inferred that

$$-\mu \frac{dB}{dt} + \frac{d(\mu B)}{dt} = 0, \quad (2.29)$$

so that

$$\frac{d\mu}{dt} = 0, \quad (2.30)$$

meaning that the magnetic moment is invariant for any given gyrating particle. This implies that as a particle moves to regions of increasing  $B$ , its  $v_{\perp}$  must increase to keep  $\mu$  constant. Since it must also conserve energy, this perpendicular kinetic energy is taken from the parallel motion, which continues to decrease to zero at which point the particle is reflected.

This is the picture for one particle, but it is interesting to consider how the distribution of a collection of particles is modified by the magnetic mirror effect (also moving into a retarding electric field). For electrons, the force in the  $z$  direction,

$$\begin{aligned} F_{\parallel} &= -\mu \frac{dB}{dz} + e \frac{d\phi}{dz} \\ &= -\frac{1}{2} \frac{mv_{\perp 0}^2}{B_0} \frac{dB}{dz} + e \frac{d\phi}{dz}, \end{aligned} \quad (2.31)$$

will lead to a  $z$  velocity as a function of  $z$  given by

$$v_z = \sqrt{v_{z0}^2 + \frac{2e\phi}{m_e} - v_{\perp 0}^2 \left( \frac{B}{B_0} - 1 \right)}, \quad (2.32)$$

where  $v_{z0}$  and  $v_{\perp 0}$  are the initial  $z$  and perpendicular velocities respectively, coinciding with the point where  $\phi = 0$ . The infinitesimal contribution to the density at  $z$ ,  $dn(z, v_z, v_{\perp 0})$ , made by particles which had the initial conditions  $v_{z0} \rightarrow dv_{z0}$ ,

$v_{\perp 0} \rightarrow dv_{\perp 0}$  is from continuity

$$\begin{aligned} dn(z, v_{z0}, v_{\perp 0}) &= v_{z0} \frac{dn(0, v_{z0}, v_{\perp 0})}{v_z} \\ &= \frac{v_{z0} dn(0, v_{z0}, v_{\perp 0})}{\sqrt{v_{z0}^2 + \frac{2e\phi}{m_e} - v_{\perp 0}^2 \left(\frac{B}{B_0} - 1\right)}} \\ &= \frac{v_{z0} dn(0, v_{z0}, v_{\perp 0})}{\sqrt{v_{z0}^2 - g(z, v_{\perp 0})}} \end{aligned} \quad (2.33)$$

where  $g(z, v_{\perp 0}) = v_{\perp 0}^2 \left(\frac{B}{B_0} - 1\right) - \frac{2e\phi}{m_e}$ . If a Maxwellian velocity distribution is assumed at the starting point,

$$dn(0, v_{z0}, v_{\perp 0}) = n_0 \frac{4}{\sqrt{\pi}} \left(\frac{m}{2k_B T_e}\right)^{\frac{3}{2}} v_{\perp 0} \exp\left(-\frac{mv_{\perp 0}^2}{2k_B T_e}\right) \exp\left(-\frac{mv_{z0}^2}{2k_B T_e}\right) dv_{\perp 0} dv_{z0} \quad (2.34)$$

and the total density is the integral over all initial conditions which can result in a particle reaching  $z$ ,

$$n(z) = n_0 \frac{4}{\sqrt{\pi}} \left(\frac{m}{2k_B T_e}\right)^{\frac{3}{2}} \int_0^\infty dv_{\perp 0} \int_{\sqrt{g(z, v_{\perp 0})}}^\infty \frac{v_{\perp 0} \exp\left(-\frac{mv_{\perp 0}^2}{2k_B T_e}\right) \exp\left(-\frac{mv_{z0}^2}{2k_B T_e}\right)}{v_{z0}^2 - g(z, v_{\perp 0})} dv_{z0}, \quad (2.35)$$

which is integrated to yield

$$n = \frac{B_0}{B} n_0 \exp\left(\frac{e\phi}{k_B T_e}\right). \quad (2.36)$$

Reassuringly, this reduces to the BR for a uniform magnetic field. The picture is incomplete, since there is one effect which has gone unnoticed thus far. If particles truly are tied to field lines then one should expect that a set of particles which initially described a cross section of  $A_0$ , where the field was  $B_0$ , should be reduced to an area  $A_1 = \frac{B_0}{B} A_0$ , where the field is  $B$ , to account for the higher field line density. The net effect of this process is to lead to an increased electron density by a factor of  $\frac{B}{B_0}$ . It is therefore the case that the combination of the effects of magnetic mirroring and this ‘squeezing’ by the field lines cancel each other out, leaving the density unchanged.

In summary, if particles are injected into a magnetic mirror, their tendency to follow their associated field lines will result in a contraction of the plasma cross section as it streams along. Despite a reduction in the plasma cross section, the density is unchanged by an exact cancellation due to reflection of particles by the mirror. Chen arrived at this same result from a different approach by considering equilibrium states in MHD [10, p. 203].

## 2.3 The magnetic dipole

It is an appropriate time to introduce the magnetic field configuration which will appear most often in this work. The magnetic dipole field has, arguably, the most fundamental magnetic field geometry, being the idealized result of a vanishingly small current loop. It can accurately describe the field of electrons, atoms, bar magnets, planets or neutron stars. The dipole properties are prescribed by a vector,  $\mathbf{M}$ , called the magnetic moment, with  $|\mathbf{M}|$  indicating the strength and the direction aligned with the local value of  $\mathbf{B}$  as it passes through the source loop. The magnetic field at a point displaced  $\mathbf{r}$  from a magnetic dipole moment  $\mathbf{M}$  is given by

$$\mathbf{B} = \frac{\mathcal{M}}{|\mathbf{r}|^3} \left( \frac{3(\hat{\mathbf{M}} \cdot \mathbf{r})\mathbf{r}}{\mathbf{r} \cdot \mathbf{r}} - \hat{\mathbf{M}} \right) \quad (2.37)$$

and has the field strength

$$B = \frac{\mathcal{M}}{|\mathbf{r}|^4} \sqrt{3(\hat{\mathbf{M}} \cdot \mathbf{r})^2 + \mathbf{r} \cdot \mathbf{r}}, \quad (2.38)$$

where  $\mathcal{M} \equiv \frac{\mu_0 M}{4\pi}$ . Due to the azimuthal symmetry of the field, cylindrical coordinates will be employed and so it will be useful here to list some key equations of the magnetic dipole, which will be used repeatedly, in these coordinates. Firstly, the two components of  $\mathbf{B}$  and the magnitude are given as

$$B_r = \frac{3\mathcal{M}zr}{(r^2 + z^2)^{\frac{5}{2}}}, \quad (2.39)$$

$$B_z = \frac{\mathcal{M}(2z^2 - r^2)}{(r^2 + z^2)^{\frac{5}{2}}}, \quad (2.40)$$

$$B = \frac{\mathcal{M}\sqrt{4z^2 + r^2}}{(r^2 + z^2)^2}. \quad (2.41)$$

Field lines,  $\mathbf{l}(a)$ , are derived from

$$d\mathbf{l} = \left( \frac{\mathbf{B}}{B} \right) da \quad (2.42)$$

where  $\mathbf{l}(a)$  gives the position of a point on the line, for some parameter  $a$ . This results in the field lines given as

$$z = \sqrt{Cr^{\frac{4}{3}} - r^2} \quad (2.43)$$

where  $C$  is some constant depending on the chosen line. A selection of these are plotted in Fig. (2.2). To make this diagram more informative, values of  $C$  are chosen such that the line density is in proportion to the field strength.

---

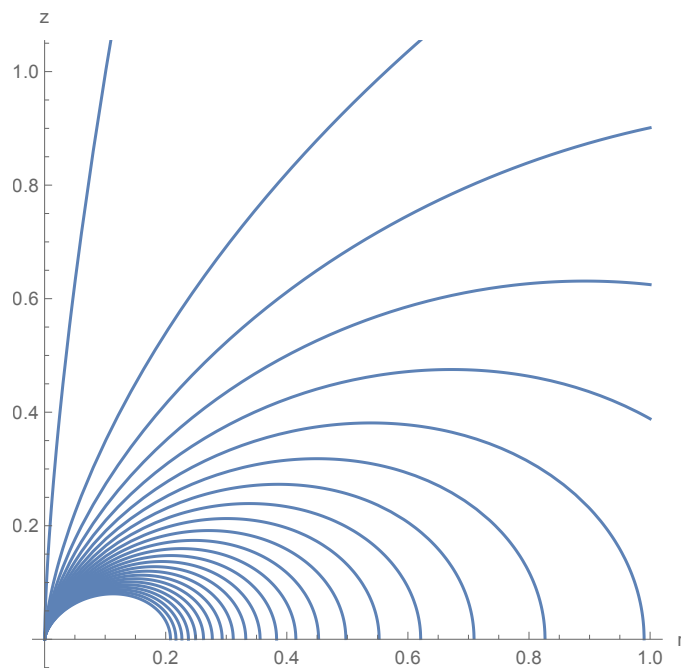


Figure 2.2: Magnetic field lines in cylindrical coordinates for a dipole centred at the origin with its moment aligned with the  $z$  axis.

## 2.4 Plasma-boundary interaction

Imagine the transient period the instant after an electrically floating wall hypothetically appears in a plasma. The early fluxes of plasma particles to the initially neutral wall will be determined from classical kinetic theory as  $\frac{1}{4}n_{j,W}\bar{v}_j$  where  $n_{j,W}$  are the values of  $j$  particle densities at the wall and  $\bar{v}_j$  is the mean of the magnitude of their velocities. Given the disparity between electron and ion thermal velocities, the wall will be overwhelmingly inundated with electrons and will consequently charge negatively. This acts to reduce  $n_{e,W}$ , according to the BR, stymieing the electron current and, in addition, acting to encourage more ions onto the surface. For the relatively low pressures I will be considering, it turns out that the electric fields are so strong that the ion current is not determined by random thermal flux, but provided by strong directed motion, far exceeding the thermal velocity. To achieve a steady state, the wall must settle on a potential suitably repulsive to electrons and attractive to ions such that their fluxes are equal. This would imply that in the vicinity of the wall there is a region where the densities of the electrons and ions are significantly different meaning that this region is also a zone of strong electric fields.

This brief discussion helps one to appreciate that the electron and ion behaviour in this region, known as the ‘sheath’, is wildly different and acts as justification for the assumptions which will now form a simple model.

### 2.4.1 Space-charge sheath

Following the derivation of Franklin [80, p. 51], consider a distinct boundary, at  $x = 0$ , where there is a transition from plasma to sheath. The first assumption is that the ions cross this boundary with a directed velocity  $u_{i0}$ , where this is much faster than their thermal velocity. Secondly, it is assumed that the plasma sheath boundary is characterized by equal particle densities and density gradients. Thirdly, it is assumed that no collisions occur in the sheath - implying no loss of momentum of the ions and no particles produced through ionization. Lastly, I assume that the electron density is everywhere described by the BR, despite the fact that this is liable to be incorrect near to the wall. The relevant equations are then: ion continuity,

$$n_i u_i = n_0 u_0 , \quad (2.44)$$

the ion equation of motion,

$$m_i u \frac{du_i}{dx} = -e \frac{d\phi}{dx} , \quad (2.45)$$

Boltzmann electron density,

$$n_e = n_0 \exp\left(\frac{e\phi}{k_B T_e}\right) , \quad (2.46)$$

and Poisson's equation,

$$\frac{d^2\phi}{dx^2} = \frac{e}{\epsilon_0} (n_e - n_i) . \quad (2.47)$$

Supplementing these are the boundary conditions:  $n_i(0) = n_e(0)$ ,  $\phi(0) = 0$  and  $\frac{d\phi}{dx}(0) = \frac{dn_i}{dx}(0) = \frac{dn_e}{dx}(0) = 0$ . Introducing the normalizations:

$$\eta = \frac{e\phi}{k_B T_e} , N_e = \frac{n_e}{n_0} , N_i = \frac{n_i}{n_0} , U_i = \frac{u_i}{c_s} , \quad (2.48)$$

equations (2.44)-(2.47) boil down to one for the potential,

$$\frac{d^2\eta}{dx^2} = \frac{1}{\lambda_{De}^2} \left[ e^\eta - \left(1 - \frac{2\eta}{U_{i0}^2}\right)^{\frac{1}{2}} \right] , \quad (2.49)$$

where it's clear that the characteristic lengthscale to which I should have normalized  $x$  with is the electron Debye length,  $\lambda_{De} = \sqrt{\frac{\epsilon_0 k_B T_e}{n_e e^2}}$ , a value which serves plasma physics as a whole to indicate the typical distance over which non-neutral regions are screened out by the plasma. Implementing this normalization by taking  $X = \frac{x}{\lambda_{De}}$  and reducing equation (2.49) to a first order equation by multiplying by  $\frac{d\eta}{dX}$  and then integrating from

$X = 0$  to a point deeper in the sheath,

$$\frac{1}{2} \left( \frac{d\eta}{dX} \right)^2 = e^\eta - 1 + U_{i0}^2 \sqrt{1 - \frac{2\eta}{U_{i0}^2}} - U_{i0}^2. \quad (2.50)$$

Before this equation can be numerically integrated, one needs to know how to commence the process and when to end it. The latter condition follows by remembering that the wall is a special location, where the ion and electron currents are equal. From this one is easily able to determine the potential at the wall by equating the particle fluxes,

$$n_0 u_{i0} = \frac{1}{4} n_0 v_{e,th} \exp\left(\frac{e\phi_w}{k_B T_e}\right), \quad (2.51)$$

which implies that

$$\eta_W = \frac{1}{2} \ln\left(\frac{m_i}{2\pi m_e U_{i0}^2}\right), \quad (2.52)$$

providing the value of  $\eta$  at which one ceases to integrate (2.50) any further.

As for initiating the integration, if one tries to numerically integrate (2.50) by taking  $\eta = 0$ ,  $\frac{d\eta}{dX} = 0$ , the potential will not change. Instead, one must search for a solution which tends asymptotically to zero. Defining  $\xi = X_W - X$ , this means that one requires  $\eta \rightarrow 0$  and  $\frac{d\eta}{d\xi} \rightarrow 0$  as  $\xi \rightarrow \infty$ . Examining solutions of the form

$$\eta = \frac{A}{\xi^n}, \quad (2.53)$$

equation (2.50) becomes in this asymptotic limit,

$$\frac{n(n+1)A}{\xi^{2+n}} \approx \frac{A}{\xi^n} \left(1 - \frac{1}{U_{i0}^2}\right) - \frac{1}{2} \frac{A^2}{\xi^{2n}} \left(\frac{3}{U_{i0}^2} - 1\right). \quad (2.54)$$

On the RHS, the coefficient of  $\xi^{-n}$  must be zero since it can have no term of equal order on the LHS ( $n \neq 2+n$ ), implying that  $U_{i0} = 1$ . This condition is the equality form of what is known as the ‘Bohm criterion’, stated as  $u_{i0} \geq u_B = \sqrt{\frac{k_B T_e}{m_i}}$ , where  $u_B$  is equal to the ion sound speed (but in this context also referred to as the Bohm velocity). The Bohm criterion is a weaker condition which follows from the requirement that the RHS of (2.50) is positive. To ensure that the remaining RHS term in  $\eta^{-2n}$  may equal the LHS, it must first be the case that  $2+n = 2n$ , giving  $n = 2$ . The coefficients must also be the same requiring in turn that  $A = -6$ . Therefore, far from the wall one can expect the potential to behave as,

$$\eta \approx -\frac{6}{\xi^2} \quad (2.55)$$

This serves as the condition to initiate numerical integration of the potential - one begins at a position far from the wall,  $\xi_0$ , with  $\eta(\xi_0) = -\frac{6}{\xi_0^2}$  and  $\frac{d\eta}{d\xi}(\xi_0) = \frac{12}{\xi_0^3}$ .



### 2.4.2 Presheath

A direct consequence of the Bohm criterion (in its equality form) is that there must be some process occurring upstream of the sheath edge to accelerate the initially stationary bulk plasma ions to  $u_B$ . Contrary to the assumption that the electric field at the sheath edge is zero, this acceleration is performed by some finite electric field in the plasma. The region of plasma over which the potential drops by  $\frac{1}{2} \frac{m_i u_{i0}^2}{e}$  is referred to as the ‘presheath’ and is typically larger in extent than the sheath. Since the electric fields in the sheath are still far stronger than those in the presheath, the assumption that  $E = 0$  at the sheath edge is not a poor one and so the findings of Section 2.4.1 are not invalidated. The only real complications arise when deciding how to stitch together the sheath and presheath solutions.

Following the derivation provided by Franklin in a paper [81], assuming quasineutrality in the presheath, the electron and ion densities, as well as their bulk speeds, will be equal. With an ionization rate per unit volume,  $g(n, x)$ , the continuity equation is stated as

$$\frac{d(un)}{dx} = g(n, x) . \quad (2.56)$$

Electrons are assumed to follow the Boltzmann relation, the location where  $n = n_0$  and  $\phi = 0$  is still taken to be in the bulk plasma, but strictly speaking this is now the presheath edge, not the sheath edge. The steady state ion fluid equation of motion is

$$m_i \frac{d(nu^2)}{dx} = neE - \frac{neu}{\mu(x, u)} , \quad (2.57)$$

where  $\mu(x, u)$  is the ion mobility. These equations are readily put into their most enlightening form by using the property of the BR that

$$\frac{dn}{dx} = -\frac{enE}{k_B T_e} , \quad (2.58)$$

to yield

$$\frac{1}{n} \frac{dn}{dx} = \frac{\frac{e}{\mu(x, u)} + \frac{2g(n, x)m_i u}{n}}{k_B T_e - m_i u^2} \quad (2.59)$$

and

$$\frac{du}{dx} = \frac{g(n, x)(k_B T_e + m_i u^2) + \frac{eu}{\mu(x, u)}}{n(k_B T_e - m_i u^2)} . \quad (2.60)$$

To avoid these equations becoming singular it must be the case that  $u < u_B$ , this result holding regardless of the generation mechanism and collisional model which have been left quite general so far. Given this limitation on the flow speed and comparing it with the Bohm criterion, one concludes that the presheath can indeed accelerate particles up to something very close to the Bohm speed at which point quasineutrality starts to

break down. Around this point, there will be some transition region where neither the sheath nor presheath models provide an adequate description and some mathematical stitching together of these two regions is required.

## 2.5 Dust charging

Dust particles gain and lose charge through a variety of processes, dominating these is donations of ions and electrons from the surrounding plasma. If these particles are destined to cross paths with a dust grain, those which are not reflected at the surface will pass into the grain material losing energy as they do. Once the ion or electron is decelerated and becomes a part of the dust, its charge now belongs to its new host too. Assuming this process is perfect - that every particle whose trajectory intersects with the grain is instantly absorbed - the problem is then to determine the rate at which particles are collected. Here I shall reproduce the most commonly used model to describe the collection of plasma particles by dust grains, the orbital motion limited (OML) theory.

The basic task of any charging theory is to consider plasma particles distant from the grain and then to determine which combinations of initial conditions (initial velocity,  $v_0$ , and impact parameter,  $b$ ) will result in trajectories exploring radial coordinates less than the grain radius,  $a$ . The defining feature of OML, which will be seen shortly, is the condition used to separate between collected and escapee particles. Assuming the plasma is collisionless, conservation of energy requires that

$$\frac{1}{2}m_j v^2 + q_j \phi(r) = \frac{1}{2}m_j v_0^2, \quad (2.61)$$

where  $m_j$  and  $q_j$  are the charge and mass of the particle of species  $j$ . Assuming spherical symmetry, angular momentum conservation requires that

$$v_t r = v_0 b, \quad (2.62)$$

where  $v_t$  is the tangential component of the particle velocity. From here, OML seeks to find the critical impact parameter,  $b_c(v_0)$ , for which a plasma particle just grazes the surface of the grain. The significance of this is that all particles with the same velocity  $v_0$  and an impact parameter  $b < b_c$  are assumed to be collected, thus giving an effective collection cross section of  $\sigma(v_0) = \pi b_c(v_0)^2$ . Evaluating (2.61) at  $r = a$  gives the velocity of a particle at the grain surface,

$$v_a = \sqrt{v_0^2 - \frac{2q_j}{m_j} \phi_d}, \quad (2.63)$$

where  $\phi_d = \phi(a)$  is the dust grain potential. One sets the conditions for a grazing collision by requiring that this speed is entirely in the tangential direction,  $v_a = v_t$ .

---

Therefore, evaluating (2.62) under this condition at the surface of the grain,

$$v_a a = v_0 b_c , \quad (2.64)$$

which is rearranged for the critical impact parameter and subsequently yielding the cross section as

$$\sigma(v_0) = \pi a^2 \left( 1 - \frac{2q_j \phi_d}{m_j v_0^2} \right) . \quad (2.65)$$

At a point afar from the grain the particle velocity is entirely radial and equal to  $v_0$ , thus the number of particles streaming through the collection cross section per second is given by  $v_0 n_j f_j(v_0) \sigma(v_0)$  (where  $f_j(v_0)$  is the velocity PDF and  $n_j$  is the total species density at infinity) and this equals the rate of collection by the dust. The current onto the grain from species,  $j$ , is the integral of the particle flux over all possible values of  $v_0$  multiplied by the particle charge,

$$I_j = q_0 n_j \int_{v_{\min}}^{\infty} v_0 f_j(v_0) \sigma(v_0) dv_0 , \quad (2.66)$$

where  $v_{\min}$  is the slowest a particle can set out while still reaching the grain - for particles which are attracted to the grain,  $v_{\min} = 0$ . Considering ions of charge  $Ze$ , assuming a MVD in equation (2.66) and evaluating the integral yields the ion current onto the grain,

$$I_i = 4\pi a^2 n_{i0} Ze \sqrt{\frac{k_B T_i}{2\pi m_i}} \left( 1 - \frac{Ze\phi_d}{k_B T_i} \right) . \quad (2.67)$$

The electron current can then be obtained from equation (2.66), this time with  $v_{\min} = \sqrt{\frac{2e\phi_d}{m_e}}$  to account for the repulsive nature of the grain,

$$I_e = -4\pi a^2 n_{e0} e \sqrt{\frac{k_B T_e}{2\pi m_e}} \exp\left(\frac{e\phi_d}{k_B T_e}\right) . \quad (2.68)$$

The equilibrium potential of the grain is the one which draws no net current,

$$\frac{dQ_d}{dt}(\phi_{d0}) = I_e + I_i = 0 , \quad (2.69)$$

with  $Q_d$  the grain charge and  $\phi_{d0}$  the equilibrium dust potential. Assuming quasineutrality far from the grain,  $Zn_{i0} = n_{e0}$ , and substituting (2.67) and (2.68) into (2.69) gives an implicit form for the normalized steady state potential,

$$\sqrt{\frac{\Theta}{\mu}} \left( 1 - \frac{Z}{\Theta} \eta_{d0} \right) = \exp(\eta_{d0}) , \quad (2.70)$$

where I have introduced the dimensionless plasma parameters  $\mu = \frac{m_i}{m_e}$  and  $\Theta = \frac{T_i}{T_e}$ . The

normalized potential has the solution

$$\eta_{d0} = \frac{\Theta}{Z} - W_0 \left( \frac{\sqrt{\mu\Theta}}{Z} \exp \left( \frac{\Theta}{Z} \right) \right), \quad (2.71)$$

where  $W_0$  is the principal branch of the Lambert  $W$  function. Obtaining a value for the grain charge involves a potentially complicated calculation, since one needs to know the charge distribution around the grain. For small grains,  $a \ll \lambda_{De}$ , the potential can effectively drop to zero, as if in vacuum, before shielding effects have a chance to take over and thus a value for the charge follows from the formula for the capacitance of an isolated charged sphere in vacuo,

$$Q_{d0} = C_d \phi_d. \quad (2.72)$$

where  $C_d = 4\pi\epsilon_0 a$ . With a little extra work one can determine the timescales of charging. In the early stages the initial electron current,  $I_e(t=0) = I_e(\phi_d=0)$ , is the dominant source and so

$$\begin{aligned} \tau_E &\approx \frac{Q_{d0}}{I_e(0)} \\ &= \frac{Q_{d0}}{a^2 e n_0} \sqrt{\frac{m_e}{8\pi k_B T_e}}, \end{aligned} \quad (2.73)$$

where the subscript 0 in the charge indicates an equilibrium value as usual. For later times, assuming that the grain is perturbed from its equilibrium charge,  $Q_d = Q_{d0} + \delta Q$ , leads to the time development

$$\begin{aligned} \frac{dQ_d}{dt} &= \frac{d(Q_{d0} + \delta Q)}{dt} = \frac{d(\delta Q)}{dt} = I(Q_{d0} + \delta Q) \\ &\approx I(Q_{d0}) + \frac{\partial I}{\partial Q_d}(Q_{d0})\delta Q \\ &= \frac{\partial I}{\partial Q_d}(Q_{d0})\delta Q, \end{aligned} \quad (2.74)$$

where the equilibrium condition,  $I(Q_{d0}) = 0$ , has been used. Differentiating the total current with  $\phi_d$  replaced by  $\frac{Q_d}{C_d}$  (i.e. this is a small particle calculation),

$$\frac{\partial I}{\partial Q_d}(Q_{d0}) = -\frac{4\pi a^2 n_0 e^2}{C_d} \left( Z \sqrt{\frac{1}{2\pi m_i k_B T_i}} + \sqrt{\frac{1}{2\pi m_e k_B T_e}} \exp \left( \frac{e Q_{d0}}{k_B T_e C} \right) \right) \quad (2.75)$$

Implying a timescale

$$\tau_L = \left[ \frac{\partial I}{\partial Q_d}(Q_{d0}) \right]^{-1} = \frac{\epsilon_0}{a n_0 e^2} \left( Z \sqrt{\frac{1}{2\pi m_i k_B T_i}} + \sqrt{\frac{1}{2\pi m_e k_B T_e}} \exp \left( \frac{e \phi_{d0}}{k_B T_e} \right) \right)^{-1}. \quad (2.76)$$

To give some typical values for all of the findings so far: for a micron sized dust grain immersed in a hydrogen plasma with  $T_e = T_i = 1\text{eV}$  and  $n_0 = 10^{15}\text{m}^{-3}$ , OML predicts

a normalized potential  $\eta_{d0} = -2.503$ , which is also the value of the potential in volts since the electron temperature is 1eV. The grain is charged negatively with a surplus of 870 electron charges and the early and late charging timescales are  $\tau_E = 1.66 \times 10^{-8}$ s and  $\tau_L = 6.25 \times 10^{-6}$ s respectively.

Like any theory, OML is limited where its assumptions begin to fail and it's time to find out when this occurs. Firstly, to safely assume that the plasma is collisionless it must be the case that the mean free path of each species,  $\lambda_j$ , is longer than the characteristic trajectory length. I did assume that particles covered an infinite distance to arrive at the grain, but in actual fact, any distance  $\gg a$  would have been suitable. Taking  $a$  as the typical trajectory lengthscale, the plasma can be assumed collisionless so long as  $\lambda_j \gg a$ . It was also assumed that the dust grain is isolated and immersed in a plasma background which is unchanging in space and time. The characteristic lengthscale of the model remains as  $a$  and  $\tau_L$  is taken as the timescale (seeing as it is the longer of the two derived). Thus, with  $L$  and  $T$  as the typical length and time scales of plasma variation, the model is valid if  $L \gg a$  and  $T \gg \tau_L$ . Even if the plasma is not time varying, if the dust moves through a non uniform region of lengthscale  $L$  with speed  $v_d$ , the dust grain witnesses change on a timescale of  $T = \frac{L}{v_d}$ .

Claiming that the dividing line between collection and escape is the trajectory of an ion which just grazes the dust may not have appeared like an assumption, given that it seems so intuitively reasonable. However, there may exist an 'absorption radius',  $R(v_0)$ , such that any particle which ventures closer than this will inevitably fall to the grain. When the particle terminates on the grain surface, it will do so with a finite radial velocity and so one should actually be interested in those trajectories which graze the absorption radius to determine the collection cross section. Particles which graze the dust do not exist rendering the OML approach invalid. It can be shown [82] that absorption radii emerge when the potential  $\phi(r)$  drops off more steeply than  $r^{-2}$  and given that the space charge distribution around a dust grain will act to screen it exponentially fast, this unfortunately seems likely to be the case. However, for grains much smaller than the Debye length, the potential can effectively drop off at its vacuum rate  $r^{-1}$  and so OML should provide reliable results here.

Given all of this, it's fair to conclude that OML is a theory most suited to small grains. Despite these shortcomings, OML remains the go to theory for the charging of nearly all spherical dust grains and probes [83] immersed in plasma.

## 2.6 Dusty plasma waves

Whilst this thesis doesn't cover the following types of wave, it is instructive to include these pieces of theory to elucidate the influence dust has in the fast and slow regimes alluded to in section 1.3.1.

### 2.6.1 Dust-ion acoustic (DIA) waves

In this regime the frequency is sufficiently high such that the heavy dust grains do not respond, but low enough for the electrons to establish thermal equilibrium with the wave potential,  $\phi$ . Accordingly, the dust density is constant at  $n_{d0}$  and the electron density is given by the BR,

$$n_e = n_{e0} \exp\left(\frac{e\phi}{k_B T_e}\right). \quad (2.77)$$

Continuity and momentum equations govern the dynamics of the ions, for planar waves propagating in the  $x$ -direction these are

$$\frac{\partial n_i}{\partial t} + \frac{\partial(n_i v_i)}{\partial x} = 0, \quad (2.78)$$

$$\frac{\partial v_i}{\partial t} = -\frac{e}{m_i} \frac{\partial \phi}{\partial x} - \frac{3k_B T_i}{m_i n_{i0}} \frac{\partial n_i}{\partial x}, \quad (2.79)$$

and closing (2.77)-(2.79) is Gauss' law,

$$\frac{\partial^2 \phi}{\partial x^2} = \frac{e}{\epsilon_0} (n_e - n_i - Z_d n_d). \quad (2.80)$$

Linearizing these equations around their background values and looking for harmonic solutions for the first order deviations of the form  $\propto \exp(i(kx - \omega t))$  yields the dispersion relation for DIA waves,

$$\omega = \frac{c_{DI} k}{\sqrt{1 + (k\lambda_{De})^2}}, \quad (2.81)$$

where  $c_{DI}$  is the dust-ion acoustic speed given by

$$c_{DI} = \sqrt{\frac{n_{i0}}{n_{e0}}} c_S \text{ and } c_S = \sqrt{\frac{k_B T_e}{m_i}}. \quad (2.82)$$

For negatively charged grains,  $n_{i0} > n_{e0}$  and so  $c_{DI} > c_S$ . This increase in phase velocity is attributed to the depleted electron population leading to an increased Debye radius and thus stronger electric fields.

### 2.6.2 Dust acoustic (DA) waves

The frequency associated with dust acoustic waves is so low that both electrons and ions are able to remain in equilibrium with the wave potential and so in addition to (2.77) the ion density follows the Boltzmann relation,

$$n_i = n_{i0} \exp\left(-\frac{e\phi}{k_B T_i}\right). \quad (2.83)$$

Dynamics of the dust are of central importance here and are determined analogously to (2.78) and (2.79) from

$$\frac{\partial n_d}{\partial t} + \frac{\partial(n_d v_d)}{\partial x} = 0, \quad (2.84)$$

$$\frac{\partial v_d}{\partial t} = -\frac{Z_d e}{m_d} \frac{\partial \phi}{\partial x}, \quad (2.85)$$

where the dust thermal velocity is assumed to be negligible. As before, Gauss' law (2.80) closes this set of equations. The dispersion relation for the perturbed quantities is found to be

$$\omega = \frac{c_{DA} k}{\sqrt{1 + (k\lambda_D)^2}}, \quad (2.86)$$

where  $c_{DA}$  is the dust acoustic speed given by

$$c_{DA} = \sqrt{\frac{k_B T_i n_{d0} Z_d^2}{m_d n_{i0}}} \quad (2.87)$$

and  $\lambda_D = (\lambda_{De}^{-2} + \lambda_{Di}^{-2})^{-\frac{1}{2}}$ . The pressures of the ions and electrons act to restore the wave whilst the inertia is provided by the dust. To avoid any confusion, I should point out that this wave is not the same as a dust crystal wave where grains are strongly coupled and the restoring force is provided by the bonding between lattice sites.

# 3 Dusty Alfvénic solitary waves

## 3.1 Background

In the previous section, two examples of well understood linear dusty plasma wave phenomena were presented for the cases of mobile and immobile dust. The subject of this chapter will be nonlinear waves and these are of the type where the dust grains remain stationary. A dusty plasma wave tends to have a non dusty counterpart (in the previous examples this was the ion-acoustic wave) and so the structure of this chapter will be to introduce the dust-free case first, with the dusty treatment (containing new, original work) following afterwards. But, before this gets started, I shall provide examples of environments suitable to host these waves and some comments on how one goes about performing theoretical analysis.

To find natural realisations of the types of waves this work will be applicable to one has to look to space, where dust and plasma are two of the main ingredients. Since the 1980's, large amplitude spiky structures have been observed to propagate through space plasmas. The electromagnetic kind, which I shall concentrate on, have been observed around the Earth's bow shock [84] and magnetopause boundary layer [85], the Jovian middle magnetosphere [86], the surface of Io [87] and comet Halley's coma [88]. These manifest themselves as pulse-like magnetic disturbances, strongly enhanced (or diminished) relative to the background field. As mentioned in the introduction, observations of dusty plasma waves in space are very limited, but the fact that dust is present in all of the planetary and comet magnetospheres just listed [89] provides an indication that dusty versions of the existing nonlinear plasma waves may also exist. In 2002 it was predicted that "Galileo and Casini data from Jupiter and Saturn dusty magnetospheres will almost certainly yield data motivating more detailed studies of nonlinear waves in dusty plasmas" [90], but so far, the predicted studies inspired by these missions have been hard to come by [91] [92] [93]. Given that minimagnetospheres occur in the dusty environment of the lunar exosphere, it is worth examining if dusty plasma effects can emerge here. Using the dust conditions in the lunar environment as found by LADEE ( $Z_d \approx 25000$ ,  $n_d \approx 10^{-3}\text{m}^{-3}$ ) with the density of the solar wind ( $n_i \approx 6 \times 10^6\text{m}^{-3}$ ), one finds a Havnes parameter of order  $10^{-6}$ , too low to expect dusty plasma effects. Whilst the putative lofted grain population responsible for horizon glow was not observed on this mission, no data was collected for altitudes below 3km and so it remains possible that more significant amounts of dust may be mobilized at lower altitudes, giving the chance that small magnetic anomalies may be regions conducive to nonlinear dusty plasma phenomena.



---

The names of the two waves under study here are the ‘Transverse Alfvénic Solitary Wave’ and the ‘Oblique Alfvénic Solitary Wave’. It was just stated that if a wave exists in a plasma then there most likely exists two (slow and fast) dusty counterparts and these waves are no exception. The slow sort, where dust inertia dominates, has been studied comprehensively [94] [95]. However, nowhere has the second counterpart been considered: that for stationary dust grains which influence the wave only by storing charge from the plasma - this work is performed for the first time here. Owing to the fact that these structures are governed by nonlinear equations, they are difficult to analyze mathematically and computer simulations play an indispensable role. Some progress can be made by considering weak disturbances and taking a perturbative approach [96], however, a complete theoretical description requires a treatment of large amplitude features. The most convenient framework for this pursuit is to look for solitary wave solutions, that is, unchanging, localised disturbances which move through the plasma. This not only presents a tractable problem, but indicates the typical speed, length scale and amplitude of these ‘spikes’ and any relationships between these quantities. Some solitary waves further qualify to be referred to as ‘solitons’, a name whose standard-model-esque “-on” suffix indicate the special property that two such solitary waves will emerge unchanged if they collide - much like an electron and proton might. This may possibly be the case for the waves under consideration here, but without proving it to be true I will avoid using the term ‘soliton’.

---

## 3.2 Transverse Alfvénic solitary waves

### 3.2.1 Dust-free

Transverse Alfvénic solitary waves without dust were first characterised by Adlam and Allen [97] in 1958, here I reproduce their derivation of the important features of this wave.

Consider a planar pulse of magnetic field propagating through a cold plasma in a direction perpendicular to the background magnetic field of strength  $B_0$  (see Fig. 3.1). In the frame in which the undisturbed plasma is stationary, the ‘lab frame’ (Fig. 3.1a), the disturbance moves in the negative  $x$  direction at a speed,  $u_0$ , with the axes oriented such that the magnetic field is purely in the  $z$  direction and gradients exist only in the  $x$  direction. The wave disturbs the plasma as it passes, sustaining itself by inducing a transverse electron current in the  $y$  direction. After the passage of the wave, a given patch of plasma is returned to its initial state, but displaced slightly in the direction of propagation. The exact form of the plasma particle trajectories has been recently found in a paper by one of the original authors, J. E. Allen, and myself [98].

Analysis is easiest in a frame moving with the disturbance, the ‘wave frame’ (Fig. 3.1b), since  $\frac{\partial}{\partial t} = 0$  for all quantities. In this frame, ions and electrons stream in from  $x_W = -\infty$  with speed  $u_0$ , interact with the disturbance and then continue to  $+\infty$  as they began. Assuming  $u_0 \ll c$ , the magnetic field is unchanged by the transformation from lab to wave frames, however, an electric field is induced in the  $y$  direction,  $E_y$ . This follows from the Lorentz transformation of electromagnetic fields, but it is more intuitive to consider the undisturbed plasma where it must be the case that  $E_y = B_0 u_0$  to ensure that the incoming particles are not inconsistently deflected in this new reference frame by the  $\mathbf{v} \times \mathbf{B}$  force. Since there is no time evolution, Faraday’s law yields no spatial variation in  $E_y$  and thus it is uniform throughout the wave frame.

The problem is tractable for arbitrary particle masses, however, I shall concentrate on an electron-ion plasma and will use any approximations arising from the disparity in their masses. The equations of motion of the ions and electrons in the  $x$  and  $y$  directions are

$$m_e u_e \frac{du_e}{dx_W} = -e(E_x + v_e B_z) , \quad (3.1)$$

$$m_e u_e \frac{dv_e}{dx_W} = -e(u_0 B_0 - u_e B_z) , \quad (3.2)$$

$$m_i u_i \frac{du_i}{dx_W} = eE_x , \quad (3.3)$$

where  $u$  and  $v$  denote velocity components in the  $x$  and  $y$  directions respectively and the heavy ion approximation means their transverse deflection can be ignored (ergo the absence of a fourth equation of motion). By combining (3.1) and (3.3) the electric field

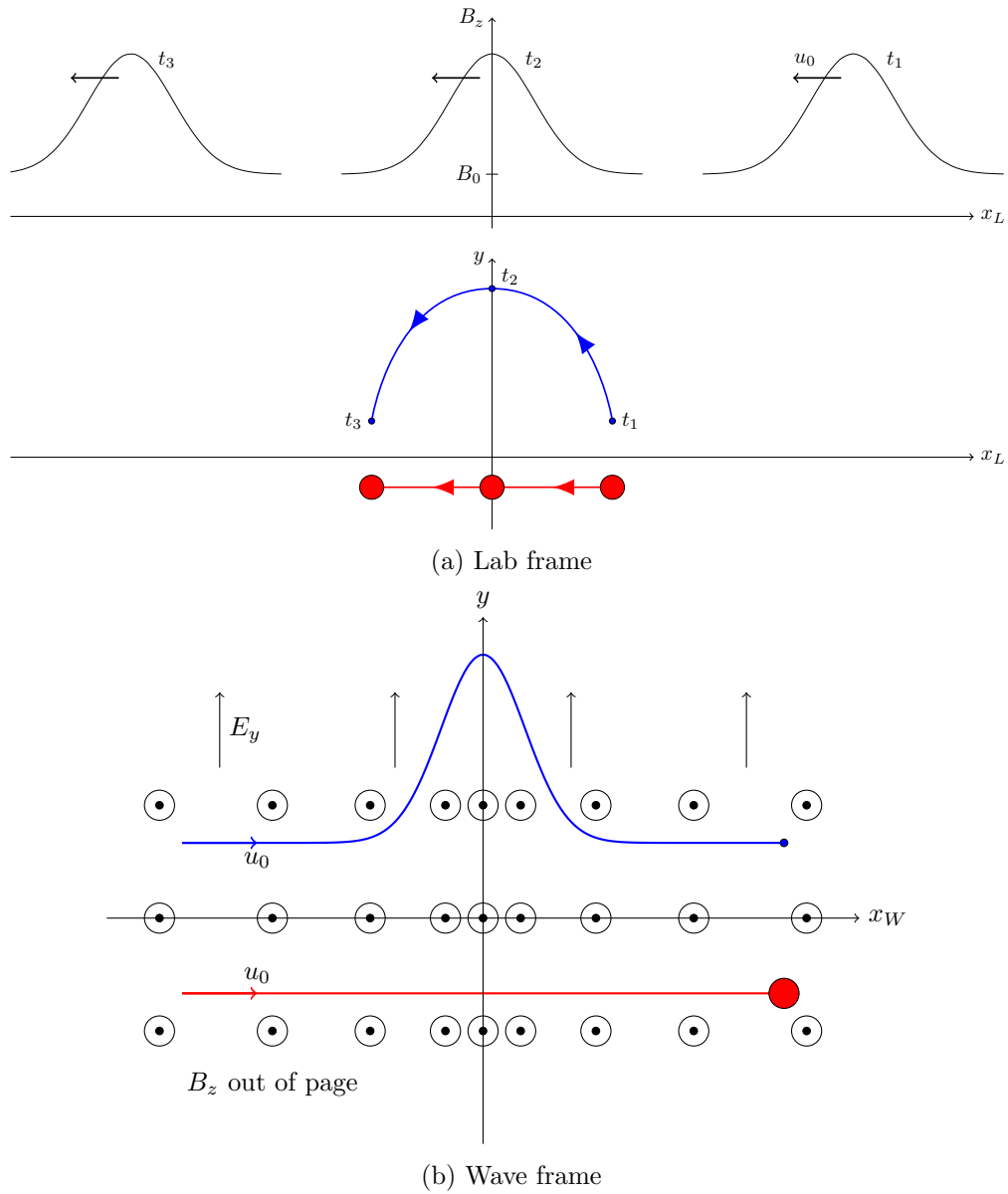


Figure 3.1: Electron (small blue particle) and ion (large red particle) trajectories and electromagnetic fields in the lab (a) and wave (b) reference frames. In (a), the times  $t_1 \rightarrow -\infty$ ,  $t_2 = 0$ ,  $t_3 \rightarrow \infty$  and so the approaching and leaving wave snapshots should be imagined to be at  $x_L \rightarrow \pm\infty$  respectively.

is eliminated,

$$m_e u_e \frac{du_e}{dx_W} + m_i u_i \frac{du_i}{dx_W} = -e v_e B_z . \quad (3.4)$$

With ion deflection negligible, the electrons make the significant contribution to the transverse current so that Faraday's Law takes the form

$$\frac{dB_z}{dx_W} = \mu_0 e n_e v_e \quad (3.5)$$

and continuity of electrons and ions implies that

$$n_e u_e = n_i u_i = n_0 u_0 . \quad (3.6)$$

These equations are closed by the assumption of quasineutrality, implemented by taking  $n_i = n_e \equiv n$  and immediately implying from the continuity equations (5.47) that  $u_i = u_e \equiv u$ . Substituting this into (3.2) and (3.4) and using the normalizations  $X_W = \frac{x_W}{d_e}$ ,  $U = \frac{u}{v_A}$ ,  $V = \frac{v}{v_*}$ ,  $\beta_z = \frac{B_z}{B_0}$  where,

$$d_e = \sqrt{\frac{m_e}{n_0 \mu_0 e^2}}, v_A = \sqrt{\frac{B_0^2}{n_0 \mu_0 m_i}}, v_* = \sqrt{\frac{B_0^2}{n_0 \mu_0 m_e}} , \quad (3.7)$$

leaves three equations from which the wave profile is derived:

$$U \frac{dU}{dX_W} = -V_e \beta_z , \quad (3.8)$$

$$U \frac{dV_e}{dX_W} = -\alpha + U \beta_z , \quad (3.9)$$

$$\frac{d\beta_z}{dX_W} = \frac{\alpha V_e}{U} , \quad (3.10)$$

where the Alfvén Mach number,  $\alpha = \frac{u_0}{v_A}$ , and in (3.8) terms of order  $\frac{m_e}{m_i}$  have been neglected. The natural lengthscale,  $d_e = \frac{c}{\omega_{pe}}$ , is the electron skin depth. The reason for normalizing the  $x$  and  $y$  velocities differently is on the physical grounds that the electrons undergo strong perpendicular deflections, reaching transverse speeds an order of magnitude in excess of their incoming speed. Practically speaking, it is a demonstrably useful normalization since all fundamental constants are successfully absorbed.

Eliminating  $V_e$  between (3.8) and (3.10) and integrating from  $X_W = -\infty$  to  $X_W$  gives

$$U = \alpha + \frac{\beta_z^2 - 1}{2\alpha} . \quad (3.11)$$

Similarly,  $V_e$  is related to  $\beta_z$  by taking the ratio of equations (3.8) and (3.9) to eliminate  $X_W$  and then using (3.11) to substitute for  $U$  and  $\frac{dU}{d\beta}$ ,

$$V_e = \pm \frac{\beta_z - 1}{2\alpha} \sqrt{(2\alpha)^2 - (1 + \beta_z)^2} , \quad (3.12)$$

where the  $\pm$  corresponds to  $X_W < 0$  and  $X_W > 0$  respectively. Finally, by substituting equations (3.11) and (3.12) into (3.10), an equation relating  $\beta_z$  and  $X_W$  is arrived at,

$$\frac{d\beta_z}{dX_W} = \pm \frac{\alpha(\beta_z - 1)\sqrt{(2\alpha)^2 - (1 + \beta_z)^2}}{2\alpha^2 + 1 - \beta_z^2}. \quad (3.13)$$

Numerical integration of this equation provides the wave profile,  $\beta_z(X_W)$ , although an analytic expression for  $X_W(\beta_z)$  may be found in this case. Solitary waves cannot exist for arbitrary values of  $\alpha$  though and it is worth introducing the notion of a Sagdeev potential to help illustrate this and to ascertain what the allowed range is. By taking the square of both sides of equation (3.13) and multiplying by  $\frac{1}{2}$ , an expression akin to energy conservation results for an imaginary particle of mass unity and position  $\beta_z$ , moving through a potential  $\phi_S(\beta_z)$  (referred to as the ‘Sagdeev potential’) with  $X_W$  playing the role of time,

$$\frac{1}{2} \left( \frac{d\beta_z}{dX_W} \right)^2 = \frac{\alpha^2(\beta_z - 1)^2(2\alpha + 1 + \beta_z)(2\alpha - 1 - \beta_z)}{2(2\alpha^2 + 1 - \beta_z^2)^2} \equiv -\phi_S(\beta_z). \quad (3.14)$$

For the case at hand  $\beta_z$  starts out at 1, meaning that the initial condition of the Sagdeev pseudo-particle is a coordinate of 1, sitting where the potential is  $\phi_S(1) = 0$ . Sagdeev potentials for three different values of  $\alpha$  are plotted in Fig. 3.2 which will be useful for the following discussion. One can visualise the time evolution of the system by imagining a ball (the Sagdeev particle) rolling along the terrain described by the potential. Stationary points of the potential (where the Sagdeev particle speed is zero) occur at the starting point,  $\beta_0 = 1$  and at  $\beta_0^\pm = -1 \pm 2\alpha$ . To ‘get the ball rolling’ the starting point must be an unstable equilibrium,  $\frac{d^2\phi_S}{d\beta^2}(1) < 0$ , which from (3.14) gives the condition that  $\alpha > 1$  and thus  $\alpha = 0.5$  in Fig. 3.2 does not qualify. If this condition is met, after a tiny push either to the left or right the Sagdeev particle will roll through the potential well until either it hits a stationary point and has its trajectory reflected or doesn’t and continues to fall. Asymptotes of (3.14) appear at  $\beta_A^\pm = \pm\sqrt{2\alpha^2 + 1}$  and the stationary points must be encountered before these to ensure that the journey back to the starting point is completed. It is thus required that  $\beta_0^- > \beta_A^-$  for rarefactive solitary waves (where the field strength decreases and field lines become less dense) and  $\beta_0^+ < \beta_A^+$  for compressive ones. The former inequality requires that  $\alpha < 0$  which contradicts the recently found requirement that  $\alpha > 1$ , meaning that a rarefactive mode does not exist. The latter results in  $\alpha < 2$  implying that compressive solitary waves do exist below this threshold speed. These two facts are reflected by the potentials for  $\alpha = 1.5$  and  $2.5$  in Fig. 3.2, where a particle released to the right along the  $\alpha = 1.5$  potential will reach a maximum coordinate of  $\beta_z = 2$  and then return back to the starting point. The  $\alpha = 2.5$  particle will continue to fall eternally. To conclude, solitary waves exist for the range of Alfvén Mach numbers  $1 < \alpha < 2$  with a characteristic width of the electron skin depth,  $d_e$ , and are compressive in nature. Now that all of the facts are in place, profiles of the plasma parameters in the wave frame are plotted in Fig. 3.3.

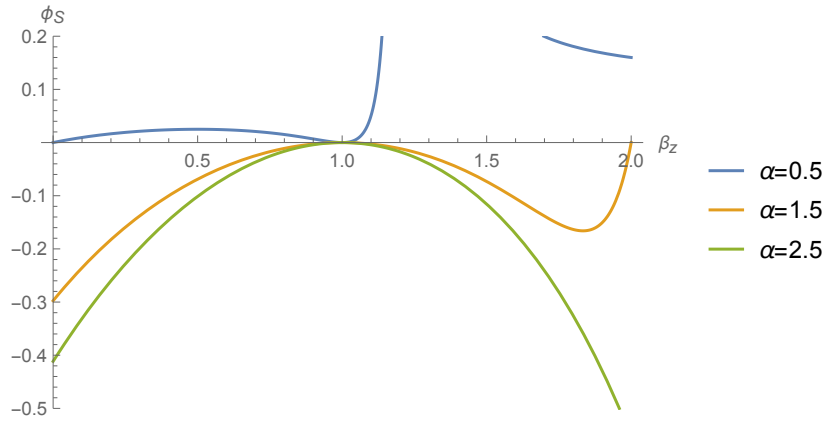


Figure 3.2: Sagdeev potential dependence on Alfvén Mach number.  $\alpha = 0.5$  is too slow to begin solitary wave formation whereas  $\alpha = 2.5$  is too fast to complete the return back to the original state.  $\alpha = 1.5$  allows  $\beta_z$  to grow from 1 to 2 and back again. All trajectories which leave  $\beta_z = 1$  going left will not return.

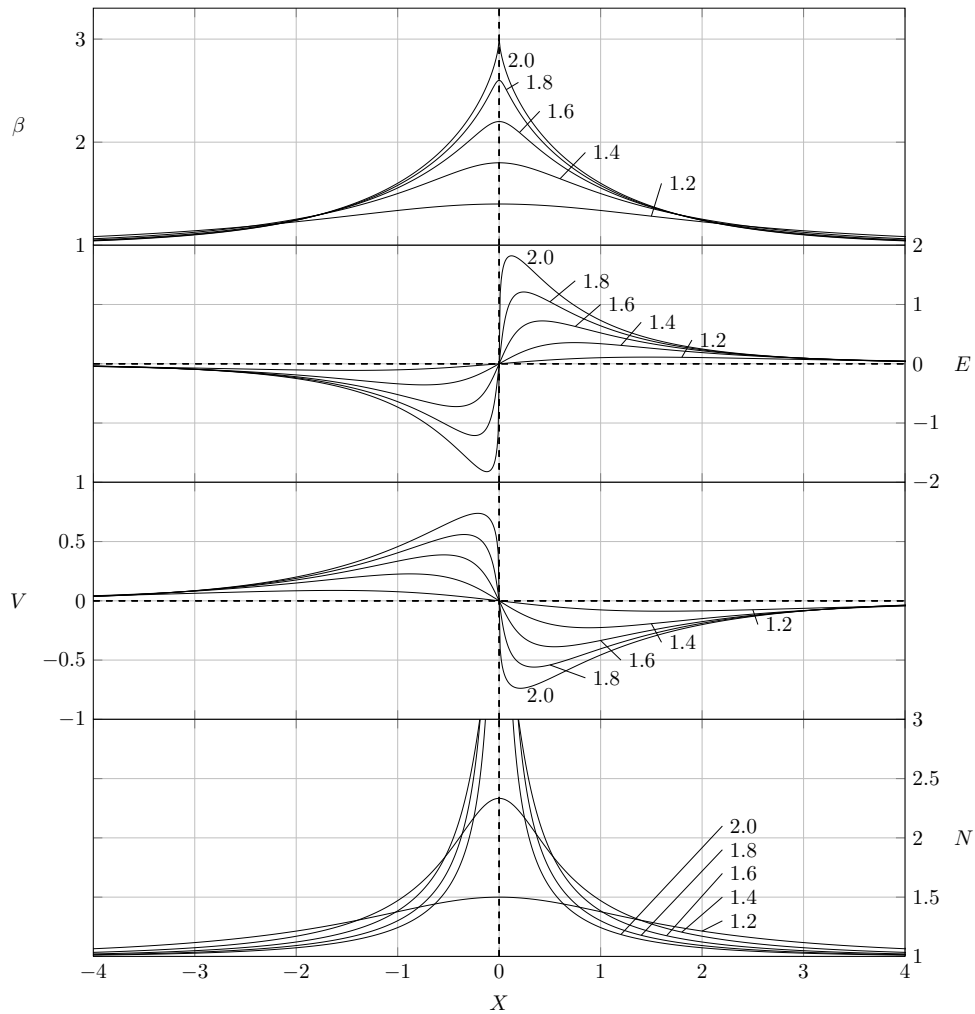


Figure 3.3: Profiles of normalized magnetic field, electric field, transverse electron velocity and plasma density for different wave speeds ( $\alpha = 1.2, 1.4, 1.6, 1.8, 2.0$ ).

Perhaps the most interesting feature of the solitary wave are these constraints on  $\alpha$  and so a method to find these where the problem need not be solved entirely is favourable. Whether or not the wave can grow in its early stages determines the minimum speed of the wave. This development phase is studied by linearising about the initial conditions,  $U = \alpha + \delta u$ ,  $\beta_z = 1 + b_z$  and then looking for evanescent solutions, that is, each first order deviation  $\propto \exp(\kappa X)$ . This yields  $\kappa = \sqrt{\alpha - \frac{1}{\alpha}}$  and the requirement that  $\kappa$  is real produces  $\alpha > 1$ , as found before. The maximum speed is set by the constraint that the plasma must keep moving to the right,  $U > 0$ . To this end, one can derive this limit from physical considerations of the flows of momentum and energy in the wave. I leave the derivations to Appendix A, where two conservation laws are useful here, the first, (A.25), stating that the momentum flux is constant at all points and is shared between the ions and the magnetic field,

$$m_i n_0 u_0 u + \frac{B_z^2}{2\mu_0} = \text{const.} \quad (3.15)$$

where  $Z_d = 0$  and electron  $x$  momentum has been ignored. The second, equation (A.28), states how energy is shared between the field and particle kinetic energy,

$$\frac{1}{2} n_0 u_0 (m_e v_e^2 + m_i u^2) + \frac{E_y B_z}{\mu_0} = \text{const.} \quad (3.16)$$

where again,  $Z_d = 0$  since this is dust-free. Since these equations have a physical interpretation which is helped by the fundamental constants, I will not normalise these quantities as previously. The flow speed of the plasma is slowest at the crest of the wave ( $x_W = 0$ ) and so to ensure that  $u$  is always positive it is only necessary to confirm that it's positive at this point. When the wave speed takes its maximum value,  $u_0 = u_{\max}$ , the plasma is just brought to rest at the crest of the wave  $u_i(x_W = 0) = 0$  - any faster and the plasma is swept up by the disturbance, no longer resembling a solitary wave. Because  $\frac{dB_z}{dx} = 0$  at the crest,  $v_e$  is zero from Faraday's law (confirmed by the profiles in Fig. 3.3). Evaluating (3.15) and (3.16) with the LHS at the crest and the RHS in the undisturbed plasma,

$$\frac{B_{max}^2}{2\mu_0} = m_i n_0 u_{max}^2 + \frac{B_0^2}{2\mu_0}, \quad (3.17)$$

$$\frac{B_0 B_{max}}{\mu_0} = \frac{1}{2} m_i n_0 u_{max}^2 + \frac{B_0^2}{\mu_0}, \quad (3.18)$$

which has the solution

$$u_{max} = 2v_A, \quad (3.19)$$

$$B_{max} = 3B_0, \quad (3.20)$$

confirming the result found previously and without the hassle of solving for the Sagdeev potential.

### 3.2.2 With dust

Now to derive the properties of a new wave by adding a stationary dust component, this is to be solved for in much the same way as before, the only equation which is modified is the quasineutrality condition, now becoming,

$$Z_d n_d + n_i - n_e = 0 , \quad (3.21)$$

which, when evaluated in the undisturbed plasma, gives

$$H + 1 - \frac{n_{e0}}{n_{i0}} = 0 , \quad (3.22)$$

where  $H \equiv \frac{n_d Z_d}{n_{i0}}$  is the Havnes parameter, a measure of how much charge is invested in the grains ( $-1 < H < \infty$ , these limits corresponding to dust-ion and dust-electron plasmas respectively). Combining the continuity equations with (3.21) and (3.22) gives the relationship between the electron and ion  $x$  velocities,

$$u_e = \frac{1 + H}{\frac{1}{u_i} + \frac{H}{u_0}} . \quad (3.23)$$

After applying the same normalizations of (3.7), the corresponding equations to (5.47) and (3.8)-(3.10) are for the dusty case

$$U_e = (1 + H) \left( \frac{1}{U_i} + \frac{H}{\alpha} \right)^{-1} , \quad (3.24)$$

$$U_i \frac{dU_i}{dX} = -V_e \beta , \quad (3.25)$$

$$\frac{dV_e}{dX} = \beta - \frac{\alpha}{U_e} , \quad (3.26)$$

$$\frac{d\beta}{dX} = \alpha(1 + H) \frac{V_e}{U_e} , \quad (3.27)$$

and these are solved in much the same way. To begin,  $U_i$  is related to  $\beta$ , eliminating  $V_e$  between (3.25) and (3.27),

$$U_i \frac{dU_i}{dX} = -\frac{U_e}{\alpha(1 + H)} \beta \frac{d\beta}{dX} . \quad (3.28)$$

Now, using (3.24) to eliminate  $U_e$ ,

$$(\alpha + H U_i) \frac{dU_i}{dX} = -\beta \frac{d\beta}{dX} , \quad (3.29)$$

and then integrating and rearranging for  $\beta$  gives

$$\beta^2 = 1 - 2\alpha(U_i - \alpha) - H(U_i^2 - \alpha^2) . \quad (3.30)$$



Now  $V_e$  is related to  $\beta$  by first eliminating  $X$  between (3.25) and (3.26),

$$\left( U_i - \frac{\alpha + HU_i}{(1+H)\beta} \right) \frac{dU_i}{dV_e} = -V_e, \quad (3.31)$$

which results in:

$$V^2 = 2 \left( \frac{\alpha \left( \sqrt{\alpha^2(1+H)^2 - H\beta^2 + H} - \alpha(1+H) \right)}{H^2} + \frac{\beta^2 - 1}{2H} + \frac{1 - \beta}{1+H} \right). \quad (3.32)$$

Substituting (3.32) and (3.30) into (3.27) gives

$$\begin{aligned} \frac{d\beta}{dX} &= \left( \frac{\alpha}{-\alpha + \sqrt{H(1-\beta^2) + \alpha^2(1+H)^2}} + 1 \right) \\ &\times \sqrt{2\alpha \left( \sqrt{\alpha^2(1+H)^2 + H(1-\beta^2)} - \alpha(1+H) \right) + H(\beta^2 - 1) + \frac{2H^2(1-\beta)}{1+H}} \end{aligned} \quad (3.33)$$

and this correctly reduces to the non-dusty case in the limit  $H \rightarrow 0$ . Now that a Sagdeev potential has been found (provided by  $\frac{1}{2} \times$  the square of the RHS of (3.33)), the framework is in place to derive the new restrictions on  $\alpha$  so that the new profiles can be plotted. Linearising (3.33) with  $B = 1 + b$  has solutions of the form  $b \propto \exp(X/L)$  if

$$L = \left( 1 + H - \frac{1}{\alpha^2(1+H)} \right)^{-\frac{1}{2}}, \quad (3.34)$$

which admits evanescent solutions so long as  $L$  is real, leading to the condition on the minimum velocity,

$$\alpha > \frac{1}{1+H} = \frac{n_{i0}}{n_{e0}}. \quad (3.35)$$

Equation (3.34) corresponds to the characteristic scale length of the pulse and demonstrates that negatively charged dust stretches the wave while positively charged dust compresses it as shown in Fig. 3.4. This is because electron depletion increases the electron skin depth, much like it resulted in an increased Debye length for the DIA wave.

Now to determine the maximum speed. The analysis of whether stationary points are met before asymptotes is more complicated than before, even though the solution itself is not. Asymptotes occur at  $\beta_c^\pm = \pm \sqrt{1 + \alpha^2(2+H)}$  and depending on  $\alpha$  and  $H$  there can be up to 4 roots (in addition to the one at  $\beta = 1$ ), which are  $\beta_0^{1,2} = \frac{H-1 \pm 2\alpha(1+H)}{1+H}$  and  $\beta_0^{3,4} = \pm \sqrt{\frac{H+\alpha^2(1+H)^2}{H}}$  (where the indices 1 and 3 denote roots where the + of the  $\pm$  is used). Roots 3 and 4 can be discarded before proceeding with the analysis since they always occur outside of the asymptotes. To prove this, if one tries to find where

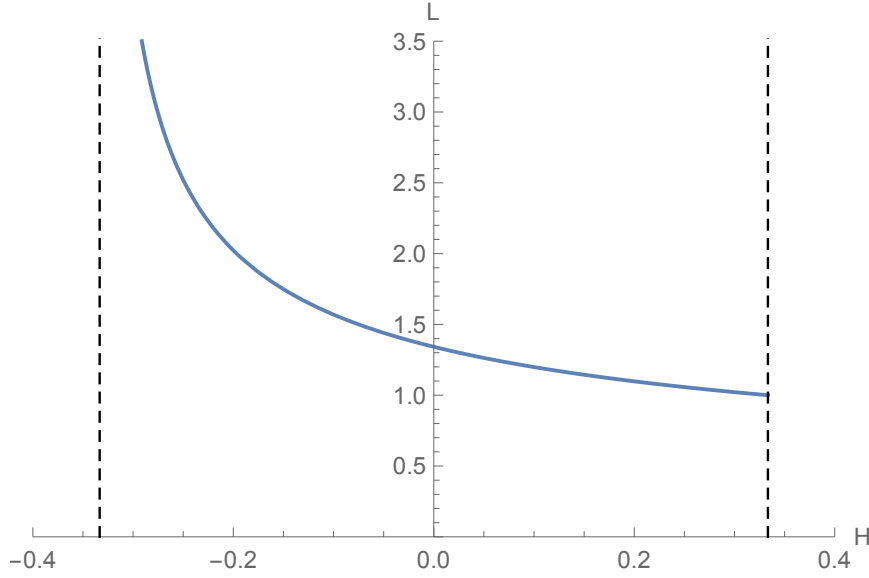


Figure 3.4: Characteristic width of a solitary wave for a speed  $\alpha = 1.5$  with varying Havnes parameter. The minimum value of  $H$  is set by equation (3.35) and the maximum follows from (3.38) - to be derived shortly.

the root occurs first:

$$\beta_0^3 < \beta_c^+, \quad (3.36)$$

$$\sqrt{\frac{H + \alpha^2(1+H)^2}{H}} < \sqrt{1 + \alpha^2(2+H)}, \quad (3.37)$$

then this implies that  $\alpha < \frac{\sqrt{-H}}{1+H}$  which, in light of (3.35), can never be true. Root 1 is the largest and thus corresponds to compressive solitary waves, the condition  $\beta_0^1 < \beta_c^+$  requires that

$$\alpha < \frac{2}{1+H} \quad (3.38)$$

and so its concluded that compressive solitary waves exist in the range  $\frac{1}{1+H} < \alpha < \frac{2}{1+H}$ , plotted in Fig. 3.5. Root 2 only exists when

$$-1 < H < \frac{1}{3}, \quad (3.39)$$

$$\text{or } \frac{1}{3} < H < 1 \text{ and } \alpha > \frac{2H}{H^2 - 1}. \quad (3.40)$$

For rarefactive solitary waves,  $\beta_0^2 > \beta_c^-$  requires  $\frac{2}{3} < H < 2$  and  $\alpha < \frac{2H}{2+H-H^2}$  which have no regions of overlap with equations (3.39) and (3.40). Thus, as in the dust-free case, there is no rarefactive mode as the Sagdeev potentials of Fig. 3.6 (a) illustrate for one example of the wave velocity.

Now that the allowed range of  $\alpha$  is known, analysis of the wave profile can commence. The modified structure is explored for a constant velocity  $\alpha = 1.5$  and varying amounts

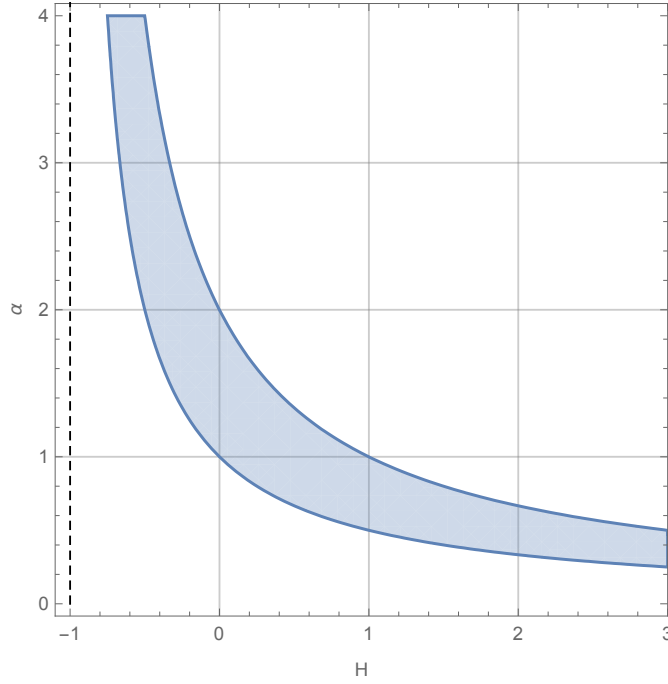
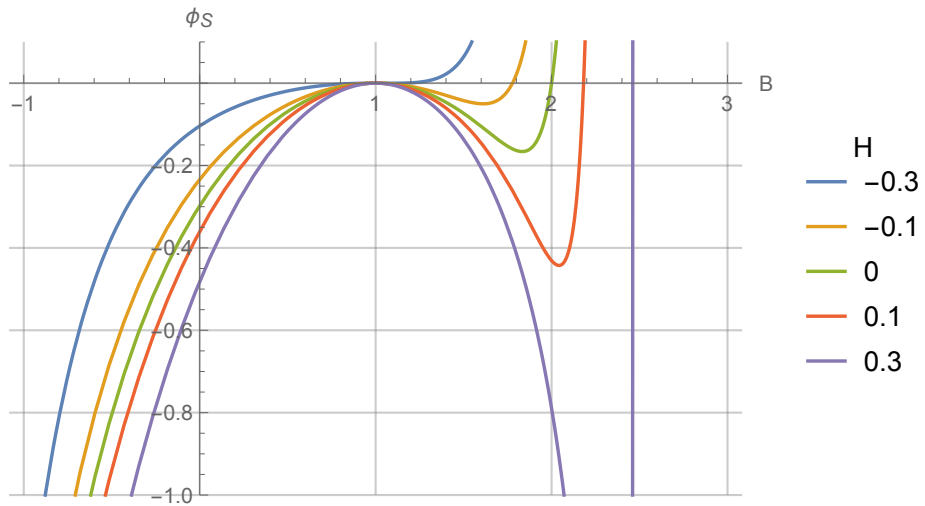


Figure 3.5: Permitted velocity range of compressive dusty solitary waves as a function of Havnes parameter.

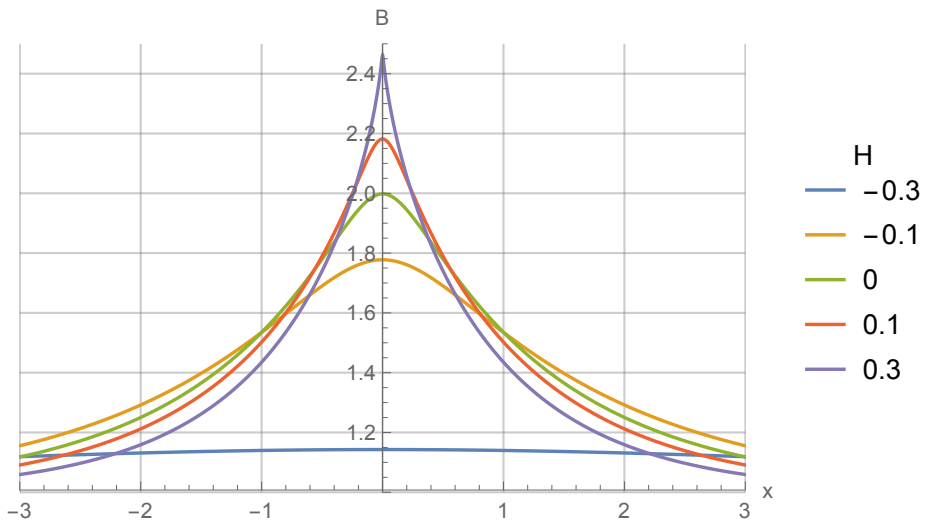
of dust charge density in Fig. 3.6 (b). One can see in the broadening of the lengthscale with increased dust as found in (3.34). Also, the amplitude of the wave reduces, for a given velocity, as the dust concentration is increased. This is because a depleted electron population provides a reduced transverse current and thus will result in a smaller magnetic field.

The asymptote at  $H = -1$  marks an area where the model breaks down. As  $H \rightarrow -1$  the electron density approaches zero and under the current model of transversely immobile ions this means that it still falls on the depleted electrons to provide all of the current. To do so with a density approaching zero, the transverse electron velocity has to approach infinity and since the transverse velocity depends on how fast they are incoming the wave speed must also approach infinity. In reality, for low enough values of  $H$ , the relatively slow ion deflection when coupled with their overwhelmingly large density will produce a current which exceeds that of the electrons. Considering the genesis of the wave, the incoming ion and electron  $x$  velocities are the same and so their relative transverse velocities can be found from the ratio of their  $y$  equations of motion as  $\frac{v_i}{v_e} = \frac{m_i}{m_e}$ . Their relative densities are given from (3.22) and so the ratio of initial transverse currents is  $\frac{j_{i0}}{j_{e0}} = \frac{n_{i0}v_i}{n_{e0}v_e} = \frac{m_e}{m_i(1+H)}$ . Finding the critical Havnes parameter  $H_c$ , such that the ions contribute as much to the current as the electrons yields:  $H_c = -1 + \frac{m_e}{m_i}$ , which marks the point at which the assumption of transversely immobile ions breaks down.

It is worth now considering an approach using the macroscopic conservation laws. The corresponding conservation equations to (3.15) and (3.16) for the dusty case are



(a) Sagdeev potentials



(b) Solitary wave profiles

Figure 3.6: Sagdeev potentials (a) and wave profiles (b) for different Havnes parameters and a Mach number of  $\alpha = 1.5$ .

given by taking  $Z_d$  to be non-zero

$$m_i n_0 u_0 u_i + \frac{B_z^2}{2\mu_0} + e Z_d n_d \int E_x dx = \text{const.} \quad (3.41)$$

$$\frac{1}{2} m_e n_0 u_0 (m_e v_e^2 + m_i u_i^2) + \frac{E_y B_z}{\mu_0} + u_0 e Z_d n_d \int E_x dx = \text{const.} \quad (3.42)$$

New terms have arisen in each equation due to the presence of the dust. It is very easy to ignore these, given that one may expect from momentum conservation a term arising from the dust like  $m_d n_d u_d^2$  which can then be temptingly disregarded due to the grains not moving. However, a very large  $m_d$  and very small  $u_d$  conspire to produce a significant term in the conservation equations, which found its way there, potentially unexpectedly, through modified quasineutrality. This non-trivial result may be easily missed and would lead one to erroneously conclude that stationary dust grains have no effect.

The electric field can be rewritten in terms of the ion speed from (3.3). This allows the integrals of (3.41) and (3.42) to be evaluated to get:

$$m_i n_0 u_0 u_i + \frac{B_z^2}{2\mu_0} + \frac{Z_d n_d m_i u_i^2}{2} = \text{const.} \quad (3.43)$$

$$\frac{1}{2} n_0 u_0 (m_e v_e^2 + m_i u_i^2) + \frac{E_y B_z}{\mu_0} + \frac{u_0 Z_d n_d m_i u_i^2}{2} = \text{const.} \quad (3.44)$$

For a wave travelling at the maximum velocity  $u_0 = u_{\text{max}}$ , with the LHS evaluated in the undisturbed plasma and the RHS evaluated at the crest,  $v_e = 0$  and  $B_z = B_{\text{max}}$ , (3.43) and (3.44) become

$$\frac{B_{\text{max}}^2}{2\mu_0} = \left(1 + \frac{H}{2}\right) m_i n_{i0} u_{\text{max}}^2 + \frac{B_0^2}{2\mu_0} \quad (3.45)$$

and

$$\frac{B_0 B_{\text{max}}}{\mu_0} = \frac{B_0^2}{\mu_0} + \frac{(1+H)m_i n_0 u_{\text{max}}^2}{2}. \quad (3.46)$$

The solution to these two equations is

$$u_{\text{max}} = \frac{2}{1+H} v_A, \quad (3.47)$$

$$B_{\text{max}} = \frac{3+H}{1+H} B_0. \quad (3.48)$$

The first is in agreement with the maximum velocity found previously. The second is extra information which gives the value of the magnetic field along the top edge of the region in Fig. 3.5, i.e. the amplitude of a solitary wave which is on the verge of breaking. For the non-dusty case, the maximum compression of the wave is a factor of 3, which is consistent with taking  $H = 0$  in (3.48).

### 3.3 Oblique Alfvénic solitary waves

Nonlinear magnetic waves fall into two main classes, those which propagate normal to the background field and those which propagate obliquely. This may seem like an obvious statement, but the physical behaviour of both is quite distinct [99]. Introducing  $\theta$  as the angle between the background magnetic field and direction of wave propagation ( $\theta = \frac{\pi}{2}$  being transverse and  $\theta = 0$  being parallel), normally moving solitary waves, which have just been covered, are restricted to a narrow range of angles,  $\theta_c \lesssim \theta \leq \frac{\pi}{2}$  and oblique waves cover the remaining range  $0 < \theta \lesssim \theta_c$ , where  $\theta_c = \frac{\pi}{2} - \sqrt{\frac{m_e}{m_i}}$  [100]. An example which illustrates these two cases side by side can be found in the surrounding plasma of the Earth's bow shock. Downstream from the region where the solar wind encounters the Earth's magnetic field at a right angle, solitary waves of the type studied previously (with scale lengths  $\frac{c}{\omega_{pe}}$ ) emerge. In practice, the plasma is most likely to be incident within the broad range of angles  $0 < \theta \lesssim \theta_c$  which results in the upstream appearance of 'oblique Alfvénic solitary waves' which have a far greater scale length,  $\frac{c}{\omega_{pi}}$ .

#### 3.3.1 Dust-free

Now to derive the features of the oblique solitary wave, following the paper of McKenzie and Doyle [101]. The method is the same as before in that one searches for stationary solutions to the equations of motion and Maxwell's equations in the wave frame, but the oblique field leads to particle motion allowed in 3 dimensions. To start, consider the effect oblique propagation has on the electromagnetic fields. Faraday's law requires that electric fields transverse to the flow are constant since  $\frac{\partial}{\partial t} = 0$ :

$$E_y = \text{const.}, \quad E_z = \text{const.}$$

With oblique solitary waves, a component of magnetic field now exists in the direction of propagation and the axes can be oriented such that at  $x = \pm\infty$ ,  $(B_x, B_y, B_z) = (B_{x0}, 0, B_{z0}) = (B_0 \cos \theta, 0, B_0 \sin \theta)$ . Since there are only spatial variations in the  $x$  direction,  $B_x$  is constant from Ampère's law, and will be written as  $B_{x0}$  from now on. Electron inertia may be ignored for oblique solitary waves [101] (justification of this is hard to find, but I offer my own in Appendix A.4, best understood after the problem is solved) which means that the fields are prescribed from:  $-\mathbf{u}_e \times \mathbf{B} = \mathbf{E}$ . Using the  $y$  and  $z$  components of this,

$$uB_z - w_e B_{x0} = E_y, \quad (3.49)$$

$$v_e B_{x0} - uB_y = E_z \quad (3.50)$$

and because the electric fields are constant, these equations can be evaluated anywhere to find their values. Taking the undisturbed plasma, where  $w_e = v_e = B_y = 0$  yields

$$E_y = u_0 B_{z0} , \quad (3.51)$$

$$E_z = 0 . \quad (3.52)$$

The equations of motion for the ions with this field configuration are

$$m_i u \frac{du}{dx} = e(v_i B_z - w_i B_y + E_x) , \quad (3.53)$$

$$m_i u \frac{dv_i}{dx} = e(w_i B_{x0} - u B_z + u_0 B_{z0}) , \quad (3.54)$$

$$m_i u \frac{dw_i}{dx} = e(u B_y - v_i B_{x0}) \quad (3.55)$$

which completes the set of equations. It is easiest to solve these by absorbing the electron motion and Ampère's law in the momentum and energy flux conservation equations which have been previously utilised to find the maximum speed of solitary waves. These are derived in Appendix A, the result being (without electron inertia and  $Z_d = 0$ ) that

$$m_i n_0 u_0 u + \frac{B_y^2 + B_z^2}{2\mu_0} = \text{const.} \quad (3.56)$$

$$m_i n_0 u_0 v_i - \frac{B_{x0} B_y}{\mu_0} = \text{const.} \quad (3.57)$$

$$m_i n_0 u_0 w_i - \frac{B_{x0} B_z}{\mu_0} = \text{const.} \quad (3.58)$$

$$\frac{1}{2} m_i n_0 u_0 (u^2 + v_i^2 + w_i^2) + \frac{E_y B_z}{\mu_0} = \text{const.} \quad (3.59)$$

Substituting (3.56)-(3.58) into the transverse ion equations of motion, (3.54) and (3.55), gives

$$U \frac{d\beta_y}{dX} = \alpha - \frac{\cos^2 \theta}{\alpha} - \beta_z \left( U - \frac{\cos^2 \theta}{\alpha} \right) , \quad (3.60)$$

$$U \frac{d\beta_z}{dX} = \beta_y \left( U - \frac{\cos^2 \theta}{\alpha} \right) , \quad (3.61)$$

where I have introduced the normalizations (some of which are the same for the transverse case):  $U = \frac{u}{v_A}$ ,  $\beta_{y,z} = \frac{B_{y,z}}{B_{z0}}$  and  $X = \frac{x}{d_i}$  with  $v_A$  the Alfvén velocity for the total background field  $B_0 = \sqrt{B_{x0}^2 + B_{z0}^2}$ ,  $d_i$  the ion skin depth and  $\alpha$  still denoting the Alfvén Mach number. To derive the Sagdeev potential for this wave, one must write things in terms of the transverse magnetic field strength,  $\beta_\perp^2 = \beta_y^2 + \beta_z^2$ . Equations (3.56), (3.60) and (3.61) then boil down to the Sagdeev potential,

$$\phi_S(\beta_\perp^2) = -\frac{1}{2} \frac{(1 - \beta_\perp^2)^2 (\beta_+^2 - \beta_\perp^2) (\beta_\perp^2 - \beta_-^2)}{(1 + 2 \left(\frac{\alpha}{\sin \theta}\right)^2 - \beta_\perp^2)^2} , \quad (3.62)$$

where

$$\beta_{\pm}^2 = \frac{(\sqrt{m} \pm 2)^2}{m} \text{ and } m = \frac{\sin^2 \theta}{\alpha^2 - \cos^2 \theta} . \quad (3.63)$$

As has been the routine so far, the first task is to determine from (3.62) the values of  $\alpha$  which provide an unstable equilibrium at  $\beta_{\perp} = 1$ . Expanding to first order about the starting point,  $\beta_{\perp} = 1 + b$ , and searching for evanescent solutions of the form  $b \propto \exp(\kappa X)$  leads to

$$\kappa^2 = \frac{1}{\alpha^2 \cos^2 \theta} (1 - \alpha^2) (\alpha^2 - \cos^2 \theta) , \quad (3.64)$$

where  $\kappa$  is normalised by  $d_i^{-1}$ . Requiring that  $\kappa$  is real constrains the initial velocity to be

$$\cos \theta < \alpha < 1 . \quad (3.65)$$

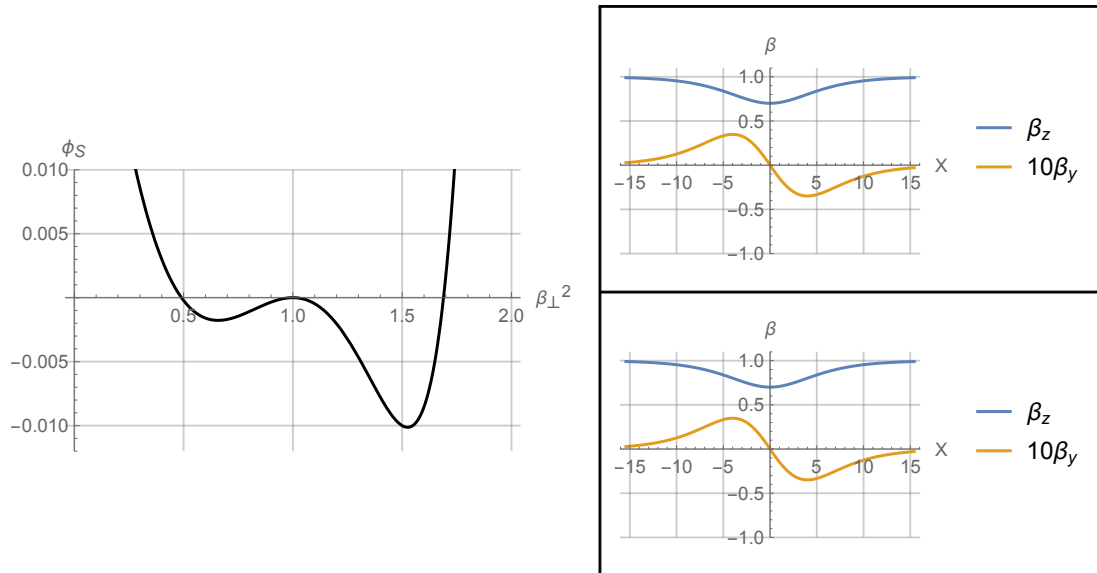
Already, markedly different behaviour can be noticed. Oblique solitary waves travel at sub-Mach speeds and this limitation is set by the physics at the start of the wave. A further contrast is that rarefactive modes exist in addition to the compressive one, that is, cases where the disturbance is a region of weakened magnetic field. I will neglect to repeat the analysis of the asymptotes and stationary points of (3.62) here, but Fig. 3.7 demonstrates one such case where the Sagdeev potential admits these two behaviours. It is found that the stationary point corresponding to the rarefactive mode is always met before the asymptote, meaning so long as (3.65) is respected, these can exist. Conversely, the compressive stationary point is only encountered before the asymptote so long as

$$\alpha < \sqrt{2(1 - \sin \theta)} \quad (3.66)$$

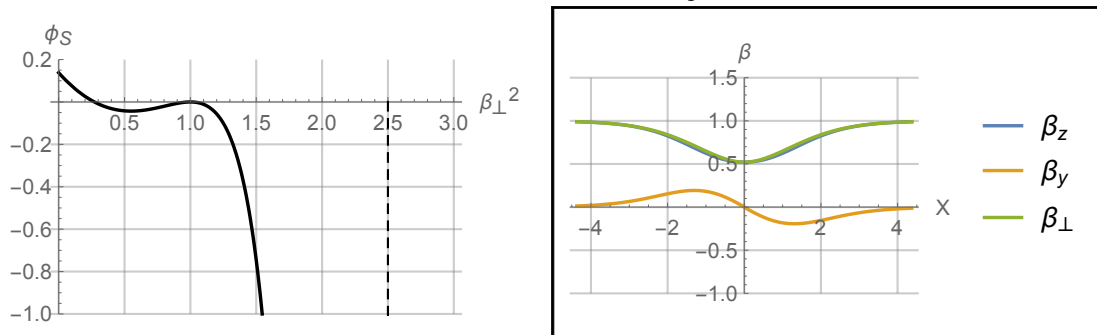
and so there is an additional speed limit placed on the compressive mode only. The range of permitted parameters according to inequalities (3.65) and (3.66) is plotted in Fig. 3.8. As compared to the rarefactive wave, the compressive wave is far more tightly restricted.

Again, there are shortcuts to obtaining these results, though there is one shortcoming to this approach which shall be seen shortly. One can obtain the first inequality (3.65), by linearizing the variables of (3.56)-(3.60) about their initial values and looking for solutions to these perturbations of the form  $\exp(\kappa x)$ . As always, the second constrained provided by the condition that  $U > 0$  is tested by considering momentum and energy. Evaluating (3.56), (3.58) and (3.59) for the limiting solitary wave travelling at  $u = u_{\max}$ , with the RHS in the undisturbed plasma and the LHS at the crest of the wave where,



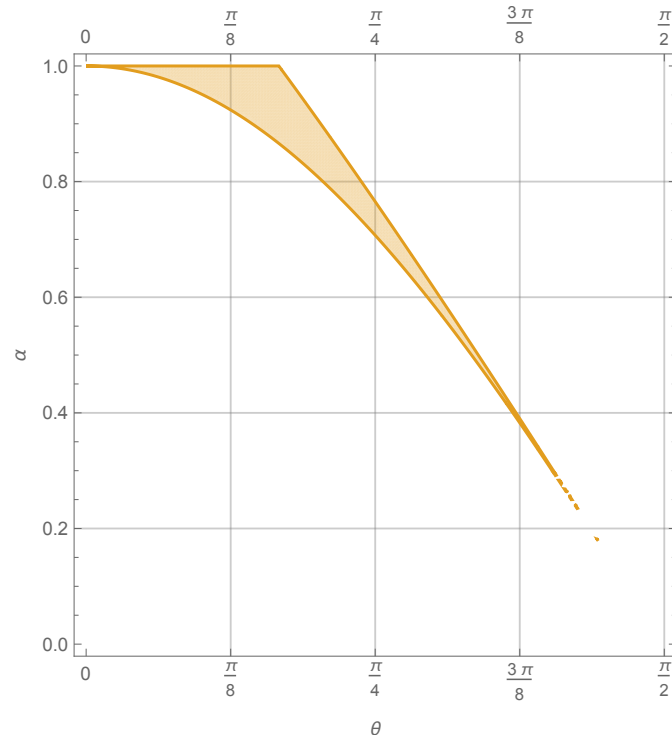


(a)  $\alpha = 0.715$  and  $\theta = \frac{\pi}{4}$

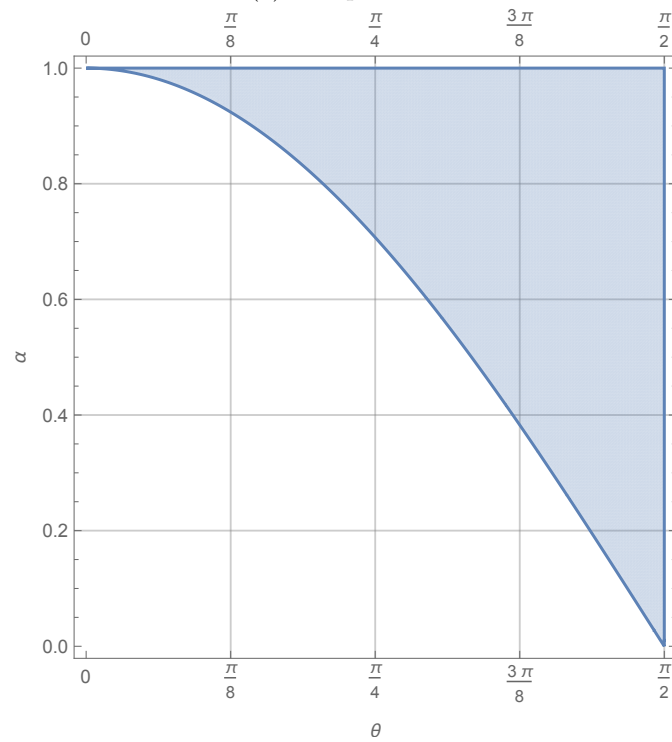


(b)  $\alpha = 0.8$  and  $\theta = \frac{3\pi}{8}$

Figure 3.7: Sagdeev potentials and associated magnetic field profiles for parameters which admit both rarefactive and compressive solitary waves (a) and only rarefactive waves (b). In conjunction with Fig. 3.8, one can verify why this choice of parameters produced this result. In (a),  $\beta_y$  is relatively weak meaning  $\beta_z \approx \beta_{\perp}$  and so only one of these is plotted.



(a) Compressive



(b) Rarefactive

Figure 3.8: Allowed regions of parameter space,  $\alpha$  and  $\theta$ , for compressive (a) and rarefactive (b) solitary waves.

$u = 0$ ,  $B_z = B_{z\max}$ ,  $w = w_{\max}$ ,  $B_y = 0$  and  $v = 0$  gives

$$\frac{B_{z\max}^2}{2\mu_0} = m_i n_{i0} u_{\max}^2 + \frac{B_{z0}^2}{2\mu_0}, \quad (3.67)$$

$$m_i n_{i0} u_0 w_{\max} - \frac{B_{z\max} B_{x0}}{\mu_0} = -\frac{B_{z0} B_{x0}}{\mu_0}, \quad (3.68)$$

$$\frac{m_i n_{i0}}{2} w_{\max}^2 + \frac{B_{z0} B_{z\max}}{\mu_0} = \frac{m_i n_{i0} u_{\max}^2}{2} + \frac{B_{z0}^2}{\mu_0}, \quad (3.69)$$

where (3.57) reduces to  $0 = 0$  and thus provides nothing useful. The solution to these simultaneous equations yields

$$u_{\max} = \sqrt{\frac{B_0^2}{\mu_0 m_i n_{i0}}} \sqrt{2(1 - \sin \theta)}, \quad (3.70)$$

$$B_{z\max} = (\sin \theta - 2) B_0, \quad (3.71)$$

$$w_{\max} = -\sqrt{\frac{B_0^2}{\mu_0 m_i n_{i0}}} \sqrt{2(1 - \sin \theta)} \left( \frac{1 + \sin \theta}{\cos \theta} \right), \quad (3.72)$$

the first of which confirms equation (3.66). The shortcoming of this approach alluded to earlier is that one cannot tell that a rarefactive mode exists. Equation (3.71) does confirm that the speed limit applies to compressive solitary waves since  $|B_{z\max}| > |B_0|$ , but that is all that can be extracted.

One final point to make is that given that electron inertia is disregarded for the oblique solitary wave and is a key component of the transverse wave, the results for the former do not reduce to those for the latter as  $\theta \rightarrow \frac{\pi}{2}$ .

### 3.3.2 With dust

It is again time to study a new wave by adding a component of immobile dust. However, the story for dusty oblique solitary waves is a bit more complicated than for transverse ones and as a result, the problem is not yet solved entirely. Necessary conditions for solitary wave existence are derived from linearisation of the wave in its early stages, but the supplementary conditions resulting from the condition that plasma flow cannot reverse remain to be solved for. An analytic expression for the Sagdeev potential could not be arrived at, so, instead I shall see what one can find out from the macroscopic conservation equations of the wave. For the last time, I refer the reader to Appendix A for the derivation of these equations. Conservation of momentum flux states that

$$m_i n_{i0} u_0 u_i + \frac{B_y^2 + B_z^2}{2\mu_0} + Z e n_d \int_{-\infty}^x E_x dx = m_i n_{i0} u_0^2 + \frac{B_{z0}^2}{2\mu_0}, \quad (3.73)$$

$$m_i n_{i0} u_0 v_i - \frac{B_y B_{x0}}{\mu_0} - e Z n_d u_0 \int_{-\infty}^x (B_z - B_{z0}) dx = 0, \quad (3.74)$$

$$m_i n_{i0} u_0 w_i - \frac{B_z B_{x0}}{\mu_0} + e Z n_d u_0 \int_{-\infty}^x B_y dx = -\frac{B_{z0} B_{x0}}{\mu_0}, \quad (3.75)$$

and the energy equation is

$$\frac{m_i n_{i0} u_0}{2} (u_i^2 + v_i^2 + w_i^2) + \frac{E_y B_z}{\mu_0} + Z e n_d u_0 \int_{-\infty}^x E_x dx = \frac{m_i n_{i0} u_0^3}{2} + \frac{E_y B_{z0}}{\mu_0}, \quad (3.76)$$

where the right hand sides have all been evaluated in the undisturbed plasma. To study the early stages of the wave, assume that  $u = u_0 + \delta u$ ,  $B_z = B_{z0} + b_z$  in momentum conservation and transverse EOM and looking for evanescent solutions of the form  $\exp(\kappa x)$  results in:

$$m_i n_{i0} u_0 (1 + H) \delta u + \frac{B_{z0}}{\mu_0} b_z = 0, \quad (3.77)$$

$$m_i n_{i0} u_0 v_i - \frac{B_{x0}}{\mu_0} B_y - \frac{e H n_{i0} u_0 b_z}{\kappa} = 0, \quad (3.78)$$

$$m_i n_{i0} u_0 w_i - \frac{B_{x0}}{\mu_0} b_z + \frac{e H n_{i0} u_0 B_y}{\kappa} = 0, \quad (3.79)$$

$$m_i u_0 \kappa v_i - e B_{x0} w_i + e u_0 b_z + e B_{z0} \delta u = 0, \quad (3.80)$$

$$m_i u_0 \kappa w_i - e u_0 B_y + e B_{x0} v_i = 0. \quad (3.81)$$

These simultaneous equations provides two solutions for the decay constant as

$$\kappa_{\pm} = \sqrt{\frac{f(\alpha) \pm \sqrt{f(\alpha)^2 - (2\alpha^2 \cos \theta H)^2}}{2\alpha^2 \cos^2 \theta}}, \quad (3.82)$$

where  $f(\alpha)$  is a quadratic equation in  $\alpha^2$ ,

$$f(\alpha) = -(1 + H)^2 \alpha^4 + (1 + \cos^2 \theta) \alpha^2 - \cos^2 \theta. \quad (3.83)$$

The presence of two solutions is the first interesting result, probably indicating that the compressive and rarefactive modes have different lengthscales. However, without solving the problem entirely, this is hard to confirm and so I would hope that future simulations can shed some light on this.

Now it needs to be determined where  $\kappa$  is real. In the numerator of (3.82), the second term which is preceded by the  $\pm$  always has a smaller magnitude than the first term. Thus, to ensure that at least one solution for  $\kappa$  is real,

$$f(\alpha) > 0. \quad (3.84)$$

This  $\pm$  term must itself be real too, which requires that

$$f(\alpha)^2 - (2\alpha^2 \cos \theta H)^2 > 0. \quad (3.85)$$

The values of  $\alpha$  and  $\theta$  which satisfy these two inequalities depend on the sign of  $H$ .

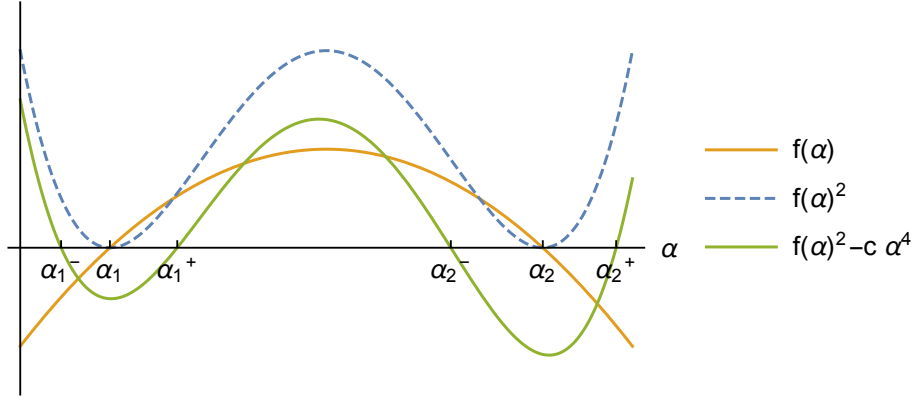


Figure 3.9: Graphical representation of the mutual solution of (3.84) and (3.85). By taking the square of  $f(\alpha)$  (dashed line), the position of the roots  $\alpha_1$  and  $\alpha_2$  stay the same. Then, by subtracting an always positive term  $c\alpha^4$  (where  $c > 0$ ), the roots of the green curve lie in pairs either side of  $\alpha_1$  and  $\alpha_2$ , providing the central maxima does not lie under the x axis (which will not be the case).

### Negatively charged dust

Finding the allowed regions of parameter space is tricky and best understood with graphical help, provided by Fig. 3.9 which should guide the reader through the upcoming analysis. Neglecting negative values, (3.84) has two roots  $\alpha_{1,2}$  (where I take  $\alpha_2 > \alpha_1$ ). The coefficient of  $\alpha^4$  is always negative which implies that the inequality (3.84) is satisfied for  $\alpha_1 < \alpha < \alpha_2$ . As described in the caption of Fig. 3.9, the roots of (3.85) occur in two pairs  $\alpha_1^\pm$  and  $\alpha_2^\pm$ , either side of  $\alpha_1$  and  $\alpha_2$  respectively. Thus, the region satisfying both (3.84) and (3.85) is  $\alpha_1^+ < \alpha < \alpha_2^-$ . Solving for these roots gives the result:

$$\frac{(\cos \theta - 1) + \sqrt{(1 + \cos \theta)^2 - 4H \cos \theta}}{2(1 + H)} < \alpha < \frac{(1 - \cos \theta) + \sqrt{(1 + \cos \theta)^2 - 4H \cos \theta}}{2(1 + H)}. \quad (3.86)$$

This reassuringly reduces to the known result, (3.65), when  $H = 0$ . The regions of parameter space are plotted in Fig. 3.10. As a general rule, the presence of dust tends to require higher speeds, more so for increasingly oblique solitary waves ( $\theta \rightarrow 0$ ). This is again probably due to the limited ability of a plasma to provide the necessary current - an electron depleted plasma encountering oblique fields will not lead to a great transverse current, unless it has a large incoming velocity to compensate for this.

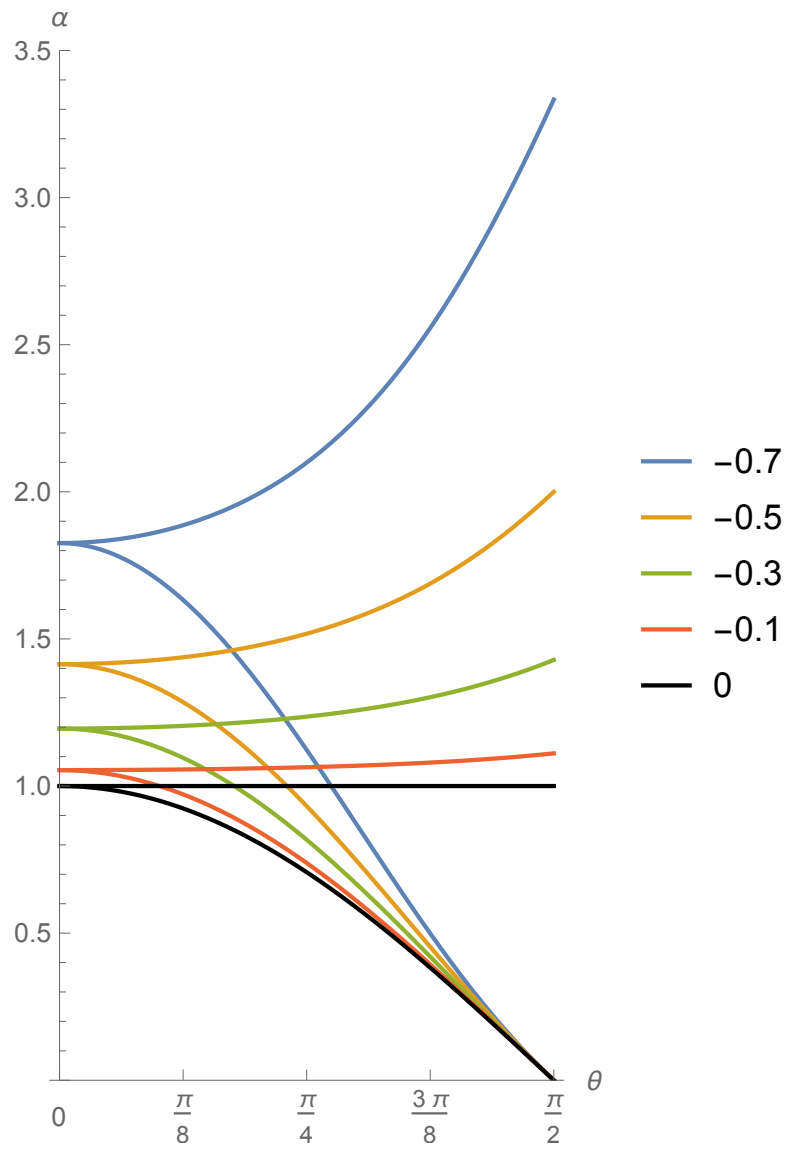


Figure 3.10: Range of allowed parameters for the oblique solitary wave with negatively charged dust. The black outline corresponds to the boundary of the region in Fig. 3.8 (b) and the other lines enclose regions of parameter space in the same way.

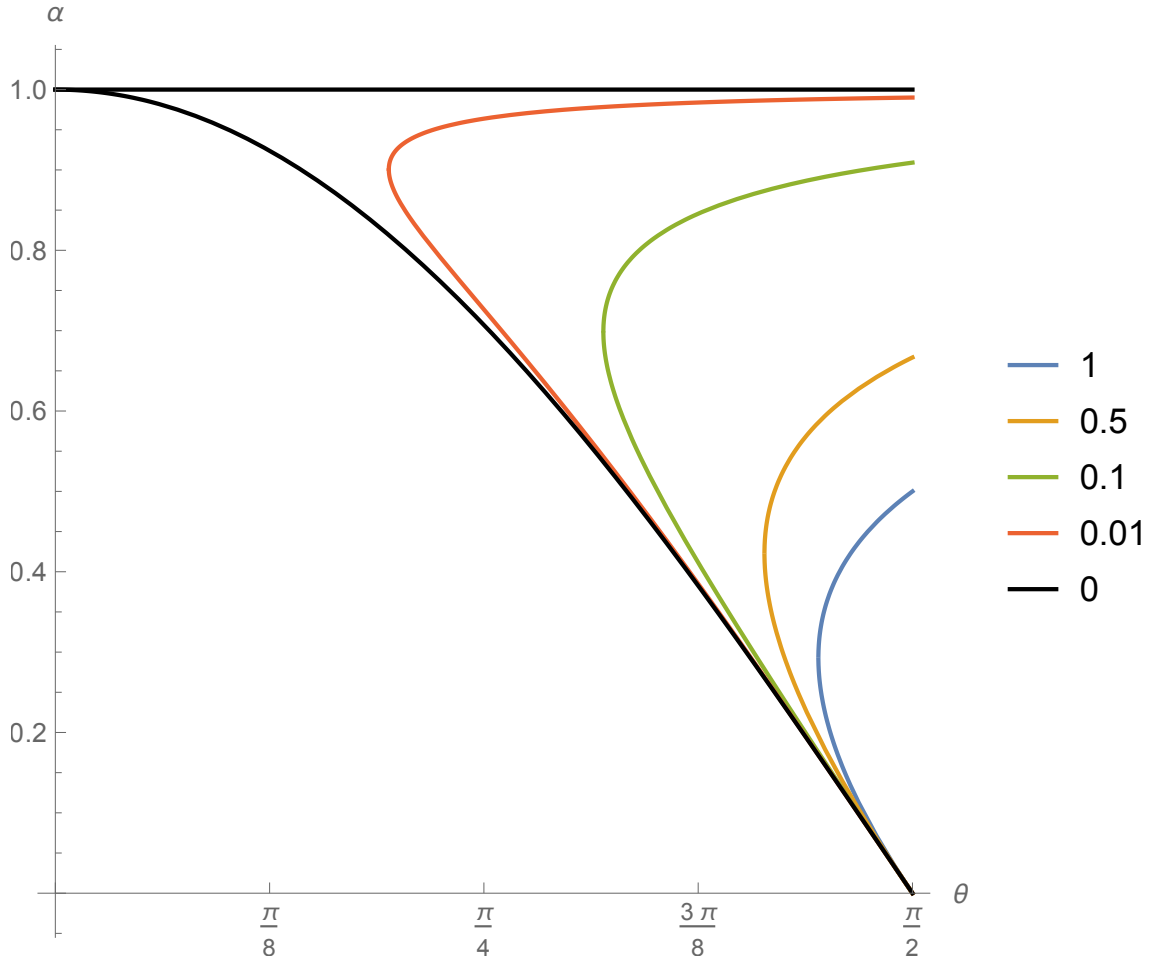


Figure 3.11: Range of allowed parameters for positively charged dust.

### Positively charged dust

When  $H > 0$ , the relative sizes of the coefficients of (3.84) mean that the roots  $\alpha_1^+$  and  $\alpha_2^-$  take a form different to the negative dust case,

$$\frac{(1 + \cos \theta) - \sqrt{(1 - \cos \theta)^2 - 4 \cos \theta H}}{2(1 + H)} < \alpha < \frac{(1 + \cos \theta) + \sqrt{(1 - \cos \theta)^2 - 4 \cos \theta H}}{2(1 + H)}. \quad (3.87)$$

The regions of parameter space described by these limits are plotted in Fig. 3.11 with the characteristic speeds being reduced in this case. A particularly novel feature is that the solitary waves do not exist for the entire range of angles, but must be sufficiently oblique such that

$$\theta > \arccos \left( 1 + 2H - 2\sqrt{H(1+H)} \right) \quad (3.88)$$

This is noticeable even for very small values of  $H$ , as seen in Fig. 3.11, even a Havnes parameter of 0.01 forbids the existence of solitary waves with  $\theta < 0.61 \text{ rad}$  ( $35^\circ$ ).

As stated at the start of this section, the story is incomplete - the regions of parameter space which allow the solitary waves to come into existence have been derived, but it remains to determine the conditions under which the flow is reversed which will restrict the zones in Figs. 3.10 and 3.11 further still. The integrals associated with the dust grains in equations (3.73)-(3.76) present a stumbling block, in the transverse case these could be dealt with by using (3.3) to eliminate the electric field, but the equations of motion are now too complicated for this trick to work.

### 3.4 Summary

In this chapter two important classes of nonlinear waves have been introduced and extended to include the effects of a stationary population of positively or negatively charged dust grains. For transverse propagation, the spatial structure and range of allowed velocities is solved for. For oblique propagation, necessary but not sufficient conditions on the speed and direction of propagation are derived. This point now marks the conclusion of the work done on dusty plasma with magnetic fields.

---



## 4 Electron distribution around a magnetic dipole

Now that the work on dusty plasmas has been presented, the next study, of a phenomenon in magnetised plasma where the dust is very sparse, can begin.

### 4.1 Experimental observations and simulations

In the introduction, it was stated that an almost interchangeable experimental arrangement is used by two different camps of physics, namely, laboratory models of lunar swirls and dusty crystal experiments. Each field's own separate motivations for performing such experiments were covered there, in this opening subsection I shall outline in more detail how they have gone about their work, what they have found out and how well their findings have been explained. This final step will then reveal which aspects this thesis can contribute to.

Two experiments attempting to model the plasma structure above a lunar swirl (of the type which does not form a mini-magnetosphere) with dipole moment perpendicular to the surface have been performed by Wang [1] in 2013 and more recently Dropmann [2] in 2016 (the names of the authors will be used to refer to each experiment). An insulating lower electrode plays the role of the lunar surface, the plasma discharge provides a laboratory solar wind and the magnetised crustal rocks are represented by a small cylindrical permanent magnet positioned under the lower electrode. The magnetic dipole moment of a magnetized moon patch has no reason to point in any particular direction and so, to cover other possibilities, experiments have also been performed with magnets oriented parallel [74] or obliquely [1] [2] to the surface, however, it is the perpendicular case which is of interest here. Parameters for both (as well as other) experiments are outlined in Table. 4.1. Some parameters are not explicitly stated in the papers: the position of the dipole below the plasma-wall boundary,  $z_0$ , is taken to

Group	$\mathcal{M}$ , T m <sup>3</sup>	$z_0$ , mm	$T_e$ , eV	Sheath width (approx.), mm	$\lambda_{\text{MFP},e}$ , mm	Electrode
Dropmann	$1.53 \times 10^{-8}$	4.7	4.9	6	17	Insulator
Wang	$1.12 \times 10^{-7}$	12	2.5	60	$2.6 \times 10^3$	Insulator
Saitou	$1.33 \times 10^{-8}$	6	2	6	29	Insulator
Law	$\mathcal{O}(10^{-8})$	$\mathcal{O}(1)$	$\mathcal{O}(1)$	$\mathcal{O}(1)$	$\mathcal{O}(10)$	Conductor

Table 4.1: Experimental parameters for dust crystal and lunar swirl studies.

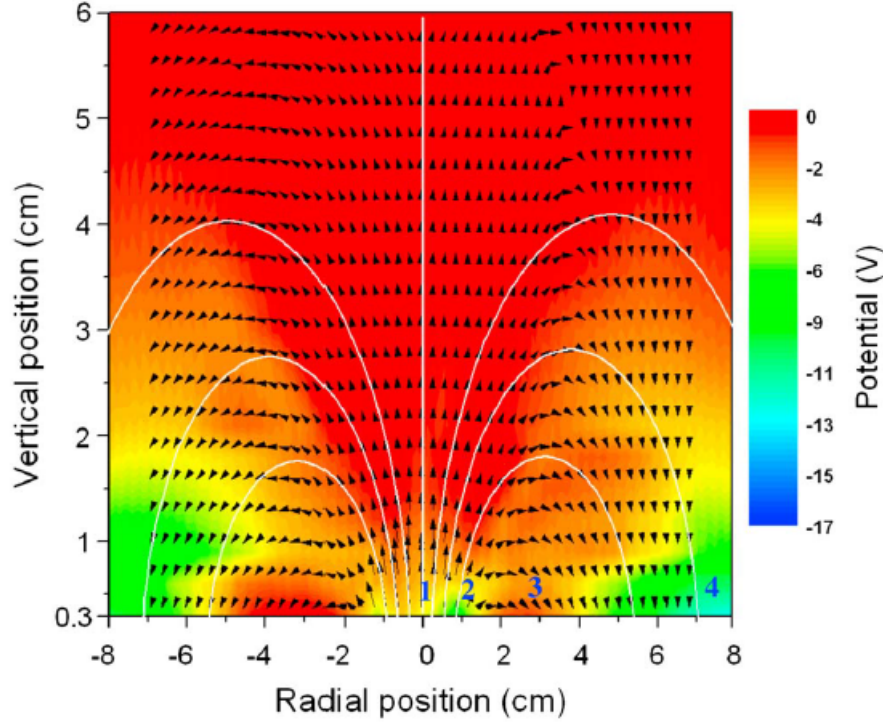


Figure 4.1: Electric potential in the sheath above an insulating electrode. Dipole magnetic field lines are also included.

be the centre of the permanent magnet; the scaled magnetic dipole moment,  $\mathcal{M} = \frac{\mu_0 m}{4\pi}$ , is derived from the field measurements provided at certain points in the plasma (usually  $B_z$  on axis just above the lower electrode) and the electron mean free path,  $\lambda_{\text{MFP},e}$ , is found using the electron-atom collision cross section in Argon [102], the background gas in all of the experiments. A stronger magnet and longer Debye length mean that the Wang arrangement is ostensibly a scaled up version of Dropmann's. It is interesting to point out that whilst Wang opted to use Langmuir and emissive probes to diagnose the plasma potential, Dropmann elected to deduce the potential by releasing charged dust grains and then tracking their trajectories.

Qualitatively similar results were obtained by both experiments: the surface potential directly above the magnet is negative and then, extending out radially, the potential becomes less negative in the lobe region (that is, where field lines are parallel to the surface) and then continuing outwards it falls back down to approach its planar behaviour as the influence of the magnet diminishes. This can be seen in Fig. 4.1, where a plot of the data from Wang [1] has been included to illustrate the profile of electric potential in the sheath. In both experiments, the strongest radial electric fields were found near to the surface and were of order  $10^4 \text{V m}^{-1}$  for Dropmann and several hundreds for Wang. The field is directed such that negative particles (if acted on purely by the electric field) will be attracted towards the lobe regions - away from the centre and inwards from the edges. For example, in Fig. 4.1 a negatively charged dust grain sitting near to the surface would be pushed towards a radius of approximately 3cm.

Whilst large-scale simulations of magnetic anomalies have been performed to resolve the kilometer scale features [103] and the formation of mini-magnetospheres [104] [105], there remains much work to be performed in characterising the charge separation which is postulated to occur on the scale of tens to hundreds of meters in regions of rapid magnetic field variation. Notable work was done by Zimmerman [4] in 2015, whose representation included the flow speed of the solar wind and photoelectrons emitted from the lunar surface. The magnetic field is not a true dipole however, since it is the result of two infinite, antiparallel currents (in the  $z$  direction) located below the surface leading to a field which falls off as  $r^{-2}$  as opposed to  $r^{-3}$  and is invariant to  $z$  translations as opposed to azimuthal ones. As far as the structure of the electric field goes, the previously shown experimental surface feature of a potential minimum flanked by two maxima was recovered.

This concludes the work done by the lunar community, now it's time to introduce the experiments where the dust is the centre of attention. The only differences between these studies and the lunar swirl ones are that the lower electrode is sometimes modified in some way to prevent the dust grains from escaping radially and said electrode is also usually conducting. The work of Saitou [3] uses very similar experimental parameters to Dropmann (see Table 4.1), but to a rather different end: the non-uniformity of the magnetic field sets up a sheared flow of dust grains which provides the possibility of producing dusty plasma vortices. There is also Law who, in unpublished work [63], performed similar experiments to investigate dust crystal dynamics with magnetic fields, on this occasion with a conducting lower electrode. Only order of magnitude estimates for Law's parameters can be given from the information provided in his short paper. In both of these experiments the dust is forced away from the axis, the time lapse of the process as observed by Law is shown in Fig. 4.2 and the motions of the negatively charged dust particles are consistent with the radial fields observed by Wang and Dropmann.

The peculiar case of dust grains becoming more tightly bound to the axis may possibly be explained when one includes the effects of ion drag [57]. A radial electric field which acts to force dust outwards will also act to attract ions inwards and these will tend to drag grains with them as they pass. This gives two competing effects and it may be that for this anomalous result the experimental parameters were favourable for the ion drag to exceed the electric force.

## 4.2 Theory of radial electric field generation

### 4.2.1 Current state

From the discussion sections of the aforementioned publications, there is a clear consensus that the influence of the magnetic field on the electrons is responsible for the radially modified sheath profile. As one progresses chronologically this becomes more specific to suggest a redistribution of the electrons which subsequently generate radial

---

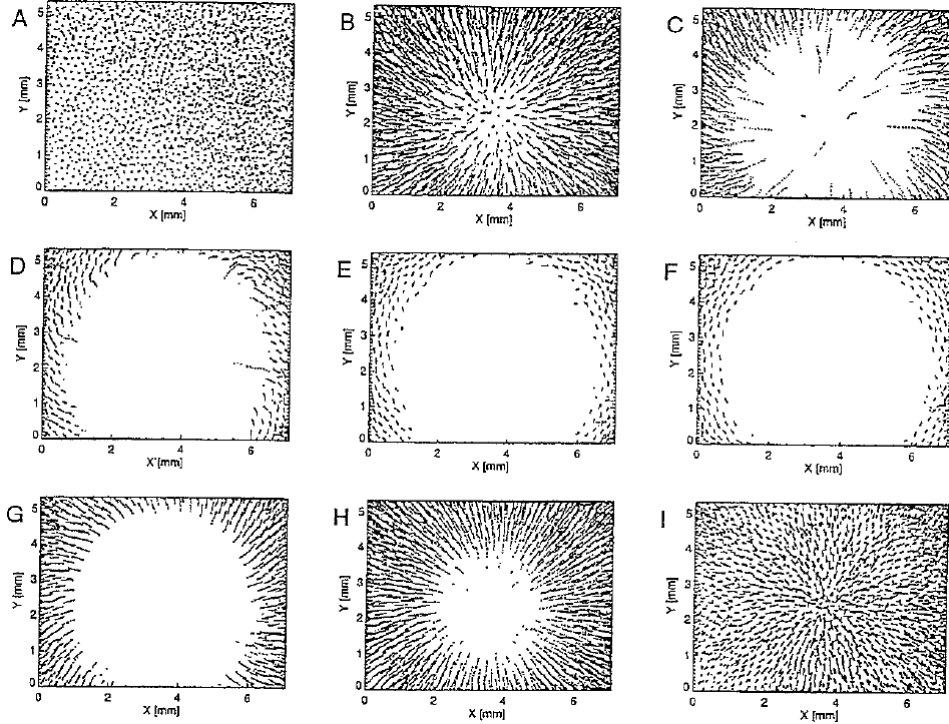


Figure 4.2: Void formation as viewed from above. An ordinary dust crystal (A) takes on a ring formation (E) after the magnet is switched on (B) and then returns to its former (I) state after the field is removed at (G). Image credit: D. A. Law

electric fields. To quote directly, starting with Law, “The radial motion of the dust, when the magnetic field is switched on or off is likely due to a modified sheath structure, possibly caused by the electrons gyrating in the strong field directly above the magnet.” In Wang’s paper, the notion of “electron shielding” is alluded to, to explain the more positive electric potential near the lobes. In this paper, he also suggests that the magnetic mirror effect is responsible for a depleted electron density on axis, leading to higher potentials than in the planar case. In light of the analysis in section 2.2.3, it seems unlikely that a reduced electron density will occur. It is more likely the case that the potential on axes is influenced instead by the charge distribution off axis - a feature Wang did not account for by erroneously assuming that  $\frac{\partial^2 \phi}{\partial r^2} = 0$  on axis. Dropmann commented that “electrons are bound by the field lines leading to a modified charge distribution” and the insight closest to the truth, in my opinion, was made by Zimmermann who commented on the electron distribution of his simulations: “The dipole lobes are magnetically inaccessible by solar wind electrons, which is consistent with reduced cross-field mobility”.

So far, all of this is conjecture and no theoretical analysis has been performed to determine where exactly these regions inaccessible to electrons are or to make predictions on how these depend on the plasma and magnet parameters.

### 4.2.2 What can be done

The first clear task is thus to perform basic theory of the electron kinetics, to ascertain what the important parameters are and to then come up with a model for their spatial distribution. To this end, I shall begin by examining what is meant when a particle is said to be ‘magnetized’. Once this is defined, it will enable a thorough analysis of where the electron behaviour is most affected by the field and thus, point to which regions are important in understanding these features. The information gained here will help to formulate a simple model for electron densities which can then be used to determine the implications for the sheath structure. The remainder of this chapter will be dedicated to that first task of electron kinetics.

---

### 4.3 Magnetization condition for particles in a dipole field

To begin with, I shall lay out a working definition for what is meant by a ‘magnetized particle’ as: A particle which has its motion dominated by the magnetic field. A first necessary criterion is immediately presented: given that the magnetic field operates on the typical length and time scales of  $\lambda_G$  and  $\tau_G$ , for it to be the dominant influence there must not be any interruptions occurring on shorter or faster scales. Such interference is most likely caused by collisions of the particles with each other or the walls which confine them. For collisions with other particles, one necessary requirement for magnetization is thus

$$\lambda \gg r_L \text{ and } \tau_c \gg \tau_L , \quad (4.1)$$

although, given that  $\lambda = v\tau$ , if one of these conditions is satisfied it must be the case the the other is automatically. For this work, the plasma is assumed to be collisionless and thus this condition will not be a concern. However, it is still possible that the wall presents a significant obstacle to magnetization. For it not to be, the distance from the particle to the wall,  $d$ , must be greater than the component of the gyroradius perpendicular to the wall, thus ensuring that the particle has enough space to complete an orbit. Defining  $\epsilon$  as the ratio of these two lengths, this condition is stated as

$$\epsilon \equiv \frac{r_L^\perp}{d} < 1 , \quad (4.2)$$

where

$$r_L^\perp = \frac{B_r}{B} r_L = \frac{cB_r}{B^2} \quad (4.3)$$

and

$$c = \frac{mv_\perp}{e} . \quad (4.4)$$

For a particle with coordinates  $(r, z)$  above a planar wall at  $z = 0$  (illustrated in Fig. 4.4), the wall to particle distance is given simply as  $d = z$  and with a magnetic dipole located below the wall at  $(0, -z_0)$  equation (4.2) becomes

$$\epsilon = \frac{1}{z} \frac{3cr(z + z_0) (r^2 + (z + z_0)^2)^{\frac{3}{2}}}{\mathcal{M}(4(z + z_0)^2 + r^2)} < 1 , \quad (4.5)$$

after the appropriate values of the field strength have been substituted in. Given the complicated form of  $\epsilon$ , the importance of wall collisions is best studied on a case by case basis. A plot of  $\epsilon$ , taking as an example the parameters of Wang, is plotted in Fig. 4.4 and shows that collisions with the wall start to become important at radii greater than 10cm. Given that the radial extent of the lower electrode in these experiments is not greater than this, it can be assumed that collisions with the wall are not an issue here.

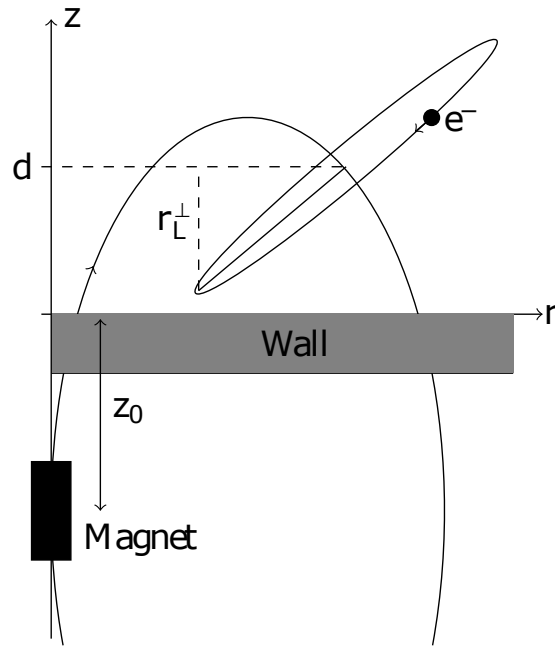


Figure 4.3: Diagram of quantities relevant to deriving the condition of particle-wall collisions. In this case the particle is comfortably able to perform an orbit without striking the wall.

Although collisions do not feature, one cannot yet conclude that particles are everywhere magnetized. In my previous definition I claimed that a magnetized particle must be ‘dominated’ by the field, the absence of collisions only keeps this possibility open. To now update my previous definition to be more specific I will class a magnetized particle as:

*A particle which has its motion accurately described by guiding centre drifts.*

Since the problem has azimuthal symmetry (and azimuthal currents will not be great enough to induce changes in the magnetic field), this is a 2D problem in  $r$  and  $z$ , implying that azimuthal motions can be ignored. Therefore, a magnetized particle is one which appears to follow a particular field line when viewed in the  $r$ - $z$  plane, for example one of those plotted in Fig. 2.2. It is then the field geometry which is to determine whether or not a particle is bound to a particular line - a particle will explore regions of space at a gyroradius from its associated line and if the magnetic field is not uniform the particle will experience a variety of field strengths in turn leading to deviations from the line it was initially following.

It is necessary to derive some lengthscale associated with the variation of the magnetic field to compare with the gyroradius of an orbiting particle. If the latter exceeds the former, then it’s inferred that the particle is exposed to such a variety of magnetic fields that it cannot be justifiably associated to just one field line. This notion of a ‘lengthscale’ has been used loosely before, but now warrants further introduction; in 1D,  $L(x)$ , signifies the typical distance over which the function undergoes appreciable change in the vicinity of  $x$ . For example, the notion that for  $\exp(\frac{x}{a})$ ,  $L = a$  may be

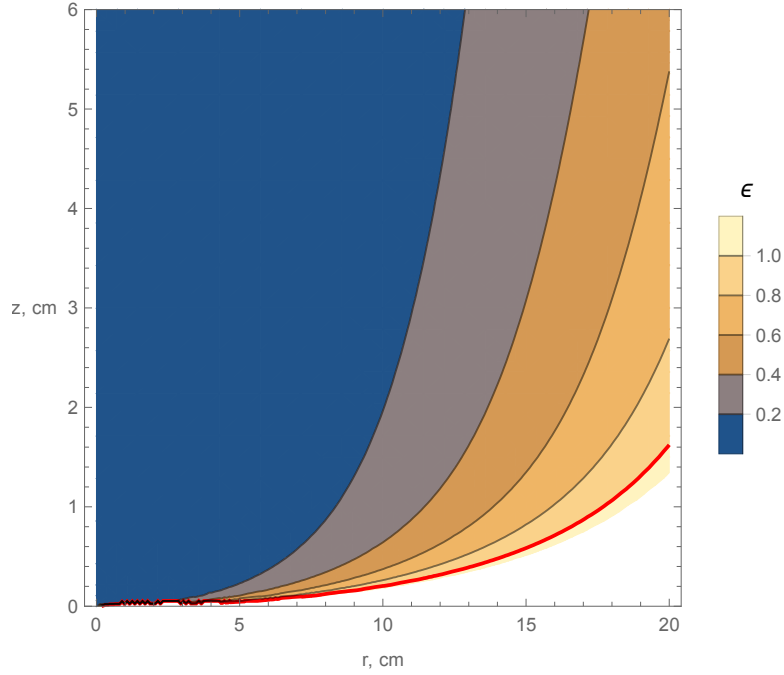


Figure 4.4: Plot of  $\epsilon$ , for the parameters of Wang. The contour  $\epsilon = 1$  is highlighted in red, below this line particles are not magnetized.

familiar. To translate this into something mathematically more rigorous, consider a function  $f(x)$  where, to first order, a deviation  $\delta x$  from  $x$  will result in a perturbation of the function

$$\Delta f(x, \delta x) = \delta x \frac{df}{dx} . \quad (4.6)$$

The function undergoes ‘appreciable change’ after a displacement  $\delta x = L_1$  (where the subscript, 1, signifies that this is a first order calculation to differentiate from the upcoming second order version) when the perturbation to  $f$  is comparable to its original value

$$|\Delta f(x, L_1)| = |f| , \quad (4.7)$$

implying that

$$L_1 = \frac{|f|}{\left| \frac{df}{dx} \right|} . \quad (4.8)$$

The same idea is now extended to second order. The motivation behind this is that the measure  $L_1 \rightarrow \infty$  as the gradient tends to zero and this can be avoided by considering higher order terms which contribute to making  $\Delta f$  nonzero. This is important here as the magnetic dipole field, soon to be analysed under this framework, has the property that  $\frac{\partial B}{\partial r} = 0$  when  $r = 0$ . To make this upgrade, some simplicity must be sacrificed in order to gain some accuracy. At second order, the magnitude of  $\Delta f$  depends on if



the deviation from  $x$  is positive or negative. Considering deviations  $\pm\delta x$ , the respective perturbations are

$$\Delta f_{\pm}(x, \delta x) = \pm\delta x \frac{df}{dx} + \frac{1}{2}(\delta x)^2 \frac{d^2f}{dx^2} \quad (4.9)$$

thus, the root mean square deviation is

$$\sqrt{\langle(\Delta f(x, \delta x))^2\rangle} = \sqrt{\frac{1}{2}(\Delta f_+^2 + \Delta f_-^2)} = (\delta x) \left( \left(\frac{df}{dx}\right)^2 + \frac{1}{4} \left(\frac{d^2f}{dx^2}\right)^2 (\delta x)^2 \right)^{\frac{1}{2}} \quad (4.10)$$

If the function undergoes appreciable change after a displacement of size  $L_2$  (the subscript, 2, here meaning ‘second order lengthscale’), then  $L_2$  is the solution of

$$\sqrt{\langle(\Delta f(x, L_2))^2\rangle} = |f(x)|, \quad (4.11)$$

which has one real unique solution

$$L_2 = \sqrt{\frac{-2 \left(\frac{df}{dx}\right)^2 + 2\sqrt{\left(\frac{df}{dx}\right)^4 + f^2 \left(\frac{d^2f}{dx^2}\right)^2}}{\left(\frac{d^2f}{dx^2}\right)^2}}. \quad (4.12)$$

In Fig. 4.5, the two measures  $L_1$  and  $L_2$  are compared for four arbitrarily chosen functions, the advantages of the latter are clear in regions where the gradient is small, since  $L_1 \rightarrow \infty$ .

Now to apply this analysis to the magnetic dipole field, and though a lengthscale of  $B$  will not be explicitly calculated, the underlying principle is the same. Consider a particle orbiting a field line (Fig. 4.6) so that at some moment in time the particle is displaced  $\delta\mathbf{x}$  from a point on the line,  $\mathbf{x}$ , with  $|\delta\mathbf{x}| = r_L$  and  $\delta\mathbf{x} \cdot \mathbf{B}(\mathbf{x}) = 0$ . The first and second order changes in the magnetic field between a point at  $\mathbf{x}$  and  $\mathbf{x} + \delta\mathbf{x}$  are respectively

$$\delta B_1 = \delta\mathbf{x}^T \nabla B(\mathbf{x}), \quad (4.13)$$

$$\delta B_2 = \frac{1}{2} \delta\mathbf{x}^T \hat{H}^B(\mathbf{x}) \delta\mathbf{x}, \quad (4.14)$$

where  $\hat{H}^B(\mathbf{x})$  denotes the Hessian matrix of  $B$  evaluated at  $\mathbf{x}$ , with elements given by

$$\hat{H}_{i,j}^B = \frac{\partial^2 B}{\partial x_i \partial x_j}, \quad (4.15)$$

where  $x_1 = r, x_2 = z, x_3 = \phi$ . Due to azimuthal symmetry, this matrix only has non zero elements in the top left  $2 \times 2$  submatrix since any deviations in the  $\hat{\phi}$  direction do not contribute to  $\delta B_{1,2}$ . For the field of a magnetic dipole, the relevant quantities

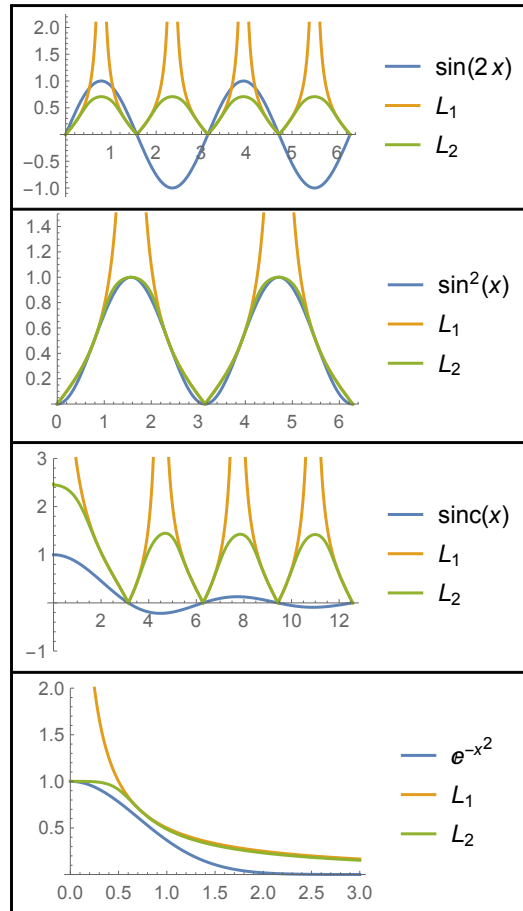


Figure 4.5: First ( $L_1$ ) and second ( $L_2$ ) order lengthscales for different functions,  $f(x)$ .

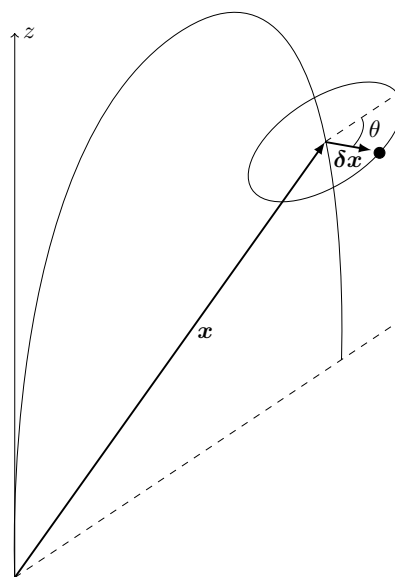


Figure 4.6: Particle performing an orbit around a field line.

become

$$\nabla B(\mathbf{x}) = -\frac{\mathcal{M}}{(r^2 + z^2)^3 \sqrt{r^2 + 4z^2}} \begin{pmatrix} 3r(r^2 + 5z^2) \\ 12z^3 \end{pmatrix} \quad (4.16)$$

for equation (4.13) and

$$\hat{H}^B(\mathbf{x}) = \frac{12\mathcal{M}}{(r^2 + z^2)^4 (r^2 + 4z^2)^{\frac{3}{2}}} \begin{pmatrix} r^6 + 10r^4z^2 + 22r^2z^4 - 5z^6 & rz^3(7r^2 + 25z^2) \\ rz^3(7r^2 + 25z^2) & 3r^4z^2 + 5r^2z^4 - 16z^6 \end{pmatrix} \quad (4.17)$$

for (4.14). Now to derive an expression for  $\delta\mathbf{x}$ . As in the 1D case, where it was necessary to average over two possible deviations  $\pm\delta x$ , the direction of  $\delta\mathbf{x}$  is not unique since the particle could be at any stage of its orbit, indicated by  $\theta$  in Fig. 4.6. This family of vectors exists in the plane which contains  $\mathbf{x}$  and is perpendicular to  $\mathbf{B}(\mathbf{x})$  and two vectors need to be found to span this space. An obvious first candidate is,  $\hat{\phi}$ , which must be a member of this plane given that  $\mathbf{B}$  has no azimuthal component. A simple choice for the second is the vector described by  $\theta = 0$ . Using  $\delta\mathbf{x} \cdot \mathbf{B} = \delta x_r B_r + \delta x_z B_z = 0$ , this unit vector is given by  $\frac{B_z}{B} \hat{r} - \frac{B_r}{B} \hat{z}$ . Combining this orthonormal basis, the set of vectors which describe the displacement of a particle from its associated field line are

$$\delta\mathbf{x} = r_L \left( \frac{B_z \cos \theta}{B} \hat{r} - \frac{B_r \cos \theta}{B} \hat{z} + \sin \theta \hat{\phi} \right), \quad (4.18)$$

Equations (4.13) and (4.14) for a particle at stage,  $\theta$ , in its orbit become after substitution of (4.16), (4.17) and (4.18)

$$\delta B_1 = \mathcal{M} \cos \theta r_L \frac{3r(r^2 + 2z^2)}{(r^2 + z^2)^{\frac{5}{2}} (r^2 + 4z^2)} \quad (4.19)$$

$$\text{and } \delta B_2 = \mathcal{M} \cos^2 \theta r_L^2 \frac{6(r^6 + 4r^4z^2 - 8r^2z^4 - 20z^6)}{(r^2 + z^2)^3 (r^2 + 4z^2)^{\frac{5}{2}}}. \quad (4.20)$$

giving the mean square value of  $\delta B = \delta B_1 + \delta B_2$ , averaged over one orbit, as

$$\begin{aligned} \langle (\delta B)^2 \rangle &= \frac{1}{2\pi} \int_0^{2\pi} (\delta B_1 + \delta B_2)^2 d\theta \\ &= \frac{1}{2} \left( \mathcal{M} r_L \frac{3r(r^2 + 2z^2)}{(r^2 + z^2)^{\frac{5}{2}} (r^2 + 4z^2)} \right)^2 \\ &\quad + \frac{3}{8} \left( \mathcal{M} r_L^2 \frac{6(r^6 + 4r^4z^2 - 8r^2z^4 - 20z^6)}{(r^2 + z^2)^3 (r^2 + 4z^2)^{\frac{5}{2}}} \right)^2. \end{aligned} \quad (4.21)$$

This is a similar position to before (equation (4.10)), where when deriving a 2D length-scale the procedure was to solve for  $r_L$  such that  $\langle (\delta B)^2 \rangle = B$  to give  $r_L$  as the lengthscale. Instead, the degree of magnetization will be indicated by the parameter  $\gamma = \frac{\sqrt{\langle (\delta B)^2 \rangle}}{B}$ , where a particle will be considered magnetized so long as  $\gamma \ll 1$ .

Particle	Energy (MeV)	Lorentz Factor	$\beta = \frac{v}{c}$	$\gamma$
Inner belt, 1 - 3 $R_E$				
Electron	0.1 - 1	1.2 - 2.96	0.55 - 0.94	$10^{-5}$ - $10^{-4}$
Proton	10 - 100	1.01 - 1.11	0.15 - 0.43	0.007 - 0.2
Outer belt, 3 - 10 $R_E$				
Electron	0.1 - 10	1.2 - 21	0.55 - 1	$10^{-4}$ - 0.05

Table 4.2: Van Allen radiation belt parameters evaluated at  $z = 0$  and  $r$  at the typical altitude

Using the equation (4.21),  $\gamma$  is expressed as

$$\gamma = \frac{c}{\mathcal{M}} \sqrt{\frac{9(r^2 + z^2)^5 \left( r^2(r^2 + 4z^2)^4 + 3\left(\frac{c}{\mathcal{M}}\right)^2 (r^2 + z^2) (r^6 + 4r^4z^2 - 8r^2z^4 - 20z^6)^2 \right)}{2(r^2 + 4z^2)^8}} \quad (4.22)$$

and the lengthscale,  $\Lambda$ , to which  $r$  and  $z$  are normalized is identified as  $\sqrt{\frac{\mathcal{M}}{c}}$ ,

$$\Lambda = \sqrt{\frac{M\mu_0 e}{4\pi m v_{\perp}}}, \quad (4.23)$$

giving a first glimpse at the characteristic size of the region of magnetization of a dipole. One point to make is that  $v_{\perp}$  is not a constant as it depends on the relative directions of the magnetic field and particle velocity. For a particle with speed  $v$ ,  $0 < v_{\perp} < v$  and so  $\sqrt{\frac{M\mu_0 e}{4\pi m v}} < \Lambda < \infty$ . However, by taking  $v_{\perp} \approx v$ , one obtains an idea of the typical lengthscales involved. In Fig. 4.7,  $\gamma$  is plotted to indicate which regions around the dipole are magnetized. It is to be understood that the contour  $\gamma = 1$  outlines the transition between the magnetized and unmagnetized regions and the contour  $\gamma = 0.1$  indicates the beginning of the strictly magnetized region. Only one quadrant has been plotted here, but one can see that the magnetized region describes an approximate figure of eight shape centred around the magnet with height and width of order  $\Lambda$ .

One example comes to mind to scrutinise the parameter,  $\gamma$ . A magnetic dipole of strength  $\frac{\mu_0 M}{4\pi} = 8 \times 10^{15}$  approximately describes the Earth's magnetic field and electrons and ions from the solar wind may become trapped by this field, performing stable orbits around magnetic field lines. These trapped populations are responsible for the Van Allen radiation belts and given that their motions are magnetized by my definition, it should be expected that these radiation belts occur in regions of low  $\gamma$ . Table 4.2 gives values of  $\gamma$  where the particle energies have been used to find the velocity and relativistic corrections to mass. Since  $\gamma$  is a function of  $r$  and  $z$ , I have decided to evaluate it at just one location: where particles pass through the equator,  $z = 0$ . Electrons in the outer and inner belts have  $\gamma$  values ranging from  $10^{-5}$  -  $10^{-2}$  thus confirming that these particles are strongly magnetized. Protons in the inner belt have  $\gamma$  values ranging from  $10^{-3}$ - $10^{-1}$  and so may also be considered magnetized, though to a lesser degree. In conclusion, some confidence is to be drawn from the fact that the metric  $\gamma$  successfully

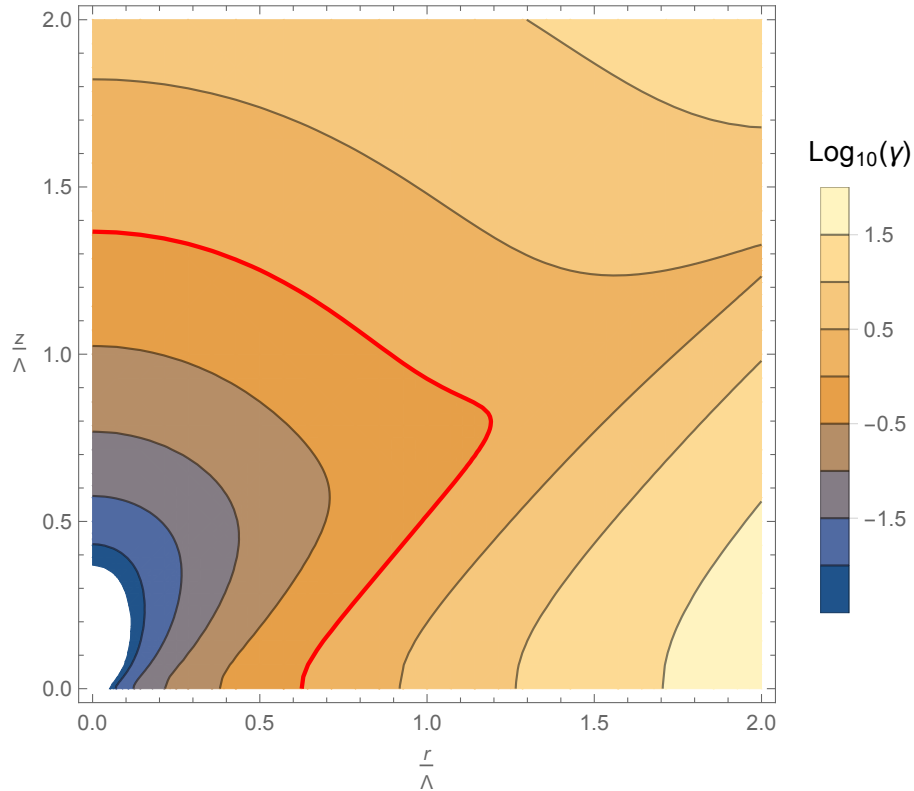


Figure 4.7: Plot of  $\gamma$  on a log scale. The contour  $\gamma = 1$  (and so  $\log_{10}(\gamma) = 0$ ) is highlighted in red.

recognises that the electrons and protons in the van Allen radiation belts are magnetized.

Now that it is clear where electrons may be considered to be magnetized, the next question concerns what the effect of this is on their distribution.

## 4.4 Electron distribution

It has been shown that electrons may be considered to be magnetized within a typical distance of  $\Lambda$  from the magnet. In the case at hand, electrons are assumed collisionless implying that electrons cannot be transported into this region via collisions. Ionization is also not significant meaning that electrons cannot access this region by being produced locally. Under these assumptions, the electrons must approach this magnetized region from the outside at an infinite distance away. The task, then, is to determine what happens to electrons approaching the magnet in this way with the expectation that the interesting behaviours will occur near this  $\Lambda$  sized region.

Without solving the equations of motion entirely, useful information can be extracted from the Lagrangian formalism. This has been used previously to determine how many secondary electrons are trapped near to the electrode of a magnetron discharge [106]. The Lagrangian for a particle (of mass,  $m$  and charge,  $q$ ) moving in an electromagnetic

field in cylindrical coordinates is

$$\mathcal{L} = \frac{1}{2}m(\dot{r}^2 + r^2\dot{\theta}^2 + \dot{z}^2) - q(\phi - \dot{r}A_r - r\dot{\theta}A_\theta - \dot{z}A_z), \quad (4.24)$$

where  $A_i$  are the components of the magnetic vector potential. Azimuthal symmetry implies  $\mathcal{L} = \mathcal{L}(r, z)$  and thus there is the conserved quantity

$$p_\theta = \frac{\partial \mathcal{L}}{\partial \dot{\theta}} = mr^2\dot{\theta} + qrA_\theta. \quad (4.25)$$

For a magnetic dipole moment  $\mathbf{M} = M\hat{z}$ , the azimuthal component of the vector potential is given by

$$A_\theta = \frac{\mu_0 M}{4\pi} \frac{r}{(r^2 + z^2)^{\frac{3}{2}}} \quad (4.26)$$

and so the conserved momentum is given as

$$p_\theta = mrv_\theta + \frac{q\mu_0 M}{4\pi} \frac{r^2}{(r^2 + z^2)^{\frac{3}{2}}}. \quad (4.27)$$

Rearranging this for  $v_\theta$ , gives an expression for the azimuthal velocity as a function of position

$$v_\theta = \frac{p_\theta}{mr} - \frac{q\mu_0 M}{4\pi m} \frac{r}{(r^2 + z^2)^{\frac{3}{2}}}. \quad (4.28)$$

Energy conservation requires that

$$\frac{1}{2}m(v_z^2 + v_r^2 + v_\theta^2) + q\phi(r, z) = \text{const.} \quad (4.29)$$

and given equation (4.28), the azimuthal velocity can be absorbed into the potential term to create an effective potential. Substituting (4.28) into (4.29) and introducing a change of notation,  $v \equiv \sqrt{v_r^2 + v_z^2}$ , to indicate the speed in the  $r$ - $z$  plane results in

$$\frac{1}{2}mv^2 + \psi(r, z, p_\theta) = \text{const.} \quad (4.30)$$

where

$$\psi(r, z, p_\theta) \equiv q\phi + \frac{1}{2m} \left( \frac{p_\theta}{r} - \frac{q\mu_0 M}{4\pi} \frac{r}{(r^2 + z^2)^{\frac{3}{2}}} \right)^2. \quad (4.31)$$

The effective potential,  $\psi$ , depends on the initial conditions of the particle which are contained in the parameter  $p_\theta$ .

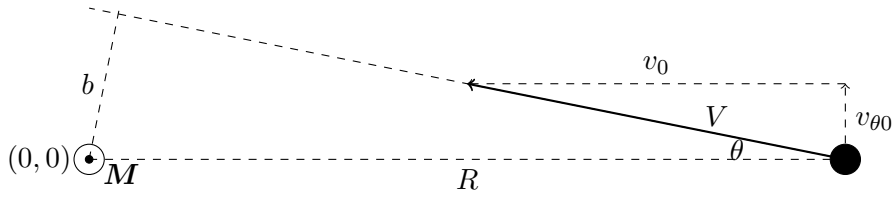


Figure 4.8: Initial condition for an incoming particle with speed  $V$  and impact parameter  $b$ , where  $R \rightarrow \infty$ .

#### 4.4.1 1D

It is instructive to first consider a simpler problem, that is, particles moving in the  $z = 0$  plane in the absence of electric fields ( $\phi = 0$ ). These particles will remain in this plane so that the only coordinate of interest is  $r$ .

#### Trajectories

Particles of speed,  $V$ , and impact parameter,  $b$ , are fired in towards the dipole from an infinite radius (see Fig. 4.8). For  $z = 0$ , equations (4.30) and (4.27) become

$$v^2 = V^2 - \frac{1}{m^2} \left( \frac{p_0}{r} - \frac{q\mu_0 M}{4\pi r^2} \right)^2 \quad (4.32)$$

and

$$p_0 = mrv_\theta + \frac{q\mu_0 M}{4\pi} \frac{1}{r}. \quad (4.33)$$

Geometric properties help to find  $p_0$  in terms of  $b$  and  $V$ , from inspection of Fig. 4.8:

$$\sin \theta = \frac{b}{R}, \quad (4.34)$$

$$\sin \theta = \frac{v_{\theta 0}}{V}, \quad (4.35)$$

$$\cos \theta = \frac{v_0}{V}, \quad (4.36)$$

where I have also defined  $v_0$  and  $v_{\theta 0}$  as the initial radial and azimuthal velocities respectively. Elimination of  $\theta$  implies that

$$v_{\theta 0} = \frac{b}{R} V \quad (4.37)$$

$$\text{and } v_0 = V \sqrt{1 - \left( \frac{b}{R} \right)^2} \quad (4.38)$$

so that

$$p_0 = \lim_{R \rightarrow \infty} \left( mbV + \frac{q\mu_0 M}{4\pi} \frac{1}{R} \right) = mbV. \quad (4.39)$$

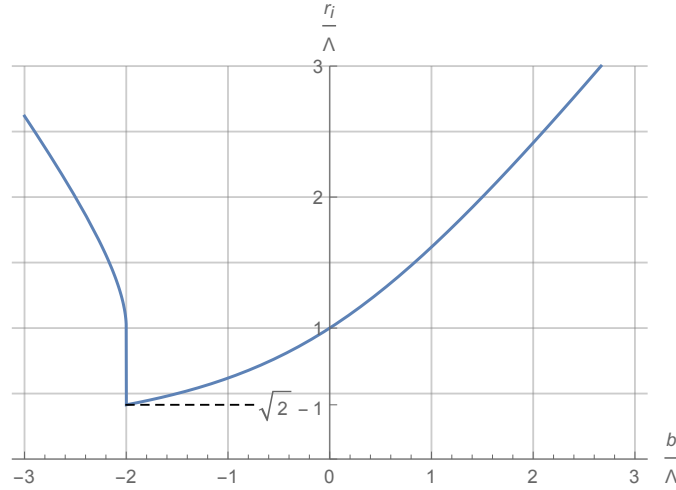


Figure 4.9: Radius of closest approach as a function of impact parameter

Substituting this into (4.32) gives

$$v^2 = V^2 - \frac{1}{m^2} \left( \frac{mbV}{r} - \frac{q\mu_0 M}{4\pi} \frac{1}{r^2} \right)^2. \quad (4.40)$$

This equation dictates the radii accessible to a particle. The innermost radius a particle can reach,  $r_{\min}(b, V)$ , is the solution of (4.40) for  $r$  when  $v = 0$  and is given by the piecewise function:

$$r_{\min} = \begin{cases} \frac{-b + \sqrt{b^2 - (2\Lambda)^2}}{2}, & b < -2\Lambda \\ \frac{b + \sqrt{b^2 + (2\Lambda)^2}}{2}, & b > -2\Lambda \end{cases} \quad (4.41)$$

As anticipated the characteristic lengthscale from equation (4.23),  $\Lambda$ , has reappeared but this time with the slight tweak that  $\Lambda = \sqrt{\frac{M\mu_0 e}{4\pi m V}}$ , that is,  $v_{\perp} \rightarrow V$ . Equation (4.41) is plotted in Fig. 4.9. There is a discontinuity at  $b = -2\Lambda$  where if the impact parameter is slightly less the electron reaches its innermost point at  $r = \Lambda$  and if  $b$  is larger the electron reaches  $r_0 = (\sqrt{2} - 1)\Lambda$ . This is illustrated by the two highlighted trajectories in Fig. 4.10. No electron can access the region  $r < r_0$  and it appears that the inner most trajectory almost begins a guiding centre drift before being sent back.

It will be useful to re-express equation (4.41) as the range of impact parameters which can be present at a radius  $r$ . This can be verified by inspection of Fig. 4.9 as being

$$b_{\min} = \begin{cases} 2\Lambda, & r_0 < r < \Lambda \\ -\frac{\Lambda^2}{r} - r, & r > \Lambda \end{cases} \quad (4.42)$$

and

$$b_{\max} = -\frac{\Lambda^2}{r} + r, \quad r > r_0. \quad (4.43)$$



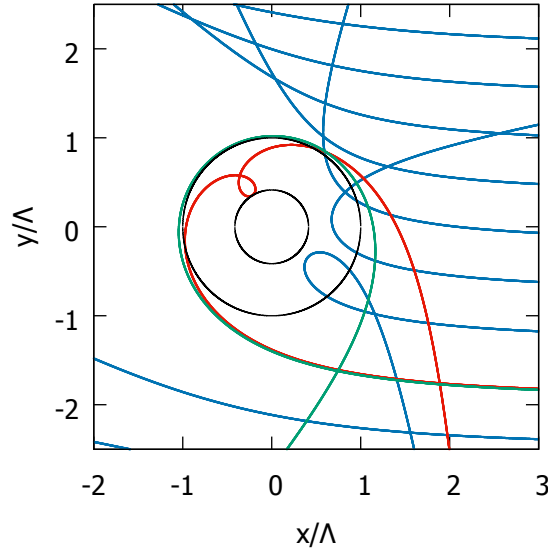


Figure 4.10: Particle trajectories for different impact parameters incident on a magnetic dipole at the origin. Highlighted are two trajectories in green and red, just either side of  $b = -2\Lambda$ . The red is just below and reaches  $r = r_0$ , the green is just above and turns back at  $r = \Lambda$ .

### Density

The previous section uncovered how fast particles move and where they may go and for this 1D example it is not much work to turn this into a statement on the particle density. Here I shall perform the calculation to derive the analytic particle density but I also explore if there are any suitable approximations to be made, with a view to finding the density in the 2D system of interest where things are not so simple.

**Exact** From the equation of continuity, the infinitesimal contribution to the density at a point  $r$  coming from particles with impact parameter  $b \rightarrow b + db$  is

$$dn(b, r) = \frac{dn(b, \infty)v_0 R}{vr}. \quad (4.44)$$

where the initial density of ‘ $b$  electrons’ is  $dn(b, \infty) = n_0 f_b(b) db$ , with  $f_b(b)$  the PDF for  $b$ . To derive  $f_b$ , referring again to Fig. 4.8, if the electrons are assumed isotropic at  $R$ , then the PDF of  $\theta$  for incoming particles ( $-\frac{\pi}{2} < \theta < \frac{\pi}{2}$ ) is uniform, given by  $f_\theta(\theta) = \frac{1}{\pi}$ . The probability distribution for  $b$  is then deduced from this as  $f_b(b) = f_\theta(\theta) \frac{d\theta}{db}$ , giving from equation (4.34):

$$f_b(b) = \frac{1}{\pi \sqrt{R^2 - b^2}} \quad (4.45)$$

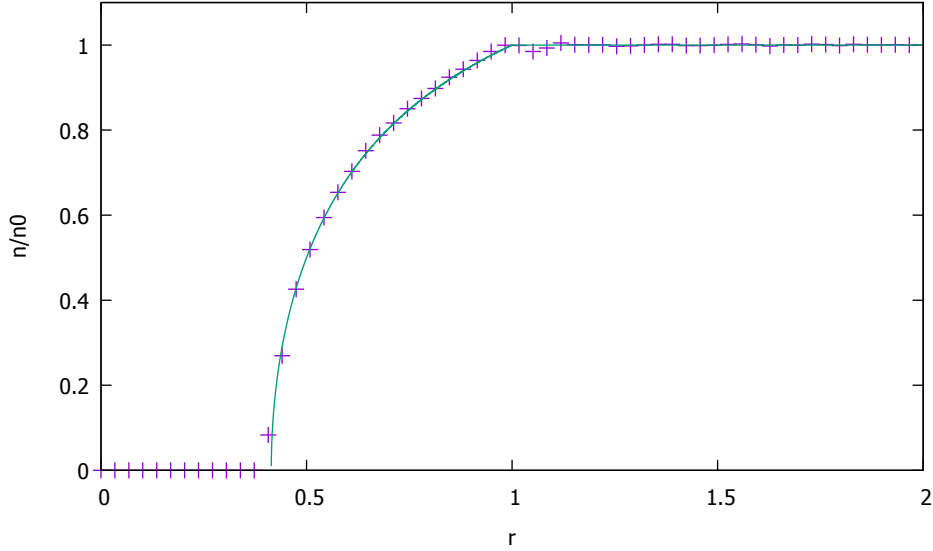


Figure 4.11: Analytic and computational comparison of electron density

At some radius,  $r$ , the density is given by the integral of (4.44) over all contributing impact parameters

$$n = n_0 \int_{b_{\min}}^{b_{\max}} \frac{f_b v_0 R}{vr} db . \quad (4.46)$$

with  $b_{\min}$  and  $b_{\max}$  given by equations (4.42) and (4.43). Substitution of (4.45) and assuming that particles are incident from afar,  $r \ll R$ , results in

$$n = n_0 \int_{b_{\min}}^{b_{\max}} \frac{1}{\pi r \sqrt{1 - \left(\frac{b}{r} - \frac{\mathcal{M}q}{mVr^2}\right)^2}} db . \quad (4.47)$$

and integration of this yields the density as

$$n(r) = \begin{cases} 0, & r < r_0 \\ \frac{n_0}{\pi} \arccos\left(\frac{\Lambda}{r} \left(\frac{\Lambda}{r} - 2\right)\right), & r_0 < r < \Lambda \\ n_0, & r > \Lambda \end{cases} \quad (4.48)$$

This function is plotted in Fig. 4.11, as expected the density is zero for  $r < r_0$ , but perhaps unexpectedly, the density changes abruptly at  $r = \Lambda$  and then remains constant. To test this expression, a simple code was written to fire in particles covering a large range of impact parameters. The particle density was then inferred by tracking the particle trajectories and seeing how much time was spent at each radius.

So far, only monoenergetic electrons have been considered, leaving the final step to extend this study to a population which follows some velocity PDF  $f_v(v)$  at infinity. The density is obtained by integrating (4.48) over  $v$ , but with a change of notation

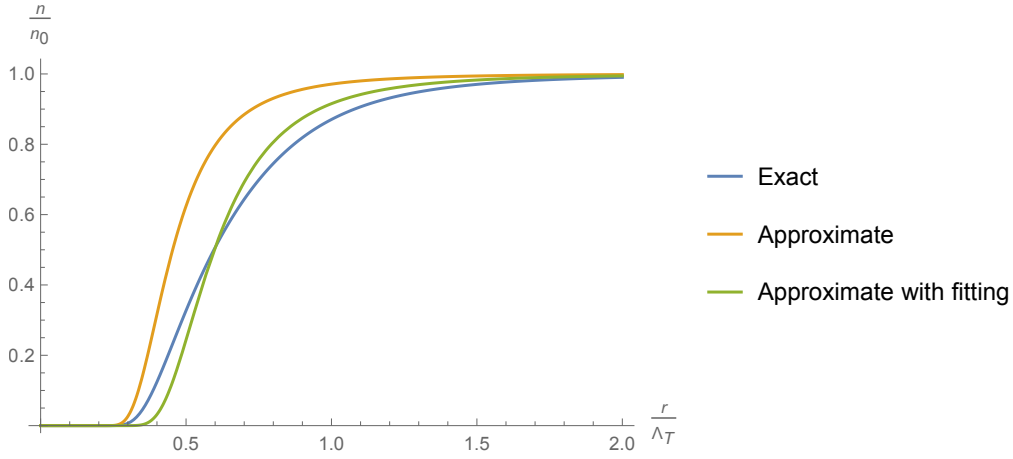


Figure 4.12: The exact electron density calculated for a Maxwellian velocity distribution, equation (4.50), in blue. Included are the particle densities trying to replicate this profile by introducing an effective electric potential. In yellow is the Boltzmann distribution for an electric potential given by equation (4.52) and in green is a Boltzmann distribution for the same potential scaled by a factor of three to better fit the exact solution.

$n_0 \rightarrow n_0 f_v(v) dv$ , where  $n_0$  still indicates the total particle density at infinity.

$$n(r) = \int_{v_{\min}}^{v_{\max}} \frac{n_0 f(v)}{\pi} \arccos\left(\frac{\mathcal{M}q - 2r\sqrt{\mathcal{M}qmv}}{mr^2v}\right) dv + \int_{\frac{\mathcal{M}q}{mr^2}}^{\infty} n_0 f(v) dv \quad (4.49)$$

where the limits are  $v_{\min} = \frac{(\sqrt{2}-1)^2 \mathcal{M}q}{mr^2}$  and  $v_{\max} = \frac{\mathcal{M}q}{mr^2}$ . In normalized units for a MVD:  $r \rightarrow \frac{r}{\Lambda_T}$ ,  $v \rightarrow \frac{v}{v_T}$ ,  $f(v) \rightarrow 2v \exp(-v^2)$  this becomes

$$n(r) = n_0 \int_{\frac{(\sqrt{2}-1)^2}{r^2}}^{\frac{1}{r^2}} \frac{2v \exp(-v^2)}{\pi} \arccos\left(\frac{1}{r\sqrt{v}} \left(\frac{1}{r\sqrt{v}} - 2\right)\right) dv + n_0 \int_{\frac{1}{r^2}}^{\infty} 2v \exp(-v^2) dv \quad (4.50)$$

The numerical result of this is plotted in Fig. 4.12, alongside are a few other curves whose meaning will become clear in the upcoming section.

**Approximate** Finding the 1D density proved to be a tractable problem, the final result being given by equation (4.50). The 2D case will not yield an analytic result, so it is worth checking to see if an approximate form can be found. A fairly crude approximation is to assume that the particle density for a given  $v$  is 0 in the region where the particles cannot access and  $n_0 f_v(v)$  where they can. Under this approximation, (4.48) is instead

$$dn(r, v) \approx \begin{cases} 0, & r < r_0(v) \\ n_0 f_v(v) dv, & r > r_0(v) \end{cases}$$

and integrating this over all velocities

$$n(r) = \int dn(r, v) = \int_0^\infty n_0 f_v(v) dv = n_0 \exp\left(\frac{(\sqrt{2}-1)^4 \mathcal{M}^2 q^2}{2mk_B T} \frac{1}{r^4}\right), \quad (4.51)$$

i.e. from this approximate picture, it is as if the density follows the Boltzmann relation for an electric potential

$$\phi = \frac{(\sqrt{2}-1)^4 \mathcal{M}^2 q}{2m} \frac{1}{r^4}. \quad (4.52)$$

This can be understood from a different perspective, if an electric potential were to represent the magnetic dipole as best it could, one key feature it would have to reproduce is to keep particles away from  $r_0$ . By conservation of energy, the effective potential must then have equipotential lines described by

$$\frac{1}{2}mV^2 = \phi(r_0). \quad (4.53)$$

Rearranging  $r_0 = (\sqrt{2}-1)\Lambda$  for  $V$  gives

$$V = \frac{(\sqrt{2}-1)^2 \mathcal{M} q}{mr_0^2}, \quad (4.54)$$

and then taking the square and multiplying by  $\frac{1}{2}m$  gives

$$\frac{1}{2}mV^2 = \frac{1}{2} \frac{(\sqrt{2}-1)^4 \mathcal{M}^2 q^2}{mr_0^4} \quad (4.55)$$

which is in a form such that  $\phi(r)$  can be found by comparison of (4.55) and (4.53) and this matches (4.52).

The exact (4.49) and approximate (4.51) densities are plotted in Fig 4.12 and one sees that the density is overestimated, but this is not unexpected. In Fig. 4.13, the density for a single particle velocity is plotted for the exact and approximate density profiles (as was performed in Fig. 4.11). Perhaps counter intuitively, the particle density remains constant for a  $r^{-4}$  potential up to the inaccessible region. Because the only goal when constructing the effective potential was for it to stop particles at  $r_0$ , the density  $r_0 < r < \Lambda$  has been overestimated as the exact solution drops to zero gradually and the approximate remains constant. To improve the situation, some intervention is required. By increasing the field strength, the error associated with overly high particle densities can be offset by an increased innermost radius. It turns out that by doing this adjustment by eye results in a best fit when the potential (4.52) is scaled up by a factor of 3 and the effect of this is illustrated in Fig. 4.13. The corresponding density for this adjusted effective potential is included in 4.12 and shows improved agreement.

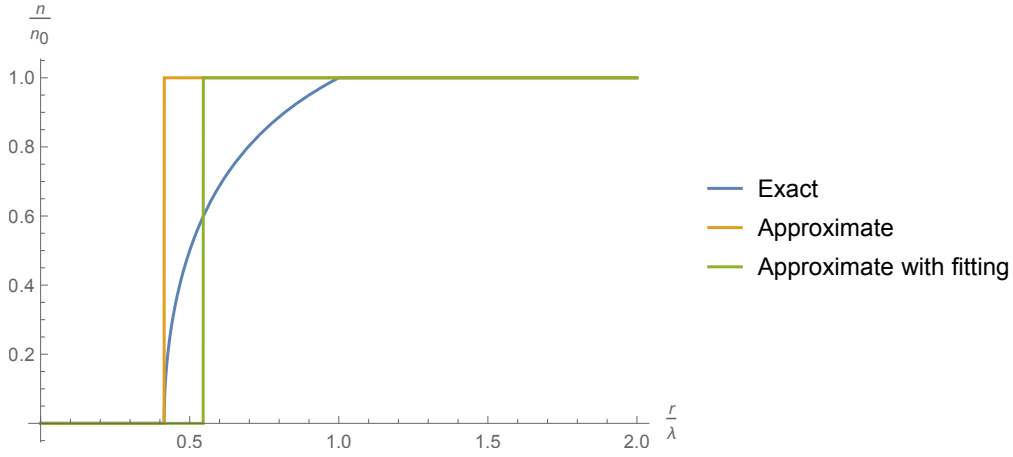


Figure 4.13: For a given electron velocity, particle densities are plotted for the magnetic dipole field (Exact), for an initial guess at the effective potential (Approximate) and an optimized version of this (Approximate with fitting).

#### 4.4.2 2D

It is now time to extend the 1D study to the one of interest, the 2D case, where particles are free to move in the  $z$  direction. In the same way as before, the first task is to determine what regions the magnetic field forbids particles from accessing.

#### Trajectories

In this case the locus of points describing the boundary of the forbidden region is given as:

$$\left( \frac{p_0}{mr} - \frac{q\mathcal{M}}{m} \frac{r}{(r^2 + z^2)^{\frac{3}{2}}} \right)^2 = V^2 \quad (4.56)$$

where  $p_0$  is the conserved quantity as defined in equation (4.27). Though it was more intuitive before to consider impact parameter instead of  $p_0$ , such a picture is not useful here and  $p_0$  will be used to characterise the incoming particles. Rearranging (4.56) for  $z$  gives the equations of the contours separating the allowed and forbidden regions (the 2D version of equation (4.41)), the nature of which depends on  $p_0$

$$\begin{cases} z > z_+, & p_0 \leq 0 \\ z_+ < z < z_-, & 0 < p_0 \leq 2\sqrt{q\mathcal{M}Vm} \\ z < z_-, & p_0 > 2\sqrt{q\mathcal{M}Vm} \end{cases}$$

where

$$z_{\pm}(r, p_0) = \sqrt{\left( \frac{q\mathcal{M}r^2}{p_0 \pm mrV} \right)^{\frac{2}{3}} - r^2}. \quad (4.57)$$

These zones are plotted in Fig. 4.14 for different values of  $p_0$ . Also highlighted in all plots is the region which is never accessible, given as  $z < z_0$ , where:

$$z_0 = z_+(r, 2\sqrt{qMVm}) \quad (4.58)$$

Since this forbidden region is just a consequence of conservation laws, it may be as readily accepted as any other result deriving from, say, energy or angular momentum conservation. However, there is a simple physical picture which illuminates why this region exists. Assuming to lowest order that inside of the magnetized region (defined as  $\gamma < 1$  in the previous chapter) the electrons are tied to magnetic field lines and that outside particles are completely unmagnetized results in the picture given in Fig. 4.15. Particles incident from above and the sides cross over the boundary and can follow their newly associated field lines to access the region near to the origin. In this picture, there are field lines which cannot be latched onto which occur to the inside of the line labeled as ‘L’. Before these inner lines can be met, line L (or a line outside of this) will intercept the particle first. This restricts the innermost electrons not to venture within a Larmor radius from L, indicated by the yellow zone of Fig. 4.15.

The two restricted regions as found from the Lagrangian approach and this physical argument are compared in Fig. 4.16 and show fairly good agreement. In fact there is one final reconciliation of these approaches. Fig. 4.14 shows that the innermost electrons have a value of  $p_0$  slightly less than 2 and the way they access this region is through a small gap at around  $r = 1$  (see  $p_0 = 1.99$ ). Electrons moving through this gap correspond to ones taking a trajectory which hugs the  $r$  axis such as the one denoted by ‘T’ in Fig. 4.15.

This is another first glimpse of a significant result: the zones in which electron motion is restricted and the resulting space charge is what I propose leads to the radial electric fields observed.

## Density

This insight, that particles effectively move freely until they meet their ‘magnetizing’ field line, inspires a novel way to calculate particle densities. It was initially the intention to use the effective electric potential approximation as demonstrated for the 1D case, however, it is not clear that this is valid when actual electric fields are also present. The important feature of this new approximation is that this method will be valid under these conditions. Recall from section 2.1 that the MVD near an absorbing boundary was modified by ‘chopping off’ the part of the distribution function corresponding to particles not returned by the wall. In this case, I propose that the magnetic field lines play an analogous role to the wall. At the point just inside of the yellow forbidden zone (Fig. 4.15) for a particle of speed  $v$ , the velocity PDF would have remained a MVD, as it was at infinity, were it not for the magnetic field. The effect of this field is to intercept any particles travelling slower than  $v$ , before they can reach this point but to leave everything travelling any faster alone. Thus, the velocity distribution should be a

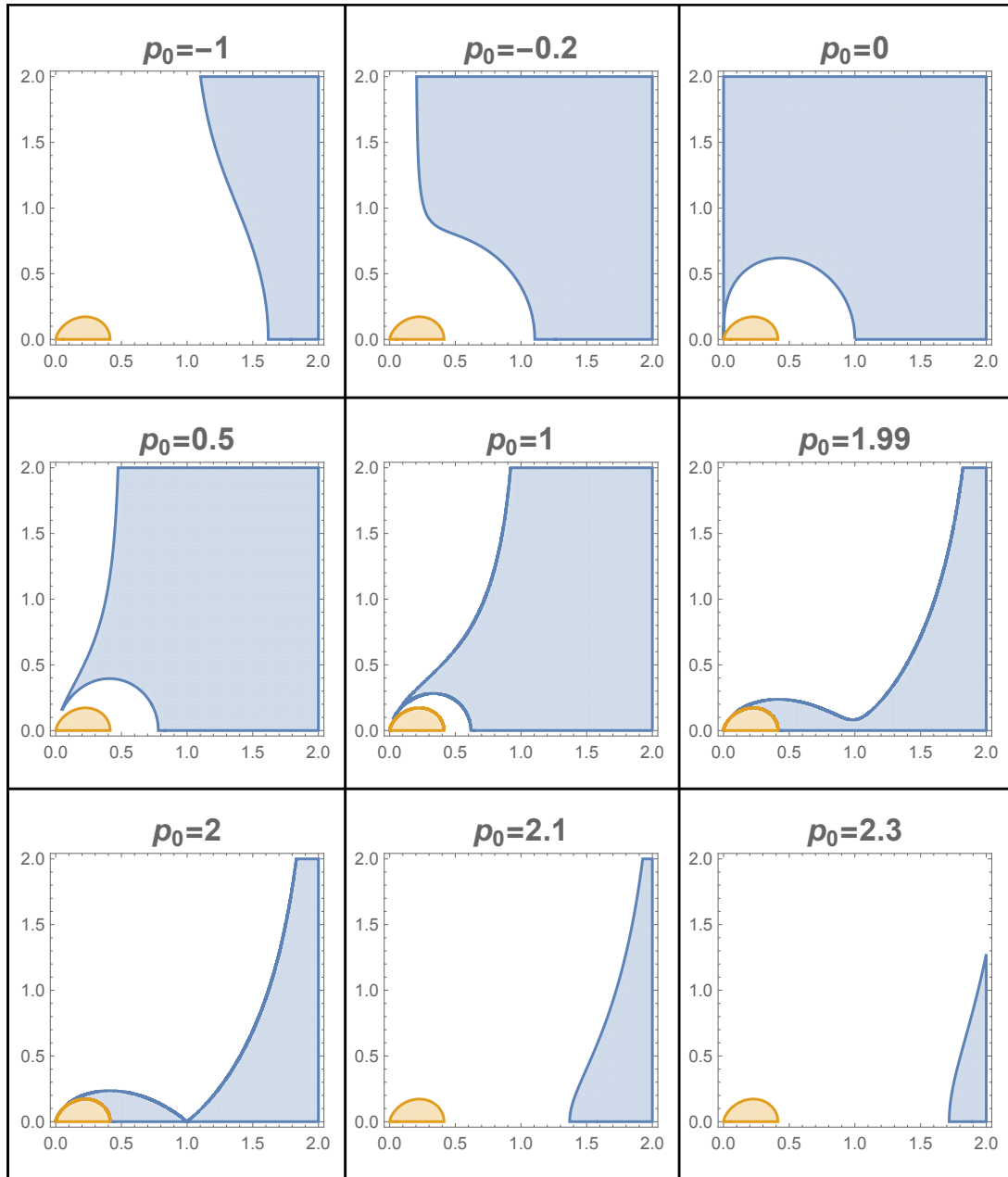


Figure 4.14: Regions (where the  $x$  axis label,  $\frac{r}{\Lambda}$ , and the  $y$  axis label,  $\frac{z}{\Lambda}$ , have been omitted in the figure to maximise area occupied by the plots) accessible to electrons shaded blue as a function of  $p_0$ . The region in yellow is not accessible for any value of  $p_0$ .

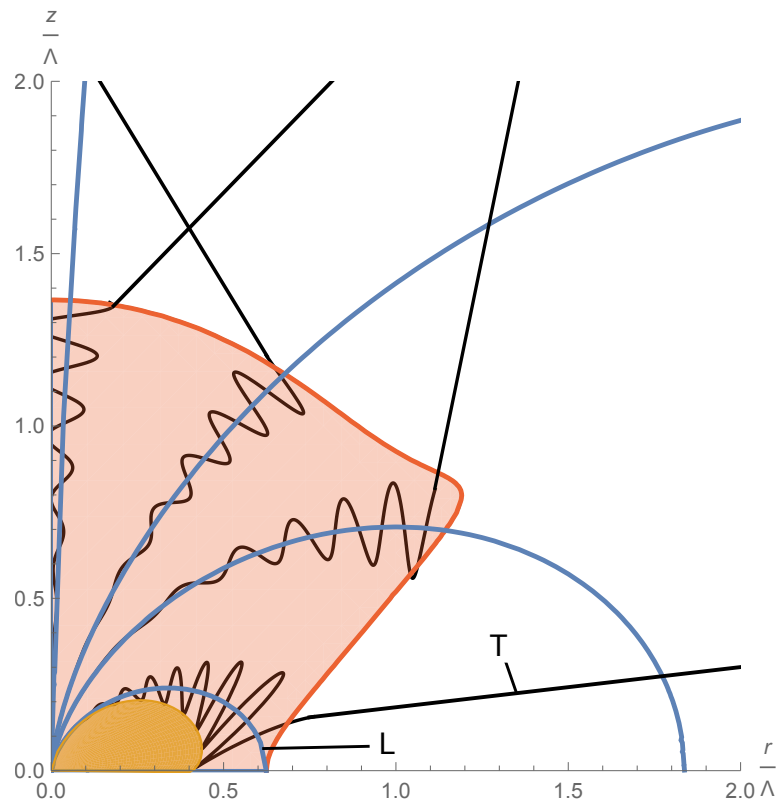


Figure 4.15: Particles enter the magnetized region (red), performing orbits the instant they make the transition. The yellow region, traced out by the particle trajectory T, may never be visited.

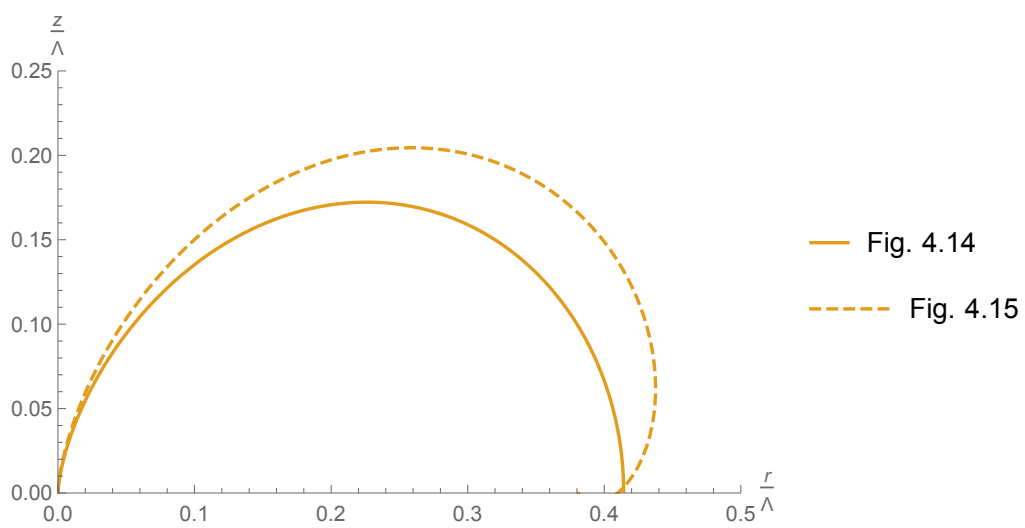


Figure 4.16: Comparison of two forbidden regions of Figs. 4.14 and 4.15



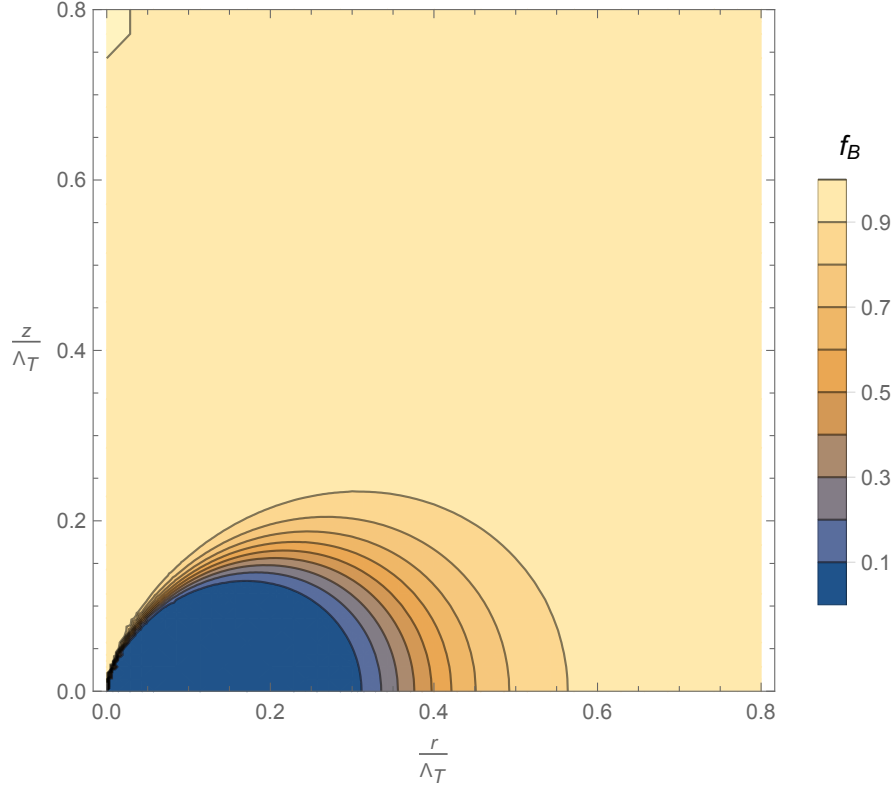


Figure 4.17: Density scaling factor introduced by magnetic screening. This plot would correspond to normalized particle density in the absence of electric fields.

MVD but with all particles slower than  $v$  missing.

The density then follows simply from the BR, but with the missing particles not accounted for:

$$\begin{aligned} n(\mathbf{x}) &= n_0 \exp\left(\frac{e\phi}{k_B T_e}\right) \int_{v(\mathbf{x})}^{\infty} f(v) dv \\ &\equiv n_0 \exp\left(\frac{e\phi}{k_B T_e}\right) f_B(\mathbf{x}) \end{aligned} \quad (4.59)$$

where

$$f_B(\mathbf{x}) = \left( \operatorname{erfc}(v(\mathbf{x})) + \frac{2v(\mathbf{x}) \exp(-v(\mathbf{x})^2)}{\sqrt{\pi}} \right), \quad (4.60)$$

and  $v(\mathbf{x})$  is velocity of a particle whose exclusion zone boundary passes through  $\mathbf{x}$ , found by inverting (4.57),

$$v(\mathbf{x}) = \frac{qM}{m} \frac{1}{r^2} \left( -1 + \sqrt{1 + \frac{r^3}{(r^2 + z^2)^{\frac{3}{2}}}} \right)^2. \quad (4.61)$$

Together, equations (4.59), (4.60) and (4.61) describe the electron density. The part corresponding to the magnetic correction, (4.60), is plotted in Fig. 4.17.

## 4.5 Comparison of electron model to observations

Now to see how well these findings correspond to the experimental observations outlined at the start of this chapter. This shall be done in a qualitative way, by checking if anything interesting occurs around the forbidden zones described by (4.57). With  $V$  taken as the thermal velocity, the regions are compared with the sheath profiles obtained by Wang, Dropmann and Saitou in Fig. 4.18.

In (a) the potential obtained by Wang is higher in the predicted electron exclusion regions, indicative of a more positive charge density. In (b) the vertical acceleration of dust grains found by Dropmann is compared to the forbidden zone. The reduced force suspending the grains at the lobes also suggests electron depletion and, again, the predicted depletion zone is, visually speaking, a good match. Given the idea that particles cannot penetrate deeper than particular field lines, it is no coincidence that the exclusion zones are mistakable for the magnetic field lines which the two authors have helpfully included in their plots. Furthermore, given the strong electric fields in the sheath, it is reassuring to have some confirmation that the mechanism by which field lines intercept particles is unaffected by electric fields.

In (c), Saitou provides a cross sectional view of how a cloud of dust grains distribute themselves in the sheath, showing a range of levitation heights and radii. The dust void formed in the centre is consistent with negatively charged grains being forced to move closer to the particularly positive region resulting from electron depletion. However, it is surprising that dust particles should levitate higher directly above this region, given that I would expect them to be pulled down towards the region as they were radially. Since the cone represents a region filled with dust, it may be the case that those outer particles sit higher as they are supported by the grains below them.

The simulations of Zimmerman require a special treatment given that the field geometry differs from a pure dipole. The derivation of the form of his field and analysis of what this implies for electron trajectories is left to Appendix B. The exclusion zone is plotted in Fig. 4.19 and shows that solar wind electrons appear to penetrate deeper than I would have predicted. One reason behind this is that the exclusion zone for electrons which approach from infinity extends to 2000m on the surface, but the  $x$  dimension of the simulation domain is 1250m implying that some electrons injected from the sides are artificially magnetized. A second curve in Fig. 4.19 marks how close an electron injected from the side can reach and confirms that these are able to go much deeper than if they had been released at an appropriately far distance.

## 4.6 Summary

The key results of this chapter are the improved understanding of electron behaviour and a way to determine their distribution with a simple model. The qualitative agreement seen with experiment builds confidence in this work - the electron density model ideally requires a more rigorous examination, but this will have to wait for the discussion of

---

---

further work. Now it is time to see what the consequences are for the sheath. The next section will outline how to implement the density given from (4.59)-(4.61) into a sheath model, with the majority devoted to explaining the computational tools which are necessary.

---

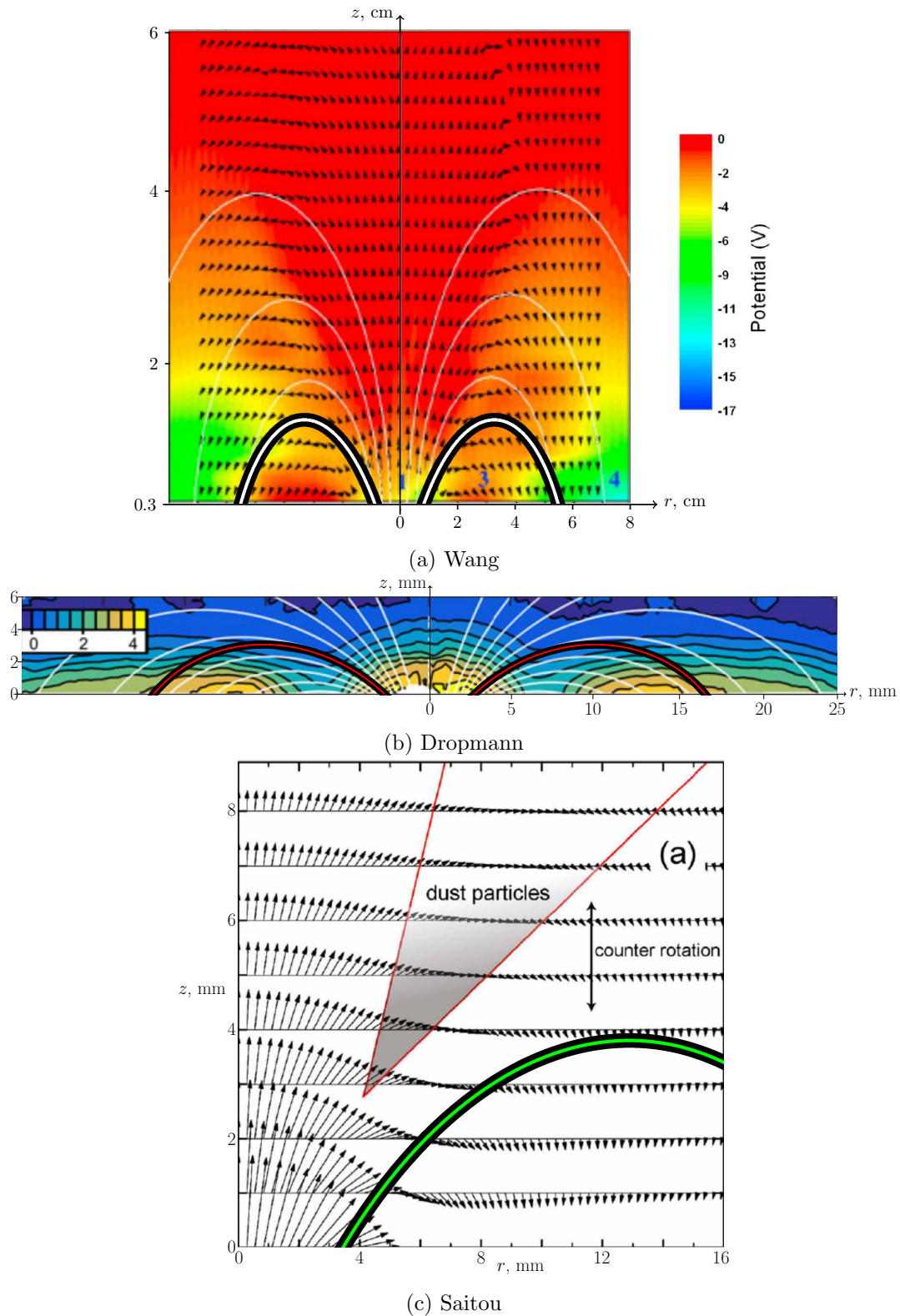


Figure 4.18: Overlays of exclusion zones calculated for electrons travelling at the thermal speed and experimental results of: (a) Wang - electric potential, (b) Dropmann - radial acceleration of dust grains in units of  $g$  and (c) Saitou - position of dust grain cloud. The colours of the exclusion boundaries are not significant and are only chosen such that they stand out from the colour schemes used by the original authors.

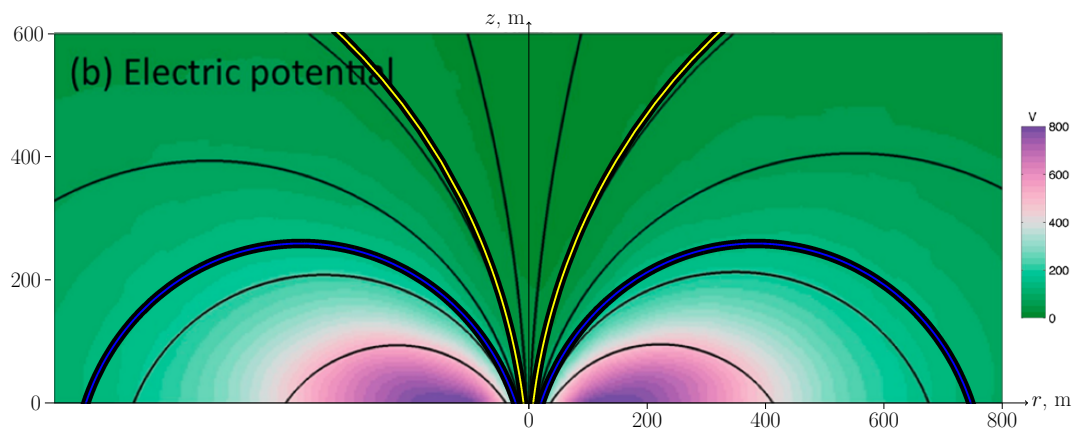


Figure 4.19: Electric potential from simulations performed by Zimmerman. The yellow curve gives the exclusion zone for thermal electrons approaching from infinity and the blue gives the exclusion zone for particles which start at the computational boundary.

## 5 Sheath model and its implementation

What is interesting to consider, now that an electron model has been formulated, is the effect this has on the sheath. It is just this aspect which is concentrated on, in other words, the goal is not to produce an accurate model of lunar swirls, where one would have to include photoelectrons, complex field geometry and the magnetic field and flow speed of the solar wind. Instead, the task is to isolate the features which arise due to the restricted movement of electrons. Because these complicating lunar swirl features are not included in the laboratory studies either, it is more accurate to say that one is trying to accurately describe lunar swirl experiments, not the swirls themselves. Also, not to forget, the results obtained here will also be useful in better characterising the sheath region of magnetised dusty crystal experiments.

### 5.1 Sheath model outline

The new sheath model, which includes the effects of magnetized electrons, is not so different methodologically from the planar sheath treatment described in the theory section 2.4: Electron density is given by an analytic expression of local properties, ion density is given from continuity as they stream through and the sheath profile is the self consistent solution of these particle densities with Poisson's equation. The big difference in the magnetized case is that variation of electron density in the radial direction now means that this is a 2D problem. Furthermore, the ions will undergo deflections caused by the radial electric fields and thus require more than just energy conservation to determine their densities. Assuming that they are not so strongly deflected that they undergo complete reflection out of the sheath, one can employ a fluid model to determine their distribution.

It is important to discuss the relative size of the sheath, tens of  $\lambda_{De}$ , and the typical lengthscale of influence of the magnet,  $\Lambda$ . If  $\Lambda \ll \lambda_{De}$ , the magnet only has an effect on electrons deep in the sheath. Given that the density of electrons down there is highly depleted by the wall electric field, the additional obstacle provided by the dipole lobe region is of little consequence. In the experiments of Law, Dropmann and Wang, it is the case that the extent of the sheath is slightly larger, but comparable, to the magnetic effects  $\Lambda \lesssim \lambda_{De}$ . In these cases, the changes to the plasma profile are basically restricted to the sheath. For situations where the magnetic field has influence all the way to the bulk plasma there are extra complications as one needs to also consider the presheath. Since I will be making comparisons to Wang and Dropmann, there is no reason to solve a problem more difficult than it needs to be and I will restrict these studies to look at

magnetic field strengths which are not so big as to have effect in the bulk plasma.

To describe the sheath model in mathematical terms, the problem to be solved is Poisson's equation in cylindrical geometry,

$$\frac{1}{r} \frac{\partial}{\partial r} \left( r \frac{\partial \phi}{\partial r} \right) + \frac{\partial^2 \phi}{\partial z^2} = \frac{e}{\epsilon_0} (n_i - n_e) , \quad (5.1)$$

with the electron density being given by

$$n_e = n_0 \exp \left( \frac{e\phi}{k_B T_e} \right) \left( \operatorname{erfc}(v(r, z)) + \frac{2v(r, z) \exp(-v(r, z)^2)}{\sqrt{\pi}} \right) , \quad (5.2)$$

where

$$v(r, z) = \frac{qM}{m} \frac{1}{r^2} \left( -1 + \sqrt{1 + \frac{r^3}{(r^2 + z^2)^{\frac{3}{2}}}} \right)^2 , \quad (5.3)$$

and the ion density resulting from the solution to the fluid equation of motion

$$(\mathbf{u}_i \cdot \nabla) \mathbf{u}_i = \frac{e}{m_i} \mathbf{E} , \quad (5.4)$$

and continuity

$$\nabla \cdot (n_i \mathbf{u}_i) = 0 . \quad (5.5)$$

The equations are to be solved in a domain of extent  $R$  and  $Z$  in the radial and vertical directions respectively. The boundary conditions are:

i  $\mathbf{r} = \mathbf{0}$ : On axis the radial electric field must be zero, thus requiring of the potential,

$$\frac{\partial \phi}{\partial r}(0, z) = 0 . \quad (5.6)$$

ii  $\mathbf{r} = \mathbf{R}$ : If the domain is much wider than the area of magnetic influence,  $R \gg \Lambda$ , then there are large distant regions where the plasma is not magnetically influenced and a planar sheath can be established. So long as the radial boundary is taken to be sufficiently far, one can use the planar sheath profile to describe the potential here,

$$\phi(R, z) = \phi_P(z) , \quad (5.7)$$

where  $\phi_P$  is the planar sheath profile, as derived in section 2.4.

iii  $\mathbf{z} = \mathbf{0}$ : Since the wall is conducting it describes an equipotential surface. Given that the previous boundary condition provides the wall potential there as  $\phi(R, 0) = \phi_P(0)$ , this must also be the wall potential everywhere,

$$\phi(r, 0) = \phi_P(0) . \quad (5.8)$$

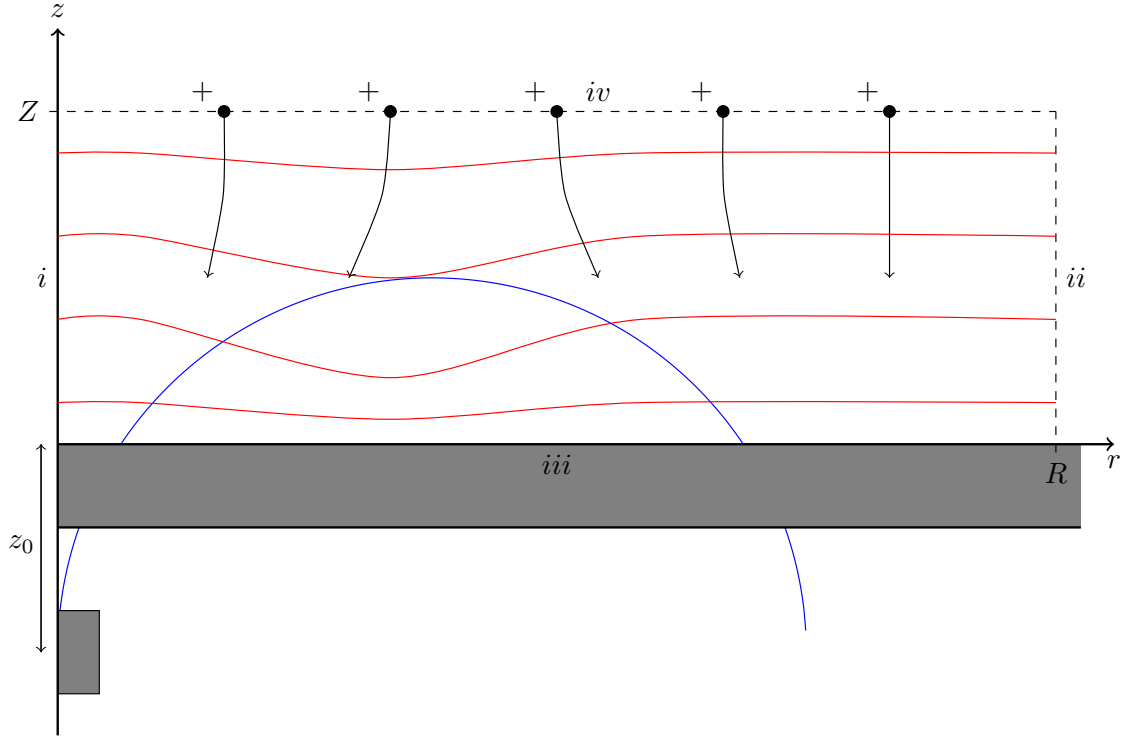


Figure 5.1: Computational domain for sheath model and expected qualitative features. The typical area of influence of the magnet (which has its midpoint at  $z_0$  below the electrode surface) is highlighted in blue and is contained within the sheath extending to a height  $Z$  and width  $R$ . Boundary conditions corresponding to those listed are given and a rough estimate of what to expect for the potentials is given in red. Trajectories of deflected ions are shown at the top.

- iv  $z = Z$ : In the same way as the boundary at  $r = R$ , if one goes far enough away from the magnet in the  $z$  direction, then one recovers the planar sheath.

$$\phi(r, Z) = \phi_P(Z) . \quad (5.9)$$

These boundary conditions, as well as other features of the model, are illustrated in Fig. 5.1.

This model entails three necessary tasks which require computational methods to accomplish. Needed is: a solver of Poisson's equation in 2D, a solver of the ion fluid density in 2D and an iterative scheme to find the self consistent solution of plasma density and potential. The remainder of this chapter will describe what exact methods are used for these three tasks and then my coding of these will be tested by benchmarking the three components against known results. First, I shall quickly dedicate a section to outline some of the basics on finite difference methods.



## 5.2 Discretisation and finite differences

When a computer is used to deal with a continuous quantity the first step must be to translate this into a form it can manage via discretisation. In 2D a function,  $u(x, y)$ , is represented by its values at a discrete set of points  $u(x_i, y_j)$  to form a matrix with elements  $u_{i,j}$ . The grid points are given by:

$$x_i = x_0 + ih \quad (5.10)$$

$$y_j = y_0 + jh \quad (5.11)$$

where  $i = 0, 1, \dots, N_x$ ,  $j = 0, 1, \dots, N_y$  and the spacing between points,  $h$ , is used to refer to any quantities being represented on the grid. For example,  $u^h$ , denotes the function  $u(x, y)$  cast onto a grid of spacing  $h$ , whereas  $u^{2h}$  would imply the same function represented on a coarser grid of twice the previous spacing. Furthermore, subscripts are used to signify specific values on the grid, i.e.  $u_{i,j}^h$  is the discretized value of  $u$  at  $(x_0 + ih, y_0 + jh)$ . The labelling convention applies to operators too, where  $\mathcal{O}^h$  has the same (albeit discretised) effect on  $u^h$  as  $\mathcal{O}$  would on  $u$ . A common class of operators worth mention is those which calculate derivatives. In the world of grid points, these operate by using ‘finite differences’ in one of three ways, depending on the selected points:

$$f'(x) \approx \frac{f(x+h) - f(x)}{h} \quad (5.12)$$

$$\approx \frac{f(x) - f(x-h)}{h} \quad (5.13)$$

$$\approx \frac{f(x+h) - f(x-h)}{2h} \quad (5.14)$$

with these three expressions referred to as ‘forward’, ‘backward’ and ‘central’ schemes respectively.

There are three operators which will be useful in this chapter and it is worthwhile introducing them now. Not unexpectedly, since the goal is to solve Poisson’s equation, the first is the Laplacian,  $\mathcal{L}^h$ , which in Cartesian coordinates operating on the potential  $\phi^h$  is, at the gridpoint  $(i, j)$ , given by

$$(\mathcal{L}^h \phi^h)_{i,j} = \frac{\phi_{i,j+1}^h + \phi_{i+1,j}^h + \phi_{i,j-1}^h + \phi_{i-1,j}^h - 4\phi_{i,j}^h}{4h^2} \quad (5.15)$$

where a central difference scheme has been employed. Later on this will require adaptation for cylindrical coordinates and there is also the issue of when  $(i, j)$  is a point on the boundary. The next two operators are special in that they regulate the movement between different grids - these operators do not correspond to anything physical. First of these is the restriction operator,  $\mathcal{R}$ . The job of this operator is to take a function defined on a grid,  $u^h$ , and to map this to the representation on a grid twice as coarse,  $u^{2h}$ . This is best understood from the illustration of Fig. 5.2, the operator given mathematically

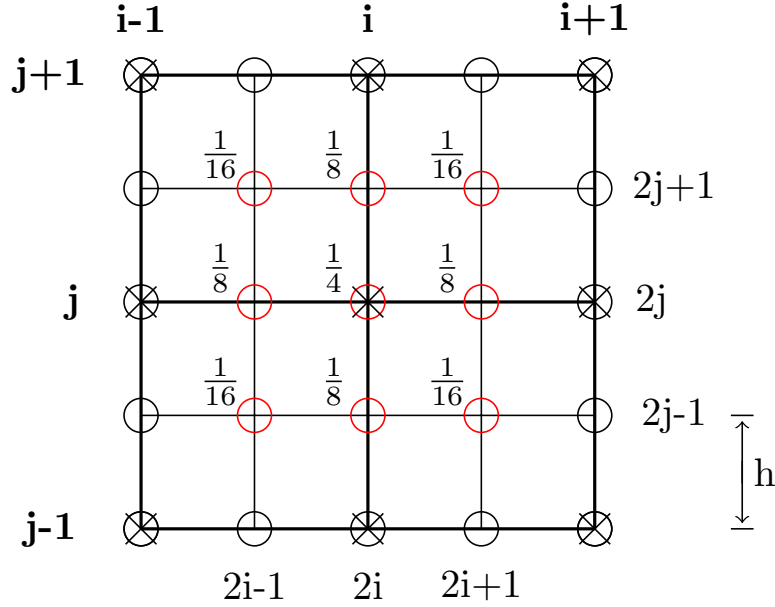


Figure 5.2: Restriction from the fine grid (circles) to the coarse grid (crosses). The coarse grid indices are written in bold on the left and top, the fine grid on the bottom and right and because the coarse grid spacing is twice as large,  $u_{i,j}^{2h}$  and  $u_{2i,2j}^h$  correspond to the value of  $u$  at the same point in space. A weighted sum of the neighbouring points highlighted in red is used to determine  $u_{i,j}^{2h}$  according to equation (5.16).

as [107, p. 42]

$$\begin{aligned}
 u_{i,j}^{2h} &= (\mathcal{R}^h u^h)_{i,j} = \frac{1}{4} u_{2i,2j}^h \\
 &+ \frac{1}{8} \left( u_{2i,2j+1}^h + u_{2i+1,2j}^h + u_{2i,2j-1}^h + u_{2i-1,2j}^h \right) \\
 &+ \frac{1}{16} \left( u_{2i+1,2j+1}^h + u_{2i+1,2j-1}^h + u_{2i-1,2j-1}^h + u_{2i-1,2j+1}^h \right) \quad (5.16)
 \end{aligned}$$

i.e. the operator, commonly known as the ‘full weighting’ (FW) operator, takes into account the values at nine points, giving greater weighting to those nearest by. Application of  $\mathcal{R}$  is akin to reducing the resolution of a jpeg image by quartering the pixel density, but taking a weighted sum around each pixel to faithfully preserve as much information as possible. The final operator is prolongation,  $\mathcal{P}$ , which performs the opposite task of restriction. Here a function  $u^{2h}$  is interpolated under the action of  $\mathcal{P}$  to fit to a finer grid, giving  $u^h$ . I should point out that whilst the purposes of  $\mathcal{P}$  and  $\mathcal{R}$  are opposite, their effects are not since prolongation has to resort to interpolation, whereas restriction uses a weighted average. To go back to the example of the jpeg, an image that has been made grainy cannot then return back to its original resolution by increasing the pixel density - information lost by restriction cannot be regained by prolongation. The way  $\mathcal{P}$  works is by a process called ‘bilinear interpolation’. As the name suggests, the value of the function at  $(x, y)$  is worked out from two successive rounds of interpolation. Both

are illustrated in Fig. 5.3, the first occurring in the  $x$  direction:

$$\phi_{x,y_1} = \frac{x_2 - x}{x_2 - x_1} \phi_{1,1} + \frac{x - x_1}{x_2 - x_1} \phi_{2,1} \quad (5.17)$$

$$\phi_{x,y_2} = \frac{x_2 - x}{x_2 - x_1} \phi_{1,2} + \frac{x - x_1}{x_2 - x_1} \phi_{2,2} \quad (5.18)$$

then, interpolation in the  $y$  direction yields the approximate value:

$$\phi_{x,y} = \frac{y_2 - y}{y_2 - y_1} \phi_{x,y_1} + \frac{y - y_1}{y_2 - y_1} \phi_{x,y_2} \quad (5.19)$$

When applied to a coarse to fine grid conversion, these equations look much simpler since  $\phi_{x,y}$  either occurs on top of, half way (in  $x$  or  $y$ ) between two, or in the centre of four coarse grid points. In these four cases elements are combined in the following ways:

$$u_{2i,2j}^h = (\mathcal{P}^{2h} u^{2h})_{2i,2j} = u_{i,j}^{2h} \quad (5.20)$$

$$u_{2i+1,2j}^h = (\mathcal{P}^{2h} u^{2h})_{2i+1,2j} = \frac{1}{2} (u_{i,j}^{2h} + u_{i+1,j}^{2h}) \quad (5.21)$$

$$u_{2i,2j+1}^h = (\mathcal{P}^{2h} u^{2h})_{i,2j+1} = \frac{1}{2} (u_{i,j}^{2h} + u_{i,j+1}^{2h}) \quad (5.22)$$

$$u_{2i+1,2j+1}^h = (\mathcal{P}^{2h} u^{2h})_{2i+1,2j+1} = \frac{1}{4} (u_{i,j+1}^{2h} + u_{i+1,j}^{2h} + u_{i,j-1}^{2h} + u_{i-1,j}^{2h}) \quad (5.23)$$

The Laplacian, prolongation and restriction operators have been presented in Cartesian coordinates here for simple demonstration. Their form in cylindrical coordinates, as well as corrections which have to be made at boundary points, are given in Appendix C.

### 5.3 Poisson solver

Now that it is understood how to translate a problem to the language of a computer, it's time to apply this to the first of the three components of my method, a solver of Poisson's equation:

$$\mathcal{L}\phi = \rho, \quad (5.24)$$

where  $\mathcal{L}$  is the Laplacian operator and  $\rho$  is what I shall call the 'source term' (charge density divided by  $\epsilon_0$ ). Discretizing this equation on a uniform grid of mesh spacing,  $h$ , these quantities take their discrete forms:

$$\mathcal{L}^h \phi^h = \rho^h. \quad (5.25)$$

This equation can be solved directly for  $\phi^h$  by inversion of the matrix  $\mathcal{L}^h$ . However, most of the time large grid sizes will render these matrices prohibitively large and inversion will take too long. The remainder of this chapter will review the alternative

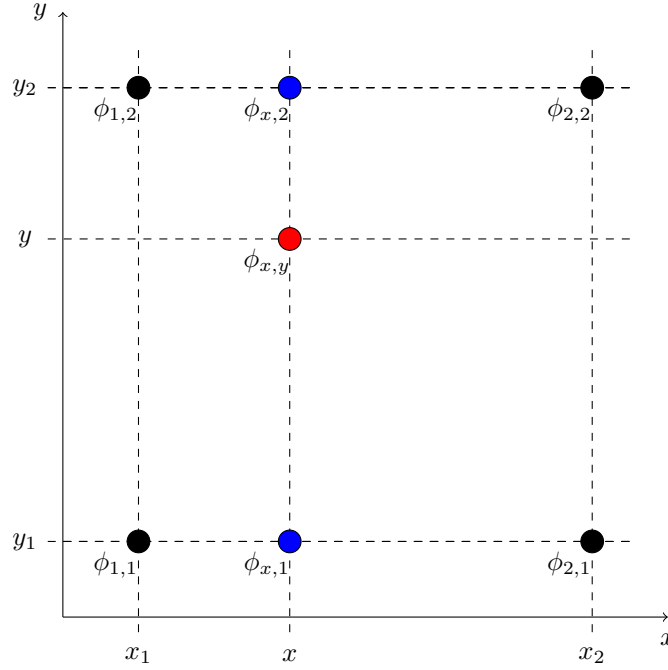


Figure 5.3: Bilinear interpretation for the general case of continuous  $x$  and  $y$  (for the prolongation operator,  $(x, y)$  will occur on fine grid sites). Intermediate values (blue)  $\phi_{x,1}$  and  $\phi_{x,2}$  are each found from a weighted sums of  $\phi_{1,1}$ ,  $\phi_{2,1}$  and  $\phi_{1,2}$ ,  $\phi_{2,2}$  respectively. Then,  $\phi_{x,y}$  is the result of another weighted sum of these two values.

computational techniques which are employed to reach a solution.

### 5.3.1 Relaxation methods

One of the most basic strategies is provided by relaxation methods, where some initial guess is gradually improved until it converges on the solution. A physical way to think about this is to recast (5.24) as a diffusion equation,

$$\frac{\partial \phi}{\partial t} = \mathcal{L}\phi - \rho, \quad (5.26)$$

so that the steady state solution,  $\frac{\partial \phi}{\partial t} = 0$ , is also the solution of (5.24). In this sense, an initial guess will eventually relax to the answer. Expressing the pseudo-time derivative in terms of a forward difference yields an equation for the development of  $\phi^h$ :

$$\phi^h(t + \delta t) = \phi^h(t) + \delta t \left( \mathcal{L}^h \phi^h - \rho^h \right) \quad (5.27)$$

which for the two dimensional case, using the cartesian Laplacian operator from (5.15), becomes

$$\phi_{i,j}^h(t + \delta t) = \phi_{i,j}^h(t) + \frac{\delta t}{h^2} \left( \phi_{i+1,j}^h(t) + \phi_{i-1,j}^h(t) + \phi_{i,j+1}^h(t) + \phi_{i,j-1}^h(t) - 4\phi_{i,j}^h(t) \right) - \rho_{i,j}^h \delta t \quad (5.28)$$

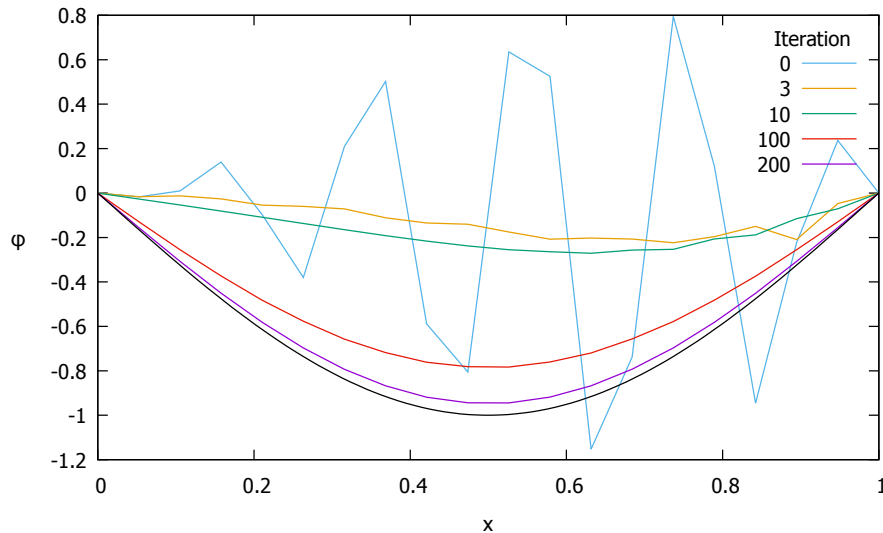


Figure 5.4: Demonstration of Jacobi relaxation for 20 grid points ( $h=0.05$ ). A poor initial guess was intentionally chosen to demonstrate that high frequency features are quickly smoothed out - then begins a long relaxation phase until the solution ( $-\sin(\pi x)$ , shown in black) is reached.

The solution can't be arrived at arbitrarily fast by making  $\delta t$  arbitrarily large however, it turns out that this method is only stable if  $\delta t \leq \frac{h^2}{4}$ . Still, one is free to take the highest value permissible for  $\delta t = \frac{h^2}{4}$  and this makes equation (5.28) become:

$$\phi_{i,j}^h(t + \delta t) = \frac{1}{4} \left( \phi_{i+1,j}^h(t) + \phi_{i-1,j}^h(t) + \phi_{i,j+1}^h(t) + \phi_{i,j-1}^h(t) \right) - \frac{h^2 \rho_{i,j}^h}{4} \quad (5.29)$$

This equation is synonymous with the 2D 'Jacobi' relaxation method. In Fig. 5.4, the result of a Jacobi method used to solve Poisson's equation in 1D for a source term  $\rho = \pi^2 \sin(\pi x)$  and boundary conditions  $\phi(0) = \phi(1) = 0$  is shown. The important lessons from this example are that relaxation methods can efficiently smooth out high frequency features, but are slow to converge. In fact, the number of iterations required to solve a problem defined on a  $J \times J$  grid is of the order  $J^2$  and given that  $J$  is commonly of order hundreds and above, this method is impractical.

Now that relaxation methods are understood, at this stage most textbooks and lecture courses implore the reader not to use them for any of their own problems, stressing that this antiquated method is not able to handle problems of any consequence. My previous discussion was not simply included for the preservation of our computational heritage however - although relaxation methods are not effective on their own, they will have a small role to play in the preferred finite difference Poisson solver: the 'multigrid algorithm'.

### 5.3.2 Multigrid methods

#### N-grid algorithm

To understand the workings of multigrid methods only the simplest case, a two grid method, need be considered. As was the case with relaxation, some framework is required to take a guess and then guide it to the solution. Call such a guess  $\tilde{\phi}^h$  which can be written as a deviation,  $v^h$  (commonly referred to as the ‘error’ or the ‘correction’), from the exact solution  $\phi^h$ ,

$$\phi^h = \tilde{\phi}^h + v^h . \quad (5.30)$$

Also, define the ‘residual’ (sometimes referred to as ‘defect’),  $d^h$ , as the difference between the density implied by the guess and the actual density:

$$d^h = \mathcal{L}^h \tilde{\phi}^h - \rho^h \quad (5.31)$$

Substitution of these two newly defined quantities into (5.25) gives the relationship between them as:

$$\mathcal{L}^h v^h = d^h \quad (5.32)$$

and so the discrepancies in the potential and density follow their own Poisson’s equation.

Given an initial guess, if one could determine the exact error the problem would be solved instantly by substitution of these two quantities into equation (5.30). The error is found by solving (5.32) for  $v^h$ , the residual being easily calculated from (5.31). However, the plan seems to have taken a fatally circular route: to find the error it is required to solve Poisson’s equation, the very equation I’d set out to avoid solving directly due to the oversized matrices involved. Of course this is not unexpected, if it were easy to evaluate the error exactly then the problem would be solved in one step which would not resemble an iterative scheme. What is needed is a fast way to estimate the error. This has to be done via some approximation, though with multigrids it might be more accurate to describe it as a ‘coarsification’.

A finite difference problem can be made computationally easier, at the expense of resolution, by evaluating on a coarser grid. This is how an approximate value for  $v^h$  is found. Rather than solving equation (5.32) at the current resolution,  $h$ , the problem is firstly cast on to a coarser grid of spacing  $H$  (where  $H$  will always be  $2h$  here):

$$\mathcal{L}^H v^H = d^H \quad (5.33)$$

This casting process is the same one referred to as ‘restriction’ previously and is mediated by the restriction operator  $\mathcal{R}$ , with  $d^H = \mathcal{R}d^h$ . Solving (5.33) is the next step and since  $\mathcal{L}^H$  has smaller dimension, the solution is easier to obtain than (5.32). In fact, for now I’ll assume that the grid,  $H$ , is sufficiently small such that  $v^H$  can be solved for exactly by, say, matrix inversion. Once  $v^H$  is found, this coarse grid error needs to be cast back onto the fine grid by some interpolation process, provided by the aforementioned prolongation operator,  $\mathcal{P}$ , acting as  $v^h = \mathcal{P}v^H$ . The approximation is now ready to be

updated:

$$\tilde{\phi}_{\text{new}}^h = \tilde{\phi}^h + v^h \quad (5.34)$$

In summary, this process can be split into the following steps:

### Coarse grid correction

- i Compute the defect on the fine grid,  $d^h$ , from (5.31).
- ii Restrict the defect to the coarse grid by  $d^H = \mathcal{R}d^h$ .
- iii Solve for the exact coarse grid error,  $v^H$ , from (5.32).
- iv Prolong the coarse grid error back to the fine by  $v^h = \mathcal{P}v^H$ .
- v Use  $v^h$  to improve the initial guess from  $\phi^h$  to  $\phi_{\text{new}}^h$  from (5.34)

These five steps will be referred to collectively as the performance of a ‘coarse grid correction’. It’s not quite ready to be put into action just yet, however, and this is where relaxation methods make a reappearance. Recall from earlier that high frequency features are efficiently smoothed out. Given that the coarse grid correction is not able to resolve components of the error below a typical wavelength  $H$ , relaxation methods can be employed to deal with the fine details. This leads to a hybrid method which combines the ideas of relaxation and coarse grid correction:

### Two grid method

1. Guess a solution on the fine grid,  $\tilde{\phi}^h$ .
2. Pre-smoothing: The input value of  $\tilde{\phi}^h$  is smoothed by  $\nu_1 > 0$  steps of a relaxation method.
3. Coarse grid correction (steps i-v from above) applied to convert  $\tilde{\phi}^h$  to  $\tilde{\phi}_{\text{new}}^h$ .
4. Post-smoothing:  $\tilde{\phi}_{\text{new}}^h$  is smoothed by  $\nu_2 > 0$  steps of a relaxation method.

All of these steps constitute one iteration of the ‘two grid method’. Depending on whether  $\tilde{\phi}_{\text{new}}^h$  meets some convergence condition it can be fed back into the machine to produce a further improved solution. A basic 1D example of this is presented in Fig. 5.5, to illustrate the significance of each step of the two grid method.

Until now it’s been assumed that the dimension of the coarse grid is small enough such that (5.33) can be solved exactly within a reasonable length of time, but what if this isn’t the case? It’s good to remind oneself that at this stage the task is effectively the same as the starting point: to solve Poisson’s equation, except this time for the more abstract quantity  $v^H$ , instead of  $\tilde{\phi}^h$ , and a source term of  $d^H$ , instead of  $\rho^h$ . Thus, there is nothing to stop one from applying the two grid framework to this mathematically identical problem, i.e. have a guess at  $v^H$ , find the associated error (strangely this is the ‘error of the error’) on a coarser grid of dimension  $2H = 4h$  which is then used to

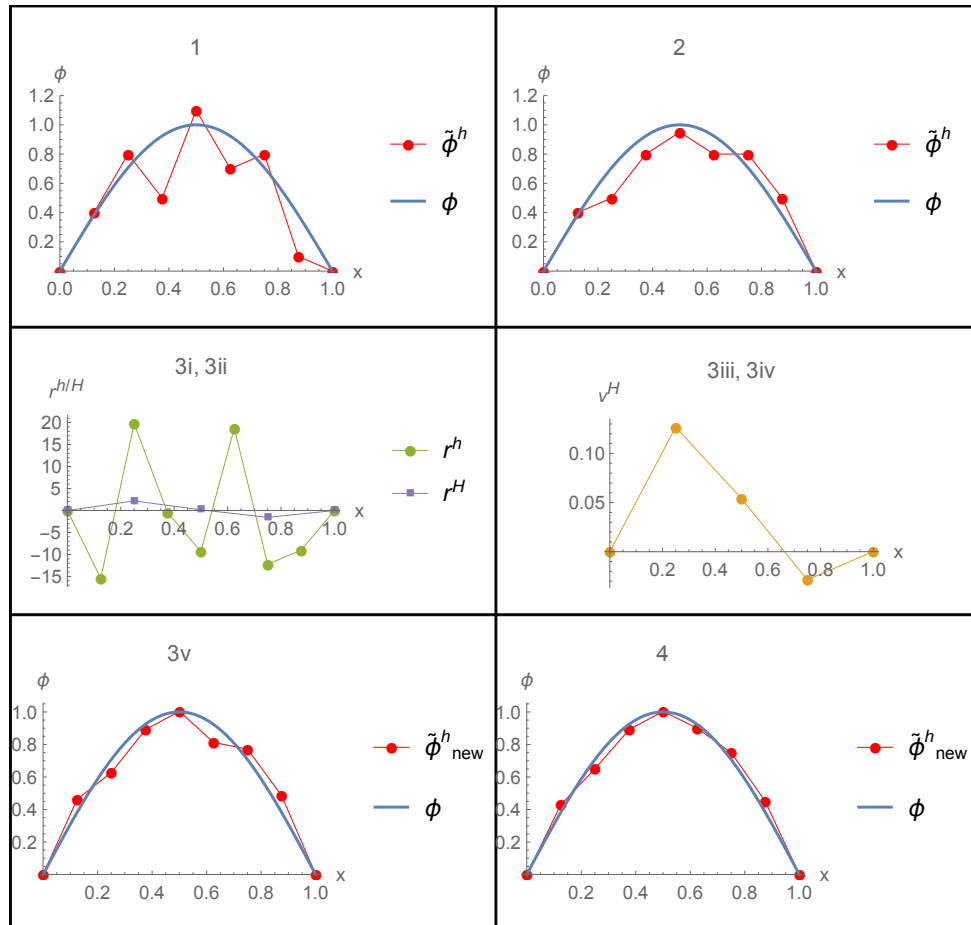


Figure 5.5: A 1D example of the two grid method, enumerated previously as 1, 2, 3 i-v, 4 (each box of this figure numbered correspondingly). For this example the source term  $\rho = -\pi^2 \sin(\pi x)$  is used, which has the solution  $\phi = \sin(\pi x)$  for boundary conditions  $\phi(0) = \phi(1) = 0$ .



hone the guess for  $v^H$ . The excursion to an extra grid earns this the title of a ‘three grid method’.

And if the dimension of the  $4h$  grid is too large for a direct solution? Then one can apply this idea recursively, going deeper until some coarsest level of an acceptably small size is reached. If this takes  $N$  grids to achieve, then the process is referred to as an  $N$ -Grid method. The journey from the finest grid, down through all of the coarse grids and back again is called a ‘cycle’ and its exact structure depends on the value of a new parameter  $\gamma$ . This number indicates how many ‘mini-cycles’ occur for each coarse grid, that is, once a restriction to the  $H$  grid is performed to get  $v^H$ ,  $\gamma$  is the number of  $v_{\text{new}}^H$  values calculated. Again, this is understood best with an accompanying illustration and so in Fig. 5.6 structures of different  $N$ -grid cycles are shown for  $\gamma$  values of 1 and 2, also referred to as ‘V’ and ‘W’ cycles respectively. The efficiency of the multigrid machine means that it is rarely necessary to take  $\gamma > 2$ .

### Full multigrid algorithm (FMG)

So far, multigrid methods have been applied within an iterative scheme: guess a solution on the fine grid and then improve this until some convergence criterion is met. It turns out to be more efficient not to make a guess at all, but to start proceedings at the level of the exact solution on the coarsest grid, say,  $3 \times 3$ . Prolonging this extremely coarse solution to the next grid up,  $5 \times 5$ , serves as the ‘guess’ for the solution at this level. Given that the  $3 \times 3$  solution was exactly correct and it has been prolonged by only one level, this guess will not be too bad. An application of a 2 grid cycle polishes this guess up and then it is ready to be prolonged to the next grid up. This process, and how it differs from an  $N$ -grid method can be seen in Fig. 5.7. The parameter  $\gamma$  has a slightly different meaning in the context of a FMG: once prolongation is performed up from a grid  $H$  to find  $\phi^{\frac{H}{2}}$ ,  $\gamma$  is the number of  $\phi_{\text{new}}^{\frac{H}{2}}$  values which are calculated before proceeding to the next grid up.

Analysis of the convergence rates of the  $N$ -grid and FMG methods is beyond the scope of this thesis, but the important result is that the number of iterations required of a  $J \times J$  grid scales as  $J$ , in contrast to  $J^2$  for relaxation methods. Incredibly, this scaling is basically independent of the dimension of the problem and so whereas a relaxation method would take  $\mathcal{O}(J^3)$  steps to solve a 3D problem, a multigrid attempt would still only require  $\mathcal{O}(J)$  steps. This is the Holy Grail of numerical analysis.

## 5.4 Self consistent Poisson-Density Solution

Now to describe the second of the three computational blocks. Multigrid methods provide the means to get from a given  $\rho$  to the implied  $\phi$ . To solve the problem at hand, there is an additional layer of complexity because  $\rho$  itself is a function of  $\phi$  and so the ultimate goal is the find the self-consistent solution which satisfies both Poisson’s equation with  $\rho(\phi)$  obeyed. The framework for this is also iterative, taking the following

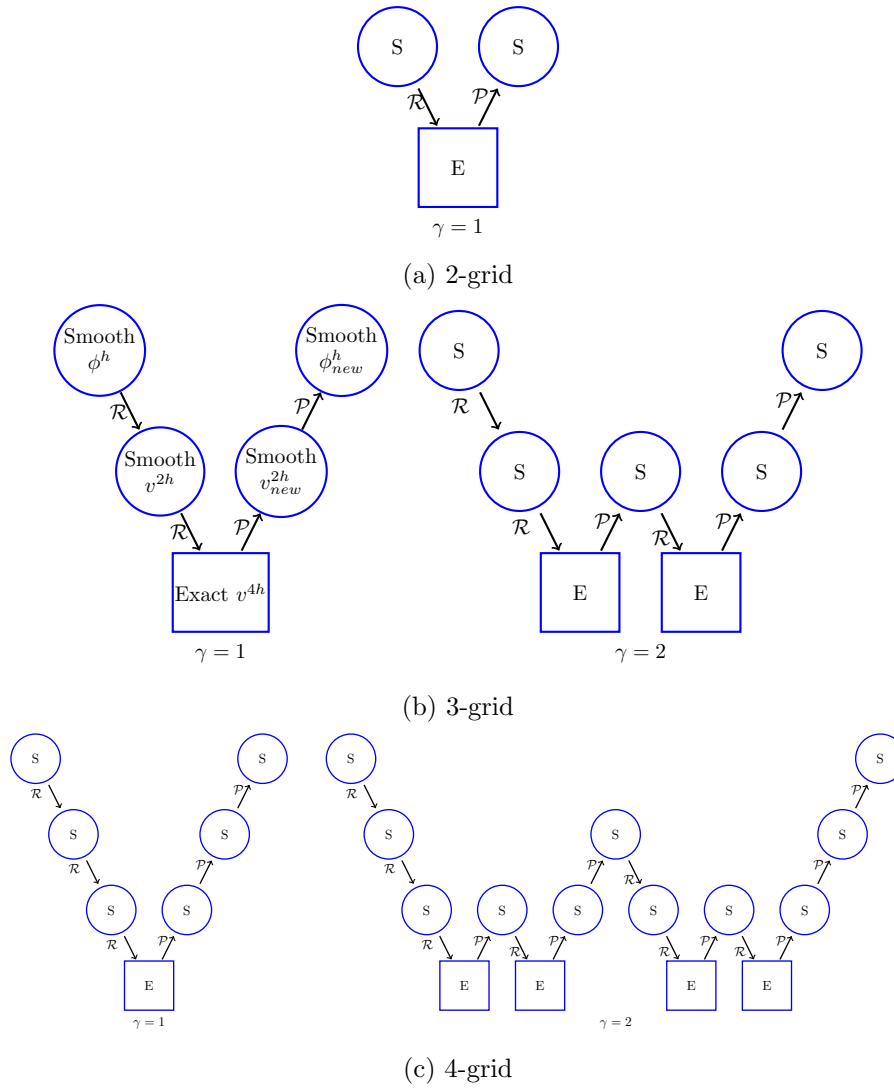


Figure 5.6: Stages of 2-grid (a), 3-grid (b) and 4-grid (c) algorithms for  $\gamma = 1, 2$ . The 3-grid example with  $\gamma = 1$  has the processes explicitly stated for clarity, the others just use ‘S’ to indicate Smoothing and ‘E’ to indicate the calculation of an Exact solution.

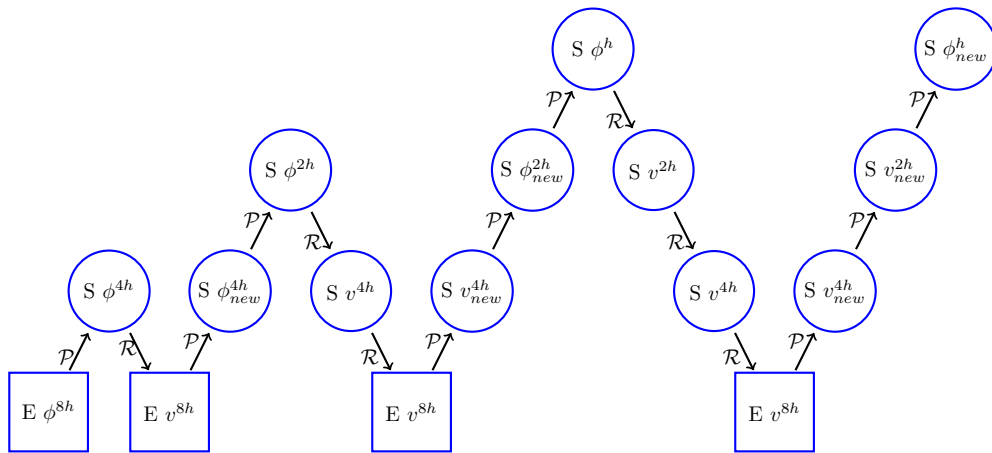


Figure 5.7: A FMG cycle for 4 grids and  $\gamma = 1$ .

structure (where superscripts indicate iteration number):

### Newton-Poisson Solver

1. Initial Density  $\rho^k(x)$
2. Solve Poisson's equation (with an FMG, for example) to find the implied potential  $\phi^k(x)$
3. Calculate the density implied by this potential  $\rho^{k+1}(x)$
4. Check how different  $\rho^k(x)$  and  $\rho^{k+1}(x)$  are.
5. If too dissimilar, go back to step 1 with initial density updated to  $\rho^{k+1}$

#### 5.4.1 Convergence

It is not guaranteed for this process to converge and it turns out that step 5 needs some modification. Analysis of the conditions required for convergence has proved hard to come by, so I will present the problem which has occurred and its subsequent resolution with the expectation that it must have been solved before somewhere else. One underlying downfall of this method has proved to be overcorrection. Say a suggested density (technically, 'source term'),  $\rho^k$ , is slightly too large then the method will prescribe a downwards kick. If this kick is too great, the overshoot may be so significant that the new density is no closer than before (or, even if it is closer, the subsequent kick makes a return to the starting point or beyond). This clumsy process continues with  $\rho$  being batted back and forth but never settling, possibly even diverging. The solution to this problem is to take a more conservative approach. Given an initial density  $\rho^k$  and an updated density  $\rho^{k+1}$ , the cautious way to proceed is not to reject  $\rho^k$  outright and to immediately adopt  $\rho^{k+1}$ , but to take a combination of the two attempts - mathematically speaking take  $(1-f)\rho^k + f\rho^{k+1}$ , where  $0 \leq f < 1$ . This more sceptical treatment of new values does potentially mean that this approach takes longer to reach an answer, but it does mean that the changes in  $\rho$  are less abrupt and will be shown to guarantee avoidance of the overcorrection pitfall described above (if  $f$  is chosen appropriately).

A simple example will be used to illustrate both the failure of the Newton-Poisson solver and then the advantages of the weighted approach. Consider Poisson's equation in 1D with the boundary conditions  $\phi(0) = \phi(L) = 0$

$$\frac{d^2\phi}{dx^2} = \rho(\phi) \tag{5.35}$$

Suppose that this is to be solved on the coarsest grid possible (this decision will be justified at the very end), consisting of only 3 points at  $x = 0, \frac{L}{2}, L$ . The two at the boundaries are both given from the boundary conditions as zero, so it is just the central

---

point to be solved for. In finite difference terminology, with  $h = \frac{L}{2}$ ,

$$\frac{\phi_1 + \phi_3 - 2\phi_2}{h^2} = \rho_2, \phi_1 = \phi_3 = 0 \quad (5.36)$$

which means that the solution for a given density is easily found by inversion of this:

$$\phi_2 = -\frac{h^2 \rho_2}{2} \quad (5.37)$$

Since only one value of density and one of potential is being solved for, the subscript 2's will be dropped. Instead, subscripts will now be used to indicate the iteration number, where  $\rho_5$ , for example, will indicate the source term after the 5th iteration. The subscript 0 goes against this rule as it will be used to indicate the exact solution,  $\rho_0$ . Now, suppose that the initial guess,  $\rho_1$ , is quite close to the answer

$$\rho_1 = \rho_0 + \delta\rho_1 \quad (5.38)$$

This results in an initial guess for the potential from (5.37) as being:

$$\begin{aligned} \phi_1 &= -\frac{h^2(n_0 + \delta\rho_1)}{2} \\ &= \phi_0 - \frac{h^2\delta\rho_1}{2} \\ &\equiv \phi_0 + \delta\phi_1 \end{aligned} \quad (5.39)$$

i.e. an error of  $\delta\rho_1$  in the density results in an error of  $-\frac{h^2\delta\rho_1}{2}$  in the potential. Now to see how this error develops as the Newton-Poisson solver gets in motion. The new density is going to be:

$$\begin{aligned} \rho_2 &= n(\phi_1) \\ &= \rho(\phi_0 + \delta\phi_1) \\ &\approx \rho_0 + \frac{\partial\rho(\rho_0)}{\partial\phi} \delta\phi_1 \\ &\equiv \rho_0 + \delta n_2 \end{aligned} \quad (5.40)$$

therefore, an initial error,  $\delta\rho_1$  has become after one step :

$$\delta\rho_2 = -\frac{\partial\rho(\rho_0)}{\partial\phi} \frac{h^2\delta\rho_1}{2} \quad (5.41)$$

To test for convergence, it must be determined if the error is shrinking:  $\left| \frac{\delta n_2}{\delta n_1} \right| < 1$ . Which, when written in terms of  $L = 2h$  requires that

$$\left| \frac{\partial\rho}{\partial\phi}(\rho_0) \frac{L^2}{8} \right| < 1 \quad (5.42)$$

Thus, as the density becomes more sensitive to changes in potential and the computational domain size increases, it becomes harder to achieve convergence. This is a concerning result as it implies that the physicist has no control over whether the problem they are interested in is tractable. That is to say, if you wish to solve a particular problem which does not satisfy the inequality (5.42), there are no values to tweak to make this possible. This is where the weighted scheme comes to the rescue, the advantages of which can be verified mathematically. In this case, the new density is a combination of the old and new:

$$\delta\rho_2 = (1 - f)\delta\rho_1 - f \frac{\partial\rho(\rho_0)}{\partial\phi} \frac{h^2\delta\rho_1}{2} \quad (5.43)$$

Which, under the same test for convergence yields:

$$f < f_{\text{crit}} = \left| \frac{2}{1 + \frac{\partial\rho(\rho_0)}{\partial\phi} \frac{L^2}{8}} \right| \quad (5.44)$$

In contrast to the previous inequality there is now a parameter,  $f$ , which the physicist can always dial down to make sure that the process converges. Before, in equation (5.42),  $f$  was fixed to be unity.

### 5.4.2 Demonstration

When put to the test, this measure works remarkably well. Take as an example:

$$\frac{d^2\phi}{dx^2} = \exp(\phi) \quad (5.45)$$

with boundary conditions  $\phi(0) = \phi(L) = 0$ . Attempts to solve this problem numerically on a 3 piece grid are shown in Fig. 5.8 for different values of  $L$ . This demonstrates that by decreasing  $f$ , at some point a malfunctioning convergence effort is fixed. However, there is a balancing act here in that whilst convergence can be guaranteed by using smaller values of  $f$ , at some point this will increase the time taken to do so - obviously, if  $f = 0$  convergence will take infinitely long because  $\rho$  will never change.

A slight drawback is that  $\rho_0$  and thus  $\frac{\partial\rho}{\partial\phi}(\rho_0)$  is only known once the problem has been solved and so the exact value of  $f_{\text{crit}}$  is unknown beforehand. This is a problem because the value chosen for  $f$  determines whether or not the method is doomed and if  $f_{\text{crit}}$  is unknown then it is difficult to recognise what a sensible value of  $f$  to take is. This problem is not too great, however, since there are still ways to estimate  $\frac{\partial\rho(\rho_0)}{\partial\phi}$  to give an order of magnitude value of  $f_{\text{crit}}$ . In the sheath, where these methods are to be applied, a reasonable guess would be the ratio of the density drop to the potential drop across the sheath  $\frac{\partial\rho(\rho_0)}{\partial\phi} \approx \frac{n_0 e}{\epsilon_0 \phi_W}$ . With some luck, this estimate may be good enough to ensure convergence. If not, with some patience, the estimate serves as a starting point for a trial and error approach: if this approximate  $f_{\text{crit}}$  is too high, keep reducing until convergence is achieved. A further step would be not just to satisfy oneself with

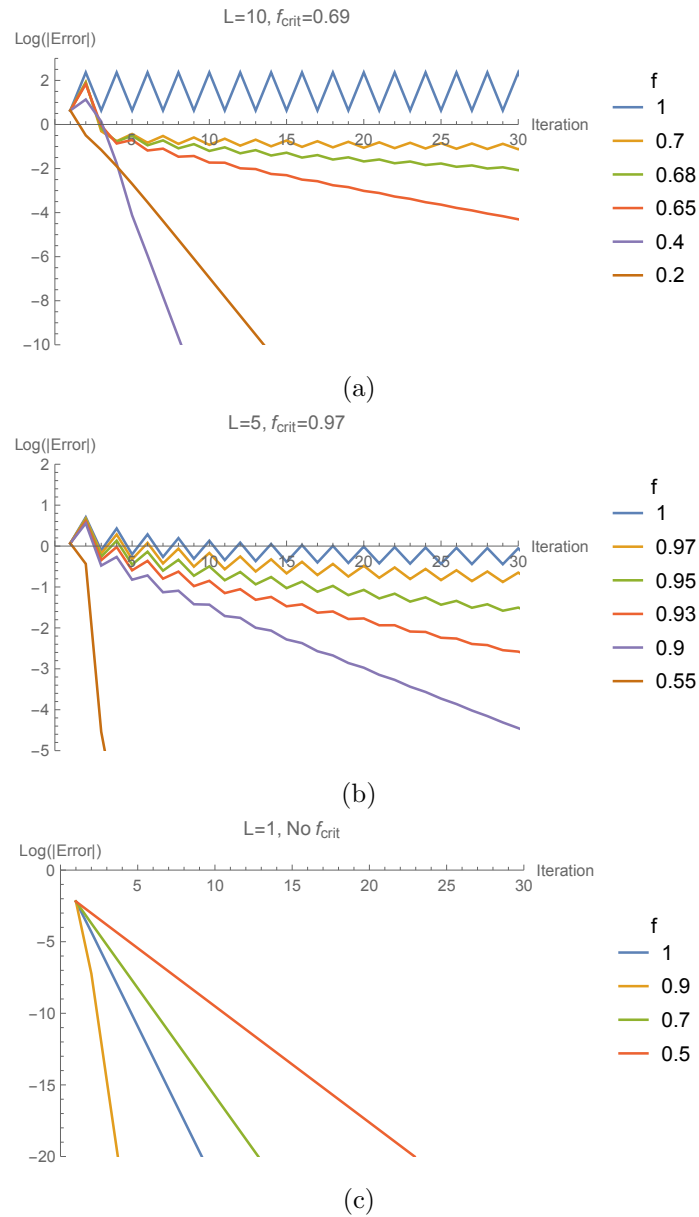


Figure 5.8: Convergence tests on large ( $L = 10$ ) to small ( $L = 1$ ) domains for different values of  $f$ .  $f = 1$  is included in all plots to demonstrate how the unweighted approach is hopeless in the cases of (a) and (b). A few selected values in the vicinity of  $f_{\text{crit}}$  are included to verify that this value marks the transition to a convergent scheme. Also, the optimum  $f$  resulting in the most rapid convergence is plotted, these values being 0.4, 0.55 and 0.9 in (a), (b) and (c) respectively.

the promise of a solution, but to find the optimal value for  $f$  so that this solution is produced as efficiently as possible. Given that the computational time involved here will be tolerable, this extra step will not be necessary.

One outstanding point needs to be addressed and that is my justification for using a 3 point grid in my analysis. The reader may not have been surprised upon learning that there are convergence issues when dealing with such a ludicrously coarse grid and may argue that these issues could surely be alleviated by using a finer grid. However, the starting point for a full multigrid algorithm is the solution on the  $3 \times 3$  grid and this acts as an influential initial condition. If convergence on the  $3 \times 3$  grid cannot be achieved, it will not be seen in any of the dependent fine grids. This is confirmed in the next section, 5.6, when the code is benchmarked - it will be seen that if Newton-Poisson convergence fails, increasing the grid sharpness has no effect.

Lastly, the previous analysis was for a 1D grid and so for the 2D case equation (5.44) incurs a factor of 2

$$f < f_{\text{crit}}^{2D} = \left| \frac{2}{1 + \frac{\partial \rho(\rho_0)}{\partial \phi} \frac{L^2}{16}} \right| \quad (5.46)$$

where  $\rho_0$  is the density at the centre of the computational domain.

## 5.5 Fluid ions

Here I describe the third and final computational method, a finite difference scheme to deduce ion densities from the continuity and fluid equations of motion. Assuming that the top of the computational domain is far enough from the wall, the ion density and velocity can be taken as uniform across this top layer. The ion properties below are then determined from successive jumps down through layers of constant  $z$ , with the equations of motion and continuity dictating how the velocity and density progress through these jumps. This is best seen through the mathematics, firstly, continuity of particles requires that

$$\frac{1}{r} \frac{\partial(rnv_r)}{\partial r} + \frac{\partial(nv_z)}{\partial z} = 0 \quad (5.47)$$

and the radial and  $z$  equations of motion are respectively (with  $F$  the force per unit mass):

$$v_r \frac{\partial v_r}{\partial r} + v_z \frac{\partial v_r}{\partial z} = F_r \quad (5.48)$$

$$v_r \frac{\partial v_z}{\partial r} + v_z \frac{\partial v_z}{\partial z} = F_z \quad (5.49)$$

Rearranging (5.47)-(5.49) for changes with respect to  $z$  yields:

$$\frac{\partial n}{\partial z} = -\frac{1}{v_z} \left[ \frac{1}{r} \frac{\partial(rnv_r)}{\partial r} + n \frac{\partial v_z}{\partial z} \right] \quad (5.50)$$

$$\frac{\partial v_r}{\partial z} = \frac{1}{v_z} \left[ F_r - v_r \frac{\partial v_r}{\partial r} \right] \quad (5.51)$$

$$\frac{\partial v_z}{\partial z} = \frac{1}{v_z} \left( F_z - v_r \frac{\partial v_z}{\partial r} \right) \quad (5.52)$$

and finally, substituting (5.52) into (5.50) to erase the  $z$  derivative gives:

$$\frac{\partial n}{\partial z} = -\frac{1}{v_z} \left[ \frac{1}{r} \frac{\partial(rnv_r)}{\partial r} + \frac{n}{v_z} \left( F_z - v_r \frac{\partial v_z}{\partial r} \right) \right] \quad (5.53)$$

Discretization of (5.51)-(5.53) provides the progression of  $v_r, v_z$  and  $n$  to the next layer down, with all of the values on the RHS's being known in previous layers. A comprehensive description of the discretization process is left to Appendix D, here I shall just illustrate the typical workings of the method. In Fig 5.9, all layers with  $z$  indices of  $j$  and higher are known and so at this stage the calculation is to find the values in the layer  $j - 1$ . This is done on a point by point basis and as an example I've picked the one labelled  $[i, j - 1]$ . Say, for example, that one wishes to find  $v_r[i, j - 1]$ , by discretizing equation (5.51) with a central difference method:

$$\frac{v_r[i, j + 1] - v_r[i, j - 1]}{2h} = \frac{1}{v_z[i, j]} \left( F_r[i, j] - v_r[i, j] \frac{(v_r[i + 1, j] - v_r[i - 1, j])}{2h} \right) \quad (5.54)$$

giving the value as:

$$v_r[i, j - 1] = v_r[i, j + 1] - \frac{2hF_r[i, j] - v_r[i, j] (v_r[i + 1, j] - v_r[i - 1, j])}{v_z[i, j]} \quad (5.55)$$

Again, the full treatment including  $v_z$  and  $n$  as well as modifications for boundary points is provided in Appendix D.

## 5.6 Benchmarking of solver

The three main computational blocks outlined previously are the multigrid solver (to determine  $\phi$  from  $\rho$ ), the ion fluid solver (to determine  $n_i$  from  $\phi$ ) and the Newton-Poisson iterator (to marry these two parts self consistently). The pieces of code describing these three processes are written by me and so before these are put to the task, they require benchmarking against simple problems to check that they perform their functions properly. If physically correct results are achieved here, then one can have faith in the output when tackling harder problems.

In the following tests a useful quantity will be the normalized error. Say the exact solution of the potential at some point is  $\phi(x, y)$  and the computed solution is  $\phi_c$ , then



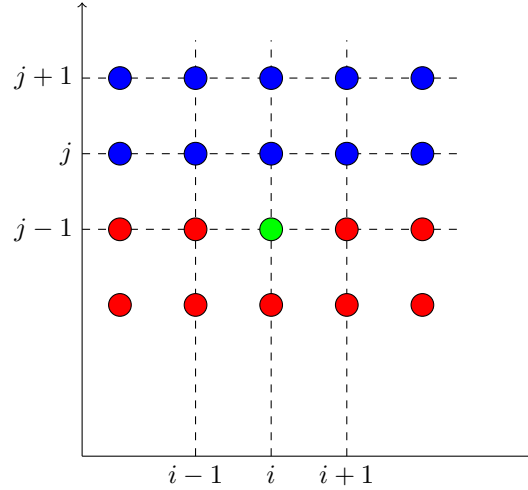


Figure 5.9: Sites where  $v_r, v_z$  and  $n$  are known are given in blue, sites where they are not are in red. The green point is another unknown, however, it is about to be evaluated by using values at the sites  $(i, j)$ ,  $(i, j+1)$ ,  $(i-1, j)$  and  $(i+1, j)$ .

define the normalized error as

$$E_\phi = \left| \frac{\phi(x, y) - \phi_c}{\phi(x, y)} \right| \quad (5.56)$$

with the same convention applying to the error of any other quantity. In the following discussion the error will always be seen on a logarithmic scale since it is the order of magnitude of which that is interesting.

### 5.6.1 Multigrid tests

To test the multigrid solver a case problem has been chosen which has an analytic solution for easy comparison. With a charge density of zero and the boundary conditions:

$$\begin{aligned} \phi(r, 0) &= \phi(r, 1) = 0 \\ \frac{\partial \phi}{\partial r}(0, z) &= 0 \\ \phi(1, z) &= \sin(kz) \end{aligned}$$

the analytic solution to Laplace's equation (Poisson with zero charge density) is given by separation of variables as

$$\phi(r, z) = \frac{I_0(kr)}{I_0(k)} \sin(kz) \quad (5.57)$$

where  $I_0$  is the 0<sup>th</sup> modified Bessel function of the first kind.

In Figs. 5.10 and 5.11 the multigrid has been put through its paces by using different values of  $J$ , the number of grid points along each axis, with the normalized error from the analytic solution (5.57) given alongside. These two figures differ in the value taken

for  $k$ , which provides some variety in the boundary condition on the right hand wall. It can be seen that for all values of  $J$ , the multigrid comes close to the analytic solution, but if errors of the order 0.01-0.1% are desired it is best to select  $J > 33$ .

### 5.6.2 Ion fluid tests

For the ion fluid component an appropriate test is to see how well it resolves the density in a planar sheath. A model 2D problem with an analytic solution has proved impossible to find, but this 1D test should suffice. As with the multigrid examination, the ion fluid code's effort at solving the ion density is plotted alongside the normalized error between this and the analytic solution in Fig. 5.12. To keep things more succinct I have opted not to cycle through different values of  $J$ . When using  $J = 129$ , the magnitude of the normalized error is typically 0.01-0.1%, the higher errors occurring at the right hand edge region and growing deeper into the sheath.

The reason the error is highest at the edge is because central difference methods cannot be applied at the domain boundary. Visually, the peculiar structure of the error in this region may look concerning, but keeping in mind the magnitude is small this is not a big issue. Just to be safe, to suppress any potential growth in the error, I will apply a smoothing function to the edge region.

### 5.6.3 Newton-Poisson tests

Now that the multigrid and ion fluid codes can be trusted, the Newton-Poisson solver can be examined by testing the entire algorithm, which is a combination of all three. To perform checks the test system will again be the planar sheath. Taking the computational box to have width 10cm and height 5cm and estimating a typical value of  $\frac{\partial \rho}{\partial \phi} \approx \frac{en_0}{\epsilon_0 \phi_W}$ , this would imply from (5.46) a suitable  $f < 0.3$ . In section 5.4.2, the convergence condition was only illustrated in 1D and so for completeness here the nature in 2D is shown in Fig 5.13. To prove that  $J$  has no bearing on the stability, two values  $J = 65$  and  $J = 129$  have been chosen. The solver is initiated with the values of the analytic result, but  $f$  is taken as 0.5 and so any slight deviation is expected to grow. Indeed, after only 10 or so cycles a slightly too high potential near the origin (i=9 in (a) and i=11 in (b)) is overcompensated for leaving it too low (i=10 and 12) and then subsequently higher (i=11 and 13) than it was in the first place marking the onset of a fatal divergence. The fact that with  $J = 65$  and  $J = 129$  the solution diverges in practically the same fashion demonstrates that the grid spacing,  $h$ , is not a relevant quantity in the analysis of Newton-Poisson convergence.

It is all very well demonstrating that the code is able to fail, even if I claimed that it would. Now it is necessary to show that by reducing  $f$ , convergence can be achieved and, what's more, this should occur when  $f \lesssim 0.3$  as determined above. To compare convergence properties the potential at a single point, somewhere near the mid-left at (2.5cm, 2.5cm), is plotted in Fig. 5.14. Figs. 5.14 (a) and 5.14 (b) correspond to the 2D plots in Figs. 5.13 (a) and 5.13 (b) and a third plot for  $J = 257$  has been included in

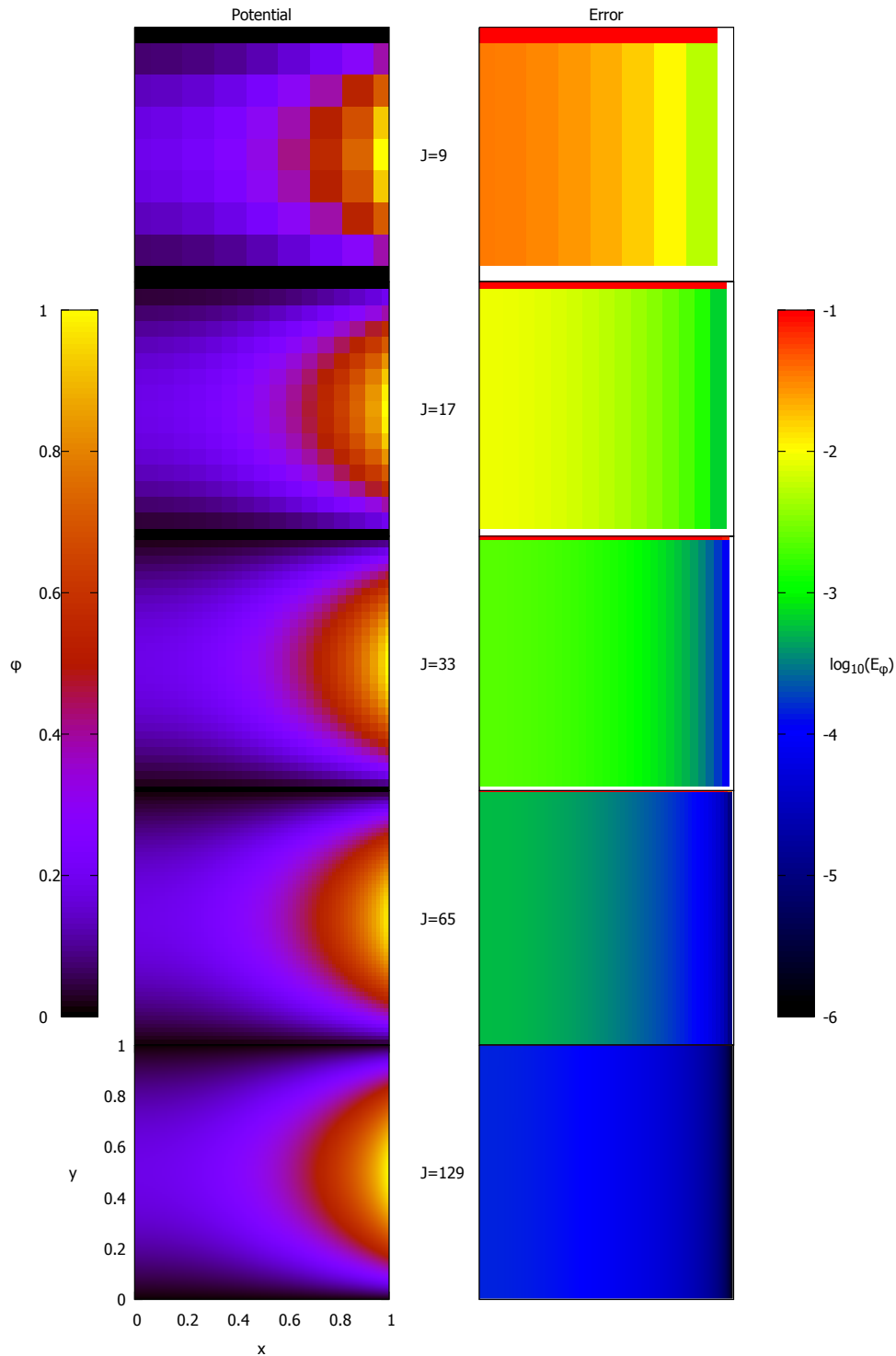


Figure 5.10: On the left are the multigrid solver's efforts at solving Laplace's equation (when  $k = 1$  in the third boundary condition) for increasing values of  $J$  and opposite are the normalized errors on a logarithmic scale. The increased error on axis probably results because a definite value of the potential is not known here, just the gradient.

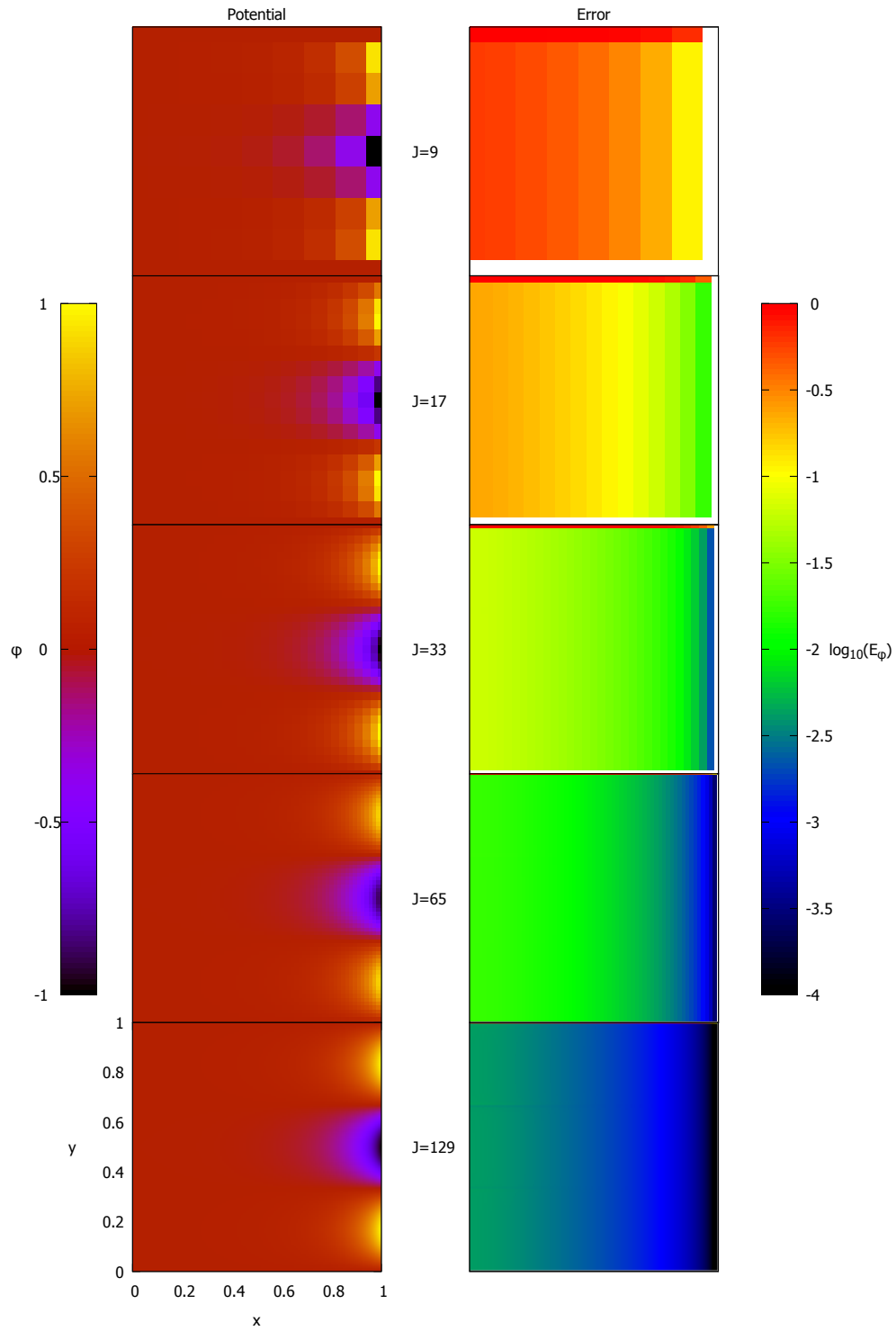
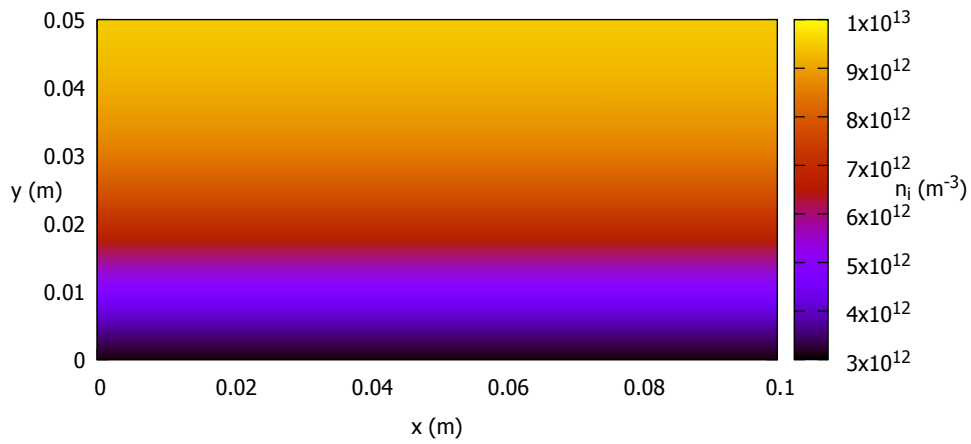
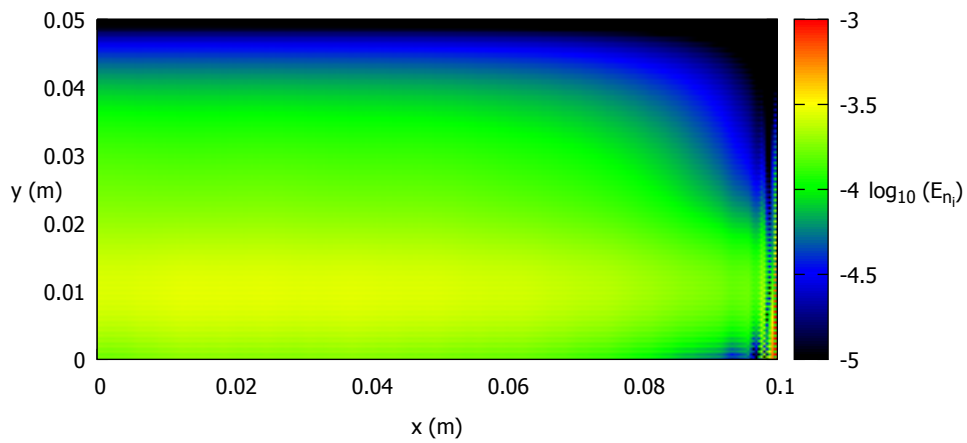


Figure 5.11: See caption for Fig. 5.10, in this case  $k = 3$ .



(a) Ion fluid code output given the potential profile of a planar sheath.



(b) Normalized error between (a) and the analytic solution on a logarithmic scale.

Figure 5.12: Analysis of ion density code error for the planar sheath. In this case  $J = 129$ .

(c) just to make extra clear that  $J$  has no influence as far as convergence or divergence is concerned. The onset of divergence at  $i \approx 10$  is replicated (although with  $f = 0.4$  rather than 0.5) and reassuringly, convergence occurs for  $f = 0.3$  and also for  $f = 0.2$  in fewer steps (probably because it is not so dangerously close to the expected  $f = 0.3$  borderline). Whilst making the grid finer can do nothing to help making the solution converge it does, of course, minimize the error of the final solution. This can be seen from the steady state values of the error, which are 0.1%, 0.02% and 0.007% for  $J$  values 65, 129 and 257 respectively.

## 5.7 Code Implementation

To recap the procedure of the code: At some given iteration (what constitutes an ‘iteration’ will be made concrete) the potential is calculated using the multigrid solver with the charge density taken from the previous iteration. From this potential the ion fluid solver and analytic electron densities are combined to find the newly implied charge density. A weighted sum of this charge density and the one from the previous iteration is to be fed to the next iteration. Thus, the performance of an iteration is the action of updating the charge density. This covers how the code proceeds, but it also requires a way to start and finish. The code is initialised with the potential profile of a planar sheath and ceases when the changes in potential between subsequent iterations is sufficiently small.

The language used is C++. For the multigrid algorithm handy example code can be found in Numerical Recipes: The Art of Scientific Computing [108, p. 1073], though this is for the case of a square domain in Cartesian coordinates with  $\phi = 0$  across the boundary. The way this code efficiently allocates memory is recycled in my code but it otherwise required major modifications to deal with the boundary conditions and coordinate system tackled here. There is also the less difficult modification in going from a square to rectangular domain.

The demands of the code are not great and it can be run on a desktop computer. For the grid dimensions used ( $512 \times 1024$ ), each iteration of the code takes approximately a second with the majority of this taken by the multigrid solver. Typically the code required around a thousand iterations to reach convergence giving a typical runtime of no longer than 20 or so minutes.

## 5.8 Summary

To conclude, a sheath model has been proposed and three computational methods essential for its solving have been tested and deemed trustworthy. Now that the means are in place to tackle the problem, the reader may be pleased to learn that this marks the end of the departure from discussion of physics.

---

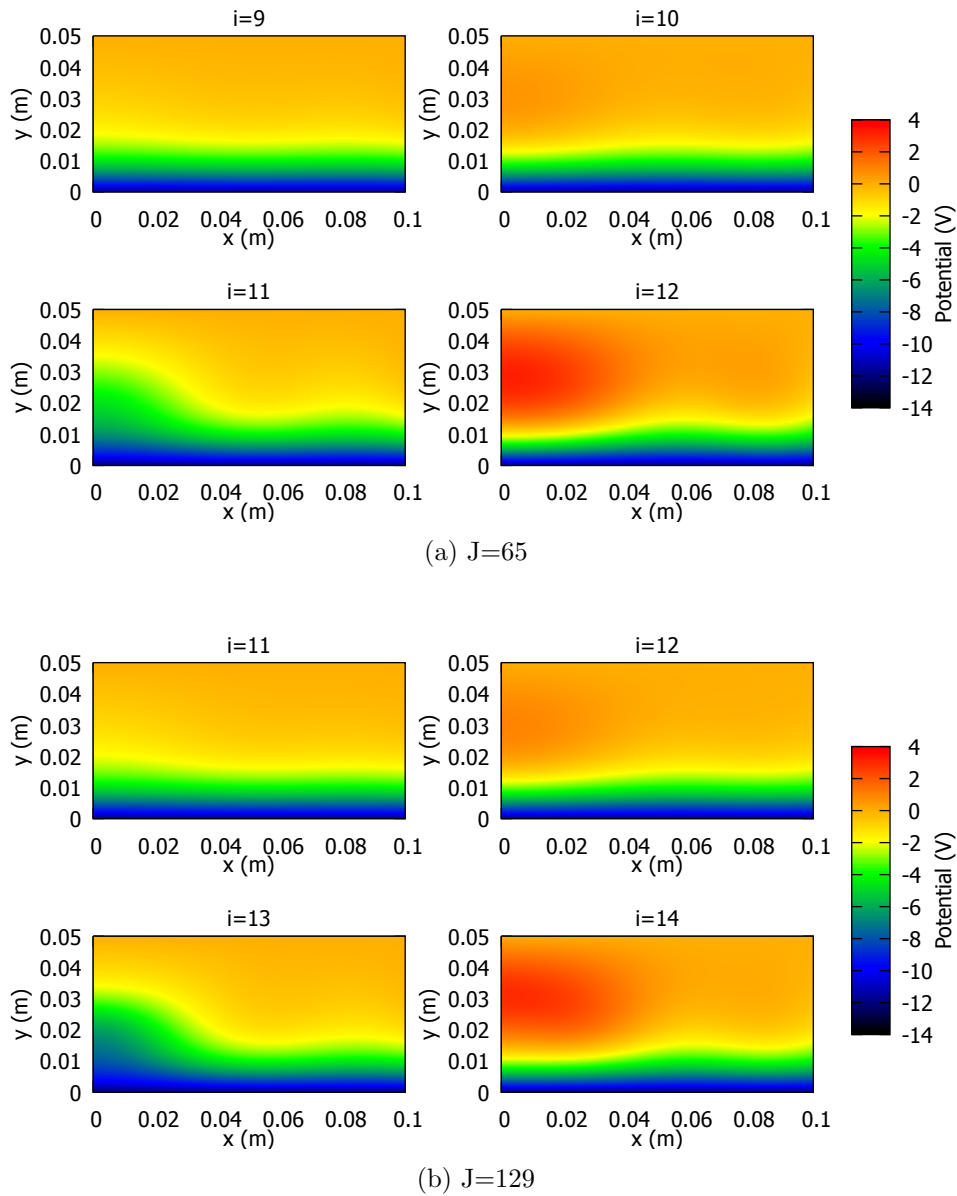


Figure 5.13: The Newton-Poisson solver is initiated on the analytic solution, but with  $f = 0.5$  which is too large. The divergence progressing through each iteration of the Newton-Poisson method,  $i$ , is shown. The fact that this is basically independent of  $J$  shows that it is futile to attempt to fix this numerical instability with finer grids (as might be an instinctive course of action).

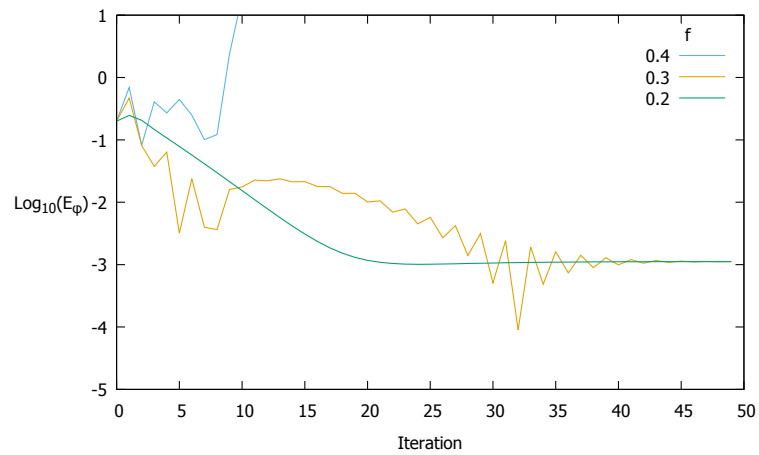
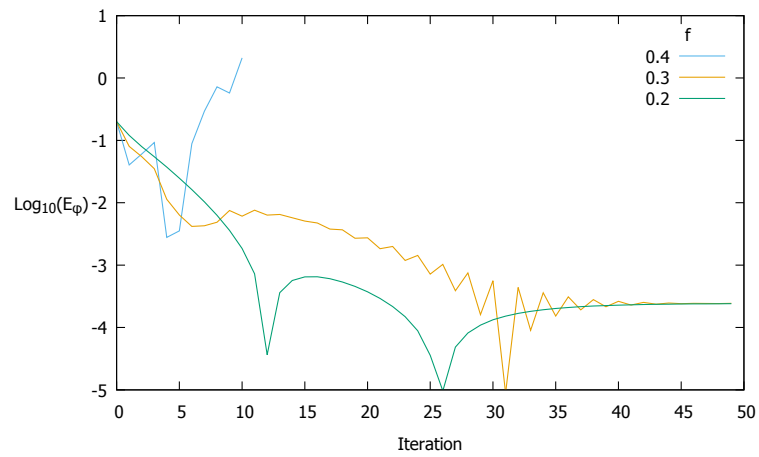
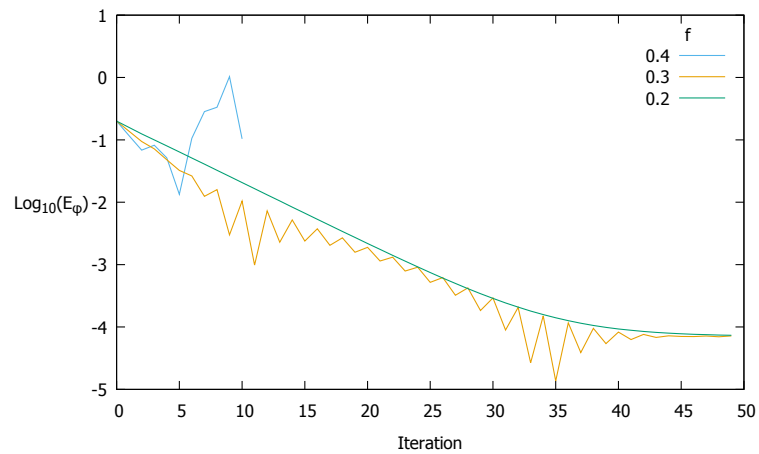
(a)  $J=65$ (b)  $J=129$ (c)  $J=257$ 

Figure 5.14: The solver is initialized with a potential 20% away from the solution. If  $f$  is low enough the solver converges and the error of the final value is improved with increasing  $J$ .



# 6 Sheath model results

## 6.1 Results

The code has been run for two sets of plasma parameters: the low density regime of Wang ( $n_0 = 1.5 \times 10^{13} \text{m}^{-3}$ ,  $T_e = 2.5 \text{eV}$ ) and the more typical discharge parameters of Dropmann ( $n_0 = 2.1 \times 10^{15} \text{m}^{-3}$ ,  $T_e = 4.9 \text{eV}$ ). The domain size was chosen such that increasing it any further yielded no discernible change in the results. This turned out to be  $15 \times 30 \text{cm}$  for Wang and  $2 \times 4 \text{cm}$  for Dropmann. Likewise, the grid spacing is the one which is small enough such that there is no reason to move to anything finer. This was ( $0.29 \text{mm} = 0.1 \lambda_{De}$ ) for Wang and ( $0.039 \text{mm} = 0.11 \lambda_{De}$ ) for Dropmann (where these are the respective Debye lengths for each experiment). The position of the magnet in the simulation is the same as in the experiments,  $12 \text{mm}$  below the electrode for Wang and  $4 \text{mm}$  below for Dropmann, as per Table 4.1, and the strategy was to explore values of magnetic moment of the same magnitude as the experiments and beyond. It turned out that magnetic fields comparable, but not quite equal, to the experiments are reached before the model breaks down, but the reasons why can be explained and are interesting.

### 6.1.1 Wang's parameters

The development of a radial space charge distribution can be seen in Fig. 6.1, where the sheath charge density is plotted for increasing magnetic moments. For  $\mathcal{M} = 4 \times 10^{-8} \text{T m}^3$  the charge density is fairly planar but as it is increased to  $8 \times 10^{-8} \text{T m}^3$  the electron depletion near to the wall leads to the appearance of a positive space charge of order  $0.5en_0$  at a radius of  $1.5 \text{cm}$  and height  $0.6 \text{cm}$  - in the absence of the magnet the space charge density would be approximately  $0.3en_0$  at this point. The effect of this positive space charge can be seen through the radial electric field (Fig. 6.2) which acts to attract negative particles to this region. The strength of this radial field reaches a maximum value of  $50 \text{V m}^{-1}$ , coinciding with the region of highest positive charge density and is about an order of magnitude less than the local vertical electric field which is  $540 \text{V m}^{-1}$ . Another effect this space charge has is that it repels the incoming sheath ions. The plot range is extended to show the development of a positive potential region high up in the sheath reaching a maximum of  $0.4 \text{V}$  (Fig. 6.3). The range of potentials is chosen as  $-0.4$  to  $0.4 \text{V}$  such as to concentrate attention on positive electric potentials.

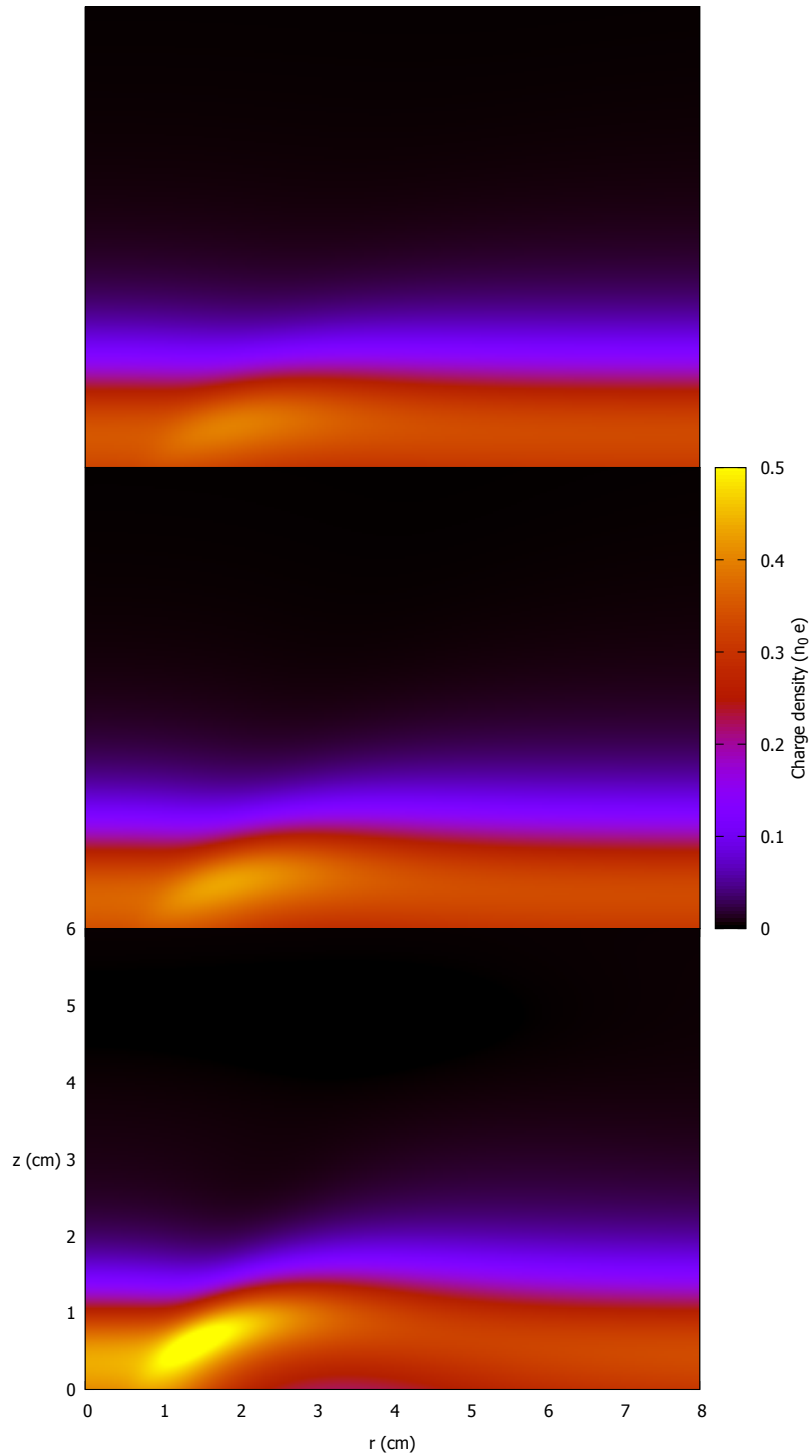


Figure 6.1: Space charge density normalised to that of the ions in the bulk plasma,  $en_0$ . From the top down, the magnetic moment is 4, 6 and  $8 (\times 10^{-8} \text{ T m}^3)$ .

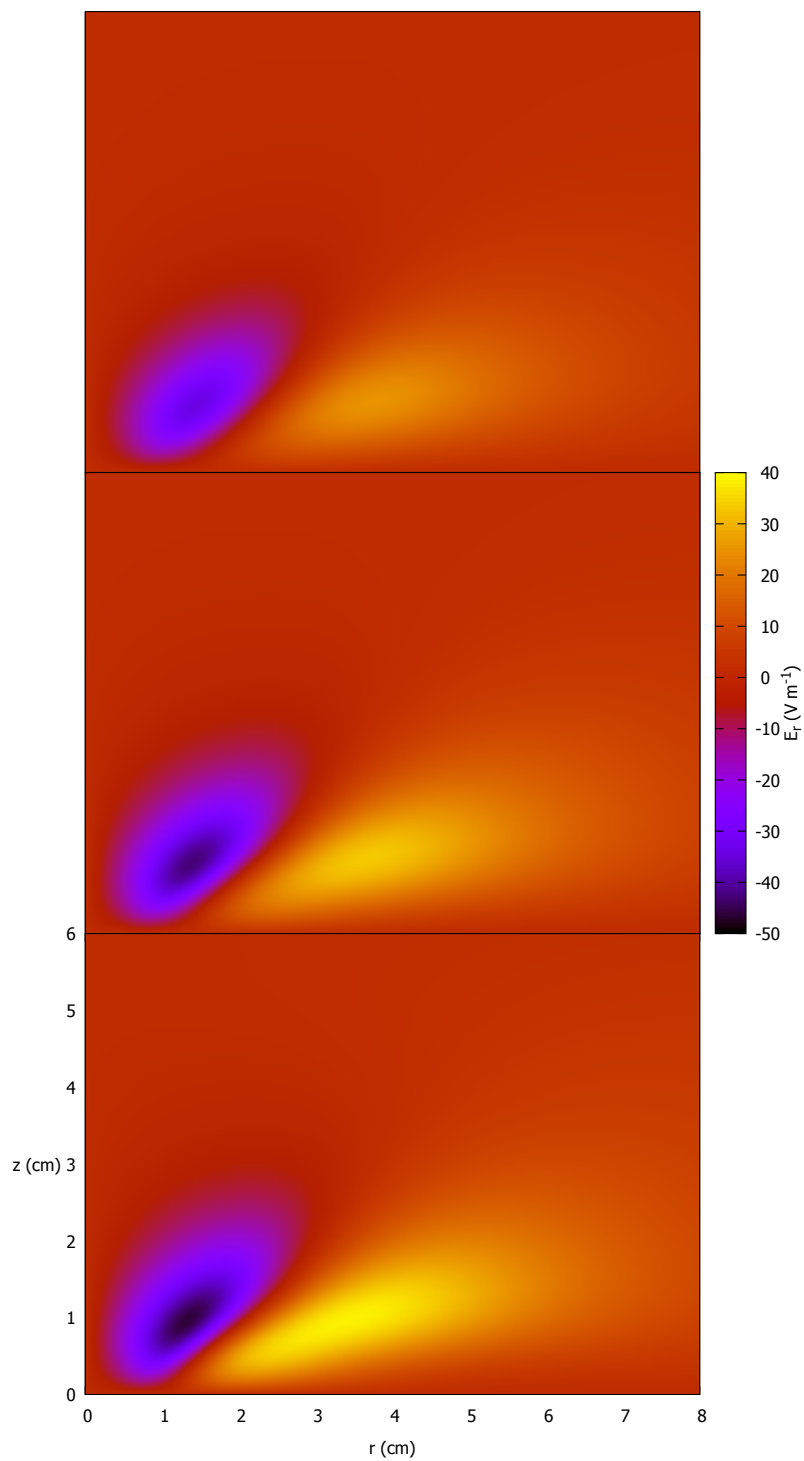


Figure 6.2: Radial electric field, from the top down, the magnetic moment is 4, 6 and 8 ( $\times 10^{-8} \text{T m}^3$ ).

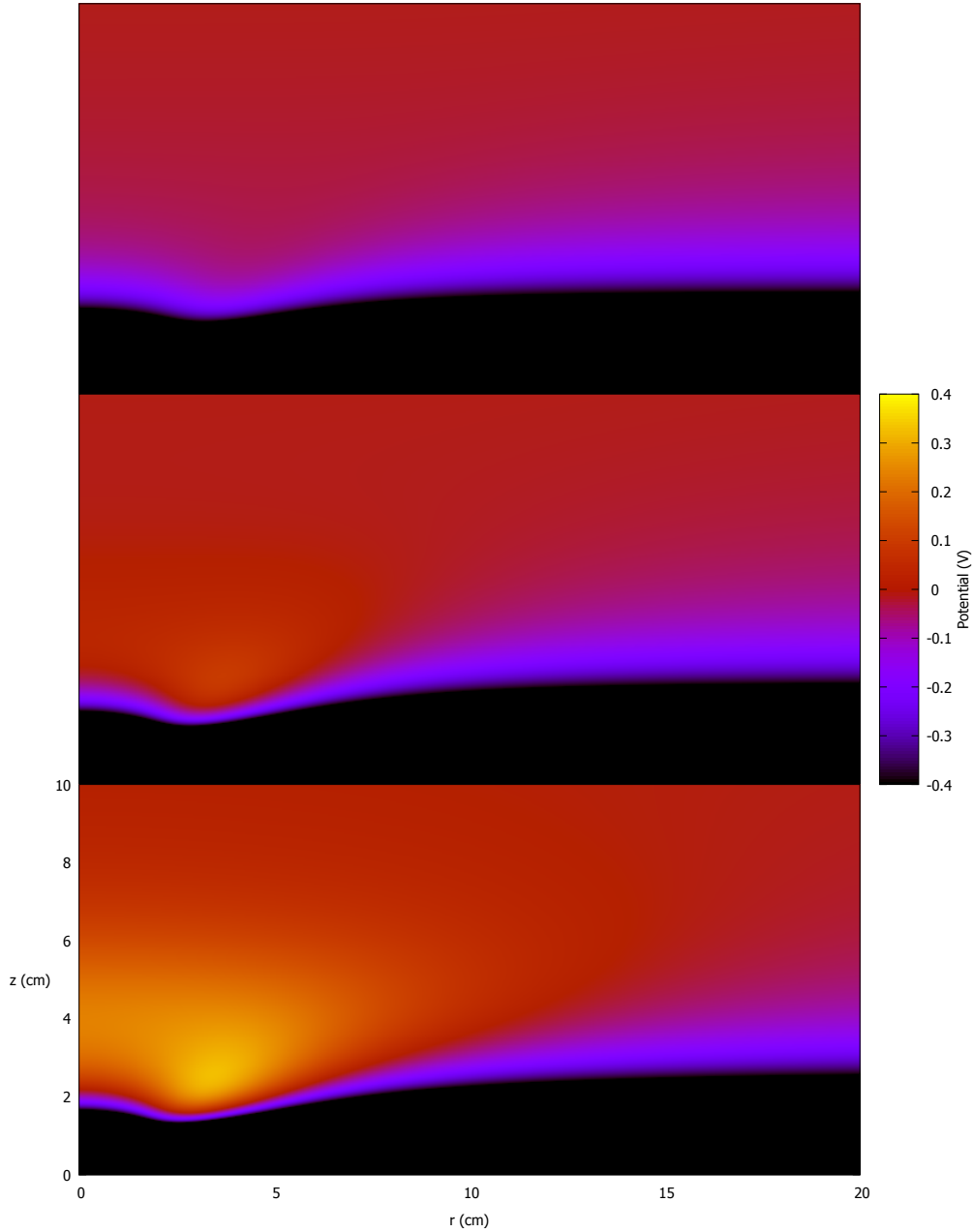


Figure 6.3: Electric potential, from the top down, the magnetic moment is 4, 6 and  $8 (\times 10^{-8} \text{T m}^3)$ . The vertical extent is extended to 10cm to capture the potential growth emerging at the sheath edge.

The maximum magnetic dipole moment (to 2.s.f) which the code could handle was  $\mathcal{M}_{\text{crit}}^W = 8.7 \times 10^{-8} \text{T m}^3$  which is a fraction 0.77 of the field used by Wang (see Table 4.1). The plasma properties for this particular value,  $\mathcal{M}_{\text{crit}}$ , are given in Fig. 6.4. Above this field strength, the ions begin to be reflected by the positive space charge and this results in failure of the fluid code which requires the ions to keep moving downwards. Whilst the potential drop in the sheath is 11.7V it only takes an increase of  $\phi_{\text{crit}} = \frac{1}{2} \frac{m_i v_B^2}{e} = 1.2 \text{V}$  to bring ions to rest. As seen in Fig. 6.4, the potential only reaches 0.5 V, which is

about half way to this limit, however the reason the code malfunctions is probably due to its iterative nature. Even if the solution it searches for does not contain  $\phi_{\text{crit}}$ , it will settle on this solution by successive overestimates and underestimates. If  $\phi$  is close enough to  $\phi_{\text{crit}}$  a guess can occur which is higher than  $\phi_{\text{crit}}$ , causing a fatal error of the fluid code. Ways to combat this will have to wait until the next section.

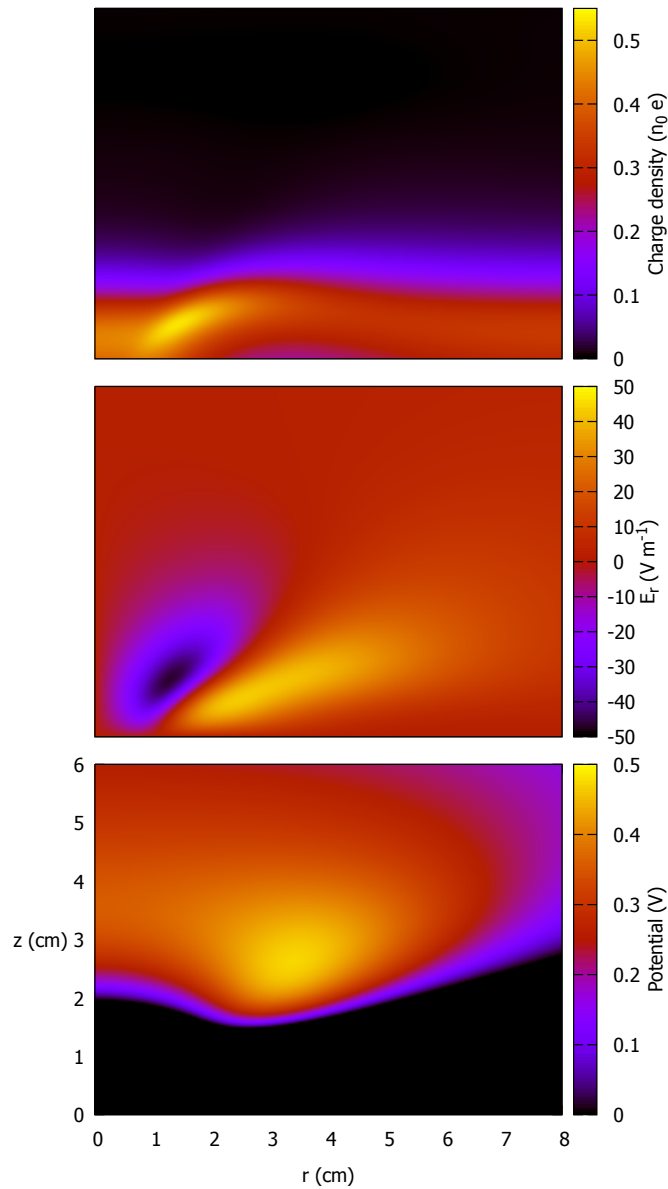


Figure 6.4: Sheath profiles for the plasma parameters of Wang and the strongest magnet that could be simulated,  $\mathcal{M} = \mathcal{M}_{\text{crit}}^W$ .

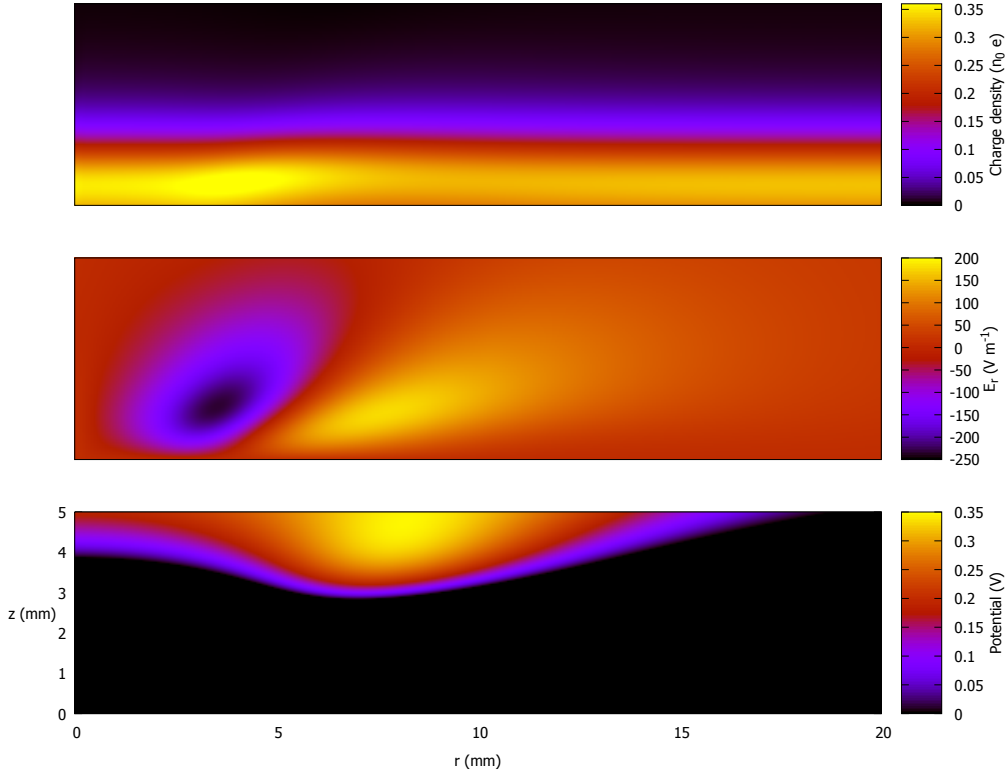


Figure 6.5: Sheath profiles for the plasma parameters of Dropmann and the strongest magnet that could be simulated,  $\mathcal{M} = \mathcal{M}_{\text{crit}}^D$ .

### 6.1.2 Dropmann's parameters

Now for results from the second set of parameters. The qualitative behaviour as the magnetic field is increased is the same here as for Wang and so I shall just present the sheath profile at one value of magnetic moment. It makes sense to again select the largest magnetic field that was possible to process,  $\mathcal{M} = \mathcal{M}_{\text{crit}}^D = 4 \times 10^{-9} \text{T m}^3$ , which is a fraction 0.26 that of the field used in Dropmann's experiment. The sheath profiles are plotted in Fig. 6.5. A potential difference of 2.45V is required to decelerate the ions to rest and so it is curious that the code should be caused to malfunction by potentials as small as 0.35V, but possible reasons why will, as before, be saved for later.

As a consequence of these weaker than hoped fields, the effects found here are not as pronounced as those for Wang. The charge density has a maximum of approximately  $0.37en_0$ , where it would otherwise have been  $0.32en_0$  without the magnet and the radial electric field in this region reaches  $240 \text{V m}^{-1}$ , an order of magnitude less than the local vertical field of  $7900 \text{V m}^{-1}$ . The closeness of the magnet to the plasma means that the magnetic lobe region remains strong for larger radii and this is the reason why the sheath profiles are more elongated in the radial direction than for Wang.

## 6.2 Analysis

Now to discuss what these results have to say on some of the burning topics in the fields of which these experiments are performed.

### 6.2.1 Ion reflection

Whilst the code ceases to operate before the regime where ions are reflected (or, at least, strongly deflected), the growth in potential near the sheath edge suggests that this will occur for magnetic fields not much stronger than those simulated. This would contradict Wang who, based on the fact that they are unmagnetized, assumed that ions pass through the sheath unaffected [74]. However, Zimmerman did observe reflected ion trajectories in his simulations [4] and, as will be seen shortly, my findings have common ground with Dropmann too.

It is interesting that this was found to happen with a conducting boundary as it was my initial expectation that ions would only be reflected by an insulating surface. My reasoning behind this is that in steady state an insulating boundary requires local currents to be zero. With the electron current severely depleted at the surface below the magnetic lobe region this patch must charge positively to repel the ions such that there is no total current. It turns out that for my simulations, the positive space charge is probably able to reflect ions without the need for surface charge, although, it is likely that an insulating boundary will enhance ion repulsion. Indeed, Dropmann concluded from his experiments that: “These [radial electric] fields significantly affect plasma ion trajectories, increasing the ion flux in certain regions and decreasing it in others, leaving portions of the surface of the glass plate shielded from the ion flux. Thus, the interaction of plasma electrons with a magnetic field can generate regions of changed electron density, creating strong electric fields that can alter the ion flow to a much greater extent than the pure interaction of these ions with the magnetic field alone would allow” [109]. What my simulations show is that this picture is probably correct, but that an insulating boundary is not necessary for strong ion deflection to occur.

### 6.2.2 Radial forces

It was radial electric fields which were postulated to lead to a void of dust forming on axis in dusty crystal experiments. Taking the recently solved sheath profile of Dropmann with a magnet of strength  $\mathcal{M} = \mathcal{M}_{\text{crit}}^D$  to best represent dusty crystal work, there is enough information to calculate the electric and ion drag forces on the grain. Ions can impart momentum to the grains in two ways, namely, direct impacts and Coulomb interaction, the total force being expressed as (derived in [110]),

$$\mathbf{F}_i = n_i m_i (\sigma_{\text{coll}} + \sigma_{\text{coul}}) v_i \mathbf{v}_i , \quad (6.1)$$

where the respective momentum collision cross sections for direct impacts (collection) and Coulomb collisions are

$$\sigma_{\text{coll}} = \pi r_d^2 \left( 1 - \frac{2e\phi_d}{m_i v_i^2} \right), \quad (6.2)$$

$$\sigma_{\text{coul}} = 2\pi b_0^2 \ln \left( \frac{b_0^2 + \lambda_{De}^2}{b_0^2 + b_c^2} \right), \quad (6.3)$$

with

$$b_0 = r_d \frac{e\phi_d}{m_i v_i^2}, \quad (6.4)$$

$$b_c = r_d \sqrt{1 - \frac{2e\phi_d}{m_i v_i^2}}. \quad (6.5)$$

Here I shall consider the radial component of (6.1), which is to be compared with the radial electric force, given simply as

$$F_{E,r} = Q_d E_r. \quad (6.6)$$

The dust grain potential (and thus its charge) will be assumed the same at all locations in the sheath. Solving for the OML potential with mono-energetic ions travelling at the Bohm speed (i.e. this is the dust potential at the sheath edge) gives a value of  $\phi_d = -19.1V$ . The dust grain diameter used by Dropmann is fairly typical at  $11.9\mu\text{m}$  and in conjunction with the grain potential this implies a charge of  $Q_d = -79000e$  (which is close to Dropmann's assumed charge of  $-10^5e$ ). The material used in most experiments for the dust is melamine formaldehyde which has a density of  $\rho_d = 1500\text{kg m}^{-3}$ , giving the mass of a dust grain at  $m_d = 1.3 \times 10^{-12}\text{kg}$ , requiring a vertical electric field to support it of magnitude  $E_z = \frac{m_d g}{Q_d} = 1030\text{V m}^{-1}$ . By inspection of the code output for the vertical field, this corresponds to a levitation height of about  $2.7\text{mm}$  above the lower electrode.

The profiles of the radial dust grain acceleration through the sheath and just at the levitation height are plotted in Fig. 6.6 (a) and (b) respectively. In this case, the electric force far exceeds that from the ions, leading to dust grain motion towards the region of positive space charge density. At the levitation height of the grains, Fig. 6.6 (b), this results in a stationary point at approximately  $r = 7.5\text{mm}$ . The maximum magnitude of the acceleration is approximately  $0.3g$ , which seems reasonable given that Dropmann observed maximum accelerations of  $4g$ , but with a magnetic moment 3.8 times greater than my simulation and with the contribution of the charged insulating surface also.

Another outstanding issue is that of the anomalous inward motion of the dust as observed by A. Dyson. To investigate this, I tried increasing the size of the dust grains as, since  $F_E \propto r_d$  and  $F_i \propto r_d^2$  (at least, for collection), one might expect this to work in the favour of the ions. Results are plotted in Fig. 6.7 and it is found that for dust diameters greater than approximately  $400\mu\text{m}$  (i.e.  $r_d > 200\mu\text{m}$ ), the ion drag exceeds the



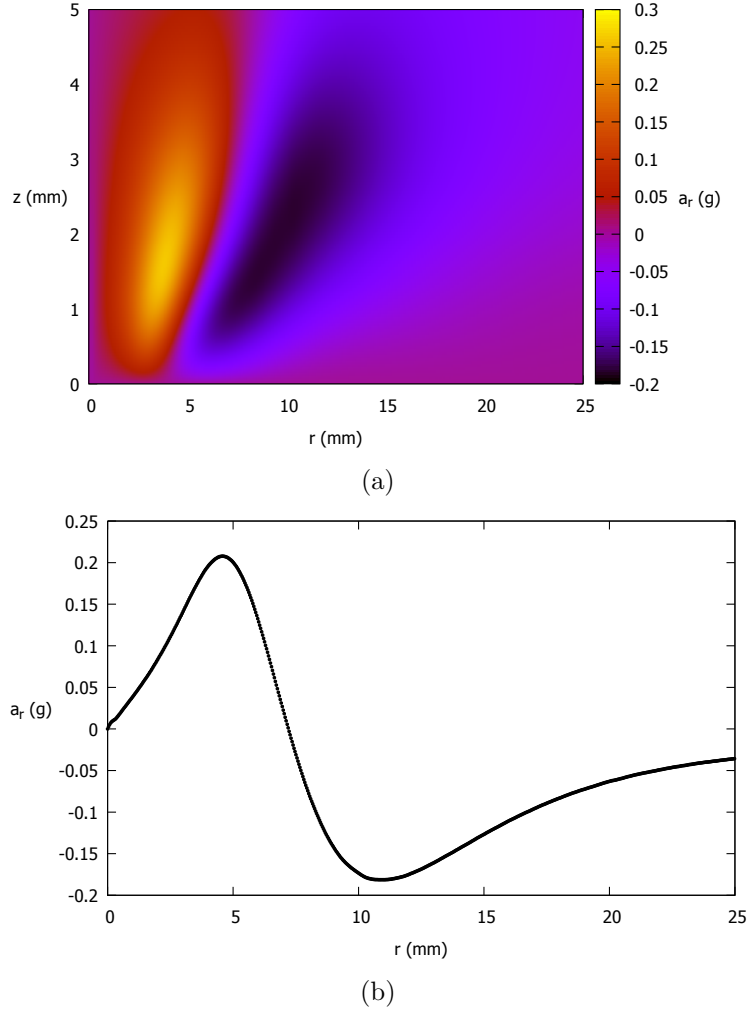


Figure 6.6: Radial acceleration (normalised to gravitational acceleration, g) in a Dropmann sheath for  $r_d = 5.95\mu\text{m}$ . The radial acceleration throughout (a) and at the estimated levitation height of  $2.7\text{mm}$  (b) is given.

electrostatic force and grains can be pushed towards the axis. However, at this diameter,  $m_d = 5.03 \times 10^{-8}\text{kg}$  and  $Q_d = 2.65 \times 10^6 e$  requiring an electric field of  $E_z = 10^6\text{V m}^{-1}$  to prevent the grain from falling to the surface. Fields of order  $10^4\text{V m}^{-1}$  resulted from my simulation, so it seems unlikely that a stable arrangement of grains of this size could be achieved. There is, of course, still the fact that the magnetic fields in my simulation are not as large as can be achieved in the laboratory and these findings do not rule out the possibility of a transition to domination of radial forcing by ions.

### 6.2.3 Azimuthal ion motion

One final point to address is the consequences radial electric fields might have for dusty crystal rotation. The neutral gas flow is viscous and thus momentum input from the ions is communicated throughout the gas. In other words, to know the neutral gas speed at some location it is essential to include the forcing from the ions everywhere. Now that the electric environment has been fully characterised, one can calculate the

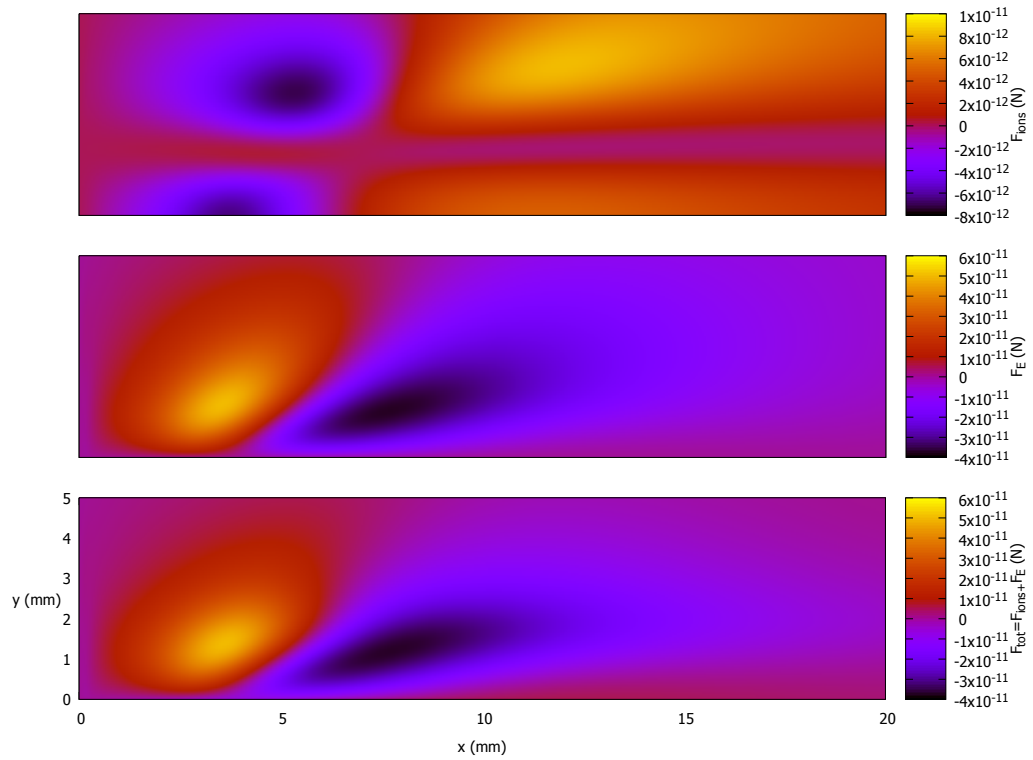
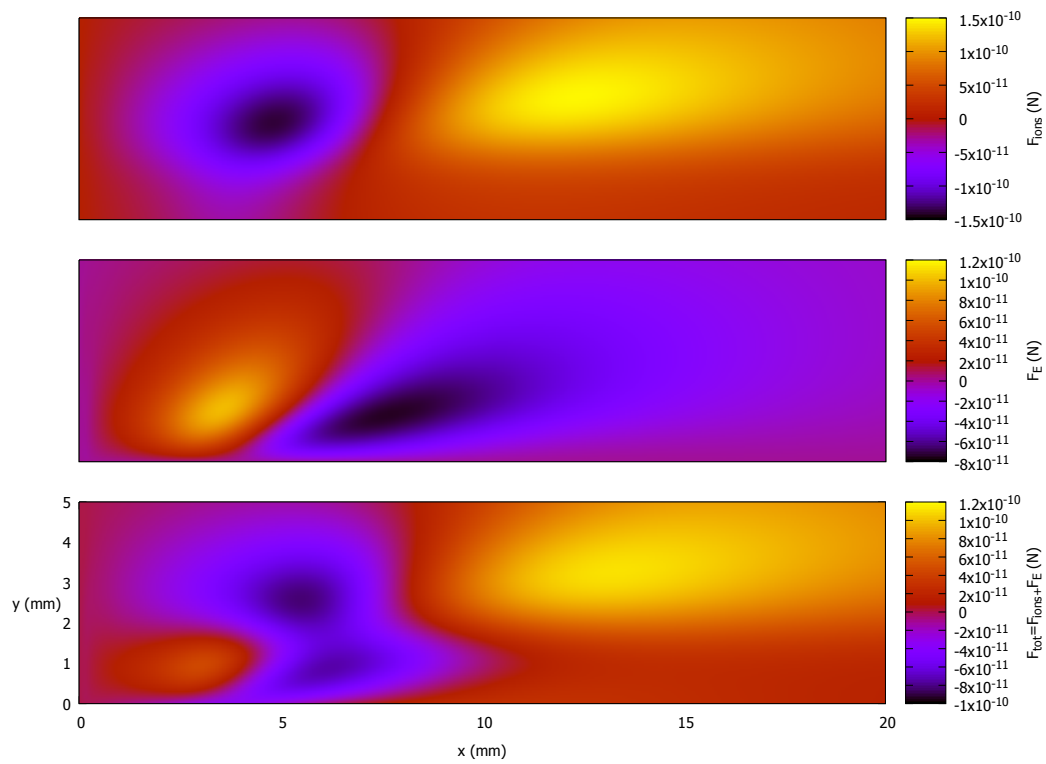
(a)  $r_d = 100\mu m$ (b)  $r_d = 200\mu m$ 

Figure 6.7: Continued overleaf.

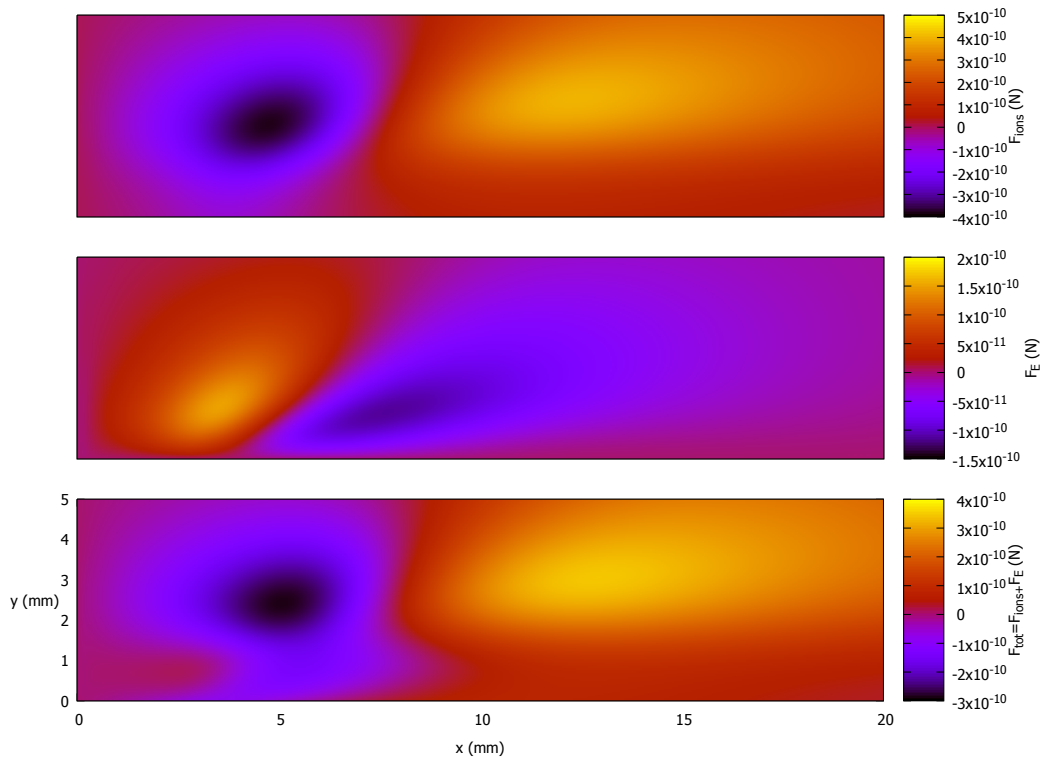
(c)  $r_d = 300\mu m$ 

Figure 6.7: Radial ion drag force,  $F_{\text{ions}}$ , electrostatic force,  $F_E$ , and their total,  $F_{\text{tot}}$ , for increasing values of dust grain radius. For  $r_d = 100\mu m$ , (a), the electric field dominates and for  $r_d = 300\mu m$ , (c), the ions do.

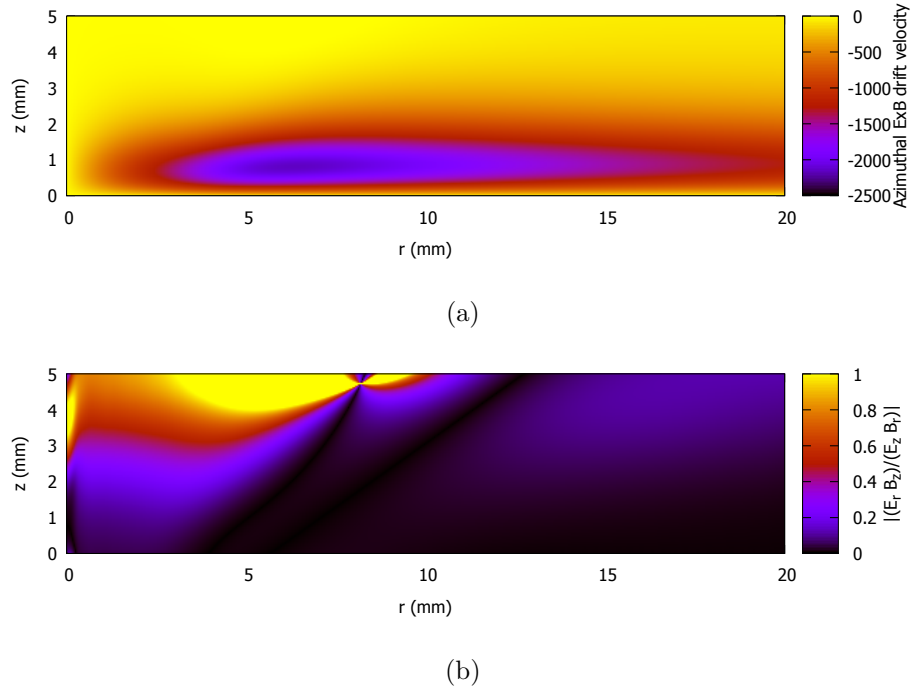


Figure 6.8:  $\mathbf{E} \times \mathbf{B}$  drift velocity (a) and ratio of contributions to  $\mathbf{E} \times \mathbf{B}$  (b)

$\mathbf{E} \times \mathbf{B}$  drift velocity and this is plotted in Fig. 6.8 (a). This shows clockwise (as viewed from above) rotation of the ions, reaching their maximum speeds deep in the sheath where the magnetic field is parallel to the surface and thus perpendicular to the strong vertical fields.

More specifically, one wishes to know if  $E_r$  has much effect. To find this out, the ratio of  $\frac{E_r B_z}{E_z B_r}$  is given in 6.8 (b). This shows that the  $E_r B_z$  contribution is significant as compared to  $E_z B_r$  near to the axis and higher up in the sheath. However, this is also an area where the azimuthal speed is relatively small and so whilst the  $E_r B_z$  term can be, in places, relatively large, its overall contribution is quite small. If higher fields could be achieved, the radial electric fields would be able to have more dominance, but as things stand it does not look like the rotation of a dusty crystal is affected by radial electric fields for these parameters.

# 7 Conclusions

In this chapter the key results of this work are collected together and suggestions for improvements and further directions of study are made.

## 7.1 Summary

This thesis documents my research on dust in magnetized plasmas for two limiting cases: where the dust leads to new collective effects and where the dust is a passenger in the plasma. These two regimes are defined in Chapter 1 as cases of “dusty plasma” and “dust in plasma” respectively and their importance is illustrated by the examples presented there. More specific context is provided at the start of each individual study, to make clear the objectives of each section and to what it could apply to. To provide some theoretical background, important results of dust and plasma physics are quoted or derived where necessary in Chapter 2.

The first study in Chapter 3 looks at the effect immobile dust grains have on two previously studied nonlinear plasma waves which propagate transversely and obliquely to the background magnetic field. For the transverse case the problem was fully solved by deriving the range of permissible velocities, plotted in Fig. 3.5, and the spatial profile of the wave, where an example can be seen in Fig. 3.6. For the oblique case, necessary restrictions on the wave direction and speed are derived by considering the conditions which permit low amplitude waves to grow, these regions of parameter space being plotted in Figs. 3.10 and 3.11. The work on oblique dusty waves is incomplete, however, as the additional restrictions imposed on large amplitude waves are not found.

The second study commences in Chapter 4, looking at plasma boundary interaction in the vicinity of a magnetic dipole with a view to shedding light on the properties of small scale lunar swirls and unexplained events in dusty crystal experiments. It is found that understanding the electron kinetics is crucial and, to this end, the remainder of the chapter is devoted to describing their behaviour and formulating a simple model to calculate their density. It is found that electrons are typically influenced within a characteristic distance,  $\Lambda$ , from the magnet, this distance being defined in equation (4.23) and the region of magnetization plotted in Fig. 4.7. This length could prove to be an important parameter to consider when aiming for self similar behaviour between laboratory swirls and real life ones. The most notable effect on the electrons is the appearance of inaccessible zones near to the lobe regions of the magnetic field as seen in Fig. 4.14, this being due to the magnetic field lines effectively capturing particles before they can penetrate any deeper, this explanation illustrated in Fig. 4.15. This insight

acts as the inspiration for a simple model to calculate electron densities (equations (4.59) - (4.61)), drawing parallels with a method employed to calculate the density near to an absorbing boundary which is introduced in section 2.1. Some confidence in my description of the electron behaviour is gained by the agreement of the theoretically predicted electron restricted zones and the regions of more positive electric potential in the experiments of Wang, Dropmann and Saitou (Fig. 4.18). However, the electron density model has yet to face more rigorous testing.

The remainder of the thesis studies the implications of this electron distribution on the sheath. The sheath model, which entails solving Poisson's equation in 2D self consistently with fluid ions and the analytic electrons of Chapter 4, is summarised at the start of Chapter 5 and requires the aid of computational methods which are outlined in the remainder of this chapter. The results of the code are given in Chapter 6 where my exploration of parameter space is sufficient to draw some interesting conclusions, but ultimately cut short by the failure of my code to deal with strong deflection of ions. It is still possible to infer that the effect of the electron restriction is to set up a space charge in the plasma strong enough to repel incoming ions as indicated by the development of a positive potential high in the sheath (Figs. 6.4 and 6.5). Calculations of the forces on dust grains indicate that a cloud of grains is likely to form a ring shape in agreement with experiments. For the parameters used in Chapter 6, it is found that dust grains could not be caused to move inwards whilst still being light enough to be levitated. The final brief exploration of azimuthal ion drifts indicate that the modified electric environment leads to only a slight alteration of the ion rotation speeds and thus probably does not greatly influence dust crystal rotation.

## 7.2 Future Work

On the solitary wave front, the most obvious extension is to complete the characterization of the oblique dusty solitary wave. This firstly entails finding the restrictions on the Mach number imposed by the maximum amplitude of the disturbance before particles are reflected. After this, deriving the spatial profiles of the wave would complete the picture. To perform both of these tasks, I am sure that numerical methods must be employed to deal with the integrals which arise in equations (3.73)-(3.76) due to the dust, however, some fresh eyes on this problem may be able to spot an analytical trick which has eluded me. Given that observational and experimental studies of waves of this type are not likely in the foreseeable future, simulation of these phenomena is necessary in order to test the validity of my findings. These may also shed light on the mysterious appearance of the two lengthscales of equation (3.82), which I have cautiously attributed to the compressive and rarefactive modes.

In terms of the dipole-boundary work, it would be very interesting to perform simulations of the electron trajectories to see exactly the electron kinetic behaviour. This would serve two purposes: firstly, to vindicate my conclusion that particles are effectively forbidden from penetrating any further than the field line which magnetises them

---

and secondly, it would provide a density profile to scrutinise my electron density model.

The sheath code is constructed to point to basic implications of the electron model and was able to perform this task, however, a Particle-in-Cell description of ion motion would be immune from the effects of ion reflection and thus would be a useful upgrade, allowing exploration of higher magnetic fields. Another possible route to ensuring the code converges is to lower the parameter  $f$ , introduced in section 5.4.1 as a way to make iterative steps less jumpy, which may have been too large for the simulations of Dropmann's parameters. A logical extension is to consider the case of magnetic dipoles oriented at an arbitrary angle to the surface, or perhaps, modification of the surface boundary condition to study insulating electrodes is another route one could take, however, this is easier said than done. It would also be an improvement to consider a more realistic magnetic field profile, rather than approximating it to lowest order as a dipole.

As for new directions, as opposed to improvements, one final suggestion is a marriage of the dipole-sheath with dust in plasma physics and comes from the fact that dust may also be magnetized, so that it is the grains themselves which have a magnetic dipole moment. Given that dipole magnetic fields have been observed to influence electron motion (and lead to electric fields which influence the ions), this could lead to the modified charging of, and interaction between, magnetized dust grains. The effects of electron kinetics will likely arise if the magnetic lengthscale,  $\Lambda$ , exceeds the dust grain radius,  $r_d$ . As a back-of-the-envelope calculation, the grain radius at which this becomes true is the solution to  $\sqrt{\frac{\mu_0 \mu_d e}{4\pi m_e v_e}} > r_d$ , where  $\mu_d$  is the magnetic moment of the dust. Now, before this is solved, the magnetic moment of a grain for a given magnetization density,  $M$ , will depend on the radius as  $\mu_d = \frac{4}{3}\pi r_d^3 M$  and so this results in the condition  $r_d > \sqrt{\frac{3m_e V}{\mu_0 M e}}$ .

Perhaps the best option, and also the easiest to to achieve in the near future, is to publish the work of this thesis and to make contact with the experimentalists whose results have provided much of my motivation. At present, the Dusty Plasma group at Imperial College is in contact with the Technological Plasmas Research group at Liverpool who have the capabilities to perform the types of experiments which feature in this thesis with a strong magnetic field of variable geometry. It would be incredibly useful to hear the thoughts and comments from those with backgrounds outside of the "theoretical and computational" which I have been providing.

# Appendices



# A Momentum and energy conservation in a dusty plasma

Macroscopic conservation laws for momentum and energy in a dusty plasma are derived which are useful for transverse and oblique solitary waves, both with and without dust. The geometry used here is the same as for the waves: gradients are only in the  $x$  direction and particles are free to move in  $x$ ,  $y$  and  $z$ . The equations of motion of the electrons and ion are,

$$m_e u_e \frac{du_e}{dx} = -e(v_e B_z - w_e B_y + E_x) , \quad (\text{A.1})$$

$$m_e u_e \frac{dv_e}{dx} = -e(w_e B_{x0} - u_e B_z + E_y) , \quad (\text{A.2})$$

$$m_e u_e \frac{dw_e}{dx} = -e(u_e B_y - v_e B_{x0}) \quad (\text{A.3})$$

and

$$m_i u_i \frac{du_i}{dx} = e(v_i B_z - w_i B_y + E_x) , \quad (\text{A.4})$$

$$m_i u_i \frac{dv_i}{dx} = e(w_i B_{x0} - u_i B_z + E_y) , \quad (\text{A.5})$$

$$m_i u_i \frac{dw_i}{dx} = e(u_i B_y - v_i B_{x0}) . \quad (\text{A.6})$$

The three components of Ampère's law are

$$\frac{dB_x}{dx} = 0 , \quad (\text{A.7})$$

$$\frac{dB_y}{dx} = \mu_0 e(n_i w_i - n_e w_e) , \quad (\text{A.8})$$

$$\frac{dB_z}{dx} = \mu_0 e(n_e v_e - n_i v_i) . \quad (\text{A.9})$$

and quasineutrality for a dusty plasma is

$$Z_d n_d + n_i - n_e = 0 , \quad (\text{A.10})$$

where one can take  $Z_d = 0$  to recover the results for a dust-free plasma.

## A.1 Momentum

### A.1.1 $x$ direction

Taking the sum of  $n_e \times$  (A.1) and  $n_i \times$  (A.4),

$$m_e n_e u_e \frac{du_e}{dx} + m_i n_i u_i \frac{du_i}{dx} = e(n_i v_i - n_e v_e) B_z + e(n_i w_i - n_e w_e) B_y + e(n_i - n_e) E_x \quad (\text{A.11})$$

and then substituting in (A.8), (A.9) and (A.10) gives

$$m_e n_e u_e \frac{du_e}{dx} + m_i n_i u_i \frac{du_i}{dx} = -\frac{B_z}{\mu_0} \frac{dB_z}{dx} + \frac{B_y}{\mu_0} \frac{dB_y}{dx} - e Z_d n_d E_x . \quad (\text{A.12})$$

Integration of this from  $x = x_0$  to  $x$  yields

$$m_e n_e u_e^2 + m_i n_i u_i^2 + \frac{B_y^2 + B_z^2}{2\mu_0} - e Z_d n_d \int_{x_0}^x E_x dx = \text{const.} \quad (\text{A.13})$$

### A.1.2 $y$ direction

The sum of  $n_e \times$  (A.2) and  $n_i \times$  (A.5) is

$$m_e n_e u_e \frac{dv_e}{dx} + m_i n_i u_i \frac{dv_i}{dx} = e(n_i w_i - n_e w_e) B_{x0} + e u_0 (n_{e0} - n_{i0}) B_z + e(n_i - n_e) E_y \quad (\text{A.14})$$

and substitution of (A.8) and (A.10) gives

$$m_e n_e u_e \frac{dv_e}{dx} + m_i n_i u_i \frac{dv_i}{dx} = \frac{B_{x0}}{\mu_0} \frac{dB_y}{dx} + e Z_d n_d (u_0 B_z - E_y) , \quad (\text{A.15})$$

which becomes, after integration,

$$u_0 (m_e n_{e0} v_e + m_i n_{i0} v_i) - \frac{B_{x0} B_y}{\mu_0} + e Z_d n_d \int_{x_0}^x (E_y - u_0 B_z) dx = \text{const.} \quad (\text{A.16})$$

### A.1.3 $z$ direction

The sum of  $n_e \times$  (A.3) and  $n_i \times$  (A.6) is

$$m_e u_e n_e \frac{dw_e}{dx} + m_i u_i n_i \frac{dw_i}{dx} = e(n_e v_e - n_i v_i) B_{x0} + e u_0 (n_{i0} - n_{e0}) B_y \quad (\text{A.17})$$

and substitution of (A.9) and (A.10) gives

$$m_e u_e n_e \frac{dw_e}{dx} + m_i u_i n_i \frac{dw_i}{dx} = \frac{B_{x0}}{\mu_0} \frac{dB_z}{dx} - Z_d n_d e u_0 B_y , \quad (\text{A.18})$$

which is integrated as before to get

$$m_e n_{e0} u_0 w_e + m_i n_{i0} u_0 w_i - \frac{B_{x0} B_z}{\mu_0} + Z_d n_d e u_0 \int_{x_0}^x B_y dx = \text{const.} \quad (\text{A.19})$$

## A.2 Energy

To start, take the sum of  $n_e u_e \times$  (A.1) and  $n_i u_i \times$  (A.4)

$$\begin{aligned} m_e n_e u_e^2 \frac{du_e}{dx} + m_i n_i u_i^2 \frac{du_i}{dx} &= e(n_i u_i v_i - n_e u_e v_e) B_z \\ &+ e(n_e u_e w_e - n_i u_i w_i) B_y + e u_0 (n_{i0} - n_{e0}) E_x, \end{aligned} \quad (\text{A.20})$$

then, the sum of  $n_e v_e \times$  (A.2) and  $n_i v_i \times$  (A.5)

$$\begin{aligned} m_e n_e u_e v_e \frac{dv_e}{dx} + m_i n_i u_i v_i \frac{dv_i}{dx} &= e(n_i v_i w_i - n_e v_e w_e) B_{x0} \\ &+ e(n_e u_e v_e - n_i u_i v_i) B_z + e(n_i u_i v_i - n_e u_e v_e) E_y \end{aligned} \quad (\text{A.21})$$

next,  $n_e w_e \times$  (A.3) and  $n_i w_i \times$  (A.6)

$$\begin{aligned} m_e n_e u_e w_e \frac{dw_e}{dx} + m_i n_i u_i w_i \frac{dw_i}{dx} &= e(n_i u_i w_i - n_e u_e w_e) B_y \\ &+ e(n_e w_e v_e - n_i w_i v_i) B_{x0}. \end{aligned} \quad (\text{A.22})$$

and finally the subsequent sum of (A.20) (A.21) and (A.22) involves cancellation of many terms on the RHS. With the substitution of (A.9) and (A.10), this becomes

$$n_e u_e \frac{dK_e}{dx} + n_i u_i \frac{dK_i}{dx} = -\frac{1}{\mu_0} E_y \frac{dB_z}{dx} - Z_d n_d e u_0 E_x. \quad (\text{A.23})$$

where  $K_e = \frac{1}{2} m_e (u_e^2 + v_e^2 + w_e^2)$  and  $K_i = \frac{1}{2} m_i (u_i^2 + v_i^2 + w_i^2)$ . Finally, integration of this yields

$$\begin{aligned} \frac{1}{2} m_e n_e u_e (u_e^2 + v_e^2 + w_e^2) + \frac{1}{2} m_i n_i u_i (u_i^2 + v_i^2 + w_i^2) \\ + \frac{E_y B_z}{\mu_0} + Z_d n_d e u_0 \int_{x_0}^x E_x dx = \text{const.} \end{aligned} \quad (\text{A.24})$$

## A.3 Summary

Four equations have been derived which correspond to conservation of energy and three components of momentum and are collected here:

$$m_e n_e u_e^2 + m_i n_i u_i^2 + \frac{B_y^2 + B_z^2}{2\mu_0} - eZ_d n_d \int_{x_0}^x E_x dx = \text{const.} \quad (\text{A.25})$$

$$m_e n_e u_e v_e + m_i n_i u_i v_i - \frac{B_{x0} B_y}{\mu_0} + eZ_d n_d \int_{x_0}^x (E_y - u_0 B_z) dx = \text{const.} \quad (\text{A.26})$$

$$m_e n_e u_e w_e + m_i n_i u_i w_i - \frac{B_{x0} B_z}{\mu_0} + Z_d n_d e u_0 \int_{x_0}^x B_y dx = \text{const.} \quad (\text{A.27})$$

$$\begin{aligned} \frac{1}{2} m_e n_e u_e (u_e^2 + v_e^2 + w_e^2) + \frac{1}{2} m_i n_i u_i (u_i^2 + v_i^2 + w_i^2) \\ + \frac{E_y B_z}{\mu_0} + Z_d n_d e u_0 \int_{x_0}^x E_x dx = \text{const.} \end{aligned} \quad (\text{A.28})$$

## A.4 Electron inertia

It is claimed at the start of section 3.3 that electron inertia may be ignored for sufficiently oblique solitary waves and here a proof of the validity of this is given. This is not done on physical grounds, instead, I check when the results which follow from ignoring electron inertia are consistent with that assumption. The electron  $y$  momentum is given from (3.50) as:

$$p_e = m_e v_e = \frac{m_e u B_y}{B_{x0}}. \quad (\text{A.29})$$

If one neglects electron momentum (and considers the dust free case), the ion  $y$  momentum comes from (A.26) as

$$p_i = m_i v_i = \frac{B_{x0} B_y}{u_0 n_0 \mu_0} \quad (\text{A.30})$$

and equations (A.29) and (A.30) are consistent with each other so long as  $\frac{p_e}{p_i} \ll 1$ , thus requiring:

$$\cos^2 \theta \gg \frac{m_e u u_0 n_0 \mu_0}{B_0^2} \approx \frac{m_e}{m_i} \quad (\text{A.31})$$

where to reach the second equation, the Alfvén speed has been used as a typical value for  $u_0$  and  $u$ . Therefore, the ion inertia dominates for oblique propagation at angles less than  $\frac{\pi}{2} - \sqrt{\frac{m_e}{m_i}}$  (c.f. the first paragraph of section 3.3).

## B Zimmerman field configuration

It proved quicker to derive the magnetic field configuration of two antiparallel currents than to find the result, so I shall provide the working here. The system of coordinates used to describe two parallel wires separated by  $h$  carrying opposite currents of magnitude  $I$  is given in Fig. B.1. The magnetic field at a point  $(x, y)$  due to the current directed into the page is

$$\mathbf{B}_1 = \frac{\mu_0 I}{2\pi r_1} (\sin(\theta_1)\hat{\mathbf{x}} - \cos(\theta_1)\hat{\mathbf{y}}) , \quad (\text{B.1})$$

and the outward current contributes

$$\mathbf{B}_2 = \frac{\mu_0 I}{2\pi r_2} (-\sin(\theta_2)\hat{\mathbf{x}} - \cos(\theta_2)\hat{\mathbf{y}}) . \quad (\text{B.2})$$

The angles can be written in terms of lengths and the coordinates as

$$\cos(\theta_1) = \frac{x + \frac{h}{2}}{r_1} \quad (\text{B.3})$$

$$\sin(\theta_1) = \frac{y}{r_1} \quad (\text{B.4})$$

$$\cos(\theta_2) = \frac{\frac{h}{2} - x}{r_2} \quad (\text{B.5})$$

$$\sin(\theta_2) = \frac{y}{r_2} \quad (\text{B.6})$$

giving the total field components

$$B_x = B_{1,x} + B_{2,x} = \frac{\mu_0 I}{2\pi} \left( \frac{1}{r_1^2} - \frac{1}{r_2^2} \right) y , \quad (\text{B.7})$$

$$B_y = B_{1,y} + B_{2,y} = -\frac{\mu_0 I}{2\pi} \left( \frac{x + \frac{h}{2}}{r_1^2} + \frac{\frac{h}{2} - x}{r_2^2} \right) . \quad (\text{B.8})$$

Using

$$r_1 = \sqrt{\left(x + \frac{h}{2}\right)^2 + y^2} , \quad (\text{B.9})$$

$$r_2 = \sqrt{\left(\frac{h}{2} - x\right)^2 + y^2} , \quad (\text{B.10})$$

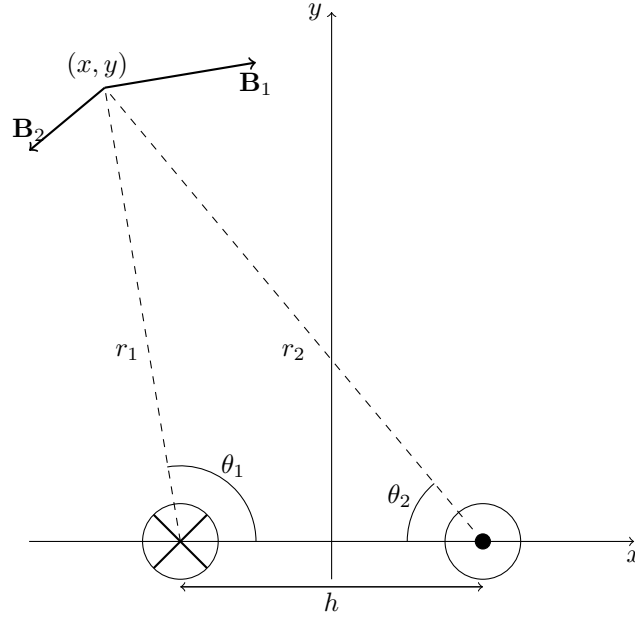


Figure B.1: Coordinate system to derive the magnetic field due to antiparallel currents.

and expanding (B.7) and (B.8) to lowest order in  $\frac{h}{x}$  and  $\frac{h}{y}$  gives

$$B_x \approx -\frac{\mu_0 I h}{2\pi} \frac{2xy}{(x^2 + y^2)^2}, \quad (\text{B.11})$$

$$B_y \approx \frac{\mu_0 I h}{2\pi} \frac{(x^2 - y^2)}{(x^2 + y^2)^2}. \quad (\text{B.12})$$

By inspection, this has the magnetic vector potential

$$\mathbf{A} = \frac{\mu_0 I h}{2\pi} \frac{x}{x^2 + y^2} \hat{\mathbf{z}} \equiv A_z(x, y) \hat{\mathbf{z}}. \quad (\text{B.13})$$

Finding the forbidden regions of this magnetic field is easy as it is in the form of a problem previously solved (section 4.4.2). The Lagrangian for a particle moving through this field is

$$\mathcal{L} = \frac{1}{2} m (v_x^2 + v_y^2 + v_z^2) + qv_z A_z, \quad (\text{B.14})$$

implying a conserved quantity,

$$p_0 = \frac{\partial \mathcal{L}}{\partial v_z} = mv_z + qA_z, \quad (\text{B.15})$$

which, for a particle of speed  $V$  incident from infinitely far away, has the range  $-mV < p_0 < mV$ . Rearranging (B.15) for  $v_z$  gives

$$v_z = \frac{p_0}{m} + \frac{qAx}{m(x^2 + y^2)} \quad (\text{B.16})$$

where  $\mathcal{A} = \frac{\mu_0 I h}{2\pi}$ . Particles are reflected when all of the velocity is taken by the  $z$  component

$$\pm V = \frac{p_0}{m} - \frac{q\mathcal{A}x}{m(x^2 + y^2)}, \quad (\text{B.17})$$

describing a locus of points

$$y = \sqrt{\frac{q\mathcal{A}x}{p_0 \pm mV} - x^2}. \quad (\text{B.18})$$

The contour of closest approach applies when the denominator of the first term in (B.18) is maximised, occurring when  $p_0 = mV$  and resulting in

$$y = \sqrt{\frac{q\mathcal{A}x}{2mV} - x^2}. \quad (\text{B.19})$$

For Zimmerman's simulations, the magnetic field at a height 125m on axis was  $3\mu\text{T}$  implying that  $\mathcal{A} = 4.69 \times 10^{-2} \text{T m}^2$ .

# C Cylindrical form of operators and boundary considerations

For simplicity, the central difference Laplacian, restriction and prolongation operators were presented in Cartesian coordinates. Here I give their cylindrical forms, which are actually used, and cover any issues which occur at the computational boundary.

## C.1 Laplacian

The Laplacian in cylindrical coordinates is

$$\nabla^2 f = \frac{1}{r} \frac{\partial f}{\partial r} + \frac{\partial^2 f}{\partial r^2} + \frac{\partial^2 f}{\partial z^2} , \quad (\text{C.1})$$

resulting in a central difference discrete form,

$$(\nabla^2 f)_{i,j}^h = \frac{f[i+1,j] - f[i-1,j]}{2ih^2} + \frac{f[i-1,j] + f[i+1,j] + f[i,j-1] + f[i,j+1] - 4f[i,j]}{h^2} . \quad (\text{C.2})$$

For the problems I solve, this only requires special considerations on axis, when  $i = 0$ . A first issue which arises is the undefined value of the first term of (C.1) due to the ratio of two zeroes. This can be resolved by using L'Hôpital's rule

$$\lim_{r \rightarrow 0} \frac{1}{r} \frac{\partial f}{\partial r} = \frac{\left( \frac{\partial^2 f}{\partial r^2} \right)}{\left( \frac{\partial r}{\partial r} \right)} = \frac{\partial^2 f}{\partial r^2} , \quad (\text{C.3})$$

thus giving

$$\nabla^2 f(0, z) = 2 \frac{\partial^2 f}{\partial r^2} + \frac{\partial^2 f}{\partial z^2} , \quad (\text{C.4})$$

which has a finite difference form (substituting  $i = 0$ )

$$(\nabla^2 f)_{0,j}^h = \frac{2f[-1,j] + 2f[1,j] + f[0,j-1] + f[0,j+1] - 4f[0,j]}{h^2} . \quad (\text{C.5})$$

This demonstrates the second issue in that grid points  $f[-1, j]$  are called for which do not exist. One could resort to forward differences in  $r$  to avoid this problem but there is a better solution. The way around this is to realise that due to azimuthal symmetry, in passing from  $r = ih$  through  $r = 0$  to the other side, one is not actually at  $r = -ih$



but at  $r = ih$ . Therefore, when  $i = 0$ , one can take the ‘ghost points’  $f[-1, j] = f[1, j]$ . This gives the Laplacian at  $r = 0$  as

$$(\nabla^2 f)_{0,j}^h = \frac{4f[1, j] + f[0, j-1] + f[0, j+1] - 4f[0, j]}{h^2}. \quad (\text{C.6})$$

## C.2 Restriction and prolongation

The job of these operators is to provide the correct weightings of points which come from different regions of  $z$  and  $r$ . Since the coordinate  $z$  is unchanged from Cartesian to cylindrical, the weighting of elements in the  $z$  direction is unchanged and I shall just mention the corrections one has to make for radial effects.

### C.2.1 Prolongation

Consider in cylindrical coordinates a fine grid point,  $f$ , which is at a radius,  $r$ , falling half way between two coarse grid points,  $F_1, F_2$ . The coarse grid points are located at  $r - h$  and  $r + h$ , their contribution to the fine grid point is weighted by the areas they occupy between themselves and  $f$ , given as  $A_1$  and  $A_2$  respectively in Fig. C.1:

$$f = \frac{A_1 F_1 + A_2 F_2}{A_1 + A_2}. \quad (\text{C.7})$$

The areas are given by

$$A_1 = \pi r^2 - \pi(r - h)^2 = \pi h(2r - h) \quad (\text{C.8})$$

$$A_2 = \pi(r + h)^2 - \pi r^2 = \pi h(2r + h) \quad (\text{C.9})$$

and so the weighted average of  $F_1$  and  $F_2$  gives

$$f = \frac{(2r - h)f_1 + (2r + h)f_2}{4r}. \quad (\text{C.10})$$

For large radii, this reduces to a Cartesian prolongation operator, where  $F_1$  and  $F_2$  have equal weighting.

### C.2.2 Restriction

In much the same way, consider a coarse grid point,  $F$ , at  $r$  with fine grid points,  $f_1$  at  $r - h$ ,  $f_3$  at  $r + h$  and  $f_2$  on top of it at  $r$ . These three points occupy areas

$$A_1 = \pi \left( r - \frac{h}{2} \right)^2 - \pi (r - h)^2 = \pi h \left( r - \frac{3h}{4} \right), \quad (\text{C.11})$$

$$A_2 = \pi \left( r + \frac{h}{2} \right)^2 - \pi \left( r - \frac{h}{2} \right)^2 = 2\pi h r, \quad (\text{C.12})$$

$$A_3 = \pi (r + h)^2 - \pi \left( r + \frac{h}{2} \right)^2 = \pi h \left( r + \frac{3h}{4} \right), \quad (\text{C.13})$$

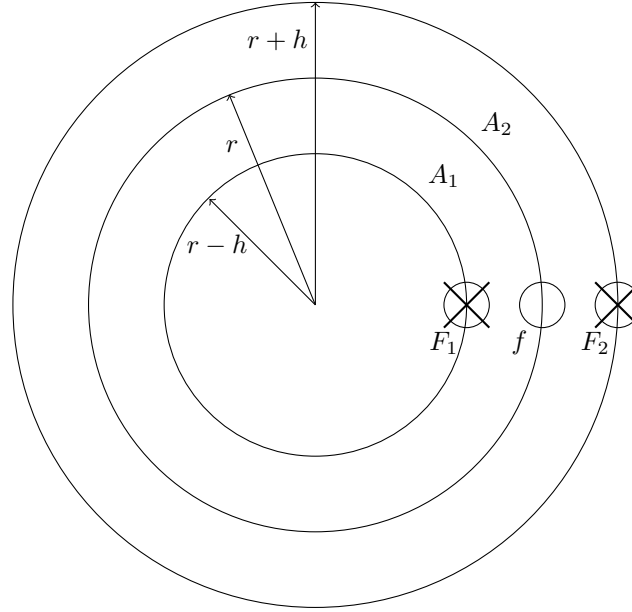


Figure C.1: Contribution of coarse grid points (crosses)  $F_1$  and  $F_2$  to the fine grid point (circle)  $f$  is weighted by the areas  $A_1$  and  $A_2$ .

and thus

$$\begin{aligned} F &= \frac{A_1 f_1 + A_2 f_2 + A_3 f_3}{A_1 + A_2 + A_3} \\ &= \frac{\left(r - \frac{3h}{4}\right) f_1 + 2r f_2 + \left(r + \frac{3h}{4}\right) f_3}{4r} . \end{aligned} \quad (\text{C.14})$$

For large  $r$ , this reduces to the Cartesian (0.25, 0.5, 0.25) weighting. Restriction also requires special attention for  $r = 0$ . Picture that a coarse grid point at  $r = 0$  occupies the circular region of radius  $r = h$ , this area being shared between the fine grid points  $f_0$  and  $f_1$  as shown in Fig. C.2. The areas in this diagram are given by

$$A_1 = \pi h^2 - \pi \left(\frac{h}{2}\right)^2 = \frac{3\pi h^2}{4} , \quad (\text{C.15})$$

$$A_2 = \frac{\pi h^2}{4} , \quad (\text{C.16})$$

and so the weighted sum gives

$$\begin{aligned} F_0 &= \frac{A_1 f_0 + A_2 f_1}{A_1 + A_2} \\ &= \frac{f_0 + 3f_1}{4} . \end{aligned} \quad (\text{C.17})$$

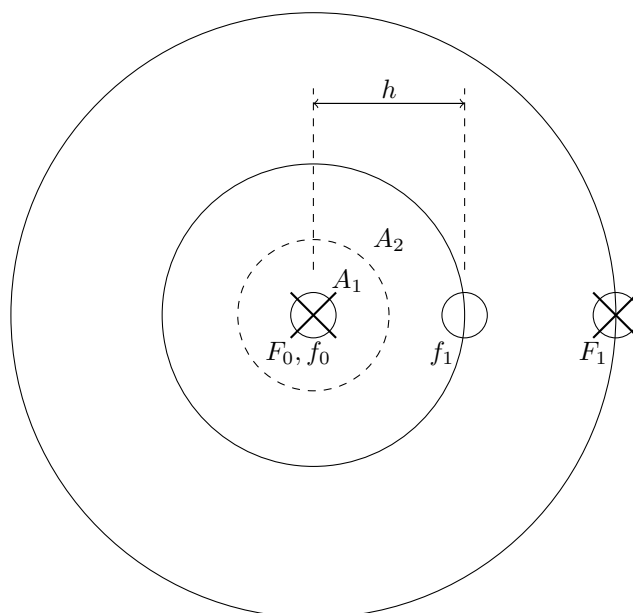


Figure C.2: Contribution of two fine grid points  $f_0$  and  $f_1$  to the coarse grid value on axis,  $F_0$ .

## D Ion fluid discretization

Here I give full expressions for how the ion density, radial velocity and vertical velocities are calculated in the finite difference scheme.

### D.1 Density, $n$

The equation to be discretised is

$$\frac{\partial n}{\partial z} = -\frac{1}{v_z} \left[ \frac{1}{r} \frac{\partial(rnv_r)}{\partial r} + \frac{n}{v_z} \left( F_z - v_r \frac{\partial v_z}{\partial r} \right) \right]. \quad (\text{D.1})$$

With values known in the rows of constant  $z$ ,  $j$  and  $j + 1$ , from central difference in  $z$  the density at a point below in the row  $j - 1$  is given as

$$n[i, j - 1] = n[i, j + 1] + \frac{2h}{v_z} \left[ \frac{1}{r} \frac{\partial(rnv_r)}{\partial r} + \frac{n}{v_z} \left( F_z - v_r \frac{\partial v_z}{\partial r} \right) \right], \quad (\text{D.2})$$

with  $i = 0, 1, 2, \dots, N$ . The exact calculation performed depends on whether the point falls on a boundary or not and these will now be presented.

#### D.1.1 $i \neq 0$ and $i \neq N$

For points not on boundaries, the  $r$  derivatives can be calculated with central differences. The two terms in square brackets on the RHS of (D.2) are given respectively as,

$$\frac{1}{r} \frac{\partial(rnv_r)}{\partial r} = \frac{1}{2hi} \left( (i + 1)n[i + 1, j]v_r[i + 1, j] - (i - 1)n[i - 1, j]v_r[i - 1, j] \right) \quad (\text{D.3})$$

$$\frac{n}{v_z} \left( F_z - v_r \frac{\partial v_z}{\partial r} \right) = \frac{n[i, j]}{v_z[i, j]} \left( F_z[i, j] - \frac{v_r[i, j] (v_z[i + 1, j] - v_z[i - 1, j])}{2h} \right). \quad (\text{D.4})$$

#### D.1.2 $i = 0$

For points at the centre, one needs to perform some simplifying algebra before discretising. The first term, (D.3), becomes

$$\begin{aligned} \frac{1}{r} \frac{\partial(rnv_r)}{\partial r} &= \frac{1}{r} \left( rn \frac{\partial v_r}{\partial r} + v_r \frac{\partial(rn)}{\partial r} \right) \\ &= n \frac{\partial v_r}{\partial r} + \frac{v_r n}{r} + v_r \frac{\partial n}{\partial r}. \end{aligned} \quad (\text{D.5})$$

At  $r = 0$ , the final term in (D.5) is eliminated since  $v_r(0) = 0$ . The second term can be found by L'Hôpital's rule as:

$$\lim_{r \rightarrow 0} \frac{v_r n}{r} = \frac{\left(\frac{\partial(v_r n)}{\partial r}\right)}{\left(\frac{\partial r}{\partial r}\right)} = \frac{\partial(v_r n)}{\partial r}(0) = n \frac{\partial v_r}{\partial r} \quad (\text{D.6})$$

where, in the last step,  $v_r(0) = 0$  has been used. Therefore, the first term of (D.2) becomes:

$$\frac{1}{r} \frac{\partial(r n v_r)}{\partial r}(0) = 2n \frac{\partial v_r}{\partial r} \quad (\text{D.7})$$

To discretise this, a forward difference method must be used:

$$\frac{1}{r} \frac{\partial(r n v_r)}{\partial r}(0) = 2n[i, j] \frac{(v_r[1, j] - v_r[0, j])}{h} = \frac{2n[i, j] v_r[1, j]}{h} \quad (\text{D.8})$$

The second term in the square brackets of (D.2) becomes after discretization and taking  $v_r = 0$ ,

$$\frac{n}{v_z} \left( F_z - v_r \frac{\partial v_z}{\partial r} \right) = \frac{n F_z}{v_z} = \frac{n[0, j] F_z[0, j]}{v_z[0, j]} . \quad (\text{D.9})$$

### D.1.3 $i = N$

At points on the right hand boundary, one must use backwards differences to evaluate derivatives. In this case the two terms I've been previously deriving are given by

$$\frac{1}{r} \frac{\partial(r n v_r)}{\partial r} = \frac{1}{hN} \left( N n[N, j] v_r[N, j] - (N - 1) n[N - 1, j] v_r[N - 1, j] \right) , \quad (\text{D.10})$$

$$\frac{n}{v_z} \left( F_z - v_r \frac{\partial v_z}{\partial r} \right) = \frac{n[N, j]}{v_z[N, j]} \left( F_z[N, j] - \frac{v_r[N, j] (v_z[N, j] - v_z[N - 1, j])}{h} \right) . \quad (\text{D.11})$$

## D.2 Radial velocity, $v_r$

In the same way as before, there is an equation requiring discretization:

$$\frac{\partial v_r}{\partial z} = \frac{1}{v_z} \left( F_r - v_r \frac{\partial v_r}{\partial r} \right) , \quad (\text{D.12})$$

and this will depend on the radius at which this is evaluated. To start, after central difference in  $z$ , the progression of  $v_r$  as one moves downwards is given by

$$v_r[i, j - 1] = v_r[i, j + 1] - 2h \frac{1}{v_z} \left( F_r - v_r \frac{\partial v_r}{\partial r} \right) . \quad (\text{D.13})$$

### D.2.1 $i \neq 0$ and $i \neq N$

For points not on boundaries, central differenced are used to calculate derivatives. Equation (D.13) becomes

$$v_r[i, j - 1] = v_r[i, j + 1] - \frac{1}{v_z[i, j]} \left( F_r[i, j] - v_r[i, j] \frac{(v_r[i + 1, j] - v_r[i - 1, j])}{2h} \right) . \quad (\text{D.14})$$

### D.2.2 $i = 0$

By symmetry, the radial velocity on axis is given simply as

$$v_r[0, j] = 0 . \quad (\text{D.15})$$

### D.2.3 $i = N$

Radial derivatives for points on the outer boundary are evaluated using backwards differences,

$$v_r[i, j + 1] = v_r[i, j - 1] - \frac{1}{v_z[N, j]} \left( F_r[N, j] - v_r[N, j] \frac{(v_r[N, j] - v_r[N - 1, j])}{h} \right) . \quad (\text{D.16})$$

## D.3 Vertical velocity, $v_z$

The discretization process continues in identical fashion for  $v_z$ . The equation dictating the evolution of  $v_z$  is

$$\frac{\partial v_z}{\partial z} = \frac{1}{v_z} \left( F_z - v_r \frac{\partial v_z}{\partial r} \right) \quad (\text{D.17})$$

and with the  $z$  derivative derived from a central difference method

$$v_z[i, j - 1] = v_z[i, j + 1] - \frac{2h}{v_z} \left( F_z - v_r \frac{\partial v_z}{\partial r} \right) . \quad (\text{D.18})$$

### D.3.1 $i \neq 0$ and $i \neq N$

Central difference methods are used for points not on boundaries, giving the fully discretized form of (D.18) as

$$v_z[i, j - 1] = v_z[i, j + 1] - \frac{2h}{v_z[i, j]} \left( F_z[i, j] - v_r[i, j] \frac{v_z[i + 1, j] - v_z[i - 1, j]}{2h} \right) . \quad (\text{D.19})$$

**D.3.2**  $i = 0$ 

At  $r = 0$ , one takes  $v_r = 0$  and uses forward difference derivatives when required,

$$v_z[0, j - 1] = v_z[0, j + 1] - \frac{2hF_z[0, j]}{v_z[0, j]} . \quad (\text{D.20})$$

**D.3.3**  $i = N$ 

At the outer boundary, backwards difference methods are used to evaluate the radial derivatives,

$$v_z[N, j - 1] = v_z[N, j + 1] - \frac{2h}{v_z[N, j]} \left( F_z[N, j] - v_r[N, j] \frac{v_z[N, j] - v_z[N - 1, j]}{h} \right) . \quad (\text{D.21})$$

All of the calculations here required values to be known in two layers of  $z$  and so I must fill in one plot-hole which is how to get the process started (when only the top layer of  $z$  is known). For this case, one must take a forward difference derivative in  $z$  to obtain a second layer and then the previous calculations which use central differences can be employed.

# E Permissions

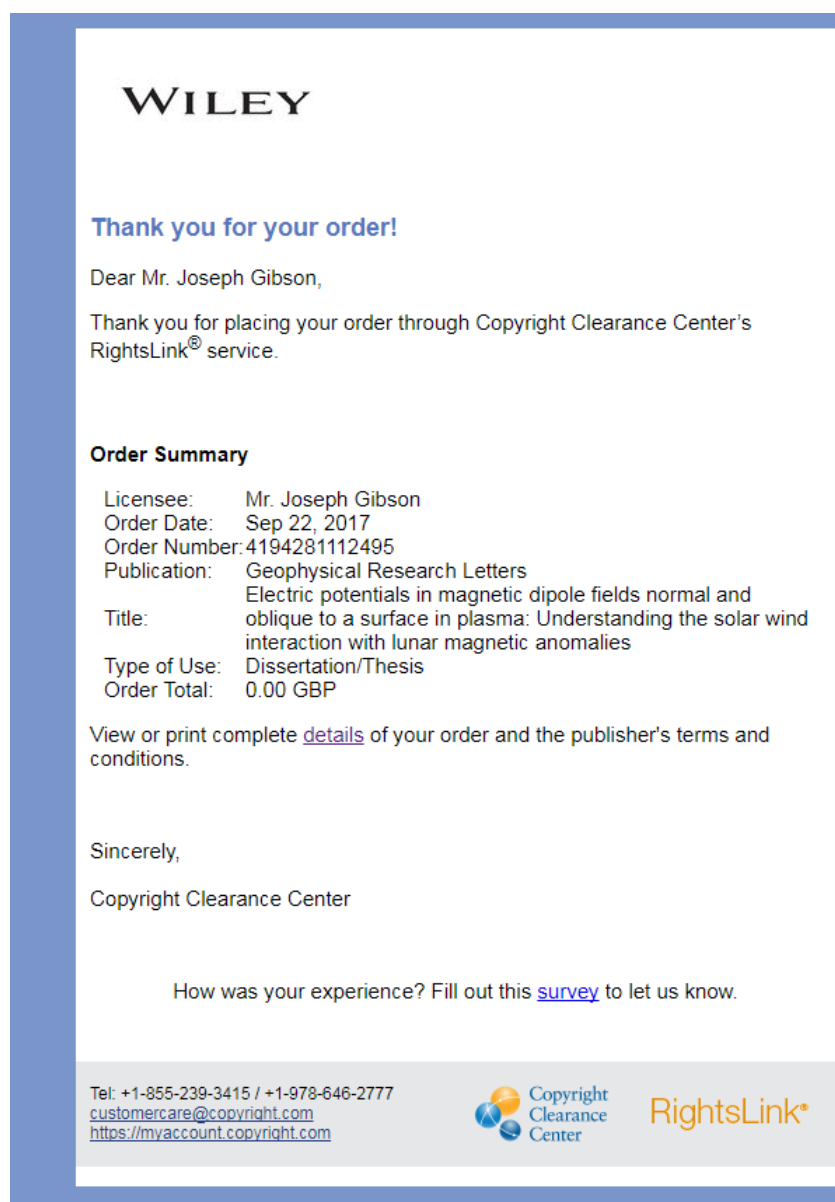


Figure E.1: Permission for Figs. 4.1 and 4.18 (a) originally in [1].



Header

**Your request has been submitted**

Dear Mr. Joseph Gibson,

Thank you for placing your request through Copyright Clearance Center's RightsLink® service.

The publisher's permissions team will review your request within five business days. Upon approval of your request, you will receive an email quoting the royalty fee and terms set by Cambridge University Press.

You must accept the fee and terms to complete the order. If you decline, your order will not be filled and you will not be charged. If Cambridge University Press denies your request, you will be notified by email.

**Order Summary**

Licensee:	Mr. Joseph Gibson
Order Date:	Sep 22, 2017
Order Number:	501312578
Publication:	Journal of Plasma Physics
Title:	Mapping of force fields in a capacitively driven radiofrequency plasma discharge
Type of Use:	Dissertation/Thesis
Order Total:	Not Available

View or print complete [details](#) of your request.

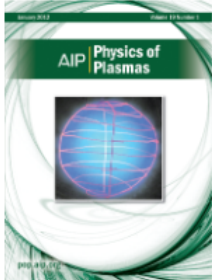
Sincerely,

Copyright Clearance Center

How was your experience? Fill out this [survey](#) to let us know.

Tel: +1-855-239-3415 / +1-978-646-2777  
[customercare@copyright.com](mailto:customercare@copyright.com)  
<https://myaccount.copyright.com>

Figure E.2: Permission for Fig. 4.18 (b) originally in [2].



**Thank you for your order!**

Dear Mr. Joseph Gibson,

Thank you for placing your order through Copyright Clearance Center's RightsLink® service.

**Order Summary**

Licensee:	Mr. Joseph Gibson
Order Date:	Sep 22, 2017
Order Number:	4194290078428
Publication:	Physics of Plasmas
Title:	Motions of dust particles in a complex plasma with an axisymmetric nonuniform magnetic field
Type of Use:	Thesis/Dissertation
Order Total:	0.00 GBP

View or print complete [details](#) of your order and the publisher's terms and conditions.

Sincerely,

Copyright Clearance Center

How was your experience? Fill out this [survey](#) to let us know.

Tel: +1-855-239-3415 / +1-978-646-2777  
[customercare@copyright.com](mailto:customercare@copyright.com)  
<https://myaccount.copyright.com>





Figure E.3: Permission for Fig. 4.18 (c) originally in [3].

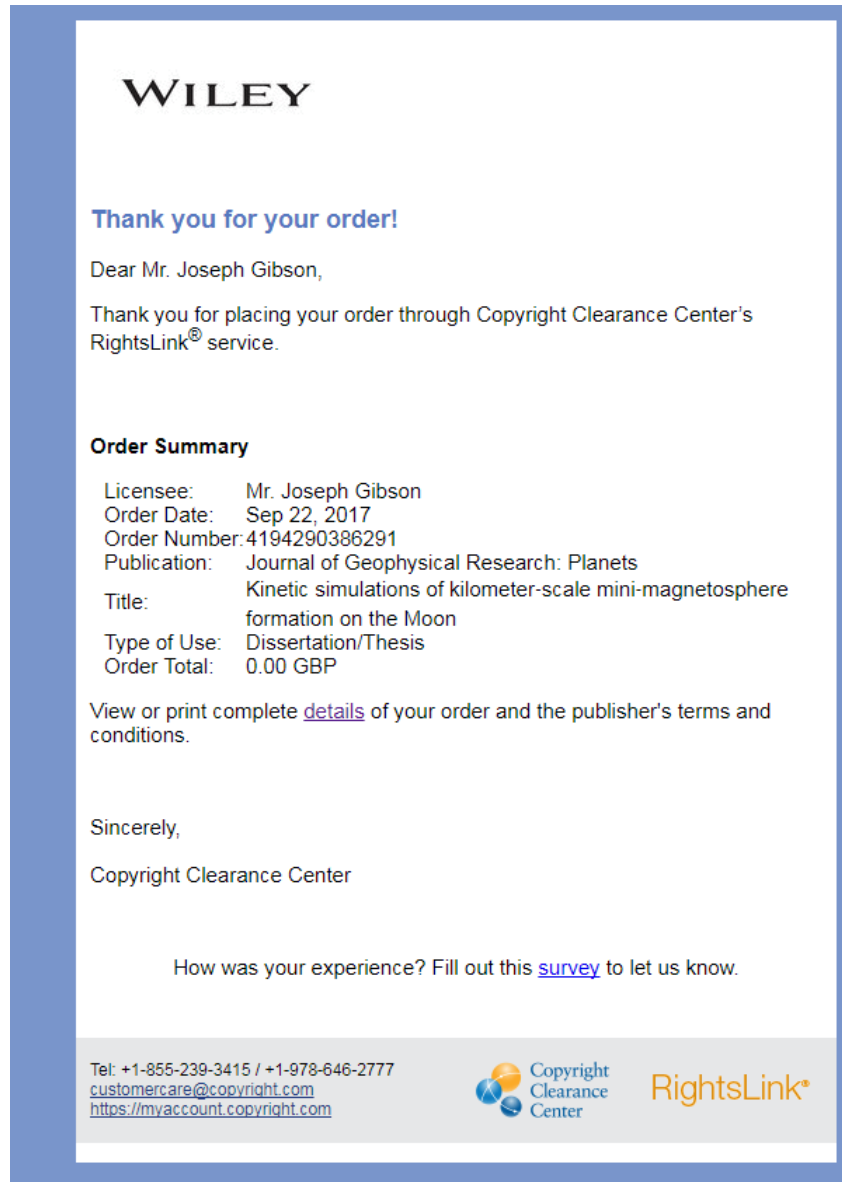


Figure E.4: Permission for Fig. 4.19 originally in [4].

# Bibliography

- [1] Wang, X., Howes, C., Horányi, M., and Robertson, S. *Geophysical Research Letters* **40**(9), 1686–1690 (2013). 17, 73, 74, 160
- [2] Dropmann, M., Chen, M., Sabo, H., Laufer, R., Herdrich, G., Matthews, L., and Hyde, T. W. *Journal of Plasma Physics* **82**(4) (2016). 17, 73, 161
- [3] Saitou, Y. *Physics of Plasmas* **23**(1), 013709 (2016). 17, 26, 75, 162
- [4] Zimmerman, M., Farrell, W., and Poppe, A. *Journal of Geophysical Research: Planets* **120**(11), 1893–1903 (2015). 17, 75, 135, 163
- [5] Alfvén, H. *Physics: 1963-1970* **4**, 306 (1964). 19
- [6] Nishikawa, K. and Wakatani, M. *Plasma Physics: basic theory with fusion applications*, volume 8. Springer Science & Business Media, (2013). 19
- [7] Jones, B. and Faraday, M. *The life and letters of Faraday*, volume 2. Cambridge University Press, (2010). 19
- [8] Crookes, W. *Journal of the Franklin Institute* **108**(5), 305–316 (1879). 19
- [9] Thomson, J. J. *The London, Edinburgh, and Dublin Philosophical Magazine and Journal of Science* **44**(269), 293–316 (1897). 19
- [10] Francis, F. C. et al. *Plasma Physics* (1984). 20, 34, 36
- [11] Christophorou, L. G. and Olthoff, J. K. *Fundamental electron interactions with plasma processing gases*. Springer Science & Business Media, (2012). 20
- [12] Tonks, L. *American Journal of Physics* **35**(9), 857–858 (1967). 20
- [13] Langmuir, I. *Electr. Rev* **26**, 731–735 (1923). 20
- [14] Langmuir, I., Found, C., and Dittmer, A. *Science* **60**(1557), 392–394 (1924). 20
- [15] Merlino, R. L. *Plasma Physics Applied* **81**, 73–110 (2006). 21
- [16] Havnes, O., Goertz, C., Morfill, G., Grün, E., and Ip, W. *Journal of Geophysical Research: Space Physics* **92**(A3), 2281–2287 (1987). 21
- [17] Laframboise, J. G. Technical report, TORONTO UNIV DOWNSVIEW (ONTARIO) INST FOR AEROSPACE STUDIES, (1966). 21

- 
- [18] Rao, N., Shukla, P., and Yu, M. Y. *Planetary and space science* **38**(4), 543–546 (1990). 21, 24
- [19] Shukla, P. and Silin, V. *Physica Scripta* **45**(5), 508 (1992). 21
- [20] Barkan, A., Merlino, R. L., and Dangelo, N. *Physics of Plasmas* **2**(10), 3563–3565 (1995). 22, 24
- [21] Merlino, R., Barkan, A., Thompson, C., and Dangelo, N. *Physics of Plasmas* **5**(5), 1607–1614 (1998). 22
- [22] Chow, V. and Rosenberg, M. *Planetary and Space Science* **43**(5), 613–618 (1995). 22
- [23] Shukla, P. and Rahman, H. *Physics of Plasmas* **3**(1), 430–431 (1996). 22
- [24] Shukla, P. and Rahman, H. *Planetary and space science* **46**(5), 541–543 (1998). 22
- [25] Jatenco-Pereira, V., CL Chian, A., and Rubab, N. (2014). 22
- [26] El-Wakil, S., Zahran, M., El-Shewy, E., and Abdelwahed, H. In *Proceedings of the 7th Conference on Nuclear and Particle Physics*, 11–15, (2009). 22
- [27] Chowdhury, N. and Mamun, A. *arXiv preprint arXiv:1707.02394* (2017). 22
- [28] Verheest, F. *Space Science Reviews* **77**(3), 267–302 (1996). 23
- [29] Meuris, P., Verheest, F., and Lakhina, G. *Planetary and space science* **45**(4), 449–454 (1997). 23
- [30] Goree, J. *Plasma Sources Science and Technology* **3**(3), 400 (1994). 23
- [31] Vladimirov, S., Ostrikov, K., Yu, M., and Stenflo, L. *Physical Review E* **58**(6), 8046 (1998). 23
- [32] Rosenberg, M. and Kalman, G. *Physical Review E* **56**(6), 7166 (1997). 23
- [33] Chen, F. F. *Physics of Plasmas* **2**(6), 2164–2175 (1995). 23
- [34] Lieberman, M. A. and Lichtenberg, A. J. *Principles of plasma discharges and materials processing*. John Wiley & Sons, (2005). 23
- [35] May, G. S. and Spanos, C. J. *Fundamentals of semiconductor manufacturing and process control*. John Wiley & Sons, (2006). 23
- [36] Selwyn, G. S., McKillop, J., Haller, K. L., and Wu, J. *Journal of Vacuum Science & Technology A: Vacuum, Surfaces, and Films* **8**(3), 1726–1731 (1990). 23
-

- 
- [37] Potter, D., Bowman, R., Peters, L., and Corporation, I. C. E. *Cost Effective IC Manufacturing, 1998-1999*. Integrated Circuit Engineering Corporation, (1997). 23
- [38] Abdullah, M. F., Osman, M. K., Somari, N. M., Ani, A. I. C., Appanan, S. P. R. S., and Hooi, L. K. In *Control System, Computing and Engineering (ICCSCE), 2016 6th IEEE International Conference on*, 507–511. IEEE, (2016). 23
- [39] Vijayakumar, P., Suresh, V. B., and Kundu, S. In *Test Conference (ITC), 2011 IEEE International*, 1–8. IEEE, (2011). 23
- [40] Selwyn, G. S., Singh, J., and Bennett, R. *Journal of Vacuum Science & Technology A: Vacuum, Surfaces, and Films* **7**(4), 2758–2765 (1989). 24
- [41] Selwyn, G. S. In *Integrated Reliability Workshop, 1995. Final Report., International*, 122–129. IEEE, (1995). 24
- [42] Olevanov, M., Mankelevich, Y. A., and Rakhimova, T. *Journal of Experimental and Theoretical Physics* **98**(2), 287–304 (2004). 24
- [43] Boufendi, L. and Bouchoule, A. *Plasma Sources Science and Technology* **11**(3A), A211 (2002). 24
- [44] Schill, R. A. *Laser and Particle Beams* **20**(02), 341–357 (2002). 24
- [45] Li, Y.-f., Konopka, U., Jiang, K., Shimizu, T., Höfner, H., Thomas, H., and Morfill, G. *Applied Physics Letters* **94**(8), 081502 (2009). 24
- [46] Kurimoto, Y., Matsuda, N., Uchida, G., Iizuka, S., Suemitsu, M., and Sato, N. *Thin Solid Films* **457**(2), 285–291 (2004). 24
- [47] Vladimirov, S. V. and Ostrikov, K. *Physics Reports* **393**(3), 175–380 (2004). 24
- [48] Ticoş, C., Jepu, I., Lungu, C., Chiru, P., Zaroschi, V., and Lungu, A. *Applied Physics Letters* **97**(1), 011501 (2010). 24
- [49] Hayashi, Y. and Tachibana, K. *Japanese journal of applied physics* **33**(6A), L804 (1994). 24
- [50] Chu, J. and Lin, I. *Physical review letters* **72**(25), 4009 (1994). 24
- [51] Thomas, H., Morfill, G., Demmel, V., Goree, J., Feuerbacher, B., and Möhlmann, D. *Physical Review Letters* **73**(5), 652 (1994). 24
- [52] Morfill, G. E. and Ivlev, A. V. *Reviews of modern physics* **81**(4), 1353 (2009). 24
- [53] Juan, W.-T., Chen, M.-H., and Lin, I. *Physical Review E* **64**(1), 016402 (2001). 26
-

- 
- [54] Nosenko, V., Zhdanov, S., Ivlev, A., Morfill, G., Goree, J., and Piel, A. *Physical review letters* **100**(2), 025003 (2008). 26
- [55] Knappek, C., Ivlev, A., Klumov, B., Morfill, G., and Samsonov, D. *Physical review letters* **98**(1), 015001 (2007). 26
- [56] De Gennes, P.-G. *Reviews of modern physics* **64**(3), 645 (1992). 26
- [57] Konopka, U., Samsonov, D., Ivlev, A., Goree, J., Steinberg, V., and Morfill, G. *Physical Review E* **61**(2), 1890 (2000). 26, 75
- [58] Cheung, F., Samarian, A., and James, B. *Physica Scripta* **2002**(T98), 143 (2002). 26
- [59] Cheung, F., Samarian, A., and James, B. *New Journal of Physics* **5**(1), 75 (2003). 26
- [60] Karasev, V. Y., Dzljeva, E., Ivanov, A. Y., and Eikhvald, A. *Physical Review E* **74**(6), 066403 (2006). 26
- [61] Carstensen, J., Greiner, F., Hou, L.-J., Maurer, H., and Piel, A. *Physics of Plasmas* **16**(1), 013702 (2009). 26
- [62] Matyash, K., Fröhlich, M., Kersten, H., Thieme, G., Schneider, R., Hannemann, M., and Hippler, R. *Journal of Physics D: Applied Physics* **37**(19), 2703 (2004). 26
- [63] Law, D. A. . 26, 75
- [64] Horányi, M., Szalay, J., Kempf, S., Schmidt, J., Grün, E., Srama, R., and Sternovsky, Z. *Nature* **522**(7556), 324–326 (2015). 26
- [65] Halekas, J., Saito, Y., Delory, G., and Farrell, W. *Planetary and Space Science* **59**(14), 1681–1694 (2011). 27
- [66] Poppe, A. and Horányi, M. *Journal of Geophysical Research: Space Physics* **115**(A8) (2010). 27
- [67] Clack, D., Kasper, J., Lazarus, A., Steinberg, J., and Farrell, W. *Geophysical research letters* **31**(6) (2004). 27
- [68] Stubbs, T., Farrell, W., Halekas, J., Burchill, J., Collier, M., Zimmerman, M., Vondrak, R., Delory, G., and Pfaff, R. *Planetary and Space Science* **90**, 10–27 (2014). 27
- [69] Stubbs, T. J., Vondrak, R. R., and Farrell, W. M. *Advances in Space Research* **37**(1), 59–66 (2006). 27
- [70] McCoy, J. E. and Criswell, D. R. In *Lunar and Planetary Science Conference Proceedings*, volume 5, 2991–3005, (1974). 27
-

- 
- [71] Coleman, P. J., Russell, C. T., Sharp, L. R., and Schubert, G. *Physics of the Earth and Planetary Interiors* **6**(1-3), 167–174 (1972). 27
- [72] Kramer, G. Y., Besse, S., Dhingra, D., Nettles, J., Klima, R., Garrick-Bethell, I., Clark, R. N., Combe, J.-P., Head, J. W., Taylor, L. A., et al. *Journal of Geophysical Research: Planets* **116**(E9) (2011). 27
- [73] Bamford, R., Alves, E., Cruz, F., Kellett, B., Fonseca, R., Silva, L., Trines, R., Halekas, J., Kramer, G., Harnett, E., et al. *arXiv preprint arXiv:1505.06304* (2015). 28
- [74] Wang, X., Horányi, M., and Robertson, S. *Journal of Geophysical Research: Space Physics* **117**(A6) (2012). 28, 73, 135
- [75] Garrick-Bethell, I., Head, J. W., and Pieters, C. M. *Icarus* **212**(2), 480–492 (2011). 28
- [76] Hemingway, D. and Garrick-Bethell, I. *Journal of Geophysical Research: Planets* **117**(E10) (2012). 28
- [77] Bamford, R., Kellett, B., Bradford, J., Todd, T. N., Benton, M., Stafford-Allen, R., Alves, E., Silva, L., Collingwood, C., Crawford, I., et al. *Acta Astronautica* **105**(2), 385–394 (2014). 29
- [78] Jaynes, E. T. *The maximum entropy formalism* **15** (1979). 31
- [79] Cameron, R. *Dust-Plasma Interactions In The Plasma Edge Region*. PhD thesis. 32
- [80] Franklin, R. N. *Oxford and New York, Clarendon Press, 1976. 258 p.* (1976). 39
- [81] Franklin, R. *Journal of Physics D: Applied Physics* **36**(22), 2821 (2003). 41
- [82] Kennedy, R. and Allen, J. *Journal of plasma physics* **69**(6), 485–506 (2003). 45
- [83] Chen, F. F. *Plasma Sources Science and Technology* **18**(3), 035012 (2009). 45
- [84] Paschmann, G., Haerendel, G., Sckopke, N., Möbius, E., Lühr, H., and Carlson, C. *Journal of Geophysical Research: Space Physics* **93**(A10), 11279–11294 (1988). 48
- [85] Stasiewicz, K., Shukla, P., Gustafsson, G., Buchert, S., Lavraud, B., Thide, B., and Klos, Z. *Physical review letters* **90**(8), 085002 (2003). 48
- [86] Petkaki, P. and Dougherty, M. K. *Geophysical research letters* **28**(2), 211–214 (2001). 48
- [87] Kivelson, M., Khurana, K., Walker, R., Warnecke, J., et al. *Science* **274**(5286), 396 (1996). 48
-



- 
- [88] Yeroshenko, Y. G., Styashkin, V., Riedler, W., Schwingenschuh, K., and Russel, C. *Astronomy and Astrophysics* **187**, 69 (1987). 48
- [89] Mann, I., Meyer-Vernet, N., and Czechowski, A. *Physics reports* **536**(1), 1–39 (2014). 48
- [90] Sauer, K., Dubinin, E., and McKenzie, J. In *AIP Conference Proceedings*, volume 649, 220–223. AIP, (2002). 48
- [91] Saleem, H. *Physics of plasmas* **13**(1), 012903 (2006). 48
- [92] Sakai, S., Watanabe, S., Morooka, M. W., Holmberg, M. K., Wahlund, J.-E., Gurnett, D. A., and Kurth, W. S. *Planetary and Space Science* **75**, 11–16 (2013). 48
- [93] Tolba, R., Moslem, W., El-Bedwehy, N., and El-Labany, S. *Physics of Plasmas* **22**(4), 043707 (2015). 48
- [94] Mamun, A. and Shukla, P. *Physics of Plasmas* **10**(11), 4341–4349 (2003). 49
- [95] Masood, W., Shah, H., Mushtaq, A., and Salimullah, M. *Journal of Plasma Physics* **75**(2), 217–233 (2009). 49
- [96] Korteweg, D. J. and De Vries, G. *The London, Edinburgh, and Dublin Philosophical Magazine and Journal of Science* **39**(240), 422–443 (1895). 49
- [97] Adlam, J. and Allen, J. *Philosophical Magazine* **3**(29), 448–455 (1958). 50
- [98] Allen, J. and Gibson, J. *Physics of Plasmas* **24**(4), 042106 (2017). 50
- [99] Ohsawa, Y. *The Physics of fluids* **29**(3), 773–781 (1986). 62
- [100] Kakutani, T., Ono, H., Taniuti, T., and Wei, C.-C. *Journal of the Physical Society of Japan* **24**(5), 1159–1166 (1968). 62
- [101] McKenzie, J. and Doyle, T. *Physics of Plasmas* **8**(10), 4367–4374 (2001). 62
- [102] Raju, G. G. *IEEE Transactions on dielectrics and electrical insulation* **11**(4), 649–673 (2004). 74
- [103] Jarvinen, R., Alho, M., Kallio, E., Wurz, P., Barabash, S., and Futaana, Y. *Geophysical Research Letters* **41**(7), 2243–2249 (2014). 75
- [104] Harnett, E. M. and Winglee, R. M. *Journal of Geophysical Research: Space Physics* **107**(A12) (2002). 75
- [105] Deca, J., Divin, A., Lapenta, G., Lembège, B., Markidis, S., and Horányi, M. *Physical review letters* **112**(15), 151102 (2014). 75
- [106] Sheridan, T. E., Goeckner, M. J., and Goree, J. *Journal of Vacuum Science & Technology A: Vacuum, Surfaces, and Films* **8**(1), 30–37 (1990). 85
-

- 
- [107] Trottenberg, U., Oosterlee, C. W., and Schuller, A. *Multigrid*. Academic press, (2000). 106
- [108] Press, W. H. *Numerical recipes 3rd edition: The art of scientific computing*. Cambridge university press, (2007). 126
- [109] Dropmann, M., Laufer, R., Herdrich, G., Matthews, L. S., and Hyde, T. W. *Physical Review E* **92**(2), 023107 (2015). 135
- [110] Bouchoule, A. *Dusty plasmas: physics, chemistry, and technological impacts in plasma processing*. John Wiley & Sons Inc, (1999). 135
-